The Dissertation Committee for Jaroon Rungamornrat
certifies that this is the approved version of the following dissertation:

A Computational Procedure for Analysis of Fractures in Three Dimensional Anisotropic Media

Committee:

Mark E. Mear, Supervisor

Eric B. Becker

K. Ravi-Chandar

Huang Rui

John L. Tassoulas

A Computational Procedure for Analysis of Fractures in Three Dimensional Anisotropic Media

by

Jaroon Rungamornrat, B.S., M.S.

Dissertation

Presented to the Faculty of the Graduate School of

The University of Texas at Austin

in Partial Fulfillment

of the Requirements

for the Degree of

Doctor of Philosophy

The University of Texas at Austin

August 2004

Acknowledgments

I wish to express my appreciation and gratitude to my advisor Professor Mark E. Mear, for his excellent guidance and encouragement throughout this research.

I would also like to thank my Advisory Committee, Professor Eric B. Becker, K. Ravi-Chandar, John L. Tassoulas, and R. Huang, for their helpful suggestions and comments and especially to Professor C. Dawson for his useful guidance. Further, my great appreciation goes to the National Science Foundation for providing financial support for this work.

I would like to extend my thanks to all my colleagues and friends. In particular, I would like to thank Dr. Yishao Lai, Dillip Maniar and Bisen Lin for their friendship and help. Last but not least, I would like to thank my parents Yookloong and Boonma. Without their love and supports I would never finish this work.

Jaroon Rungamornrat

The University of Texas at Austin
August 2004

A Computational Procedure for Analysis of Fractures in Three Dimensional Anisotropic Media

Publication No. ____________________

Jaroon Rungamornrat, Ph.D.
The University of Texas at Austin, 2004

Supervisor: Mark E. Mear

A symmetric Galerkin boundary element method (SGBEM) is developed for analysis of fractures in three dimensional anisotropic, linearly elastic media, and the method is coupled with standard finite element procedures. Important features of the technique are that the formulation is applicable to general anisotropy, the kernels in the governing integral equations are only weakly-singular (of order $1/r$) hence allowing the application of standard C^o elements in the numerical treatment, and a special crack tip element is utilized which allows general mixed-mode fracture data (*viz.* the stress intensity factors) to be efficiently determined as a function of position along the crack front.

The weakly-singular, weak-form displacement and traction integral equations which constitute a basis for the SGBEM are obtained via a regularization technique. The technique utilizes a particular decomposition for the stress fundamental solution and for the strongly-singular kernel in order to facilitate an integration by parts via Stokes' theorem. The final integral equations contain only weakly-singular kernels (given explicitly in terms of a line integral) which are applicable to general anisotropic materials. These weakly-singular kernels are obtained by solving a system of partial differential equations via the Radon transform.

A symmetric formulation is developed by a suitable use of the weakly-singular displacement and traction integral equations. As part of the numerical implementation, a Galerkin approximation strategy is utilized to discretize the governing integral equations. Standard isoparametric C^o elements are employed everywhere except along the crack front where a special crack-tip elements is used. To demonstrate the accuracy and versatility of the method, various examples for cracks in both unbounded and finite domains are considered.

Finally, a symmetric coupling of the SGBEM and the standard finite element method is established. The coupling strategy exploits the versatility and capability of the finite element method to treat structures with complex geometry and loading, while employing the SGBEM to efficiently and accurately treat a (local) region containing the crack. In the numerical implementation, both conforming and nonconforming discretization along the interface of the two regions are treated. In addition, the coupling of the SGBEM with a commercial finite element code is explored and successfully implemented. Several examples are presented to illustrate the capability and accuracy of the method.

Contents

List of Tables

List of Figures

Chapter 1

INTRODUCTION

Significant progress in failure analysis over the past four decades has aided in the design and analysis of fracture critical and flaw/damage tolerant structures. Until recently, stress analysis of cracks has, for the most part, been limited to situations where the flaws can be treated either within the context of a two-dimensional boundary value problem or within the context of a relatively simple three-dimensional problem. It is now recognized, however, that to ensure the safety and integrity of complex structural components, it is necessary to be able to perform fully three-dimensional stress analysis for complex crack and component geometries, and this necessitates the use of numerical techniques developed specifically for this purpose.

For a wide variety of fracture mechanics applications, any inelastic deformation which may exist is contained within a small region near the crack tip (*viz.* small scale yielding pertains) and, as a consequence, a stress analysis based upon linear elasticity is appropriate. In this context, the quantities sought are the stress intensity factors which provide a measure of the dominant behavior of the stress field in the vicinity of the crack front. In three dimensional applications, fracture problems are often fully mixed-mode and it is necessary to have a computational procedure which can independently and accurately resolve all three stress intensity factors as functions of position along the crack front.

The purpose of this work is to develop such a computational procedure for treatment of three-dimensional boundary value problems involving cracks in anisotropic media. The methodology can be classified as a symmetric Galerkin boundary element method (SGBEM), and it has the important feature that it involves only weakly-singular kernels which are given in an explicit and simple form for general anisotropy. For the special case of isotropic material behavior the method is closely related to one developed by Li and Mear [28] and Li *et al.* [29], but it should be noted that the extension to general anisotropy necessitates the development of a new set of governing integral equations (or, more specifically, the development of a new set of kernels for these integral equations). The weakly-singular SGBEM developed here is well suited for a coupling with the standard finite element method (FEM), and such a coupling is implemented as part of this work. This coupled procedure allows for an accurate treatment of the crack (and a region of the domain in the neighborhood of the crack) while taking advantage of the efficient and flexible modeling capabilities of the FEM for treating the bulk of the structure.

In the next section we provide a review of the boundary element method (BEM) as applied to three-dimensional fracture analysis. We remark that there has been relatively little work in this area for anisotropic material behavior and, in particular, there appears to be no previous developments for weakly-singular, symmetric Galerkin boundary element methods. The chapter concludes with an overview of the specific theoretical and numerical developments which comprise this dissertation.

1.1 BEM for linearly elastic fracture analysis

An attractive feature of the boundary element method is that, in the absence of body force, the governing equations involve only integrals over the boundary of the domain rather than its volume. Unfortunately, when the standard boundary element formulation (in terms of a displacement integral equation obtained from Somigliana's identity) is specialized to fracture problems it suffers from a degeneracy associated with the fact that the integral equation lacks information about the traction acting on the crack faces (e.g Cruse [11]). One approach to overcome this difficulty is to employ a multi-domain technique in which the displacement integral equation is employed separately for sub-domains obtained by partitioning the body along a 'fictitious surface' which passes along the crack surface (e.g. [5], [35]). However, this technique gives rise to practical difficulties associated with introducing and treating the fictitious surfaces (especially when several cracks are to be treated), and it is generally recognized that it is advantageous to pursue an alternative approach in which a traction integral equation is used either instead of or in addition to a displacement integral equation.

Now, a traction integral equation can be readily obtained from Somigliana's identity by use of the strain-displacement relations and Hooke's law, but the integral equation obtained in this direct fashion contains a strongly-singular kernel (of order $1/r^3$) and its validity requires that the gradient of the displacements be continuous (e.g. [7], [32]). The strongly-singular kernel requires special theoretical and numerical considerations and, in particular, C^1 elements must be adopted for a proper numerical treatment of the integral equation (e.g. [20]).

Toward alleviating the difficulties posed by the strongly-singular kernel, singularity-reduced traction integral equations have been sought through a regularization process involving an integration by parts. In the context of three dimensional crack modeling, the first such singularity-reduced traction integral equations appears to be the Cauchy-singular (of order $1/r^2$) relation obtained independently by Bui [9] and Weaver [43]. Their integral equation is restricted to mode-I loading of a planar crack in an unbounded domain, but the result was later generalized by Slάdek and Slάdek [37] to allow treatment of curved cracks and mixed mode loading. It should be noted that while the kernel appearing in these equations is Cauchy-singular rather than strongly-singular, there remains the requirement that the derivatives of the relative crack-face displacement be continuous. In an attempt to further reduce the order of the kernel, Cruse [12], Liu and Rudophi [30], and Slάdek and Tanaka [38] exploited certain identities to obtain 'weakly-singular' traction integral equations, but the nature of the requirement on the regularity of the crack-face displacement data remains unclear for these integral relations.

The first weakly-singular, weak-form traction integral equation for fracture analysis is that by Gu and Yew [21]. Their development rests upon Weaver's [43] Cauchy-singular traction integral equation and, as such, is restricted to an isolated planar crack subjected to mode-I loading. A generalization of this work was carried out by Xu and Ortiz [46] who developed a variational boundary integral equation to treat an isolated crack with arbitrary geometry and mixed-mode loading. To obtain their integral equation, Xu and Ortiz [46] utilized the fact that the crack-face displacement can be represented in terms of a continuous distribution of dislocation loops. An important feature of this traction integral equation is that it involves a weakly-singular kernel (of order $1/r$) and, as a consequence, the crack-face displacement data need only be continuous hence allowing standard C^o elements to be employed in the numerical treatment. The limitation of the work is that it applies only for a crack in an unbounded domain.

Li and Mear [28] and Li *et al.* [29] presented a systematic technique for regularizing both the displacement and traction integral equations associated with three dimensional isotropic media, and by using this technique they were able to obtain a pair of weakly-singular, weak-form integral equations applicable to cracks in a finite domain. We remark that their final formulation is closely related to that of Bonnet [8], although the latter work is for elasticity problems in the absence of a crack. Li *et al.* [29] used the pair of weakly-singular displacement and traction integral equations as the basis for a symmetric Galerkin boundary element method, and they successfully implemented the formulation to allow treatment of general boundary value problems for bodies containing cracks. An important aspect of their numerical implementation is the use of a special crack tip element; the element has the novel feature that there exist degrees of freedom associated with nodes on the crack front and these degrees of freedom are directly related to the stress intensity factors. Using this special element, Li *et al.* [29] and Xiao [45] were able to obtain highly accurate stress intensity factor data for mixed-mode fracture problems even when relatively coarse meshes were employed. However, the formulation is applicable only to isotropic solids, and the technique employed to obtain the regularized integral equations does not readily lend itself to a generalization to treat material anisotropy.

1.1.1 Anisotropy

The presence of material anisotropy significantly increases the complexity of boundary value problems and, in fact, it can give rise to mixed-mode fracture conditions even for simple crack configurations and applied loads which would be otherwise strictly mode-I were the material isotropic. A need to treat material anisotropy arises in a variety of applications including those involving single crystals (e.g. single crystal turbine blades, various micro-electro-mechanical devices), those involving fracture of anisotropic rock and, perhaps most commonly, those involving the failure of composite materials. It should be noted that modeling anisotropic material behavior within the context of singular integral equations is quite challenging due to the complexity of the associated fundamental solutions.

Work on integral equation modeling for cracks in three-dimensional anisotropic media is modest in comparison to such work for isotropic material behavior. *Sáze et al.* [35] utilized the displacement fundamental solution of Pan and Chou [34] to obtain a displacement integral equation suitable for use in a standard boundary element method. Their formulation is specific to transversely isotropic materials and requires that the multi-domain approach be employed in order to treat a crack. The singularity-reduced traction integral developed by Slάdek and Slάdek [37] which was discussed earlier actually applies to general anisotropy, but (in addition to the limitations already mentioned) it explicitly involves the stress fundamental solution which is difficult to compute for anisotropic material behavior. More recently, Slάdek *et al*. [39] established completely regularized integral equations for anisotropic media which are applicable to cracks in both unbounded and finite domains. However, for the integral to be valid there remains the requirement that the displacement data be C^1 and, further, the integral equations involve both the gradient of the displacement fundamental solution and the stress fundamental solution.

Work toward developing weak-form, weakly-singular traction integral equations for cracks in anisotropic media is particularly limited. Becache *et al*. [4] utilized a double layer potential technique along with the Fourier transform to obtain a regularized integral equation for three dimensional anisotropic elastodynamics. Their final result is in the frequency domain and is left expressed in terms of the Fourier transform variables associated with the spatial coordinates. In principle, the result can be specialized to the static case by taking a limit in which the frequency tends to zero, but the treatment of this limiting process as well as the subsequent inversion of the Fourier transform appears to be quite complicated. Recently, Xu [47] utilized Lothe's [31] expression for the interaction energy between dislocation loops to extend the formulation by Xu and Ortiz [46] to allow treatment of material anisotropy. The resulting integral equation contains a weakly-singular kernel but its application is limited to a crack in an unbounded domain. A SGBEM treatment for finite domains, in terms of a set of weakly-singular, weak form integral equations analogous to that developed for isotropy by Li *et al*. ([29]) has not previously been established.

1.1.2 Drawback of BEM for large problems

Boundary element methods were originally devised to model elastic bodies in the absence of cracks, but it is their use in stress analysis of cracks which is of primary interest here. The SGBEM developed by Li *et al.* ([29]) (and extended in this work to account for material anisotropy) can certainly be used to analyze boundary values problems in which a crack is not present but, as the geometry to be modeled becomes increasingly more complex, it tends to become computationally expensive as compared with the standard finite element method. Even though the SGBEM gives rise to a symmetric coefficient matrix, the matrix is dense and each of its entries must be computed by means of a double surface integration involving a weakly-singular kernel. In contrast, the FEM involves a sparse coefficient matrix the entries of which are readily computed. This motivates the development of a coupled SGBEM-FEM strategy in which the SGBEM is used to model the crack and a region immediately surrounding the crack, while the FEM is used to model the remainder of the (possibly very complex) domain.

Within the context of elastic boundary value problems without cracks, there has been significant work directed toward coupling the standard BEM with the FEM (e.g. [36], [14], [15]) and toward coupling a strongly-singular SGBEM with the FEM (e.g. [17], [22], [48]). With regard to the weakly-singular SGBEM of Li *et al.* ([29]), Xiao [45] developed the equations governing a SGBEM-FEM coupling and Frangi and Novati [16] recently implemented these equations for the special case of pure traction boundary value problems. It should be noted that the latter coupling has been carried out only for the case in which the SGBEM and FEM meshes conform on the interface separating the two regions and, of course, it is restricted to isotropic materials.

Here, a SGBEM-FEM coupling is pursued for treatment of three dimensional cracks in general anisotropic media and, importantly, the coupling is carried out in such a way that it allows independent mesh refinements to be employed on the SGBEM and FEM regions. The overall strategy is to utilize the SGBEM to model a local region containing the fractures, to employ the extensive capabilities of the FEM to treat the remaining domain, and to couple the two models together through a weak enforcement of the traction and displacement continuity conditions. A special case of this coupling is that which arises when the meshes conform on the interface, but we emphasize that the freedom to mesh the two regions independently can in certain cases significantly simplify the modeling effort. We also note that the formulation and implementation is carried out for general boundary value problems without restrictions on the type of boundary conditions which can be applied on the regular boundary.

1.2 Overview of the dissertation

As stated above, the objective of this dissertation is to develop a computational technique for analysis of fractures in three-dimensional, anisotropic linearly elastic media. The remainder of the dissertation is organized as follows.

In Chapter 2, a systematic procedure is followed to establish weakly-singular, weak-form integral equations for displacement discontinuities in linearly elastic, anisotropic media. Singularity-reduced displacement and traction integral equations are first obtained for an isolated displacement discontinuity. A regularization of the Cauchy singular (order $1/r^2$) and strongly-singular (order $1/r^3$) kernels which appear in the standard formulation is accomplished by constructing certain decompositions for the kernels, and then employing these decompositions to affect an integration by parts via Stokes' theorem. The decompositions themselves involve kernels which are weakly-singular, and these kernels are evaluated in explicit and concise form through an application of the Radon transform. Representations for the elastic fields induced by dislocations are discussed in addition to those for cracks in order to allow a connection to be made to relevant literature on dislocation mechanics. Finally, the formulation is extended to cracks in a finite domain. The regularization process for this case is analogous to that for an isolated crack except that the integral equations contain additional terms associated with the finite boundary of the domain. The displacement and traction integral equations which are obtained apply to both embedded and surface breaking cracks.

In Chapter 3, a symmetric Galerkin boundary element method (SGBEM) is established for analysis of cracks in both unbounded and finite domains. The technique is based upon the weakly-singular, weak-form traction and displacement integral equations developed in Chapter 2. Important features of the formulation are that it is symmetric, the integral equations contain only weakly-singular kernels (of order $1/r$), and it is applicable to general material anisotropy. In the numerical implementation, standard C^o isoparametric elements are employed everywhere except along the crack front where the special crack tip element developed by Li *et al.* ([29]) is utilized. This element incorporates the proper asymptotic crack-tip behavior by means of special degrees of freedom at nodes along the crack front and, importantly, the stress intensity factors are given directly in terms of these degrees of freedom. To demonstrate the versatility and accuracy of the method, several numerical examples are considered for cracks in an unbounded domain and for embedded and surface breaking cracks in a finite domain. It is found that highly accurate stress intensity factor data can be obtained, even for mixed-mode problems, using relatively coarse meshes.

In Chapter 4, a symmetric coupling of the SGBEM and the standard FEM is established. The strategy followed is to utilize the SGBEM for treatment of the crack and a region immediately surrounding the crack, while employing standard

FEM techniques for the remainder of the structure. Symmetry of the coupled formulation is achieved by properly combining a system of integral equations governing the region treated by the SGBEM with a weak statement (obtained in the usual way from the principle of virtual work) governing the region modeled by the FEM. In the development and implementation, both conforming and nonconforming discretizations at the interface separating the two regions are considered to allows independent meshing of the SGBEM and FEM regions. Various examples, especially ones involving surface breaking cracks, are treated to illustrate the accuracy, robustness and versatility of the coupled SGBEM-FEM strategy. Finally, a coupling of the SGBEM with the commercial software package ABAQUS is carried out within the context of both conforming and nonconforming meshes.

Chapter 2

Weakly-singular Integral Equations for Displacement Discontinuities

Consider a homogeneous, anisotropic, linearly elastic domain containing an isolated displacement discontinuity as shown schematically in Figure 2.1. The surface of the discontinuity is comprised of an upper and lower surface[1] S^+ and S^-, respectively, and these surfaces are geometrically coincident such that their unit normals (taken to be directed 'into' the discontinuity) satisfy $n_i^+ = -n_i^-$. It is assumed that the domain in which the discontinuity is embedded is free of body force and that remote loading is absent. Further, it is assumed that, as is typical, the traction acting on the discontinuity is locally self-equilibrated in that it satisfies $\boldsymbol{t}^+ = -\boldsymbol{t}^-$ at each point on the geometrically coincident surfaces.

Somigliana's identity is readily specialized to this case, with the result being an integral relation giving the displacement $\boldsymbol{u}$ at a point $\boldsymbol{x}$ in the domain in terms

---

[1] Here and in what follows, the superscripts + and - are used to indicate that the quantity is associated with the 'upper' and 'lower' surface of the crack, respectively.

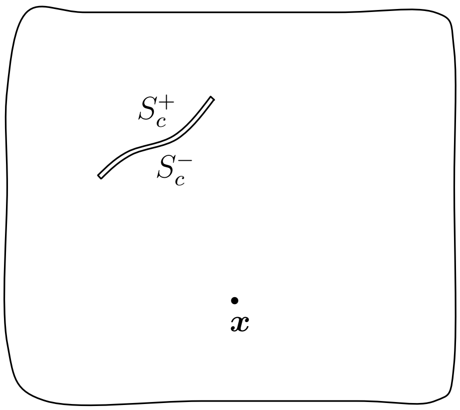

Figure 2.1: Schematic of an isolated discontinuity.

of data on the surface of the discontinuity. With $S \equiv S^+$ and $n_i \equiv n_i^+$, this well known result takes the form

$$u_p(\boldsymbol{x}) = -\int_S S_{ij}^p(\boldsymbol{\xi} - \boldsymbol{x})\, n_i(\boldsymbol{\xi})\, \Delta u_j(\boldsymbol{\xi})\, dS(\boldsymbol{\xi}) \tag{2.1}$$

in which the kernel S_{ij}^p corresponds to the stress induced by a unit concentrated load acting in the p^{th} coordinate direction[2], and where $\Delta u_j(\boldsymbol{\xi}) = u_j^+(\boldsymbol{\xi}) - u_j^-(\boldsymbol{\xi})$ denotes the jump in displacement across the discontinuity (i.e. the relative displacement of the two geometrically coincident surfaces associated with the displacement discontinuity). Utilizing this form of Somigliana's identity, an integral relation for the stress is readily obtained as

$$\sigma_{lk}(\boldsymbol{x}) = \int_S \Sigma_{ij}^{lk}(\boldsymbol{\xi} - \boldsymbol{x})\, n_i(\boldsymbol{\xi})\, \Delta u_j(\boldsymbol{\xi})\, dS(\boldsymbol{\xi}) \tag{2.2}$$

where

$$\Sigma_{ij}^{lk} \equiv E_{lkpq} \frac{\partial S_{ij}^p}{\partial \xi_q} \tag{2.3}$$

---

[2] The use of both superscripts and subscripts in expressing the *cartesian* components of tensor valued quantities is simply a matter of notational convenience. See Appendix A for a description of the notation adopted for the fundamental solution.

in which E_{lkpq} are the elastic moduli. These integral relations apply for points $\boldsymbol{x}$ which are not on the surface of the discontinuity and, owing to the Cauchy-type singular kernel in (2.1) and the strongly-singular kernel in (2.2), proper care must be exercised in considering a limit as $\boldsymbol{x}$ approaches this surface. In particular, when (2.2) is to be utilized to obtain a relation for the traction on the surface of the discontinuity, it is necessary to properly treat and interpret the limit in terms of a Hadamaard finite part integral.

We now distinguish two special types of displacement discontinuities: the first is a dislocation for which $b_i \equiv \Delta u_i$ is a prescribed constant, and the second is a crack for which the traction $t_i \equiv t_i^+ = -t_i^-$ is prescribed and the relative displacement Δu_i is to be determined (subject to the condition that it vanishes along the edge of the discontinuity, *viz.* the crack front). For the latter case it is important to note that the displacement relation (2.1) does not contain information about the traction acting on the discontinuity, hence it is 'degenerate' in this sense and does not provide a basis for obtaining a useful integral equation for the unknown relative crack-face displacements. Instead, attention must necessarily be directed toward the stress relation (2.2) and, specifically, toward its use in obtaining a traction integral equation.

Now, for either of these two types of discontinuities it is of interest to regularize the integral relations to render them more suitable for numerical analysis. What is sought is to reduce the 'strength' of the singularity associated with the kernels by means of an integration by parts. Such results are well known in the field of dislocation mechanics (e.g. Hirth and Lothe [24]; Lothe [31]), and more recently there has been significant work directed towards achieving such regularization for cracks (e.g. Xu and Ortiz [46], Li and Mear [28], Becache *et al.* [4], Xu [47]). The purpose of the work presented in this chapter is to provide a straightforward, complete development of such singularity-reduced integral equations for application to displacement discontinuities in anisotropic media.

2.1 Development of singularity-reduced relations

We first provide an overview of the regularization strategy utilized to obtain singularity-reduced integral relations, after which we develop in detail the kernels which appear in these relations. The development is carried out in the context of an isolated discontinuity as introduced above, but we emphasis that the primary objective of this work is to develop a full set of weakly-singular, weak-form equations applicable to treatment of cracks in a finite domain, and these results will be established using the results obtained for an isolated discontinuity. In this context we remark that whereas a displacement integral equation following from (2.1) is not essential for treating an isolated crack (when it is the relative displacements Δu_i or, more specifically, the stress intensity factors which are sought), its counterpart for finite domains is relevant for developing strategies to treat general fracture problems. For this reason, a singularity-reduced displacement integral equation is discussed even for the case of an isolated discontinuity.

Toward developing the singularity-reduced integral equations, we first establish their existence in terms of certain weakly-singular kernels. Explicit partial differential equations governing these kernels are derived and, after the overall form of the integral equations is established, these differential equations are solved by an application of the Radon transform. Results are obtained for general displacement discontinuities, but these results then specialized for treatment of dislocations and cracks. We begin with the displacement integral equation after which a treatment of the stress is provided leading, finally, to a weakly-singular, weak-form traction integral equation.

2.1.1 Displacement

As a means to develop a singularity-reduced displacement integral equation, we introduce a decomposition for S^p_{ij} which is analogous to that utilized by Li and Mear [28] in their treatment of isotropic media. Specifically, we write

$$S^p_{ij}(\boldsymbol{\xi} - \boldsymbol{x}) = F^p_{ij}(\boldsymbol{\xi} - \boldsymbol{x}) + H^p_{ij}(\boldsymbol{\xi} - \boldsymbol{x}) \tag{2.4}$$

in which

$$H^p_{ij} \equiv \delta_{pj} \frac{\partial}{\partial \xi_i} \left(\frac{1}{4\pi r} \right) = -\frac{1}{4\pi} \frac{(\xi_i - x_i)\delta_{pj}}{r^3} \tag{2.5}$$

where $r = \|\boldsymbol{\xi} - \boldsymbol{x}\|$ is the distance between the field point $\boldsymbol{\xi}$ and the source point $\boldsymbol{x}$. Since

$$S^p_{ij,i} = H^p_{ij,i} = -\delta_{pj}\ \delta(\boldsymbol{\xi} - \boldsymbol{x}) \tag{2.6}$$

in which $\delta(\boldsymbol{\xi} - \boldsymbol{x})$ is the 3-D Dirac delta function centered at $\boldsymbol{x}$, it follows that F^p_{ij} is divergence free *everywhere* including the source point $\boldsymbol{x}$. This fact implies the existence of the representation (see Appendix C)

$$F^p_{ij}(\boldsymbol{\xi} - \boldsymbol{x}) = \epsilon_{ikm} \frac{\partial G^p_{mj}(\boldsymbol{\xi} - \boldsymbol{x})}{\partial \xi_k} \tag{2.7}$$

where the kernel G^p_{mj} is weakly-singular at $\boldsymbol{\xi} = \boldsymbol{x}$ in the sense that it is of order $1/r$ as $r \to 0$. Using (2.4) and (2.5), and expressing the 'stress fundamental solution' S^p_{ij} in terms of the 'displacement fundamental solution' U^i_j, equation (2.7) gives rise to the following system of partial differential equations to be solved for the kernel G^p_{mj}:

$$\epsilon_{ikm} \frac{\partial G^p_{mj}(\boldsymbol{\xi} - \boldsymbol{x})}{\partial \xi_k} = E_{ijab} \frac{\partial U^p_a(\boldsymbol{\xi} - \boldsymbol{x})}{\partial \xi_b} - \delta_{pj} \frac{\partial}{\partial \xi_i} \left(\frac{1}{4\pi r} \right) \tag{2.8}$$

For isotropic material behavior it is relatively simple to evaluate G^p_{mj} by means of a 'direct integration' of these partial differential equations (see Li and Mear [28]), but such an approach is extremely difficult, if not impossible, for general anisotropy due to the complicated nature of the fundamental solution. However, an explicit solution can be obtained in a straightforward fashion by exploiting the Radon transform, and this solution will be presented further below.

Now, using (2.4) and (2.7) to re-express the stress fundamental solution which appears in the displacement integral relation (2.1), and then integrating by parts via Stokes' theorem, we obtain

$$\begin{aligned} u_p(\boldsymbol{x}) &= \int_S G^p_{mj}(\boldsymbol{\xi}-\boldsymbol{x})\, D_m \Delta u_j(\boldsymbol{\xi})\, dS(\boldsymbol{\xi}) - \oint_{\partial S} G^p_{mj}(\boldsymbol{\xi}-\boldsymbol{x})\, \Delta u_j(\boldsymbol{\xi})\, d\xi_m \\ &- \int_S H^p_{ij}(\boldsymbol{\xi}-\boldsymbol{x})\, n_i(\boldsymbol{\xi})\, \Delta u_j(\boldsymbol{\xi})\, dS(\boldsymbol{\xi}) \qquad (2.9) \end{aligned}$$

where

$$D_m = n_l \epsilon_{lsm} \frac{\partial}{\partial \xi_s} \qquad (2.10)$$

is a surface differential operator. We note that the kernel $H^p_{ij} n_i$ (which also arises in the context of integral representations for Laplace's equation) is weakly-singular hence the integral relation (2.9) does in fact involve only weakly-singular kernels. With $\boldsymbol{y} \epsilon S$ being a point on the surface of the discontinuity, the limit $\boldsymbol{x} \rightarrow \boldsymbol{y}$ is now readily taken with the result

$$\begin{aligned} \frac{1}{2}\Sigma u_p(\boldsymbol{y}) &= \int_S G^p_{mj}(\boldsymbol{\xi}-\boldsymbol{y})\, D_m \Delta u_j(\boldsymbol{\xi})\, dS(\boldsymbol{\xi}) - \oint_{\partial S} G^p_{mj}(\boldsymbol{\xi}-\boldsymbol{y})\, \Delta u_j(\boldsymbol{\xi})\, d\xi_m \\ &- \int_S H^p_{ij}(\boldsymbol{\xi}-\boldsymbol{y})\, n_i(\boldsymbol{\xi})\, \Delta u_j(\boldsymbol{\xi})\, dS(\boldsymbol{\xi}) \qquad (2.11) \end{aligned}$$

in which $\Sigma u_p(\boldsymbol{y}) = u^+_p(\boldsymbol{y}) + u^-_p(\boldsymbol{y})$. While this relation is not of primary interest in our development, it does provides the additional information required to (separately) determine the displacement of the upper and lower surfaces of the discontinuity. Before pursuing the displacement equation further, we turn our attention to establishing the existence of singularity-reduced relations for the stress and traction.

2.1.2 Stress and traction

The kernel $\Sigma_{ij}^{lk}(\boldsymbol{\xi}-\boldsymbol{x})$ which appears in the stress relation (2.2) is strongly-singular in the sense that it is of order $1/r^3$ as $r \to 0$. Toward establishing a singularity-reduced alternative to (2.2), we first note that (see Appendix A)

$$\Sigma_{ij,i}^{lk}(\boldsymbol{\xi}-\boldsymbol{x}) = -\frac{\partial}{\partial \xi_i}\Big[E_{ijkl}\delta(\boldsymbol{\xi}-\boldsymbol{x})\Big] \tag{2.12}$$

and

$$\Sigma_{ij,l}^{lk}(\boldsymbol{\xi}-\boldsymbol{x}) = -\frac{\partial}{\partial \xi_l}\Big[E_{ijkl}\delta(\boldsymbol{\xi}-\boldsymbol{x})\Big] \tag{2.13}$$

That is, the divergence of Σ_{ij}^{lk} with respect to either ξ_i or ξ_l vanishes everywhere except at the source point $\boldsymbol{x}$ where it possesses a singularity in terms of the derivative of the Dirac-delta function. This observation motivates a decomposition of $\Sigma_{ij}^{lk}(\boldsymbol{\xi}-\boldsymbol{x})$ as

$$\Sigma_{ij}^{lk}(\boldsymbol{\xi}-\boldsymbol{x}) = \tilde{\Sigma}_{ij}^{lk}(\boldsymbol{\xi}-\boldsymbol{x}) + D_{ij}^{lk}(\boldsymbol{\xi}-\boldsymbol{x}) \tag{2.14}$$

in which

$$D_{ij}^{lk}(\boldsymbol{\xi}-\boldsymbol{x}) = -E_{ijkl}\;\delta(\boldsymbol{\xi}-\boldsymbol{x}) \tag{2.15}$$

and where $\tilde{\Sigma}_{ij}^{lk}$ is divergence free (with respect to ξ_i and ξ_l) *everywhere* including the source point $\boldsymbol{x}$. It then follows that there exists a representation in the form (see Appendix C)

$$\tilde{\Sigma}_{ij}^{lk}(\boldsymbol{\xi}-\boldsymbol{x}) = \epsilon_{ism}\frac{\partial}{\partial \xi_s}\epsilon_{lrt}\frac{\partial}{\partial \xi_r}C_{mj}^{tk}(\boldsymbol{\xi}-\boldsymbol{x}) \tag{2.16}$$

where the kernel C_{mj}^{tk} is weakly-singular at $\boldsymbol{\xi}=\boldsymbol{x}$ in the sense that it is of order $1/r$ as $r \to 0$. Upon combining (2.14), (2.15) and (2.16), and then expressing Σ_{ij}^{lk} in terms of the displacement fundamental solution, we obtain the system of differential equations governing C_{mj}^{tk} as

$$\epsilon_{ism}\frac{\partial}{\partial \xi_s}\epsilon_{lrt}\frac{\partial}{\partial \xi_r}C_{mj}^{tk}(\boldsymbol{\xi}-\boldsymbol{x}) = E_{lkpq}E_{ijab}\frac{\partial^2 U_a^p(\boldsymbol{\xi}-\boldsymbol{x})}{\partial \xi_q \partial \xi_b} + E_{ijkl}\delta(\boldsymbol{\xi}-\boldsymbol{x}) \tag{2.17}$$

We defer solution of these equations until the next section.

We now return to (2.2) and use the results presented above to obtain a singularity-reduced relation for the stress field induced by the displacement discontinuity. A key observation in this regard is that, for any point $\boldsymbol{x}$ in the domain (i.e. $\boldsymbol{x} \notin S$), the validity of (2.2) is unaltered by replacing the kernel Σ_{ij}^{lk} with $\tilde{\Sigma}_{ij}^{lk}$; this follows immediately from the decomposition (2.14) and the fact that, for $\boldsymbol{x} \notin S$, the term involving the integral of the Dirac delta function vanishes. Combining (2.2) (with Σ_{ij}^{lk} first replaced by $\tilde{\Sigma}_{ij}^{lk}$) and the representation (2.16), integrating by parts via Stokes' theorem and utilizing the translational property of the kernel C_{mj}^{tk} to exchange a derivative with respect to ξ_r for one with respect to $-x_r$, we obtain

$$\sigma_{lk}(\boldsymbol{x}) \quad = \quad \epsilon_{lrt} \frac{\partial \Omega_{tk}}{\partial x_r} \tag{2.18}$$

where the quantity

$$\Omega_{tk}(\boldsymbol{x}) = -\oint_{\partial S} C_{mj}^{tk}(\boldsymbol{\xi} - \boldsymbol{x})\, \Delta u_j(\boldsymbol{\xi})\, d\xi_m + \int_S C_{mj}^{tk}(\boldsymbol{\xi} - \boldsymbol{x})\, D_m \Delta u_j(\boldsymbol{\xi})\, dS(\boldsymbol{\xi}) \tag{2.19}$$

involves only weakly-singular kernels.

The relation (2.18) for the stress at an internal point $\boldsymbol{x}$ is well suited to obtain an integral equation for the traction acting at a point $\boldsymbol{y} \in S$ on the surfaces of discontinuity. Indeed, to do so we simply form $n_l(\boldsymbol{y})\sigma_{lk}(\boldsymbol{x})$ and take a limit as $\boldsymbol{x} \to \boldsymbol{y}$ with the result

$$t_k(\boldsymbol{y}) \quad = \quad D_t \Omega_{tk}(\boldsymbol{y}) \tag{2.20}$$

Finally, a weakly-singular weak-form traction integral equation follows by multiplying (2.20) by a continuous test function $\Delta\tilde{u}_k(\boldsymbol{y})$, integrating the result with respect to the entire surface of discontinuity, and employing Stokes' theorem to obtain

$$\int_S t_k(\boldsymbol{y})\, \Delta\tilde{u}_k(\boldsymbol{y})\, dS(\boldsymbol{y}) \quad = \quad \oint_{\partial S} \Delta\tilde{u}_k(\boldsymbol{y})\, \Omega_{tk}(\boldsymbol{y}) dy_t - \int_S D_t \Delta\tilde{u}_k(\boldsymbol{y})\, \Omega_{tk}(\boldsymbol{y})\, dS(\boldsymbol{y}) \tag{2.21}$$

2.1.3 Solution for G^p_{mj} and C^{tk}_{mj}

The existence of the kernels G^p_{mj} and C^{tk}_{mj} has been established, and it has been shown that that these two kernels are governed by the system of differential equations (2.8) and (2.17), respectively. In this section we provide a solution for the kernels through an application of the Radon transform. (See Appendix B for a summary of certain results concerning the Radon transform which are relevant to our development.) As a starting point, we summarize the use of the Radon transform to obtain the displacement fundamental solution. This procedure is well known (we note in particular the description given by Bacon *et al.* [2]), but it is presented here since certain intermediate results will be needed in the development to follow.

For a unit point load acting in an unbounded anisotropic solid, Navier's equation (governing the displacement fundamental solution) takes the form

$$E_{ijkl}\frac{\partial^2 U^p_k(\boldsymbol{\xi}-\boldsymbol{x})}{\partial \xi_l \partial \xi_j} = -\delta_{ip}\,\delta(\boldsymbol{\xi}-\boldsymbol{x}) \tag{2.22}$$

Upon an application of the Radon transform we find

$$z_l z_j E_{ijkl}\frac{\partial^2 \widehat{U}^p_k(\boldsymbol{z},\alpha-\boldsymbol{z}\cdot\boldsymbol{x})}{\partial^2 \alpha^2} = -\delta_{ip}\,\delta(\alpha-\boldsymbol{z}\cdot\boldsymbol{x}) \tag{2.23}$$

where $\hat{f}(\boldsymbol{z},\alpha-\boldsymbol{z}\cdot\boldsymbol{x})$ denotes the transform of a function $f(\boldsymbol{\xi}-\boldsymbol{x})$ (in the transform domain $\{\alpha,\boldsymbol{z}\}$ in which α is a scalar and $\boldsymbol{z}$ is a unit vector). With $(\boldsymbol{z},\boldsymbol{z})_{ik} \equiv z_j E_{jikl} z_l$, (2.23) can be solved for $\partial^2 \widehat{U}^p_k/\partial\alpha^2$ with the result

$$\frac{\partial^2 \widehat{U}^p_a(\boldsymbol{z},\alpha-\boldsymbol{z}\cdot\boldsymbol{x})}{\partial \alpha^2} = -(\boldsymbol{z},\boldsymbol{z})^{-1}_{ap}\,\delta(\alpha-\boldsymbol{z}\cdot\boldsymbol{x}) \tag{2.24}$$

where $(\boldsymbol{z},\boldsymbol{z})^{-1}$ denotes the inverse of the tensor $(\boldsymbol{z},\boldsymbol{z})$. An application of the inverse Radon transform then leads to

$$U^i_j(\boldsymbol{\xi}-\boldsymbol{x}) = \frac{1}{8\pi^2 r}\oint_{\boldsymbol{z}\cdot\boldsymbol{r}=0}(\boldsymbol{z},\boldsymbol{z})^{-1}_{ij}\;ds(\boldsymbol{z}) \tag{2.25}$$

in which the integral is to be evaluated over a unit circle $\|\boldsymbol{z}\| = 1$ on a plane normal to the vector $\boldsymbol{r} = \boldsymbol{\xi} - \boldsymbol{x}$ as shown schematically in Figure 2.2. Note that the integrand is well-defined at every point along the contour as a result of the positive definiteness of $(\boldsymbol{z}, \boldsymbol{z})$ and, clearly, the kernel U^i_j is singular only at $\boldsymbol{\xi} = \boldsymbol{x}$ and is of order $1/r$ as $r \rightarrow 0$.

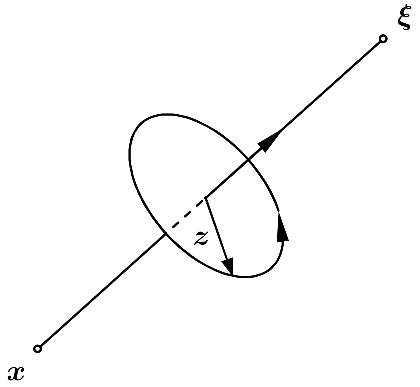

Figure 2.2: Schematic indicating contour of integration for the displacement fundamental solution.

Kernel G^p_{mj}

Taking the Radon transform of (2.8), we obtain

$$\epsilon_{ikm} z_k \frac{\partial \hat{G}^p_{mj}(\boldsymbol{z}, \alpha - \boldsymbol{z}\cdot\boldsymbol{x})}{\partial \alpha} = E_{ijab} z_b \frac{\partial \hat{U}^p_a(\boldsymbol{z}, \alpha - \boldsymbol{z}\cdot\boldsymbol{x})}{\partial \alpha} - \delta_{pj} z_i \frac{\partial}{\partial \alpha} \widehat{\left(\frac{1}{4\pi r}\right)} \tag{2.26}$$

Taking the derivative of (2.26) with respect to α, noting that (see Appendix B)

$$\frac{\partial^2}{\partial \alpha^2} \widehat{\left(\frac{1}{4\pi r}\right)} = -\delta(\alpha - \boldsymbol{z}\cdot\boldsymbol{x}) \tag{2.27}$$

and utilizing (2.24), we obtain

$$\epsilon_{ikm} z_k \, \frac{\partial^2 \hat{G}^p_{mj}(\boldsymbol{z}, \alpha - \boldsymbol{z} \cdot \boldsymbol{x})}{\partial \alpha^2} = \Omega_{ijp} \, \delta(\alpha - \boldsymbol{z} \cdot \boldsymbol{x}) \tag{2.28}$$

in which

$$\Omega_{ijp} = \delta_{pj} z_i - E_{ijdc} z_c (\boldsymbol{z}, \boldsymbol{z})^{-1}_{pd} \tag{2.29}$$

Now, a particular solution of (2.28) can readily be constructed by expressing Ω_{ijp} in terms of the product of $\epsilon_{ikm} z_k$ and a certain function as follows:

$$\begin{aligned}
\Omega_{ijp} &= \delta_{ia} \Omega_{ajp} \\
&= \delta_{ia} \delta_{kb} z_k z_b \Omega_{ajp} \\
&= (\epsilon_{ikm} \epsilon_{abm} + \delta_{ib} \delta_{ka}) z_k z_b \Omega_{ajp} \\
&= \epsilon_{ikm} \epsilon_{abm} z_k z_b \Omega_{ajp} + z_i z_a \Omega_{ajp} \\
&= \epsilon_{ikm} z_k \Bigg[\epsilon_{abm} z_b \Omega_{ajp} \Bigg]
\end{aligned} \tag{2.30}$$

Note that the epsilon-delta identity $\epsilon_{ijk} \epsilon_{ipq} = (\delta_{jp} \delta_{kq} - \delta_{jq} \delta_{kp})$ has been used along with the fact that $z_a \Omega_{ajp} = 0$. With (2.30) and the fact that $\epsilon_{abm} z_a z_b = 0$, (2.28) becomes

$$\epsilon_{ikm} z_k \frac{\partial^2 \hat{G}^p_{mj}(\boldsymbol{z}, \alpha - \boldsymbol{z} \cdot \boldsymbol{x})}{\partial \alpha^2} = \epsilon_{ikm} z_k \Bigg[- \epsilon_{abm} z_b z_c \, (\boldsymbol{z}, \boldsymbol{z})^{-1}_{pd} \, E_{ajdc} \; \delta(\alpha - \boldsymbol{z} \cdot \boldsymbol{x}) \Bigg] \tag{2.31}$$

and a particular solution of (2.31) follows by inspection with the result

$$\frac{\partial^2 \hat{G}^p_{mj}(\boldsymbol{z}, \alpha - \boldsymbol{z} \cdot \boldsymbol{x})}{\partial \alpha^2} = -\epsilon_{abm} z_a z_c \, (\boldsymbol{z}, \boldsymbol{z})^{-1}_{pd} \, E_{ajdc} \; \delta(\alpha - \boldsymbol{z} \cdot \boldsymbol{x}) \tag{2.32}$$

By employing the Radon transform inversion, the kernel G^p_{mj} in physical domain is obtained as

$$G^p_{mj}(\boldsymbol{\xi} - \boldsymbol{x}) = \frac{1}{8\pi^2 r} (\epsilon_{abm} E_{ajdc}) \oint_{\boldsymbol{z} \cdot \boldsymbol{r} = 0} z_b z_c \; (\boldsymbol{z}, \boldsymbol{z})^{-1}_{pd} \; ds(\boldsymbol{z}) \tag{2.33}$$

As in the case for the displacement fundamental solution (2.25), the kernel G^p_{mj} is singular only at $\boldsymbol{\xi} = \boldsymbol{x}$ and is of order $1/r$ as $r \to 0$.

Kernel C^{tk}_{mj}

Upon taking the Radon transform of (2.17) and utilizing (2.24), we find that

$$\epsilon_{ism}\epsilon_{lrt}z_s z_r \frac{\partial^2 \hat{C}^{tk}_{mj}(\boldsymbol{z}, \alpha - \boldsymbol{z}\cdot\boldsymbol{x})}{\partial\alpha^2} = \Lambda_{ijkl}\ \delta(\alpha - \boldsymbol{z}\cdot\boldsymbol{x}) \tag{2.34}$$

where

$$\Lambda_{ijkl} = E_{ijkl} - E_{ijeo}\, E_{dnkl}\ z_o z_d\ (\boldsymbol{z},\boldsymbol{z})^{-1}_{en} \tag{2.35}$$

Proceeding in a fashion analogous to that used to obtain G^p_{mj}, we seek a particular solution of (2.34) by expressing Λ_{ijkl} in terms of a product between the linear operator $\epsilon_{ism}\epsilon_{lrt}z_s z_r$ and a certain function. With the use of the epsilon-delta identity and the fact that $z_a\Lambda_{ajkl} = 0$, we obtain

$$\begin{aligned}
\Lambda_{ijkl} &= \delta_{ia}\Lambda_{ajkl} \\
&= \delta_{ia}\delta_{ps}z_s z_p\,\Lambda_{ajkl} \\
&= (\epsilon_{ism}\epsilon_{apm} + \delta_{ip}\delta_{sa})z_s z_p \Lambda_{ajkl} \\
&= \epsilon_{ism}\epsilon_{apm}z_s z_p\,\Lambda_{ajkl} + z_i z_a \Lambda_{ajkl} \\
&= \epsilon_{ism}\epsilon_{apm}z_s z_p\,\Lambda_{ajkl}
\end{aligned} \tag{2.36}$$

Upon a further manipulation (now 'on the index l') we find

$$\begin{aligned}
\Lambda_{ijkl} &= \epsilon_{ism}\epsilon_{apm}z_s z_r\,\delta_{pr}\delta_{lb}\Lambda_{ajkb} \\
&= \epsilon_{ism}\epsilon_{apm}z_s z_r(\epsilon_{lrt}\epsilon_{bpt} + \delta_{lp}\delta_{rb})\Lambda_{ajkb} \\
&= \epsilon_{ism}\epsilon_{pam}\epsilon_{lrt}\epsilon_{pbt}z_s z_r\Lambda_{ajkb} + \epsilon_{ism}\epsilon_{alm}z_s z_b\Lambda_{ajkb} \\
&= \epsilon_{ism}\epsilon_{lrt}z_s z_r \Bigg[\epsilon_{pam}\epsilon_{pbt}\Lambda_{ajkb}\Bigg]
\end{aligned} \tag{2.37}$$

in which the epsilon-delta identity has been used yet again along with the fact that $z_b\Lambda_{ajkb} = 0$. With (2.34) and (2.37), it is evident that a particular solution for $\partial^2\hat{C}^{tk}_{mj}/\partial\alpha^2$ is given by

$$\frac{\partial^2 \hat{C}^{tk}_{mj}(\boldsymbol{z}, \alpha - \boldsymbol{z}\cdot\boldsymbol{x})}{\partial\alpha^2} = \epsilon_{pam}\epsilon_{pbt}\Lambda_{ajkb}\delta(\alpha - \boldsymbol{z}\cdot\boldsymbol{x}) \tag{2.38}$$

and the kernel $C^{tk}_{mj}(\boldsymbol{\xi}-\boldsymbol{x})$ is obtained by utilizing the Radon transform inversion formula with the result

$$C^{tk}_{mj}(\boldsymbol{\xi}-\boldsymbol{x}) = -\frac{1}{8\pi^2 r}\oint_{\boldsymbol{z}\cdot\boldsymbol{r}=0} \epsilon_{pam}\epsilon_{pbt}\Lambda_{ajkb}\ ds(\boldsymbol{z}) \tag{2.39}$$

By exploiting the identity $(\boldsymbol{z},\boldsymbol{z})_{ij}\ (\boldsymbol{z},\boldsymbol{z})^{-1}_{ij} = 3$, a more concise relation is obtained as

$$C^{tk}_{mj}(\boldsymbol{\xi}-\boldsymbol{x}) = \frac{1}{8\pi^2 r}A^{tkeo}_{mjdn}\oint_{\boldsymbol{z}\cdot\boldsymbol{r}=0} z_o z_d\ (\boldsymbol{z},\boldsymbol{z})^{-1}_{en}\ ds(\boldsymbol{z}) \tag{2.40}$$

where A^{tkeo}_{mjdn} is a constant (which depends only on the moduli) given by

$$A^{tkeo}_{mjdn} \quad = \quad \epsilon_{pam}\epsilon_{pbt}\Big(E_{dnkb}E_{ajeo} - \frac{1}{3}E_{ajkb}E_{dneo}\Big) \tag{2.41}$$

Note that the kernel C^{tk}_{mj} is also singular only at $\boldsymbol{\xi}=\boldsymbol{x}$ and is of order $1/r$ as $r\to 0$.

Summary of the kernels

Let K^{ik}_{jl} be the fourth order tensor defined by

$$K^{ik}_{jl} \equiv \frac{1}{8\pi^2 r}\oint_{\boldsymbol{z}\cdot\boldsymbol{r}=0} (\boldsymbol{z},\boldsymbol{z})^{-1}_{ij}\, z_k z_l\ ds(\boldsymbol{z}) \tag{2.42}$$

Then the displacement fundamental solution U^i_j, the kernel G^p_{mj} and the kernel C^{tk}_{mj} can be expressed in succinct form in terms of this single tensor as

$$U^j_i(\boldsymbol{\xi}-\boldsymbol{x}) \quad = \quad K^{ik}_{jk} \tag{2.43}$$

$$G^p_{mj}(\boldsymbol{\xi}-\boldsymbol{x}) \quad = \quad \epsilon_{abm}E_{ajdc}\ K^{pb}_{dc} \tag{2.44}$$

$$C^{tk}_{mj}(\boldsymbol{\xi}-\boldsymbol{x}) \quad = \quad A^{tkeo}_{mjdn}\ K^{eo}_{nd} \tag{2.45}$$

in which A^{tkeo}_{mjdn} is given by (2.41).

We remark that, in a fashion analogous to one which is well known for the displacement fundamental solution, an alternative form for K^{ik}_{jl} in terms of an integral on the real line can be readily obtained. Indeed, upon expressing $\boldsymbol{z}$ as

$\boldsymbol{z} = \boldsymbol{a}\cos\alpha + \boldsymbol{b}\sin\alpha,\ \ \alpha \in [0, 2\pi]$ in which $\boldsymbol{a}$ and $\boldsymbol{b}$ are two orthonormal vectors which lie in a plane perpendicular to $\boldsymbol{r} = (\boldsymbol{\xi} - \boldsymbol{x})$, it can be shown that

$$K_{jl}^{ik} = \frac{1}{4\pi^2 r} \int_{-\infty}^{\infty} \frac{\tilde{\Gamma}_{ij}(p)\,\Theta_{kl}(p)}{(1+p^2)|\boldsymbol{\Gamma}(p)|}\, dp \tag{2.46}$$

where $p = \tan\alpha$,

$$\begin{aligned} \Gamma_{ij} &= (\boldsymbol{a},\boldsymbol{a})_{ij} + \{(\boldsymbol{a},\boldsymbol{b})_{ij} + (\boldsymbol{a},\boldsymbol{b})_{ji}\}p + (\boldsymbol{b},\boldsymbol{b})_{ij}\, p^2\ , && (2.47) \\ \tilde{\Gamma}_{ij}\Gamma_{jk} &= |\boldsymbol{\Gamma}(p)|\delta_{ik}\ , && (2.48) \\ \Theta_{kl} &= a_k a_l + (a_k b_l + a_l b_k)p + b_k b_l p^2\,, && (2.49) \end{aligned}$$

$|\boldsymbol{\Gamma}(p)|$ denotes the determinant of the matrix $\boldsymbol{\Gamma}$ and where, for example, $(\boldsymbol{a},\boldsymbol{b})_{ij} = a_k E_{kijl} b_l$. The evaluation of this integral (via contour integration) involves, as usual, determining the roots of a sextic equation (e.g. [42], [44]), and differs from the standard treatment for the displacement fundamental solution only in a minor way associated with the additional term Θ_{kl} and the two simple poles at $p = \pm\sqrt{-1}$ which arise from the presence of $z_k z_l$ in (2.42).

2.2 Dislocations and cracks

The integral relations developed above apply to isolated displacement discontinuities of general type. Of particular interest are dislocations and cracks, and in this section we discuss these two special cases.

2.2.1 Dislocations

For the special case of a dislocation for which $b_i \equiv \Delta u_i$ is constant, the singularity-reduced integral equation (2.9) gives rise to a generalization of Burgers' equation for anisotropic media given by

$$u_p(\boldsymbol{x}) = -\oint_{\partial S} b_j\, G_{mj}^{p}(\boldsymbol{\xi} - \boldsymbol{x})\, d\xi_m - \frac{1}{4\pi} b_p\, \Omega(\boldsymbol{x}) \tag{2.50}$$

where

$$\Omega(\boldsymbol{x}) = \frac{4\pi}{3} \int_S H^p_{ip}(\boldsymbol{\xi} - \boldsymbol{x})\, n_i(\boldsymbol{\xi})\, dS(\boldsymbol{\xi}) \tag{2.51}$$

is the solid angle to the surface. As shown in Appendix D, the solid angle can be computed in terms of an integral on ∂S as

$$\Omega(\boldsymbol{x}) = 4\pi \int_{\partial S} \omega_m(\boldsymbol{\xi}, \boldsymbol{x})\, d\xi_m \tag{2.52}$$

with the 'generating function' ω_m given by

$$\omega_m(\boldsymbol{\xi}, \boldsymbol{x}) = \frac{1}{3} \int_{\Gamma(\boldsymbol{x})} \epsilon_{mrt}\, H^p_{rp}(\boldsymbol{\xi} - \boldsymbol{z})\, dz_t \tag{2.53}$$

in which $\Gamma(\boldsymbol{x})$ is any path, originating at $\boldsymbol{x}$ and extending to infinity, which does not intersect the discontinuity. For example, when $\Gamma(\boldsymbol{x})$ is a straight line we readily obtain

$$\omega_m(\boldsymbol{\xi}, \boldsymbol{x}) = \frac{1}{4\pi} \frac{\epsilon_{mkt} e_k p_t}{(1 + e_i p_i)} \frac{1}{r} \tag{2.54}$$

in which $\boldsymbol{p}$ is a unit vector along the path (directed toward $\boldsymbol{x}$) and $e_k \equiv (\xi_k - x_k)/r$. A piecewise-linear path is also readily treated, so in this sense it is always possible to choose a path which does not intersect the discontinuity and which is such that a simple closed-form relation for ω_m can be obtained. Having determined ω_m, we can now evaluate the displacement entirely in terms of a line integral as

$$u_p(\boldsymbol{x}) = -\int_{\partial S} b_j\, [G^p_{mj} + \delta_{jp}\omega_m]\, d\xi_m \tag{2.55}$$

We remark that the jump in displacement across the discontinuity is manifested in the fact that the path must be taken to be directed 'away from' the discontinuity in such a way that it does not intersect the surface.

A line integral representation for the stress field is obtained from (2.18) as

$$\sigma_{lk}(\boldsymbol{x}) = -\,\epsilon_{lrt} \frac{\partial}{\partial x_r} \oint_{\partial S} b_j\, C^{tk}_{mj}(\boldsymbol{\xi} - \boldsymbol{x}) d\xi_m \tag{2.56}$$

and a weakly-singular, weak-form traction integral equation follows from (2.21). A line integral representation for the energy associated with the presence of an array of dislocation loops is also readily obtained. For purposes of discussion, assume now that two dislocations are present, the first with edge ∂S^1 and Burgers' vector b_i^1 and the second with edge ∂S^2 and Burgers' vector b_i^2. Toward developing an expression for the interaction energy W_{int} associated with these two dislocations, let $\sigma_{kl}^{(1)}$ and $\sigma_{kl}^{(2)}$ be the stress fields induced by the first and second dislocation were it present in the absence of the other, so that

$$W_{int} = \frac{1}{2} \int_{S^1} \sigma_{kl}^{(2)} \, n_k^1 \, b_l^1 \, dS + \frac{1}{2} \int_{S^2} \sigma_{kl}^{(1)} \, n_k^2 \, b_l^2 \, dS \tag{2.57}$$

in which the superscripts on the surfaces of integration and the unit normals serve to indicate with which dislocation they are associated. Upon use of (2.56) and an application of Stokes' theorem, it can then be shown that

$$W_{int} = - \oint_{\partial S^1} \oint_{\partial S^2} b_k^1 \, b_j^2 \, C_{mj}^{tk}(\boldsymbol{\xi} - \boldsymbol{y}) \, dy_t \, d\xi_m \tag{2.58}$$

We remark that the contributions arising from each dislocation in the expression (2.56) can be combined to obtain this final simple form due to the fact that, in the integral expressions where it occurs, $C_{mj}^{tk}(\boldsymbol{\xi} - \boldsymbol{x})$ can be replaced with $C_{tk}^{mj}(\boldsymbol{x} - \boldsymbol{\xi})$ without altering the value of the integral (see Li and Mear (1998) for a discussion of this result); indeed, the specific form of the kernel $C_{mj}^{tk}(\boldsymbol{x} - \boldsymbol{\xi})$ to be obtained above satisfies the equality $C_{mj}^{tk}(\boldsymbol{\xi} - \boldsymbol{x}) = C_{tk}^{mj}(\boldsymbol{x} - \boldsymbol{\xi})$. The self energy for each dislocation has the exact same form as (2.58) except that the right hand side is to be multiplied by 1/2 and, of course, both of the Burgers' vectors and line integrals which appear are taken to be those associated with the particular dislocation for which an expression for the self energy is sought. Note also that, upon a proper interpretation of terms, these expressions for energy follow directly from the weak-form traction integral equation.

2.2.2 Cracks in an unbounded domain

Consider a crack on which tractions $t_i \equiv t_i^+ = -t_i^-$ are prescribed. What is sought is the relative crack-face displacement Δu_i, and the weakly-singular weak-form traction integral equation provides a basis for a numerical procedure to determine these quantities. The relative crack-face displacement must vanish along the crack front, and consistent with this we chose the test function $\Delta\tilde{u}_i$ to also possess this feature. Then the contribution from the line integral terms in (2.21) vanish and the weak-form traction integral equation simplifies to

$$\int_S t_k(\boldsymbol{y})\, \Delta\tilde{u}_k(\boldsymbol{y})\, dS(\boldsymbol{y}) \quad = \quad -\int_S \int_S C_{mj}^{tk}(\boldsymbol{\xi} - \boldsymbol{y})\, [D_t \Delta\tilde{u}_k(\boldsymbol{y})]\, [D_m \Delta u_j(\boldsymbol{\xi})]\, dS(\boldsymbol{\xi}) dS(\boldsymbol{y}) \tag{2.59}$$

We emphasize that the kernel in this integral equation is weakly-singular (so that the integrals exist in the ordinary sense and the crack displacement data need only be continuous) and that it represents a symmetric weak-form equation for the unknown crack-face displacements. Once these quantities are determined, other information of interest (i.e. the displacement and stress field and, most importantly, the stress intensity factors) can readily be found. A discussion of the use of this equation as the basis for a computational procedure will be provided in the next chapter within the context of the general strategy for treating cracks in a finite domain.

2.2.3 Additional discussion of the kernels

Relation to previously obtained kernels

It is evident from the representations (2.7) and (2.16) that the kernels G_{mj}^p and C_{mj}^{tk} are not unique (also see Appendix C). Indeed, given a particular pair of kernels $\{G_{mj}^p, C_{mj}^{tk}\}$, the quantities $\{\bar{G}_{mj}^p, \bar{C}_{mj}^{tk}\}$ for which

$$\bar{G}_{mj}^p = G_{mj}^p + \frac{\partial L_j^p}{\partial \xi_m} \quad , \quad \bar{C}_{mj}^{tk} = C_{mj}^{tk} + \frac{\partial M_j^{tk}}{\partial \xi_m} + \frac{\partial N_{mj}^k}{\partial \xi_t} \tag{2.60}$$

are also valid kernels. Here L_j^p, M_j^{tk} and N_{mj}^k are arbitrary, but for our purposes it suffices to restrict attention to quantities which are a function of $\boldsymbol{\zeta} = (\boldsymbol{\xi} - \boldsymbol{x})$ and which are homogeneous of degree $\lambda = 0$.

Now, for the special case of isotropy, Li and Mear [28] carried out a direct integration of (2.7) to obtain the particular kernel

$$G_{mj}^p(\boldsymbol{\zeta}) = \frac{1}{8\pi(1-\nu)r}\left[(1-2\nu)\epsilon_{mpj} + \epsilon_{ajm}\frac{\zeta_a\zeta_p}{r^2}\right] \tag{2.61}$$

in which ν is Poisson's ratio. We remark that this kernel is identical to that appearing in Burgers' equation [10] for the displacement field induced by a dislocation. For anisotropy, we are not aware of a solution for the kernel G_{mj}^p in the form (2.33), but a closely related result is given by Leibfried [27] in terms of a Fourier integral. We also note that, when specialized to isotropy, the kernel given by (2.33) reduces to (2.61) along with an additional term which can be expressed in the form $\partial L_j^p/\partial\xi_m$ (see Appendix E).

For isotropy, Li and Mear [28] obtained the particular kernel C_{mj}^{tk} given by

$$C_{mj}^{tk}(\boldsymbol{\zeta}) = \frac{\mu}{4\pi(1-\nu)r}\left[(1-\nu)\delta_{kt}\delta_{jm} + 2\nu\delta_{km}\delta_{jt} - \delta_{kj}\delta_{tm} - \frac{\zeta_k\zeta_j}{r^2}\delta_{tm}\right] \tag{2.62}$$

in which μ is the shear modulus. The first kernel obtained for isotropy appears to be that of Blin [6] in his analysis of the interaction energy for dislocation loops (also see Hirth and Lothe [24]). Blin's kernel differs from (2.62) by terms of the form $\partial M_j^{tk}/\partial\xi_m$ and $\partial N_{mj}^k/\partial\xi_t$ (see Appendix E) and, while the simplicity of (2.62) may be preferable for numerical analysis, the two kernels are equivalent by (2.60). We remark that other (equivalent) kernels have been obtained within the context of integral equation representations for boundary value problems in isotropic linear elasticity, and we note in particular the work of Nedelec [33] and Bonnet [8].

For anisotropy the only previously available explicit kernel seems to be that developed by Lothe [31] in his analysis of the interaction energy for dislocation loops.

Lothe's kernel is given by

$$C_{mj}^{tk}(\boldsymbol{\xi}-\boldsymbol{x}) = -\frac{1}{8\pi^2 r}\oint_{|\boldsymbol{z}|=1} \epsilon_{umv}\epsilon_{wts} z_v z_s \Big[E_{ujkw} - z_c z_d (\boldsymbol{z},\boldsymbol{z})^{-1}_{en} E_{ujec} E_{dnkw} \Big] dS \tag{2.63}$$

and in Appendix E it is demonstrated that the kernel given by (2.40) is in fact equivalent to this kernel.

Properties of the kernels

We now focus attention on the specific kernel G_{mj}^{p} given by (2.33) and the specific kernel C_{mj}^{tk} given by (2.40). Since it will appear in the integral equations to be developed further below for a finite domain, we also discuss the displacement fundamental solution. Noting that the tensor $(\boldsymbol{z},\boldsymbol{z})$ is symmetric and that the integrands in both (2.33) and (2.40) are even with respect to the components of $\boldsymbol{z}$ which appear, we deduce that

$$\left.\begin{array}{lllllll} G_{mj}^{p}(\boldsymbol{\xi}-\boldsymbol{y}) & = & G_{mj}^{p}(\boldsymbol{y}-\boldsymbol{\xi}) & & & & \\ C_{mj}^{tk}(\boldsymbol{\xi}-\boldsymbol{y}) & = & C_{mj}^{tk}(\boldsymbol{y}-\boldsymbol{\xi}) & , & C_{mj}^{tk}(\boldsymbol{\xi}-\boldsymbol{y}) & = & C_{tk}^{mj}(\boldsymbol{\xi}-\boldsymbol{y}) \\ U_{i}^{j}(\boldsymbol{\xi}-\boldsymbol{y}) & = & U_{i}^{j}(\boldsymbol{y}-\boldsymbol{\xi}) & , & U_{i}^{j}(\boldsymbol{\xi}-\boldsymbol{y}) & = & U_{j}^{i}(\boldsymbol{\xi}-\boldsymbol{y}) \end{array}\right\} \tag{2.64}$$

Additional properties of interest for the kernels follow by a consideration of elastic material symmetry.

For purposes of discussion, assume that the material has a plane of symmetry and introduce a local cartesian coordinate system $\{\zeta_1,\zeta_2,\zeta_3\}$ which has its origin at the source point $\boldsymbol{x}$ and for which $\zeta_1 = 0$ defines the plane of material symmetry. Let $\boldsymbol{\xi}$ be a given point and let $\boldsymbol{\xi}^*$ be its 'image' obtained by a reflection across the plane $\zeta_1 = 0$ as shown schematically in Figure 2.3. With $\boldsymbol{r} = (\boldsymbol{\xi}-\boldsymbol{x})$ and $\boldsymbol{r}^* = (\boldsymbol{\xi}^*-\boldsymbol{x})$, we have $r^* = r$ and $r^*_\alpha = \delta^*_{\alpha\beta} r_\beta$ where Greek indices are used to indicate components

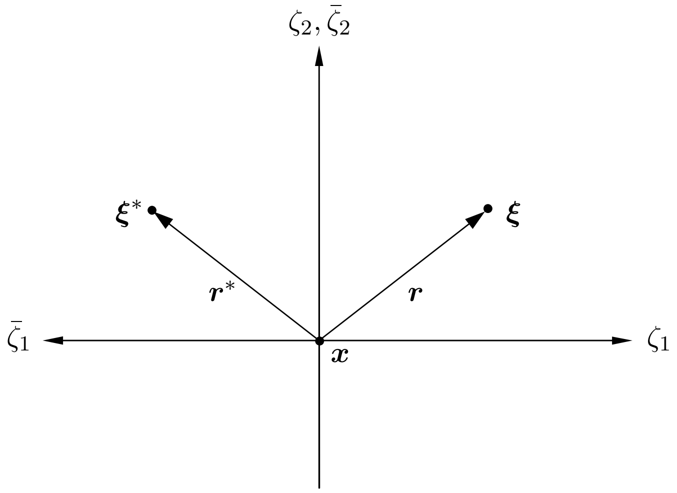

Figure 2.3: Coordinate system $\{\zeta_1, \zeta_2, \zeta_3\}$ with $\zeta_1 = 0$ corresponding to a plane of material symmetry.

with respect to the local coordinate system and where

$$\delta^*_{\alpha\beta} = \begin{cases} -1 & , \alpha = \beta = 1 \\ 1 & , \alpha = \beta = 2,3 \\ 0 & , \alpha \neq \beta \end{cases} \tag{2.65}$$

We now introduce yet other local coordinate system $\{\bar{\zeta}_1,\bar{\zeta}_2,\bar{\zeta}_3\}$ which has its origin at $\boldsymbol{x}$ and satisfies $\bar{\zeta}_1 = -\zeta_1$, $\bar{\zeta}_2 = \zeta_2$ and $\bar{\zeta}_3 = \zeta_3$. Note that this is the left-handed coordinate system which is obtained through a 'reflection' of the $\{\zeta_i\}$ system across the plane $\zeta_1 = 0$.

Consider the kernel G^p_{mj} and let its components relative to the $\{\zeta_i\}$ system be denoted $G^\gamma_{\alpha\beta}$ and its components relative to the $\{\bar{\zeta}_i\}$ system be denoted $\bar{G}^\gamma_{\alpha\beta}$. From the fact that $\zeta_1 = 0$ is a plane of material symmetry, we deduce the correspondence

$$\bar{G}^\gamma_{\alpha\beta}(\boldsymbol{\xi}^* - \boldsymbol{x}) = G^\gamma_{\alpha\beta}(\boldsymbol{\xi} - \boldsymbol{x}) \tag{2.66}$$

and then upon a coordinate transformation (taking due account of the alternating symbol which appears in G^p_{mj}) we find

$$\begin{aligned} G^{\gamma}_{\alpha\beta}(\boldsymbol{\xi}^* - \boldsymbol{x}) &= -\delta^*_{\alpha\delta}\delta^*_{\beta\eta}\delta^*_{\gamma\rho}\bar{G}^{\rho}_{\delta\eta}(\boldsymbol{\xi}^* - \boldsymbol{x}) \\ &= -\delta^*_{\alpha\delta}\delta^*_{\beta\eta}\delta^*_{\gamma\rho}G^{\rho}_{\delta\eta}(\boldsymbol{\xi} - \boldsymbol{x}) \end{aligned} \tag{2.67}$$

Similarly, we obtain

$$C^{\gamma\delta}_{\alpha\beta}(\boldsymbol{\xi}^* - \boldsymbol{x}) = \delta^*_{\alpha\eta}\delta^*_{\beta\kappa}\delta^*_{\gamma\rho}\delta^*_{\delta\lambda}C^{\rho\lambda}_{\eta\kappa}(\boldsymbol{\xi} - \boldsymbol{x}) \tag{2.68}$$

and

$$U^{\beta}_{\alpha}(\boldsymbol{\xi}^* - \boldsymbol{x}) = \delta^*_{\alpha\eta}\delta^*_{\beta\kappa}U^{\kappa}_{\eta}(\boldsymbol{\xi} - \boldsymbol{x}) \tag{2.69}$$

The properties (2.64) and (2.67)-(2.69) play an important role in reducing the computational effort involved in evaluating the kernels $\{U^j_i, G^p_{mj}, C^{tk}_{mj}\}$.

2.3 Cracks in a finite domain

Consider a finite body which contains an embedded or surface breaking crack as shown schematically in Figure 2.4. The boundary of the domain which the body occupies consists of an 'ordinary' boundary S_o and the crack surface $S^+_c \cup S^-_c$. Consistent with the previous development for an isolated crack, attention is restricted to cases in which body force is absent and for which the traction loading on the crack is such that $t^+_i = -t^-_i$. Further, we let $S_c \equiv S^+_c$ and, for convenience, we introduce $S = S_o \cup S_c$.

Now, Somigliana's identity gives the displacement u_p at a location $\boldsymbol{x}$ within the domain as

$$u_p(\boldsymbol{x}) = \int_{S_o} U^p_j(\boldsymbol{\xi} - \boldsymbol{x})\, t_j(\boldsymbol{\xi})\, dS(\boldsymbol{\xi}) - \int_S S^p_{ij}(\boldsymbol{\xi} - \boldsymbol{x})\, n_i(\boldsymbol{\xi})\, v_j(\boldsymbol{\xi})\, dS(\boldsymbol{\xi}) \tag{2.70}$$

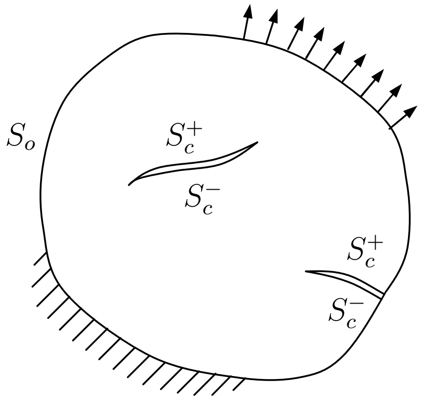

Figure 2.4: Schematic of a finite body containing cracks.

where the quantity

$$v_j(\boldsymbol{\xi}) \;=\; \begin{cases} u_j(\boldsymbol{\xi}) & , \quad \boldsymbol{\xi} \in S_o \\ \Delta u_j(\boldsymbol{\xi}) & , \quad \boldsymbol{\xi} \in S_c \end{cases} \tag{2.71}$$

has been introduced for convenience. From the expression for the displacement, we readily obtain an integral relation for the stress at points within the domain as

$$\sigma_{lk}(\boldsymbol{x}) \;=\; \int_{S_o} S_{lk}^{j}(\boldsymbol{\xi}-\boldsymbol{x})\, t_j(\boldsymbol{\xi})\, dS(\boldsymbol{\xi}) + \int_{S} \Sigma_{ij}^{lk}(\boldsymbol{\xi}-\boldsymbol{x})\, n_i(\boldsymbol{\xi})\, v_j(\boldsymbol{\xi})\, dS(\boldsymbol{\xi}) \tag{2.72}$$

We seek a regularization of these integral expressions and, specifically, we seek a pair of weakly-singular, weak-form displacement and traction integral equations which form the basis of a symmetric Galerkin boundary element method analogous to that developed for isotropy by Li *et al*. [29]. We note that if the boundary value problem under consideration is one in which tractions are prescribed on the entire surface, then a weak-form traction integral equation suffices to obtain a symmetric formulation. However, when displacements are prescribed on a portion of the ordinary boundary a symmetric formulation can only be achieved by employing both a weak-form traction integral equation and a weak-form displacement integral equation.

Consider first the displacement given by (2.70). Since the displacement fundamental solution is weakly-singular, only the term involving the stress fundamental solution requires regularization. Such a regularization is readily achieved by employing the decomposition (2.4) and then integrating by parts over the *entire* surface via Stokes' theorem. After carrying out this process, the limit as $\boldsymbol{x}$ tends to a point on the ordinary boundary can be easily formed, and with $\boldsymbol{y} \in S_o$ being any such point we find

$$\begin{aligned} \frac{1}{2}u_p(\boldsymbol{y}) &= \int_S G^p_{mj}(\boldsymbol{\xi}-\boldsymbol{y})D_m v_j(\boldsymbol{\xi})dS(\boldsymbol{\xi}) - \int_S n_i(\boldsymbol{\xi})H^p_{ij}(\boldsymbol{\xi}-\boldsymbol{y})v_j(\boldsymbol{\xi})dS(\boldsymbol{\xi}) \\ &+ \int_{S_o} U^p_j(\boldsymbol{\xi}-\boldsymbol{y})t_j(\boldsymbol{\xi})dS(\boldsymbol{\xi}) \end{aligned} \tag{2.73}$$

We remark that a limit in which $\boldsymbol{x}$ tends to a point on the crack surface can also be treated (see (2.11) for the case of an isolated crack) but, owing to the fact that the crack is subjected only to prescribed tractions, such an expression is not required for establishing a symmetric formulation. Upon multiplying (2.73) by a test function $\tilde{t}_p$ and integrating the result over the ordinary surface S_o, we obtain a weakly-singular, weak-form displacement integral as

$$\begin{aligned} \frac{1}{2}\int_{S_o} u_p(\boldsymbol{y})\,\tilde{t}_p(\boldsymbol{y})\,dS(\boldsymbol{y}) &= \int_{S_o}\tilde{t}_p(\boldsymbol{y})\int_S G^p_{mj}(\boldsymbol{\xi}-\boldsymbol{y})D_m v_j(\boldsymbol{\xi})\,dS(\boldsymbol{\xi})\,dS(\boldsymbol{y}) \\ &- \int_{S_o}\tilde{t}_p(\boldsymbol{y})\int_S n_i(\boldsymbol{\xi})H^p_{ij}(\boldsymbol{\xi}-\boldsymbol{y})v_j(\boldsymbol{\xi})\,dS(\boldsymbol{\xi})\,dS(\boldsymbol{y}) \\ &+ \int_{S_o}\tilde{t}_p(\boldsymbol{y})\int_{S_o} U^p_i(\boldsymbol{\xi}-\boldsymbol{y})t_i(\boldsymbol{\xi})\,dS(\boldsymbol{\xi})\,dS(\boldsymbol{y}) \end{aligned} \tag{2.74}$$

Consider next the stress given by (2.72). To regularize this integral relation, we utilize the decomposition (2.4) for the Cauchy-type singular kernel S^j_{lk} and the decomposition (2.14) for the strongly-singular kernel Σ^{lk}_{ij}, and then we carry out an integration by parts vis Stokes' theorem. The resulting singularity-reduced stress relation is then used to form a traction integral equation for points $\boldsymbol{y} \in S_o \cup S_c$ via a limiting process similar to that employed in the context of an isolated crack. The final form of traction integral equation is given by

$$
\begin{aligned}
c(\boldsymbol{y})t_k(\boldsymbol{y}) &= D_t \int_S C^{tk}_{mj}(\boldsymbol{\xi}-\boldsymbol{x}) D_m \Delta v_j(\boldsymbol{\xi}) dS(\boldsymbol{\xi}) + D_t \int_{S_o} G^j_{tk}(\boldsymbol{\xi}-\boldsymbol{y}) t_j(\boldsymbol{\xi}) dS(\boldsymbol{\xi}) \\
&- \int_{S_o} n_l(\boldsymbol{y}) H^j_{lk}(\boldsymbol{\xi}-\boldsymbol{y}) t_j(\boldsymbol{\xi}) dS(\boldsymbol{\xi}) \qquad (2.75)
\end{aligned}
$$

where $c = 1/2$ for $\boldsymbol{y} \in S_o$ whereas $c = 1$ for $\boldsymbol{y} \in S_c$. Finally, a weak-form traction integral equation is obtained from (2.75) as

$$
\begin{aligned}
-\int_S c(\boldsymbol{y}) t_k(\boldsymbol{y}) \tilde{v}_k(\boldsymbol{y}) dS(\boldsymbol{y}) &= \int_S D_t \tilde{v}_k(\boldsymbol{y}) \int_S C^{tk}_{mj}(\boldsymbol{\xi}-\boldsymbol{y}) D_m v_j(\boldsymbol{\xi}) dS(\boldsymbol{\xi}) dS(\boldsymbol{y}) \\
&+ \int_S D_t \tilde{v}_k(\boldsymbol{y}) \int_{S_o} G^j_{tk}(\boldsymbol{\xi}-\boldsymbol{y}) t_j(\boldsymbol{\xi}) dS(\boldsymbol{\xi}) dS(\boldsymbol{y}) \\
&+ \int_S \tilde{v}_k(\boldsymbol{y}) \int_{S_o} n_l(\boldsymbol{y}) H^j_{lk}(\boldsymbol{\xi}-\boldsymbol{y}) t_j(\boldsymbol{\xi}) dS(\boldsymbol{\xi}) dS(\boldsymbol{y}) \quad (2.76)
\end{aligned}
$$

where

$$
\tilde{v}_k(\boldsymbol{y}) = \begin{cases} \tilde{u}_k(\boldsymbol{y}) & , \quad \boldsymbol{y} \in S_o \\ \Delta\tilde{u}_k(\boldsymbol{y}) & , \quad \boldsymbol{y} \in S_c \end{cases} \qquad (2.77)
$$

in which $\tilde{u}_k$ and $\Delta\tilde{u}_k$ are test functions associated with S_o and S_c, respectively.

The weakly-singular, weak-form displacement integral equation (2.74) and the weakly-singular, weak-form traction integral equation (2.76) represent a generalization to anisotropic materials of the work by Li and Mear [28] for isotropic materials. These integral equations form a basis for the symmetric Galerkin boundary element method to be developed in Chapter 3.

Chapter 3

SGBEM for Analysis of Fractures in 3D Anisotropic Media

In this chapter, a symmetric Galerkin boundary element method (SGBEM) is developed for the analysis of three-dimensional anisotropic, linearly elastic bodies containing fractures. The formulation is based upon the weakly-singular, weak-form displacement and traction integral equations developed in Chapter 2. An important feature of the formulation is that it allows C^o elements to be used, and in the numerical implementation followed here standard isoparametric elements are employed everywhere except along the crack front.

Along the crack front, a special crack-tip element is utilized which properly captures the (asymptotic) behavior of the relative crack-face displacements. An important feature of this special crack tip element is that it contains degrees of freedom associated with the nodes along the crack front, and these degrees of freedom correspond, in essence, to the mixed-mode stress intensity factors. As a consequence, the stress intensity factors are obtained directly from the solution of the governing discretized equations without need for some type of indirect post-processing technique. To demonstrate the accuracy and versatility of the method, various examples are treated for cracks in an unbounded domain and for embedded and surface breaking cracks in a finite domain.

3.1 Symmetric weak formulation

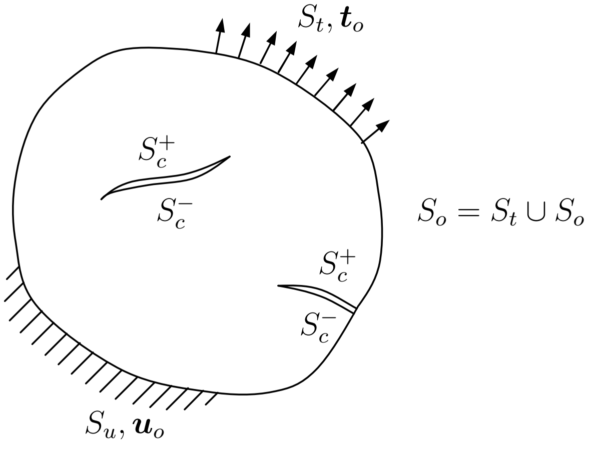

Figure 3.1: Schematic of an elastic body containing cracks.

Consider a homogeneous, anisotropic, linearly elastic body containing an embedded or surface breaking crack as shown schematically in Figure 3.1. The boundary of the domain is comprised of an 'ordinary' boundary S_o and the (geometrically coincident) upper and lower crack surfaces S_c^+ and S_c^-; for our purposes it suffices to consider the single crack surface $S_c \equiv S_c^+$ and we refer to $S = S_o \cup S_c$ as the 'total' surface of the domain. The ordinary boundary S_o is partitioned into a portion S_u on which displacements are prescribed and a portion S_t on which tractions are prescribed. As in Chapter 2, attention is restricted to cases in which body force is absent and in which the loading on the crack surfaces is such that the traction applied to S_c^+ is equal and opposite to that applied to S_c^-.

The weakly-singular, weak-form displacement and traction integral equations developed in Chapter 2 are recalled here as

$$\begin{aligned}
\frac{1}{2}\int_{S_o} v_p(\boldsymbol{y})\,\tilde{t}_p(\boldsymbol{y})\,dS(\boldsymbol{y}) &= \int_{S_o} \tilde{t}_p(\boldsymbol{y}) \int_S G^p_{mj}\ D_m v_j(\boldsymbol{\xi})\ dS(\boldsymbol{\xi})\,dS(\boldsymbol{y}) \\
&- \int_{S_o} \tilde{t}_p(\boldsymbol{y}) \int_S n_i(\boldsymbol{\xi})\ H^p_{ij}\ v_j(\boldsymbol{\xi})\ dS(\boldsymbol{\xi})\,dS(\boldsymbol{y}) \\
&+ \int_{S_o} \tilde{t}_p(\boldsymbol{y}) \int_{S_o} U^p_i\ t_i(\boldsymbol{\xi})\ dS(\boldsymbol{\xi})\,dS(\boldsymbol{y}) \qquad (3.1)
\end{aligned}$$

$$\begin{aligned}
-\int_S c(\boldsymbol{y}) t_k(\boldsymbol{y}) \tilde{v}_k(\boldsymbol{y}) dS(\boldsymbol{y}) &= \int_S D_t \tilde{v}_k(\boldsymbol{y}) \int_S C^{tk}_{mj}\ D_m v_j(\boldsymbol{\xi})\ dS(\boldsymbol{\xi}) dS(\boldsymbol{y}) \\
&+ \int_S D_t \tilde{v}_k(\boldsymbol{y}) \int_{S_o} G^j_{tk}\ t_j(\boldsymbol{\xi})\ dS(\boldsymbol{\xi}) dS(\boldsymbol{y}) \\
&+ \int_S \tilde{v}_k(\boldsymbol{y}) \int_{S_o} n_l(\boldsymbol{y})\ H^j_{lk}\ t_j(\boldsymbol{\xi})\ dS(\boldsymbol{\xi}) dS(\boldsymbol{y}) \qquad (3.2)
\end{aligned}$$

where

$$v_j(\boldsymbol{\xi}) = \begin{cases} u_j(\boldsymbol{\xi}) & , \quad \boldsymbol{\xi} \in S_o \\ \Delta u_j(\boldsymbol{\xi}) & , \quad \boldsymbol{\xi} \in S_c \end{cases} \quad , \quad \tilde{v}_k(\boldsymbol{y}) = \begin{cases} \tilde{u}_k(\boldsymbol{y}) & , \quad \boldsymbol{y} \in S_o \\ \Delta \tilde{u}_k(\boldsymbol{y}) & , \quad \boldsymbol{y} \in S_c \end{cases} \qquad (3.3)$$

and where

$$c(\boldsymbol{y}) = \begin{cases} \frac{1}{2} & , \quad \boldsymbol{y} \in S_o \\ 1 & , \quad \boldsymbol{y} \in S_c \end{cases} \qquad (3.4)$$

The weakly-singular kernels $\{U^p_i, G^p_{mj}, C^{tk}_{mj}\}$ appearing in these integral equations are given explicitly (for general anisotropy) by

$$\begin{aligned}
U^j_i(\boldsymbol{\xi} - \boldsymbol{y}) &= K^{ik}_{jk} \qquad (3.5) \\
G^p_{mj}(\boldsymbol{\xi} - \boldsymbol{y}) &= \epsilon_{abm} E_{ajdc}\ K^{pb}_{dc} \qquad (3.6) \\
C^{tk}_{mj}(\boldsymbol{\xi} - \boldsymbol{y}) &= A^{tkeo}_{mjdn}\ K^{eo}_{nd} \qquad (3.7)
\end{aligned}$$

where E_{ijkl} are the elastic moduli,

$$A^{tkeo}_{mjdn} = \epsilon_{pam}\epsilon_{pbt}(E_{dnkb}E_{ajeo} - \frac{1}{3}E_{ajkb}E_{dneo}) \qquad (3.8)$$

and

$$K_{jl}^{ik} \quad = \quad \frac{1}{8\pi^2 r} \oint_{\boldsymbol{z}\cdot\boldsymbol{r}=0} (\boldsymbol{z},\boldsymbol{z})_{ij}^{-1} \; z_k z_l \; ds(\boldsymbol{z}) \tag{3.9}$$

in which $r = ||\boldsymbol{\xi} - \boldsymbol{y}||$, $(\boldsymbol{z},\boldsymbol{z})_{jk} = z_i E_{ijkl} z_l$ and the integral is to be evaluated over a unit circle $\|\boldsymbol{z}\| = 1$ on a plane normal to the vector $\boldsymbol{r} = (\boldsymbol{\xi} - \boldsymbol{x})$. The quantity

$$H_{ij}^{p}(\boldsymbol{\xi} - \boldsymbol{y}) \quad = \quad \frac{1}{4\pi} \frac{(\xi_i - y_i)\delta_{pj}}{r^3} \tag{3.10}$$

is independent of material properties and we note that the kernel $n_i H_{ij}^{p}$ is weakly-singular.

To obtain a symmetric system of integral equations governing the boundary value problem we proceed as follows. On the surface S_u on which displacement data is prescribed we employ the displacement integral equation (3.1) with $\tilde{\boldsymbol{t}} = \boldsymbol{0}$ on S_u, on the surface S_t on which traction data is prescribed we utilize the traction integral equation (3.2) with $\tilde{\boldsymbol{v}} = \boldsymbol{0}$ on $S_u \cup S_c$ and, finally, on crack surface S_c we use the traction integral equation (3.2) with $\tilde{\boldsymbol{v}} = \boldsymbol{0}$ on $S_u \cup S_t$. The resulting formulation can be expressed in the concise form

$$\begin{array}{ccccccc}
\mathcal{A}_{uu}(\tilde{\boldsymbol{t}}, \boldsymbol{t}) & + & \mathcal{B}_{ut}(\tilde{\boldsymbol{t}}, \boldsymbol{u}) & + & \mathcal{B}_{uc}(\tilde{\boldsymbol{t}}, \Delta\boldsymbol{u}) & = & \mathcal{R}_1(\tilde{\boldsymbol{t}}) \\
\mathcal{B}_{ut}(\boldsymbol{t}, \tilde{\boldsymbol{u}}) & + & \mathcal{C}_{tt}(\tilde{\boldsymbol{u}}, \boldsymbol{u}) & + & \mathcal{C}_{tc}(\tilde{\boldsymbol{u}}, \Delta\boldsymbol{u}) & = & \mathcal{R}_2(\tilde{\boldsymbol{u}}) \\
\mathcal{B}_{uc}(\boldsymbol{t}, \Delta\tilde{\boldsymbol{u}}) & + & \mathcal{C}_{ct}(\Delta\tilde{\boldsymbol{u}}, \boldsymbol{u}) & + & \mathcal{C}_{cc}(\Delta\tilde{\boldsymbol{u}}, \Delta\boldsymbol{u}) & = & \mathcal{R}_3(\Delta\tilde{\boldsymbol{u}})
\end{array} \tag{3.11}$$

in which the bi-linear integral operators $\mathcal{A}_{PQ}, \mathcal{B}_{PQ}$ and $\mathcal{C}_{PQ}$ (with $P, Q \in \{u, t, c\}$) are defined by

$$\mathcal{A}_{PQ}(\boldsymbol{X}, \boldsymbol{Y}) \quad = \quad \int_{S_P} D_t X_p(\boldsymbol{y}) \int_{S_Q} U_i^p \; Y_i(\boldsymbol{\xi}) \; dS(\boldsymbol{\xi}) \, dS(\boldsymbol{y}) \tag{3.12}$$

$$\mathcal{B}_{PQ}(\boldsymbol{X}, \boldsymbol{Y}) \quad = \quad \int_{S_P} X_k(\boldsymbol{y}) \int_{S_Q} G_{mj}^{k} \; D_m Y_j(\boldsymbol{\xi}) \; dS(\boldsymbol{\xi}) \, dS(\boldsymbol{y})$$

$$- \int_{S_P} X_k(\boldsymbol{y}) \int_{S_Q} H^k_{mj}\; n_m(\boldsymbol{\xi})\; Y_j(\boldsymbol{\xi})\; dS(\boldsymbol{\xi})\, dS(\boldsymbol{y}) \qquad (3.13)$$

$$\mathcal{C}_{PQ}(\boldsymbol{X},\boldsymbol{Y}) \;=\; \int_{S_P} D_t X_k(\boldsymbol{y}) \int_{S_Q} C^{tk}_{mj}\; D_m Y_j(\boldsymbol{\xi})\; dS(\boldsymbol{\xi})\, dS(\boldsymbol{y}) \qquad (3.14)$$

and the linear operators $\mathcal{R}_1, \mathcal{R}_2$ and $\mathcal{R}_3$ are given (in terms of the prescribed displacement and traction data) by

$$\mathcal{R}_1(\tilde{\boldsymbol{t}}) \;=\; \mathcal{F}_u(\tilde{\boldsymbol{t}},\boldsymbol{u}) - \mathcal{B}_{uu}(\tilde{\boldsymbol{t}},\boldsymbol{u}) - \mathcal{A}_{ut}(\tilde{\boldsymbol{t}},\boldsymbol{t}) \qquad (3.15)$$

$$\mathcal{R}_2(\tilde{\boldsymbol{u}}) \;=\; -\mathcal{F}_t(\tilde{\boldsymbol{u}},\boldsymbol{t}) - \mathcal{C}_{tu}(\tilde{\boldsymbol{u}},\boldsymbol{u}) - \mathcal{B}_{tt}(\boldsymbol{t},\tilde{\boldsymbol{u}}) \qquad (3.16)$$

$$\mathcal{R}_3(\Delta\tilde{\boldsymbol{u}}) \;=\; -2\mathcal{F}_c(\Delta\tilde{\boldsymbol{u}},\boldsymbol{t}) - \mathcal{C}_{cu}(\Delta\tilde{\boldsymbol{u}},\boldsymbol{u}) - \mathcal{B}_{tc}(\boldsymbol{t},\Delta\tilde{\boldsymbol{u}}) \qquad (3.17)$$

with

$$\mathcal{F}_P(\boldsymbol{X},\boldsymbol{Y}) \;=\; \frac{1}{2}\int_{S_P} X_i(\boldsymbol{y})\; Y_i(\boldsymbol{y})\, dS(\boldsymbol{y}) \qquad (3.18)$$

Note that (owing to the properties of the kernels discussed in Chapter 2)

$$\mathcal{A}_{pq}(\boldsymbol{X},\boldsymbol{Y}) \;=\; \mathcal{A}_{qp}(\boldsymbol{Y},\boldsymbol{X}) \qquad (3.19)$$

$$\mathcal{C}_{pq}(\boldsymbol{X},\boldsymbol{Y}) \;=\; \mathcal{C}_{qp}(\boldsymbol{Y},\boldsymbol{X}) \qquad (3.20)$$

hence the formulation (3.11) is in fact in a symmetric form. Finally, note that for the special case of a crack in an unbounded domain the formulation reduces to

$$\mathcal{C}_{cc}(\Delta\tilde{\boldsymbol{u}},\Delta\boldsymbol{u}) = -2\mathcal{F}_c(\Delta\tilde{\boldsymbol{u}},\boldsymbol{t}) \qquad (3.21)$$

3.2 Numerical Implementation

3.2.1 Discretization

A Galerkin strategy is adopted to construct an approximate solution to the system of integral equations (3.11). The total surface of the domain, including the ordinary boundary $S_o = S_u \cup S_t$ and the crack surface S_c, is discretized using standard two dimensional isoparametric C^o elements everywhere except along the crack front; along the crack front, a special crack tip element is utilized as discussed further below.

In the context of the discretization, we introduce trial and test functions

$$\begin{aligned} \boldsymbol{u} &= \boldsymbol{\Phi}_t^{\mathrm{T}} \boldsymbol{U} \quad , \quad & \tilde{\boldsymbol{u}} &= \boldsymbol{\Phi}_t^{\mathrm{T}} \tilde{\boldsymbol{U}} \quad & \text{on } S_t \quad & (3.22) \\ \Delta \boldsymbol{u} &= \boldsymbol{\Phi}_c^{\mathrm{T}} \Delta \boldsymbol{U} \quad , \quad & \Delta \tilde{\boldsymbol{u}} &= \boldsymbol{\Phi}_c^{\mathrm{T}} \Delta \tilde{\boldsymbol{U}} \quad & \text{on } S_c \quad & (3.23) \\ \boldsymbol{t} &= \boldsymbol{\Phi}_u^{\mathrm{T}} \boldsymbol{T} \quad , \quad & \tilde{\boldsymbol{t}} &= \boldsymbol{\Phi}_u^{\mathrm{T}} \tilde{\boldsymbol{T}} \quad & \text{on } S_u \quad & (3.24) \end{aligned}$$

in which, with $_Q \in \{u, t, c\}$, $\boldsymbol{\Phi}_Q$ is a column vector of nodal basis functions associated with S_Q, $\boldsymbol{\Phi}_Q^{\mathrm{T}}$ denotes the transpose of $\boldsymbol{\Phi}_Q$, and $\{\boldsymbol{U}, \boldsymbol{T}, \Delta\boldsymbol{U}\}$ and $\{\tilde{\boldsymbol{U}}, \tilde{\boldsymbol{T}}, \Delta\tilde{\boldsymbol{U}}\}$ are column vectors of nodal quantities.

Employing (3.22)-(3.24) we obtain a discrete form of (3.11) which, upon exploiting the arbitrariness of the test functions, leads to the system of linear algebraic equations

$$\begin{bmatrix} \boldsymbol{A}_{uu} & \boldsymbol{B}_{ut} & \boldsymbol{B}_{uc} \\ \boldsymbol{B}_{ut}^{\mathrm{T}} & \boldsymbol{C}_{tt} & \boldsymbol{C}_{tc} \\ \boldsymbol{B}_{uc}^{\mathrm{T}} & \boldsymbol{C}_{ct}^{\mathrm{T}} & \boldsymbol{C}_{cc} \end{bmatrix} \begin{bmatrix} \boldsymbol{T} \\ \boldsymbol{U} \\ \Delta\boldsymbol{U} \end{bmatrix} = \begin{bmatrix} \boldsymbol{R}_1 \\ \boldsymbol{R}_2 \\ \boldsymbol{R}_3 \end{bmatrix} \tag{3.25}$$

where the sub-matrices $\boldsymbol{A}_{PQ}$, $\boldsymbol{B}_{PQ}$ and $\boldsymbol{C}_{PQ}$ (with $_P, _Q \in \{u, t, c\}$) correspond to the integral operators $\mathcal{A}_{PQ}, \mathcal{B}_{PQ}, \mathcal{C}_{PQ}$, and where the column vectors $\boldsymbol{R}_1$, $\boldsymbol{R}_2$ and $\boldsymbol{R}_3$ correspond to the integral operators $\mathcal{R}_1$, $\mathcal{R}_2$, $\mathcal{R}_3$.

Note that $\boldsymbol{A}_{uu}$ is symmetric and positive definite whereas $\boldsymbol{C}_{tt}$ and $\boldsymbol{C}_{cc}$ are symmetric and negative definite, so that in general the system of linear equations (3.25) has a symmetric, non-definite coefficient matrix. Note also that for a pure traction boundary value problem the coefficient matrix is strictly negative definite (once the problem has been properly constrained to eliminate rigid body motion).

3.2.2 Evaluation of sub-matrices

Evaluation of the sub-matrices $\boldsymbol{A}_{PQ}$, $\boldsymbol{B}_{PQ}$ and $\boldsymbol{C}_{PQ}$ appearing in (3.25) requires a double surface integration involving a weakly-singular kernel. To do this effectively necessitates that the kernels $\{U_i^j, G_{mj}^p, C_{mj}^{tk}\}$ be computed efficiently and that an accurate numerical integration strategy be adopted to perform the surface integrals.

Treatment of the kernels

The kernels $\{U_i^j, G_{mj}^p, C_{mj}^{tk}\}$ are defined in terms of a line integral over a unit circle $\|\boldsymbol{z}\| = 1$ on a plane normal to the vector $\boldsymbol{r}$ (see equation (3.9)). Were this line integral computed independently for every source point $\boldsymbol{x}$ and field point $\boldsymbol{\xi}$ arising in the numerical evaluation of the sub-matrices, the resulting computational time would be excessive. For this reason, we introduce an interpolation strategy to approximate these kernels to (arbitrary) specified accuracy.

Toward developing such an interpolation strategy, let $\{r, \theta, \phi\}$ be a spherical coordinate system which has its origin at $\boldsymbol{\xi}$ and for which $\theta \in [0, 2\pi]$ and $\phi \in [0, \pi]$. Then the quantity K_{jl}^{ik} defined by (3.9) can be expressed in the form

$$K_{jl}^{ik}(\boldsymbol{\xi} - \boldsymbol{x}) = \frac{1}{r}\ \bar{K}_{jl}^{ik}(\theta, \phi) \tag{3.26}$$

in which the 'angular function' $\bar{K}_{jl}^{ik}(\theta, \phi)$ is given by

$$\bar{K}_{jl}^{ik}(\theta, \phi) = \frac{1}{8\pi^2} \oint_{\boldsymbol{z}\cdot\boldsymbol{r}=0} (\boldsymbol{z}, \boldsymbol{z})_{ij}^{-1}\ z_k z_l\ ds(\boldsymbol{z}) \tag{3.27}$$

The function $\bar{K}_{jl}^{ik}$ is to be interpolated over $[0, 2\pi] \times [0, \pi]$, and to do so we introduce a two dimensional grid obtained by discretizing the intervals $[0, 2\pi]$ and $[0, \pi]$ into sub-intervals. Let $\theta_{(i)}$ (for $i = 1, 2, ..., N_\theta$) be nodal points on $[0, 2\pi]$ and let $\phi_{(i)}$ (for $i = 1, 2, ..., N_\phi$) be nodal points on $[0, \pi]$. The approximation of $\bar{K}_{jl}^{ik}$ is then given by

$$\bar{K}^{ik}_{jl}(\theta,\phi) \approx \sum_{i=1}^{N_\theta}\sum_{j=1}^{N_\phi} \bar{K}^{ik}_{jl}(\theta_{(i)},\phi_{(j)})\varphi_{ij}(\theta,\phi) \tag{3.28}$$

in which $\varphi_{ij}(\theta,\phi)$ are basis functions associated with nodal points $(\theta_{(i)},\phi_{(j)})$, and where $\bar{K}^{ik}_{jl}(\theta_{(i)},\phi_{(j)})$ are nodal values obtained by evaluating (3.27). We remark that while the interpolation strategy has been illustrated for the quantity $\bar{K}^{ik}_{jl}$, it can be utilized separately for each of the three kernels $\{U^j_i, G^p_{mj}, C^{tk}_{mj}\}$.

By employing the properties of the kernels given by (2.64) and (2.67)-(2.69), the domain used for constructing the approximation can be significantly reduced. The minimum domains that are required for various specific types of anisotropy are summarized in Table 3.1. Note that the angular coordinates appearing in the table are for a spherical coordinate system which is associated with the local frame used to develop (2.67)-(2.69). Also note that the values of the kernels for angular coordinates outside the minimum domains are readily obtained using the properties of the kernels.

Materials	ϕ	θ
Cubic	$[0,\pi/4]$	$[0,\pi/4]$
Transversely isotropic	$[0,\pi/2]$	$[0,\pi/4]$
Orthotropic	$[0,\pi/2]$	$[0,\pi/2]$
Monoclinic	$[0,\pi/2]$	$[0,\pi]$
General anisotropic	$[0,\pi/2]$	$[0,2\pi]$

Table 3.1: Minimum region of interpolation for different material symmetries.

For the numerical examples to be presented below, the following specific interpolation strategy has been followed. The intervals associated with the partitioning of the angular coordinates are taken to be uniform, standard quadratic interpolants are employed over the resulting grid, and the nodal values of the kernels are obtained by using gaussian quadrature to evaluate the loop integral. The number of subregions and the order of the gaussian quadrature are chosen to ensure that interpolated values of the kernels are highly accurate (such that any error associated with evaluating the kernels has an insignificant effect upon the final numerical solution of the boundary valued problem).

Double surface integration

Since the kernels are weakly-singular, all the surface integrals exist in the ordinary sense. Nonetheless, a special numerical treatment is required to efficiently and accurately evaluate these integrals due to the fact that, when the integration involves neighboring pairs of elements, the integrands are 'nearly-singular'. To perform the integrations we adopt the numerical integration scheme used by Li *et al.* [29] in their development of a SGBEM for isotropy. Details of the integration technique are given by Xiao [45].

3.2.3 Special crack tip element

For a crack in a linearly elastic, anisotropic solid, the relative crack-face displacement in the neighborhood of the crack front exhibits a square-root behavior (e.g. [1], [41]). To account for this behavior, we adopt the crack tip element originally introduced by Li *et al.* [29] for isotropy. With reference to the 'master crack-tip element' indicated in Figure 3.2, we take the crack front to lie along $\eta = -1$ and we introduce special element shape functions

$$\psi'_{(i)}(\xi,\eta) = \frac{\sqrt{1+\eta}}{A_{(i)}}\ \psi_{(i)}(\xi,\eta) \quad \text{(no sum on } i\text{)} \tag{3.29}$$

where $\psi_{(i)}(\xi,\eta)$ are standard shape functions associated with the i^{th} node, and

$$A_{(i)} = \begin{cases} \sqrt{1+\eta_{(i)}} & \text{for } \eta_{(i)} \neq -1 \\ 1/2 & \text{for } \eta_{(i)} = -1 \end{cases}$$

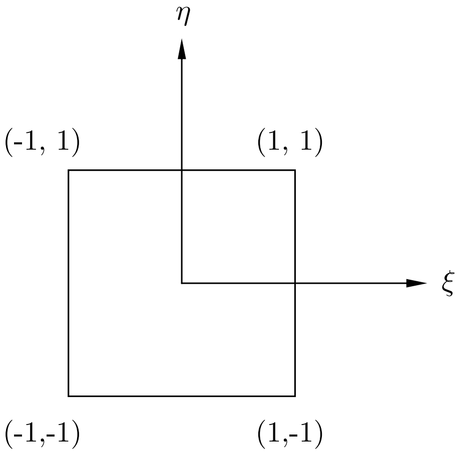

Figure 3.2: Master element corresponding to special crack tip elements where $\eta = -1$ is associated with the crack front.

in which $(\xi_{(i)}, \eta_{(i)})$ are the coordinates of the i^{th} node. The relative crack-face displacement is then given by

$$\Delta \boldsymbol{u} = \sqrt{1+\eta} \sum_{i=1}^{N_e} \frac{\boldsymbol{u}_{(i)}}{A_{(i)}} \psi_{(i)}(\xi, \eta) \tag{3.30}$$

where N_e denotes the number of nodes on the element and $\boldsymbol{u}_{(i)}$ are nodal quantities. Note that, for nodes which are not on the crack front, $\boldsymbol{u}_{(i)}$ corresponds directly to the nodal value of the relative crack-face displacement. However, for nodes which are on the crack front $\boldsymbol{u}_{(i)}$ is associated with the *gradient* of the relative crack-face displacement; this feature will be discussed further below in the context of the stress intensity factors.

We remark in passing that when the crack front intersect the ordinary boundary (i.e. the case of a surface breaking crack) the crack tip element, as well as the elements on the ordinary boundary adjacent to the crack tip element, must be modified to maintain compatibility of the displacement data. The treatment of such surface breaking cracks follows the work of Li *et al.* [29].

Determination of Stress intensity factors

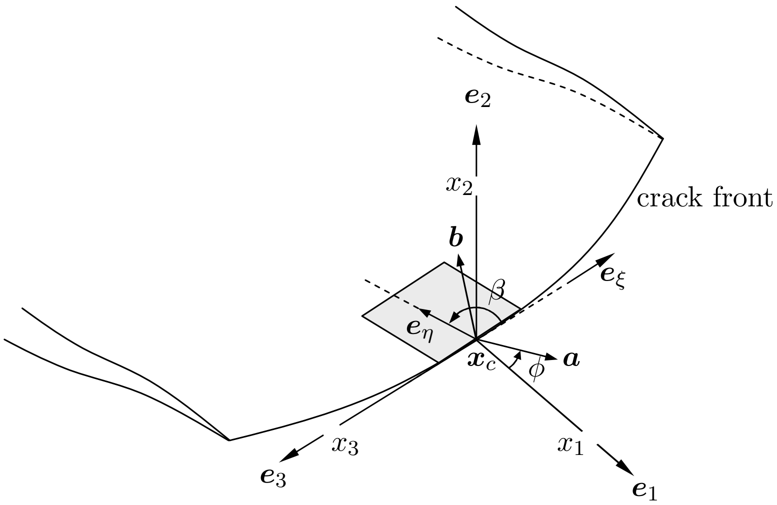

Figure 3.3: Local coordinate system used in determining the stress intensity factors.

Consider a point $\boldsymbol{x}_c$ which is on the crack front, and at this point introduce a local cartesian coordinate system $\{x_1, x_2, x_3\}$ with unit base vector $\{\boldsymbol{e}_1, \boldsymbol{e}_2, \boldsymbol{e}_3\}$ as indicated in Figure 3.3. The unit vector $\boldsymbol{e}_1$ is taken to lie in the plane defined by the crack surface local to $\boldsymbol{x}_c$, $\boldsymbol{e}_3$ is taken to be directed tangent to the crack front at $\boldsymbol{x}_c$, and $\boldsymbol{e}_2$ follows from the right-handed rule. For an anisotropic solid, the stress intensity factors at $\boldsymbol{x}_c$ can then be expressed in terms of the relative crack-face displacements in the vicinity of the crack tip as ([1] and [47])

$$K_k(\boldsymbol{x}_c) = \frac{\sqrt{2\pi}}{4} B_{kl} \lim_{x_1 \to 0^-} \left(\frac{\Delta u_l(\boldsymbol{x})}{\sqrt{-x_1}} \right) \tag{3.31}$$

with

$$B_{kl} = -\frac{1}{2\pi}\int_0^{2\pi}\Big[(\boldsymbol{a},\boldsymbol{b})_{km}(\boldsymbol{b},\boldsymbol{b})^{-1}_{mn}(\boldsymbol{b},\boldsymbol{a})_{nl} - (\boldsymbol{a},\boldsymbol{a})_{kl}\Big]d\phi. \tag{3.32}$$

where $\boldsymbol{a}$ and $\boldsymbol{b}$ are orthonormal vectors contained in the plane $x_3 = 0$, ϕ is the angle between $\boldsymbol{a}$ and $\boldsymbol{e}_1$ indicated in Figure 3.3, and $(\boldsymbol{a},\boldsymbol{b})_{ij} = a_m E_{imnj} b_n$ in which E_{imnj} are the elastic moduli. We emphasize that the components of all quantities appearing in the expressions above are relative to the local coordinate system $\{x_i\}$.

Let $(\xi_c, -1)$ denote the coordinates on the master element corresponding to the point $\boldsymbol{x}_c$ in physical space. Forming a Taylor series expansion of $\psi_{(i)}(\xi,\eta)$ about this point, we find from (3.30) that the relative crack-face displacement in the vicinity of the point $\boldsymbol{x}_c$ satisfies

$$\Delta\boldsymbol{u}(\boldsymbol{x}) = 2\sqrt{1+\eta}\,\Big[\boldsymbol{u}^o(\boldsymbol{x}_c) + \mathcal{O}(\xi-\xi_c) + \mathcal{O}(\eta+1)\Big] \tag{3.33}$$

with

$$\boldsymbol{u}^o(\boldsymbol{x}_c) = \sum_i \boldsymbol{u}_{(i)}\psi_{(i)}(\xi_c,-1) \tag{3.34}$$

being a constant (which, since $\psi_{(i)}(\xi_c,-1) = 0$ for nodes not on the crack front, only involves data associated with nodes on the crack front). To proceed, let $\boldsymbol{r}^*(\xi,\eta) = \boldsymbol{x}(\xi,\eta) - \boldsymbol{x}_c$ be the (relative) position vector to points on the crack surface in the vicinity of $\boldsymbol{x}_c$, and note that the Taylor series expansion of this vector about $(\xi_c,-1)$ is given to the first order by

$$\boldsymbol{r}^* = (\xi-\xi_c)J_1\boldsymbol{e}_\xi + (\eta+1)J_2\boldsymbol{e}_\eta \tag{3.35}$$

where

$$J_1 = \left|\left|\frac{\partial\boldsymbol{r}^*}{\partial\xi}(\xi_c,-1)\right|\right| \quad , \quad \boldsymbol{e}_\xi = \frac{1}{J_1}\frac{\partial\boldsymbol{r}^*}{\partial\xi}(\xi_c,-1) \tag{3.36}$$

$$J_2 = \left|\left|\frac{\partial\boldsymbol{r}^*}{\partial\eta}(\xi_c,-1)\right|\right| \quad , \quad \boldsymbol{e}_\eta = \frac{1}{J_2}\frac{\partial\boldsymbol{r}^*}{\partial\eta}(\xi_c,-1) \tag{3.37}$$

Then forming $x_1 = \boldsymbol{r}^* \cdot \boldsymbol{e}_1$ (and noting that $\boldsymbol{e}_\xi = -\boldsymbol{e}_3$) it follows that

$$1 + \eta = -\frac{x_1}{J_2 \sin\beta} \tag{3.38}$$

where β is the angle indicated in Figure 3.3 which satisfies $\sin\beta = -\boldsymbol{e}_\eta \cdot \boldsymbol{e}_1$. Using (3.38) and (3.33) we obtain

$$\Delta\boldsymbol{u}(\boldsymbol{x}) = 2\sqrt{\frac{-x_1}{J \sin\beta}}\,\left[\boldsymbol{u}^o(\boldsymbol{x}_c) + \mathcal{O}(\xi - \xi_c) + \mathcal{O}(\eta + 1)\right] \tag{3.39}$$

Finally, combining (3.39) with (3.31) and forming the limit $\boldsymbol{x} \rightarrow \boldsymbol{x}_c$ (i.e. $\xi \rightarrow \xi_c$ and $\eta \rightarrow -1$) we obtain the stress intensity factors as

$$K_k(\boldsymbol{x}_c) = \sqrt{\frac{\pi}{2J \sin\beta}}\; B_{kl}\left[\boldsymbol{u}^o(\boldsymbol{x}_c) \cdot \boldsymbol{e}_l(\boldsymbol{x}_c)\right] \tag{3.40}$$

Note that the stress intensity factors are given directly in terms of the special degrees of freedom associated with the nodes along the crack front. We remark that for the numerical results to follow, a nine-node crack tip element (based upon a standard quadratic element) is utilized.

3.3 Numerical results

To demonstrate the capabilities of the SGBEM for stress analysis of cracks, we now treat various example problems including ones for cracks in an unbounded domain and ones for embedded and surface breaking cracks in a finite domain. Four different types of materials are considered: an isotropic material (with Poisson's ratio $\nu = 0.3$ unless stated otherwise), barium titanate, zinc and a graphite-reinforced composite. The latter three are transversely isotropic materials and the elastic constants which characterize them are given in Table 3.2. Note that barium titanate is only mildly anisotropic whereas zinc and the graphite-reinforced composite exhibit a high degree of anisotropy. Indeed, note that for zinc the modulus along the axis of elastic symmetry is about one-third that for the plane of isotropy, whereas for the graphite-reinforced composite the modulus along the axis of symmetry is about ten-times that for the plane of isotropy. These materials have been selected since they represent (transversely) anisotropic materials which have very different material response.

Materials	E_{1111}	E_{1122}	E_{1133}	E_{3333}	E_{1313}
Barium titanate	16.80	7.80	7.10	18.90	5.46
Zinc	16.09	3.35	5.01	6.10	3.83
Graphite composite	2.130	1.013	0.808	20.996	0.587

Table 3.2: Elastic constants for barium titanate, zinc and a graphite-reinforced composite (x10^6 psi, [26], [25]). The axis of symmetry is taken along the x_3 coordinate direction.

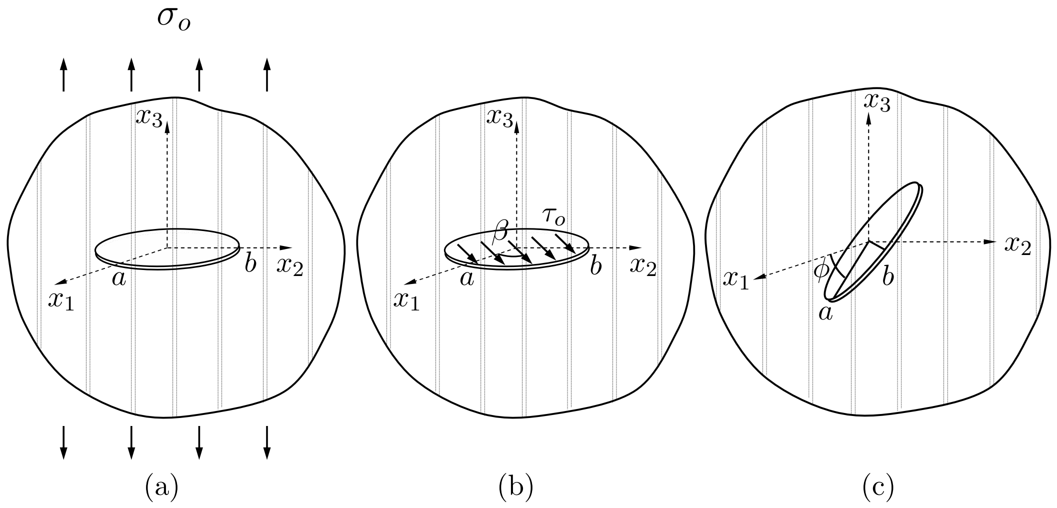

Figure 3.4: An elliptical crack subjected to three types of loading: (a) uniform remote tension σ_o in x_3-direction, (b) uniform shear traction τ_o applied to both crack surfaces and (c) uniform pressure p_o applied to both crack surfaces.

3.3.1 Elliptical Crack in unbounded domain

Consider an elliptical crack in an unbounded domain as indicated in Figure 3.4. The major and minor semi-axes of the crack are denoted a and b, respectively, and we note that $a = b$ corresponds to a penny-shaped crack. The material in which the crack is embedded is taken to be transversely isotropic with the axis of material symmetry along the x_3 coordinate direction, and the three loading conditions indicated in the figure are considered.

The numerical results to be presented below are obtained utilizing the meshes depicted in Figure 3.5. The meshes shown are for a penny-shaped crack; those used to treat an elliptical crack are obtained from these by means of an affine transformation (i.e. a simple 'stretching'). Results for the stress intensity factors along the crack front are given in terms of the angle θ which is defined such that

$$x_1 = a\cos\theta \ , \quad x_2 = b\sin\theta \ , \quad x_3 = 0 \quad ; \quad \theta \in [0, 2\pi] \tag{3.41}$$

Remote tension

We consider first the case indicated in 3.4(a) which is that for uniform remote tension applied in the direction of the axis of material symmetry (i.e. in the x_3 coordinate direction) with the crack oriented such that it lies in the plane of isotropy. We remark that for this case only the mode-I stress intensity factor K_I exists, and it can be shown that the stress intensity factor (as a function of position on the crack front) is independent of the elastic constants [26]. Nonetheless, we treat both zinc and barium titanate in order to ensure the validity of the SGBEM implementation.

Numerical results for K_I, along with the exact solution K_I^{exact} [26], are shown in Figure 3.6 for crack aspect ratios $a/b \in \{1, 2, 3\}$. From the figure it is evident that highly accurate results are obtained even for (the very course) Mesh 1 except in the vicinity of $\theta \in \{0^o, 90^o\}$ where the numerical results deviate slightly from the exact solution. To examine the quality of the results more carefully, the stress intensity factors at $\theta \in \{0^o, 90^o\}$ are shown for zinc in Table 3.3; the corresponding results for barium titanate are similar. Note that $\theta = 0^o$ is the location where the minimum value of the stress intensity factor occurs and $\theta = 90^o$ is that where the maximum value occurs [26]. We now focus attention on $\theta = 90^o$ since this is where the error is greatest for the coarse mesh, and we note that even for the aspect ratio $a/b = 3$ the error in the calculated stress intensity factor is less than 2%. The fact that the error tends to increase with increasing aspect ratio is not surprising since the meshes for the elliptical cracks are obtained by simply ‘stretching’ the mesh originally designed for a penny-shaped crack.

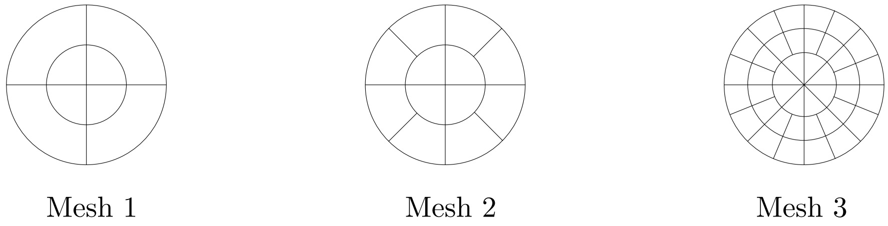

Figure 3.5: Meshes used in analysis of a penny-shaped crack ($a = b$). For elliptical crack, meshes are obtained by simply stretching these meshes.

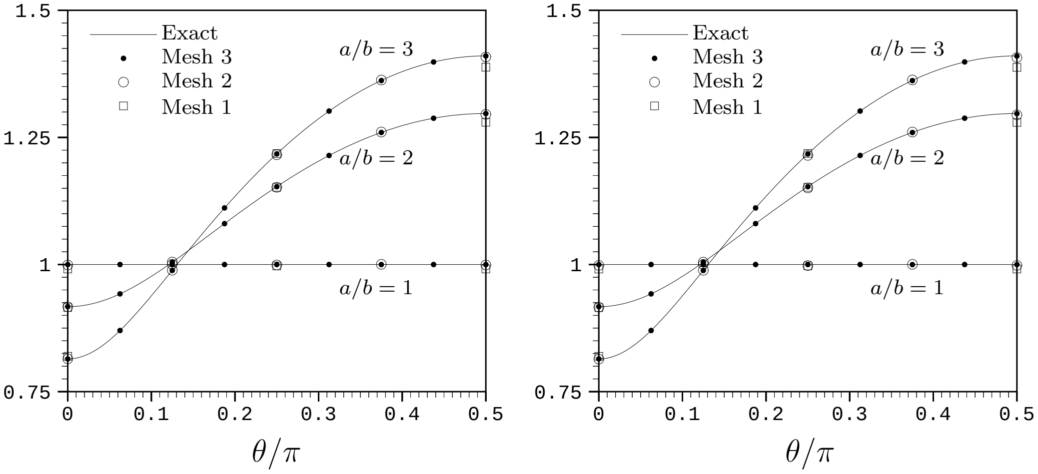

(a)

(b)

Figure 3.6: Normalized mode-I stress intensity factor ($\frac{K_I}{2\sigma_o}\sqrt{\frac{\pi}{b}}$) for an elliptical crack under uniform remote tension σ_o. Results are for (a) barium titanate and (b) zinc.

	$a/b = 1$	$a/b = 2$		$a/b = 3$	
Mesh	$\theta = 0^o, 90^o$	$\theta = 0^o$	$\theta = 90^o$	$\theta = 0^o$	$\theta = 90^o$
1	0.9913	0.9980	0.9865	1.0064	0.9839
2	0.9983	0.9989	0.9978	0.9995	0.9976
3	0.9999	1.0000	0.9998	1.0001	0.9998

Table 3.3: Normalized stress intensity factors, K_I/K_I^{exact}, at $\theta \in \{0^o, 90^o\}$ for an elliptical crack with aspect ratio $a/b \in \{1, 2, 3\}$. Loading is uniform remote tension σ_o and the material is zinc.

Applied shear traction

Consider now an elliptical crack subjected to uniform shear traction τ_o as shown in Figure 3.4(b). The orientation of the load applied to the upper crack surface is designated by an angle β measured from the x_1-axis as indicated in the figure. As a consequence of the anti-symmetric nature of the loading, only the mode-II and mode-III stress intensity factors $\{K_{II}, K_{III}\}$ are present. We note that an exact solution is available for this boundary value problem [26], and numerical results obtained using the three meshes will be contrasted with this exact solution. Results have been obtained for all three transversely isotropic materials introduced above, but since the results are all qualitatively similar (in terms of their accuracy) results are only reported for zinc.

The mode-II and mode-III stress intensity factors are shown in Figure 3.7 for $\beta = 45^o$ and in Figure 3.8 for $\beta = 90^o$. It is evident that the numerical results are in excellent agreement with the analytical solution except that the coarse mesh gives rise to small errors near the major and minor axes of the crack. For $\beta = 90^o$, numerical values of K_{II} at $\theta = 90^o$ and K_{III} at $\theta = 0^o$ are presented in Table 3.4 for $a/b \in \{1, 3\}$. From the table, it is evident that highly accurate results (with the error being a fraction of one percent) are obtained using Mesh 2 and Mesh 3. For Mesh 1, the error in the results is about 1.5% for a penny-shaped crack and about 3% for an elliptical crack with $a/b = 3$.

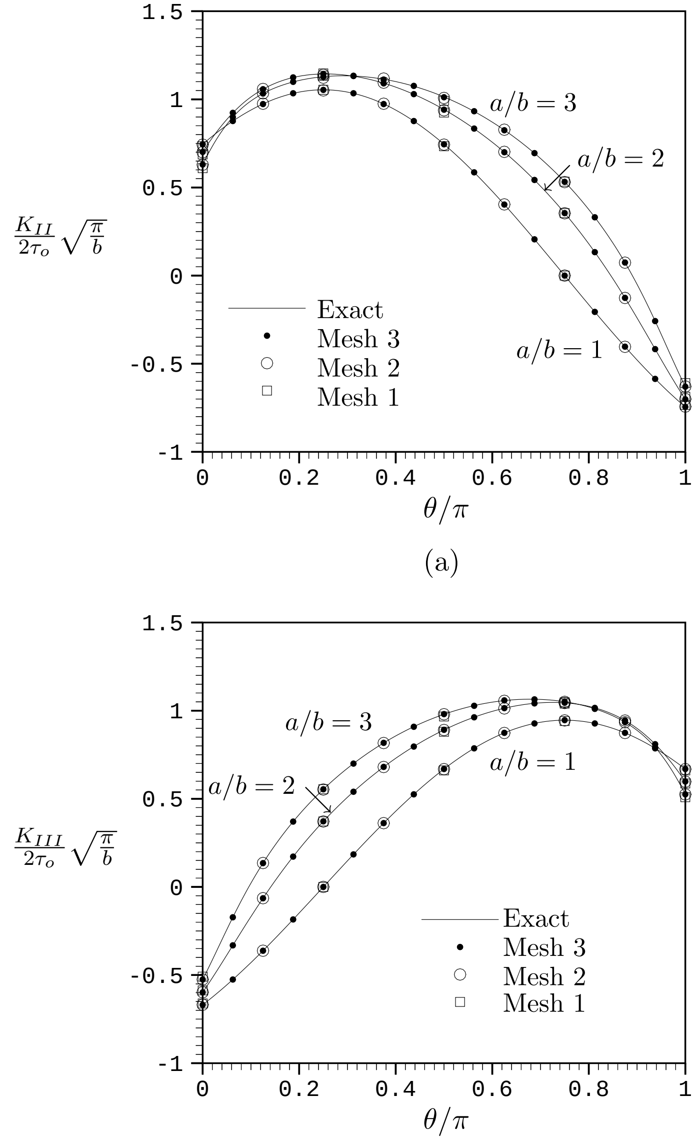

(a)

(b)

Figure 3.7: (a) Normalized mode-II and (b) normalized mode-III stress intensity factors for an elliptical crack subjected to uniform shear traction with $\beta = 45^o$. Material is zinc.

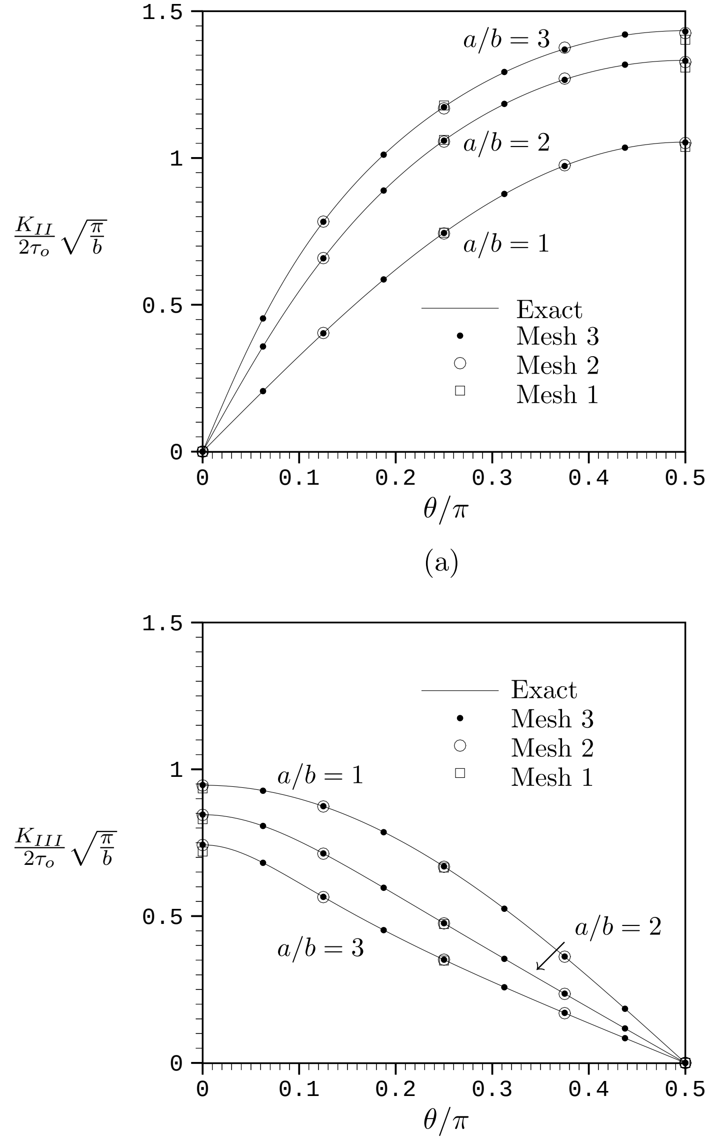

(a)

(b)

Figure 3.8: (a) Normalized mode-II and (b) normalized mode-III stress intensity factors for an elliptical crack subjected to uniform shear traction with $\beta = 90^o$. Material is zinc.

Mesh	$a/b = 1$		$a/b = 3$	
	K_{II}/K_{II}^{exact} $\theta = 90^o$	K_{III}/K_{III}^{exact} $\theta = 0^o$	K_{II}/K_{II}^{exact} $\theta = 90^o$	K_{III}/K_{III}^{exact} $\theta = 0^o$
1	0.9846	0.9886	0.9783	0.9694
2	0.9969	0.9991	0.9942	0.9993
3	0.9994	1.0004	0.9981	1.0003

Table 3.4: Stress intensity factors, normalized by the exact solution [26], for a penny-shaped crack ($a/b = 1$) and an elliptical crack with $a/b = 3$. Loading is uniform shear traction in the x_2-direction ($\beta = 90^o$) and the material is zinc.

Inclined crack under uniform pressure

To demonstrate the capability of the method to treat mixed-mode conditions induced by material anisotropy, we consider a pressurized elliptical crack which lies in a plane which does not coincide with the plane of material isotropy, Figure 3.4(c). The angle between the normal to the plane of the crack and the axis of elastic symmetry is denoted by ϕ, and the applied uniform pressure is denoted by p_o. Here we treat the single crack orientation $\phi = 45^o$, and we again adopt the three meshes shown in Figure 3.5. We remark that an exact solution to this boundary value problem is not available.

The stress intensity factors, as a function of angular position θ along the crack front, are shown in Figure 3.9 for zinc and in Figure 3.10 for a graphite-reinforced composite. The agreement between the solutions obtained from each mesh indicates good convergence, high accuracy and only slight mesh dependence. We remark that were the material isotropic, the problem would be strictly mode-I. For the transversely isotropic materials treated, the material anisotropy gives rise to mixed-mode condition and, in fact, the mode-II and mode-III stress intensity factors are of the same order as the mode-I stress intensity factor.

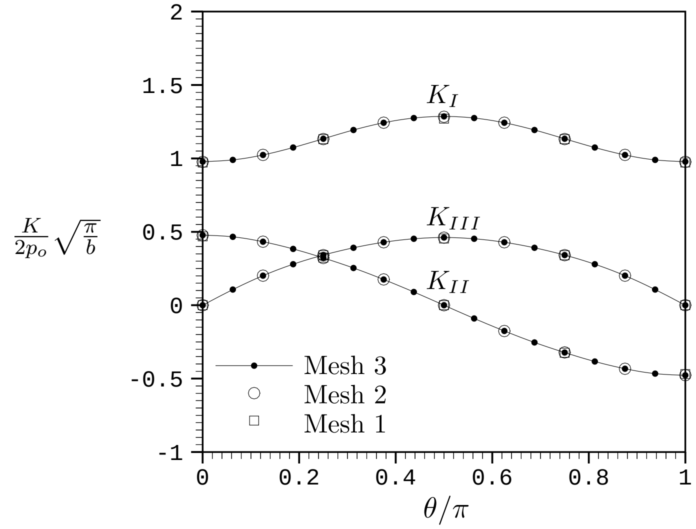

(a)

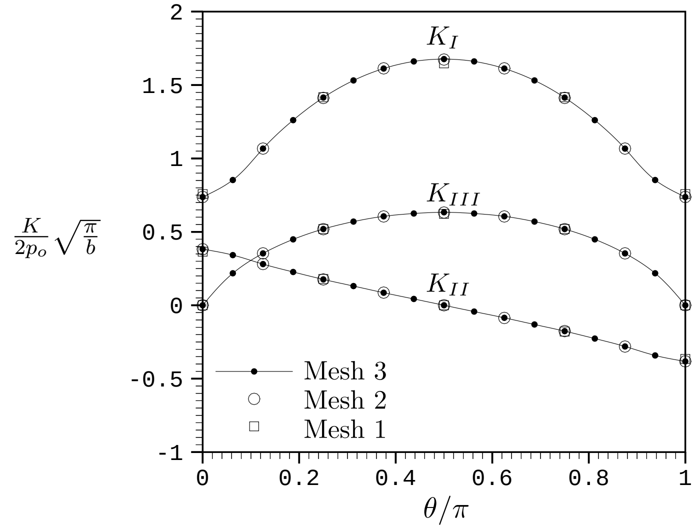

(b)

Figure 3.9: Normalized mode-I, mode-II and mode-III stress intensity factors for an elliptical crack under uniform pressure p_o. Numerical results are for (a) penny-shaped crack and an (b) elliptical crack with $a/b = 3$ embedded in zinc with $\phi = 45^o$.

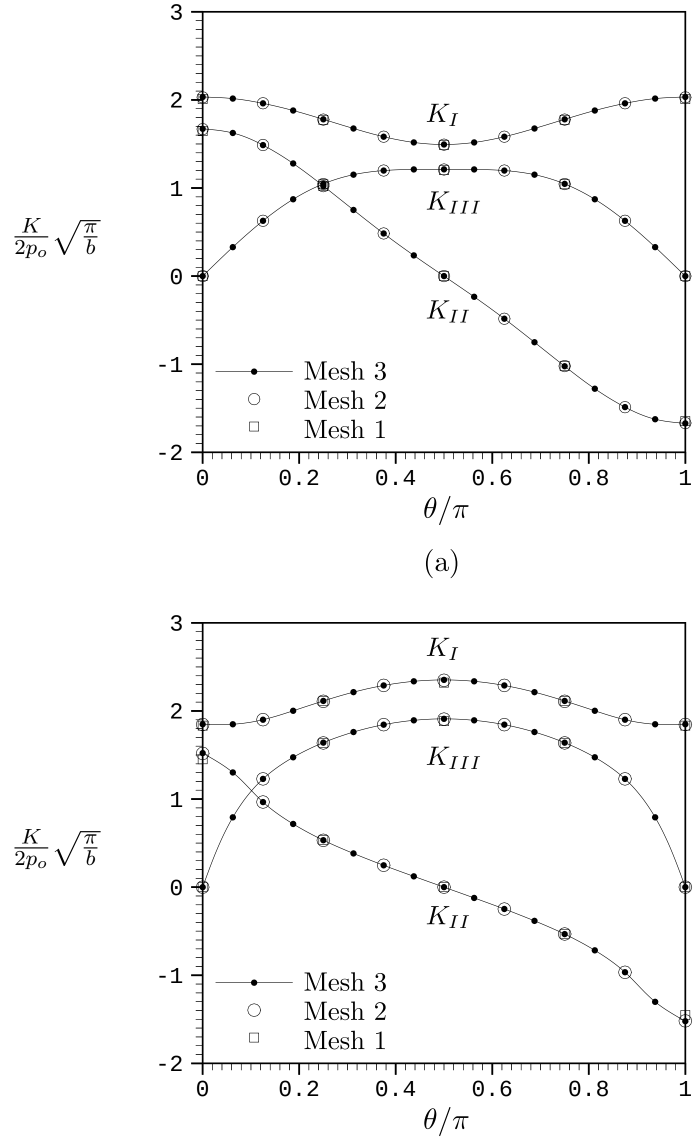

(a)

(b)

Figure 3.10: Normalized mode-I, mode-II and mode-III stress intensity factors for an elliptical crack under uniform pressure p_o. Numerical results are for (a) penny-shaped crack and an (b) elliptical crack with $a/b = 3$ embedded in a graphite-reinforced composite with $\phi = 45^o$.

3.3.2 Cracks in a finite domain

To demonstrate the capability of the method for stress analysis of cracks in a finite domain, we consider several problems involving both embedded and surface breaking cracks. Mixed-mode conditions induced by both applied loading and material anisotropy are treated.

Penny shaped crack in a cylinder

Consider a solid circular cylinder of radius R and length $2L$ which contains a penny-shaped crack of radius a as shown in Figure 3.11(a). Uniform normal traction σ_o and torque T_o applied at the ends of the cylinder are considered, and the material is assumed to be transversely isotropic with the axis of elastic symmetry oriented at

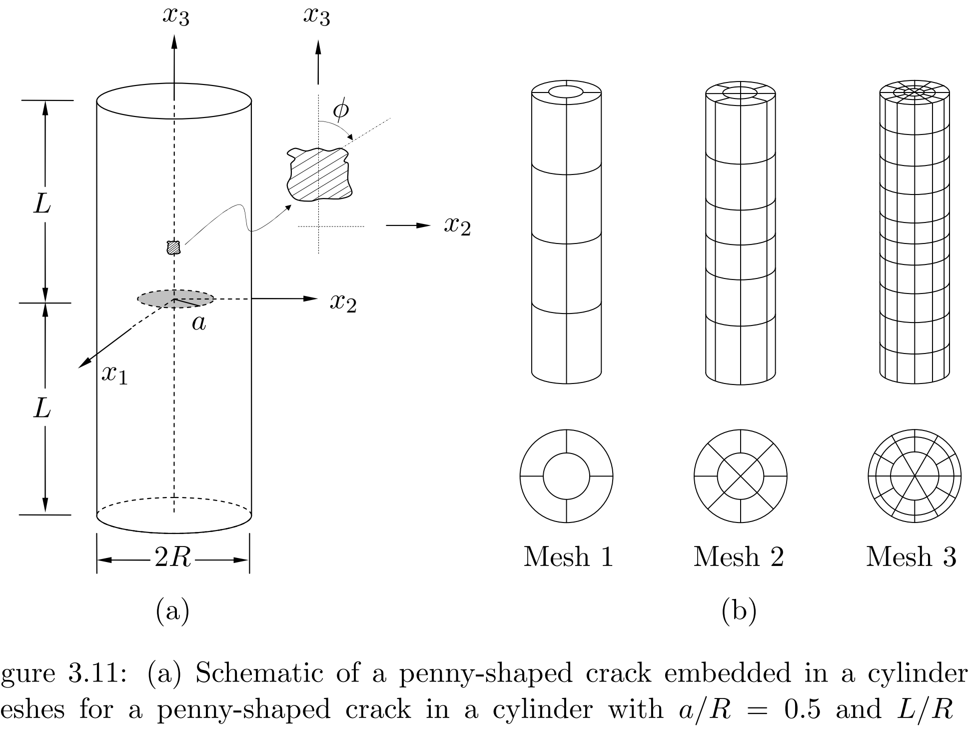

Figure 3.11: (a) Schematic of a penny-shaped crack embedded in a cylinder, (b) Meshes for a penny-shaped crack in a cylinder with $a/R = 0.5$ and $L/R = 4$. Meshes for a crack are shown below those for the boundary.

an angle ϕ relative to the axis of the cylinder. Two transversely isotropic materials, zinc and a graphite-reinforced composite, are treated and the dimensions of the problem are taken such that $a/R = 0.5$ and $L/R = 4$. The three meshes shown in Figure 3.11(b) are employed to obtain the numerical results.

We treat first the pure mode-I problem in which applied uniform normal traction σ_o is applied at the ends of the cylinder and for which the axis of elastic symmetry coincides with the axis of the cylinder (i.e. $\phi = 0$). The stress intensity factors obtained for each mesh are shown in Table 3.5 where the values are normalized by a reference stress intensity factor which is that obtained from Mesh 3 ($K_I^{ref} = 0.6978 \sqrt{\pi a}\, \sigma_o$ for zinc and $K_I^{ref} = 0.6783 \sqrt{\pi a}\, \sigma_o$ for a graphite-reinforced composite). Next, we consider the cylinder subjected to torque T_o at both ends and we note that this loading gives rise to a pure mode-III problem. The numerical results, normalized by $K_{III}^{ref} = 0.2148 \sqrt{\pi a}\ \tau_o$ for zinc and $K_{III}^{ref} = 0.2148 \sqrt{\pi a}\ \tau_o$ for a graphite-reinforced composite in which $\tau_o = 2T_o/\pi R^3$, are given in Table 3.6. From these two sets of results, it is evident that the computed stress intensity factors for Mesh 1 and Mesh 2 are in good agreement with that for Mesh 3 (within about 0.5% for Mesh 2, and about 1% for Mesh 1 except for the case of zinc with uniform normal traction in which the difference is about 2.5%). Note also that the stress intensity factor for torsion loading seems to exhibit no dependence upon the material properties.

Finally, we treat the fully mixed-mode problem which is introduced by the application of uniform normal traction σ_o at both ends of the cylinder with a misalignment between the axis of elastic symmetry and the axis of the cylinder ($\phi \neq 0$). All stress intensity factors $\{K_I, K_{II}, K_{III}\}$ are introduced and their numerical values, as a function of an angular position θ measured from x_1 axis, are presented for $\phi \in \{30^o, 60^o\}$ in Figure 3.12 for zinc and in Figure 3.13 for a graphite-reinforced composite. Note that only the mode-I stress intensity factor is present if an isotropic material is considered and the result (with $\nu = 0.3$) obtained from Mesh 3 is included in those plots for comparison. We conclude from these results that numerical solutions exhibit good convergence and only a few degrees of freedom are required to obtain accurate results. In addition, we remark that for this particular problem the orientation of the axis of elastic symmetry gives rise to mixed-mode stress intensity factors which have the same order of magnitude.

	K_I/K_I^{ref}	
Mesh	Zinc	Graphite composite
1	0.9774	0.9919
2	0.9952	0.9975
3	1.0000	1.0000

Table 3.5: Stress intensity factor for a penny-shaped crack in a cylinder subjected to uniform normal traction σ_o at the ends. Numerical results are for zinc and a graphite-reinforced composite.

	K_{III}/K_{III}^{ref}	
Mesh	Zinc	Graphite composite
1	0.9904	0.9920
2	0.9967	0.9972
3	1.0000	1.0000

Table 3.6: Stress intensity factor for a penny-shaped crack in a cylinder subjected to torque T_o at the ends. Numerical results are for zinc and a graphite-reinforced composite.

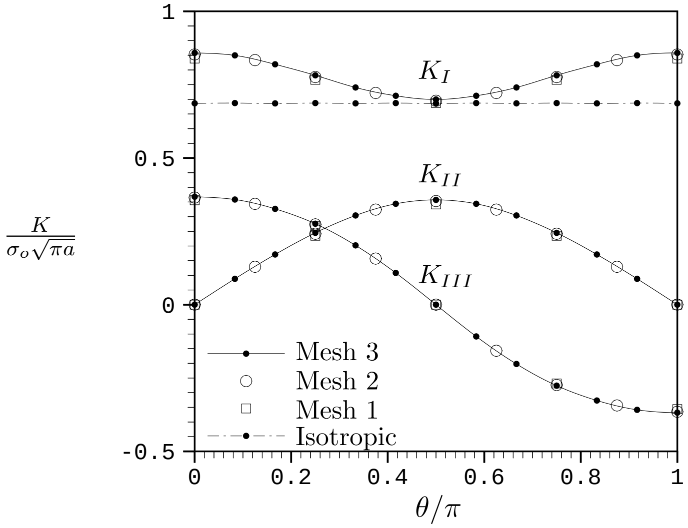

(a)

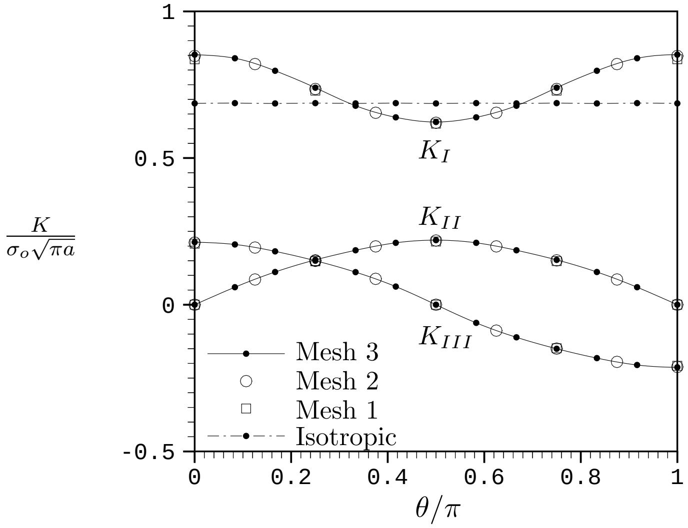

(b)

Figure 3.12: Normalized mode-I, mode-II and mode-III stress intensity factors for a penny-shaped crack in a cylinder under uniform normal traction σ_o at the ends. Numerical results are for zinc and for two material orientations (a) $\phi = 30^o$ and (b) $\phi = 60^o$. For isotropic material, K_I is obtained from Mesh 3.

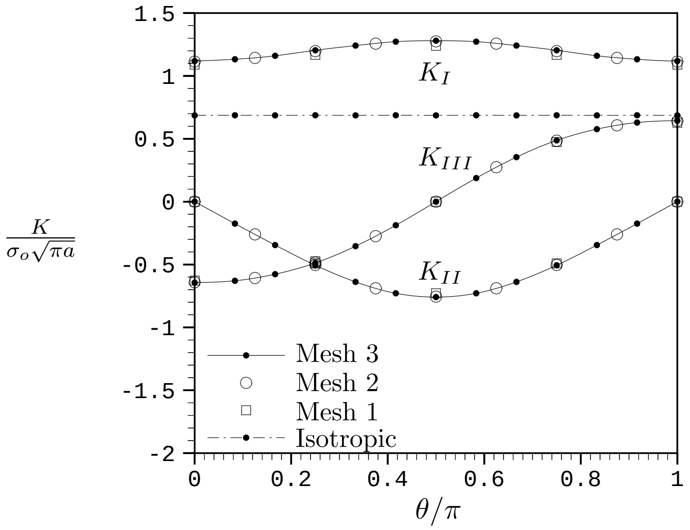

(a)

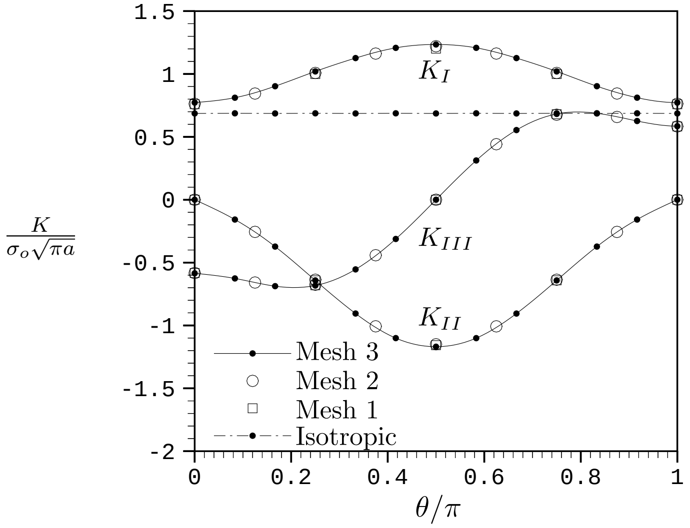

(b)

Figure 3.13: Normalized mode-I, mode-II and mode-III stress intensity factors for a penny-shaped crack in a cylinder under uniform normal traction σ_o at the ends. Numerical results are for a graphite-reinforced composite and for two material orientations (a) $\phi = 30^o$ and (b) $\phi = 60^o$. For isotropic material, K_I is obtained from Mesh 3.

Circumferential crack in a cylinder

Consider a solid circular cylinder of radius R and length $2L$ which contains a circumferential crack of depth a as shown in Figure 3.14(a). The cylinder is made from transversely isotropic material where the angle between the axis of elastic symmetry and the axis of the cylinder is denoted by ϕ. In the analysis, dimensions of the problem are such that $a/R = 0.5$ and $L/R = 4$ and three meshes utilized are adopted as shown in Figure 3.14(b). Similar to previous example, two types of loading, uniform normal traction σ_o and torque T_o applied at both ends of the cylinder, are treated.

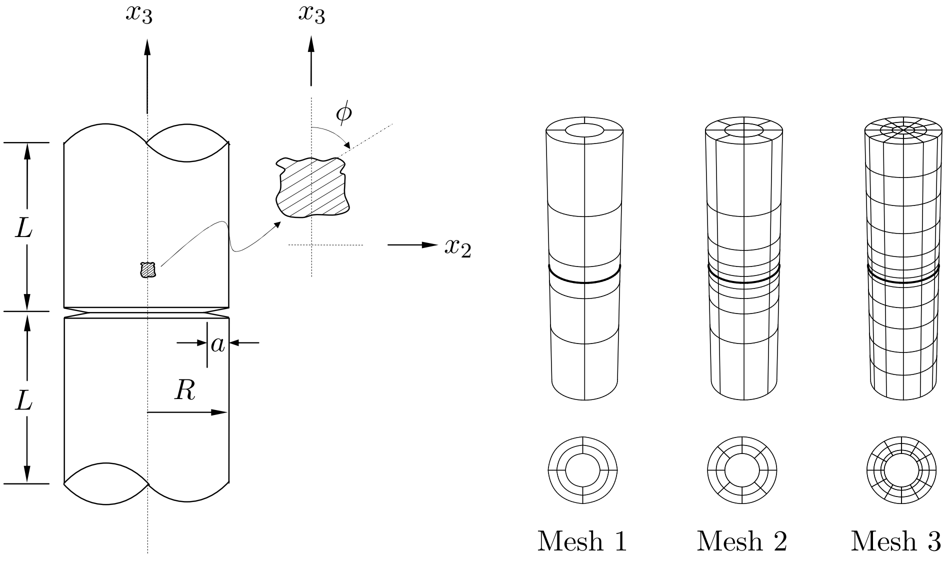

(a) (b)

Figure 3.14: (a) Schematic of a circumferential crack in a cylinder, (b) Meshes for circumferential crack in a cylinder with $a/R = 0.5$ and $L/R = 4$. Mesh for crack is shown below that for boundary.

First, we treat the case that the axis of elastic symmetry is coincide with the axis of the cylinder and, as a consequence, the applied normal traction and applied torque give rise to pure mode-I and mode-III stress intensity factors, respectively. Two sets of numerical results associated with each type of loading and two materials considered (zinc and a graphite-reinforced composite) are presented in Table 3.7 and Table 3.8 where values are normalized by that obtained from Mesh 3. It can be concluded from these results that the stress intensity factors obtained for each mesh show excellent agreement with each other; specifically by comparing with the results from Mesh 3, the difference is less than 0.6% for Mesh 2 and 1.5% for Mesh 1. Similar to the previous example, it is observed that the pure mode-III stress intensity factor (associated with applied torque T_o) obtained for Mesh 3 is independent of material properties.

Next, we treat the fully mixed-mode problem which is introduced by the application of uniform normal traction σ_o at both ends of the cylinder and the misalignment between the axis of elastic symmetry and the axis of the cylinder ($\phi \neq 0$). The distribution of normalized stress intensity factors are obtained for three meshes and presented in Figure 3.15 for zinc and in Figure 3.16 for a graphite-reinforced composite. The pure mode-I stress intensity factor for an isotropic material with $\nu = 0.3$ is also included for comparison. An excellent agreement between the numerical results for each mesh and slight mesh dependence are observed. We remark also that material anisotropy plays an important role for this particular problem and it gives rise to mixed-mode stress intensity factors with comparable magnitude.

	K_I/K_I^{ref}	
Mesh	Zinc	Graphite composite
1	0.9904	0.9912
2	0.9963	0.9961
3	1.0000	1.0000

Table 3.7: Stress intensity factor for a circumferential crack in a cylinder subjected to uniform normal traction σ_o at the ends. Results are for zinc and a graphite-reinforced composite where the values are normalized by that obtained from Mesh 3 ($K_I^{ref} = 1.9753\,\sqrt{\pi a}\,\sigma_o$ for zinc and $K_I^{ref} = 1.9311\,\sqrt{\pi a}\,\sigma_o$ for a graphite-reinforced composite).

	K_{III}/K_{III}^{ref}	
Mesh	Zinc	Graphite composite
1	0.9873	0.9867
2	0.9948	0.9949
3	1.0000	1.0000

Table 3.8: Stress intensity factor for a circumferential crack in a cylinder subjected to torque T_o at the ends. Results are for zinc and a graphite-reinforced composite where the values are normalized by that obtained from Mesh 3 ($K_{III}^{ref} = 2.9809\,\sqrt{\pi a}\,\tau_o$, $\tau_o = 2T_o/\pi$ for zinc and $K_{III}^{ref} = 2.9818\,\sqrt{\pi a}\,\tau_o$ for a graphite-reinforced composite).

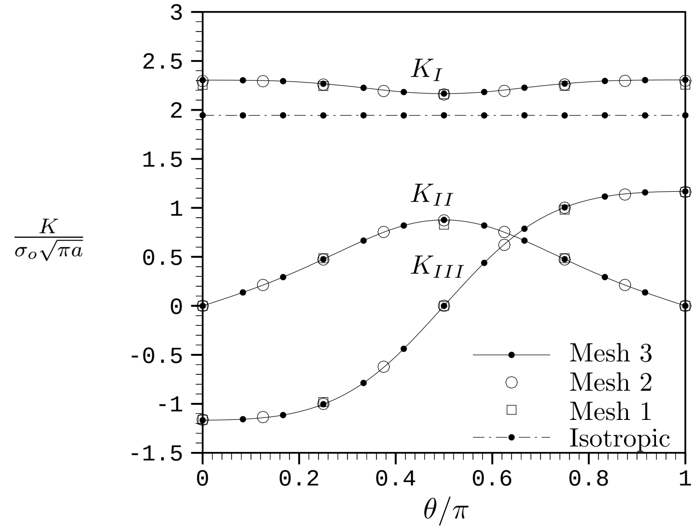

(a)

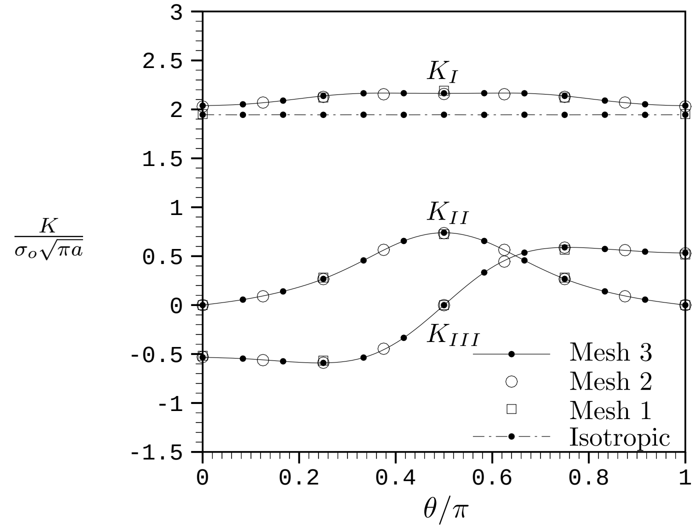

(b)

Figure 3.15: Normalized mode-I, mode-II and mode-III stress intensity factors for a circumferential crack in a cylinder under uniform normal traction σ_o at the ends. Numerical results are for zinc and for two material orientations (a) $\phi = 30^o$ and (b) $\phi = 60^o$. For isotropic material, K_I is obtained from Mesh 3.

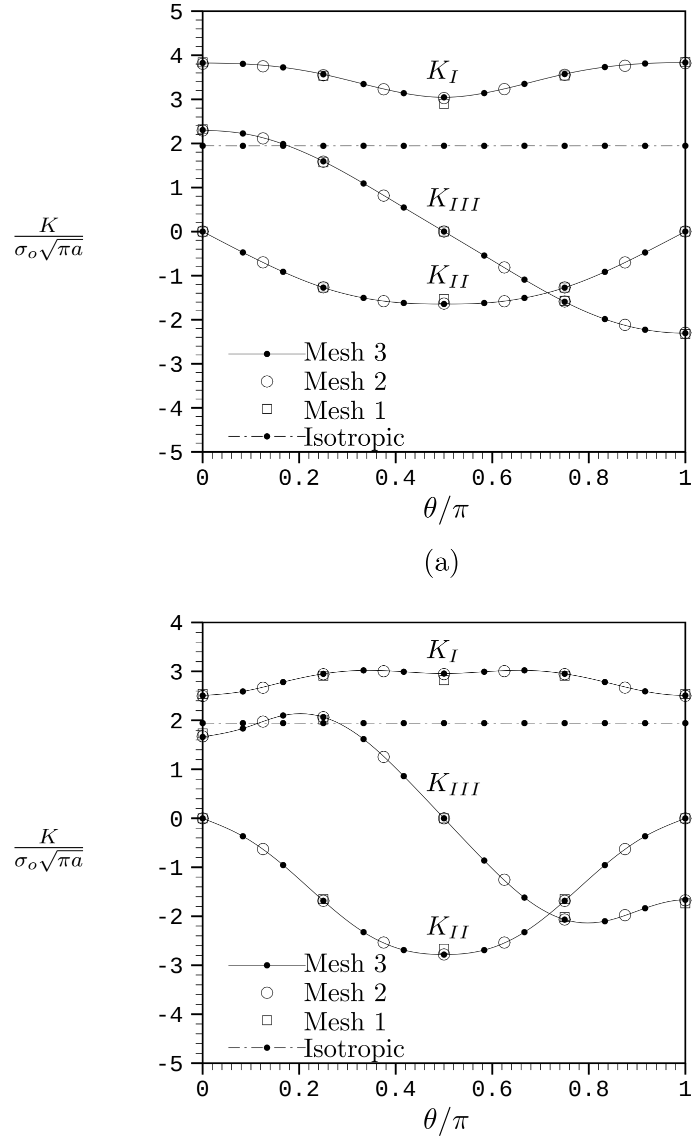

(a)

(b)

Figure 3.16: Normalized mode-I, mode-II and mode-III stress intensity factors for a circumferential crack in a cylinder under uniform normal traction σ_o at the ends. Numerical results are for a graphite-reinforced composite and for two material orientations (a) $\phi = 30^o$ and (b) $\phi = 60^o$. For isotropic material, K_I is obtained from mesh 3.

Through crack in a plate

Consider a rectangular plate of length $2L$, width W and thickness t which contains a through crack of length $2a$ as shown in Figure 3.17(a). The plate is subjected to a uniform normal traction σ_o at both ends and it is made from a transversely isotropic material where its axis of elastic symmetry directs along the loading direction. In the analysis, the geometry of the plate are taken such that $L/W = 1.0$, $W/t = 4$ and $W/a = 4$, two materials, zinc and a graphite-reinforced composite, are treated and three meshes are adopted as shown in Figure 3.17(b). While the loading considered introduces the pure mode-I stress intensity factor, the stress intensity factor varies along the crack front and its distribution is of interest.

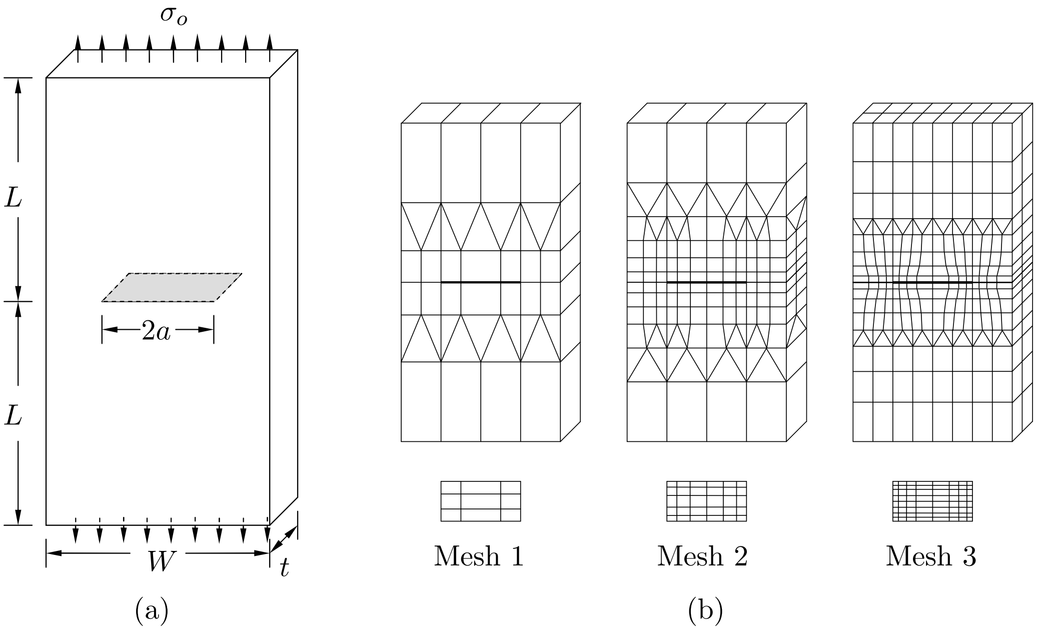

Figure 3.17: (a) Schematic of a rectangular plate containing a through crack, (b) Meshes used in the analysis which satisfy $L/W = 1.0$, $W/t = 4$ and $W/a = 4$. Meshes for a crack are shown below those for the boundary.

The computed stress intensity factors at the center of the crack front are reported in Table 3.9 for both zinc and a graphite-reinforced composite. The numerical values are normalized by the result obtained from Mesh 3 which is given by $K_{mid}^{ref} = 1.3242 \sqrt{\pi a}\, \sigma_o$ for zinc and $K_{mid}^{ref} = 1.3999 \sqrt{\pi a}\, \sigma_o$ for a graphite-reinforced composite. The distribution of K_I, as a function of an arc length s along the crack front measured from the center of the plate, are presented in Figure 3.18 for these two materials. To examine the effect of material anisotropy on values of the stress intensity factor, the result for an isotropic material with $\nu = 0.3$ is obtained for Mesh 3 and included in the plot.

The good agreement between results obtained for each mesh indicates that the results are very accurate especially in the central region of the crack (less than 1% difference for Mesh 1 and 0.2% for Mesh 2 at the center of the crack front). The higher discrepancy of the results for each mesh is observed in the region near the surface breaking points where the order of singularity is not a square root. Based upon obtained results in which the stress intensity factor tends to zero as the surface breaking point is approached, it suggests that the order of singularity is less than square root for three materials considered.

	K_{mid}/K_{mid}^{ref}	
Mesh	Zinc	Graphite composite
1	0.9901	0.9961
2	0.9988	0.9994
3	1.0000	1.0000

Table 3.9: Stress intensity factor at the center of the crack front for a through crack in plate subjected to uniform normal traction at the ends. Numerical results are for zinc and a graphite-reinforced composite.

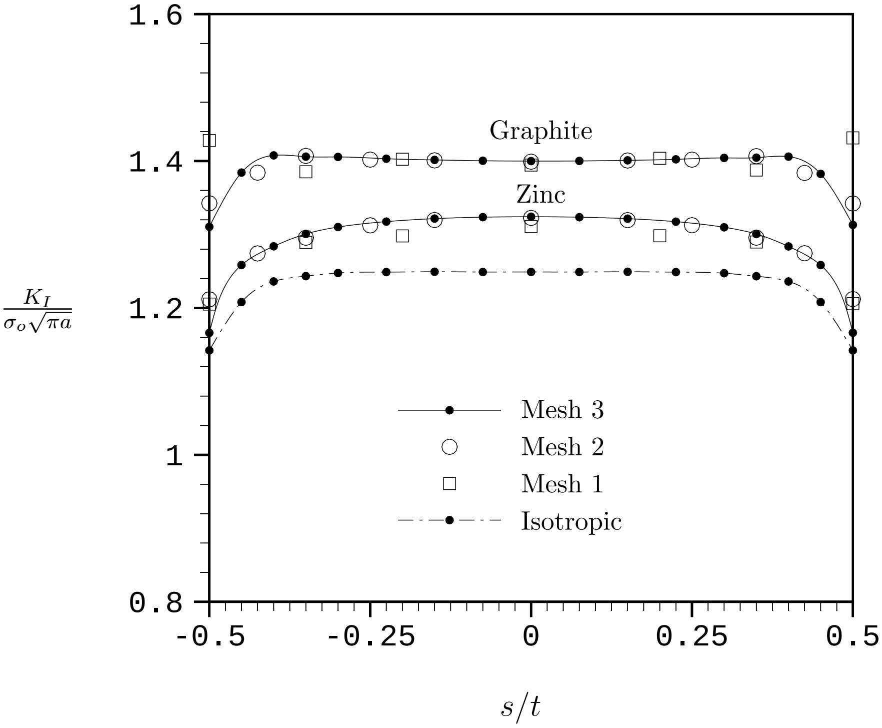

Figure 3.18: Normalized mode-I stress intensity factor for a through crack in a plate subjected to uniform normal traction σ_o at the ends. Numerical results are for zinc, a graphite-reinforced composite and an isotropic material. The result for the isotropic material is shown for mesh 3.

Quarter elliptical cracks at circular hole in thin plate

We consider next a rectangular thin plate containing a circular hole of radius R at the center. Quarter-elliptic surface breaking cracks are present at the hole as shown schematically in Figure 3.19. The dimensions used in the analysis are such that $a/t = 0.2$, $a/c = 0.8$, $R/t = 2$, $R/W = 0.2$ and $H/W = 2$ which are the same as those used by Xiao [45]. Three materials including an isotropic material with $\nu = 0.3$, zinc and a graphite-reinforced composite are treated where the axis of

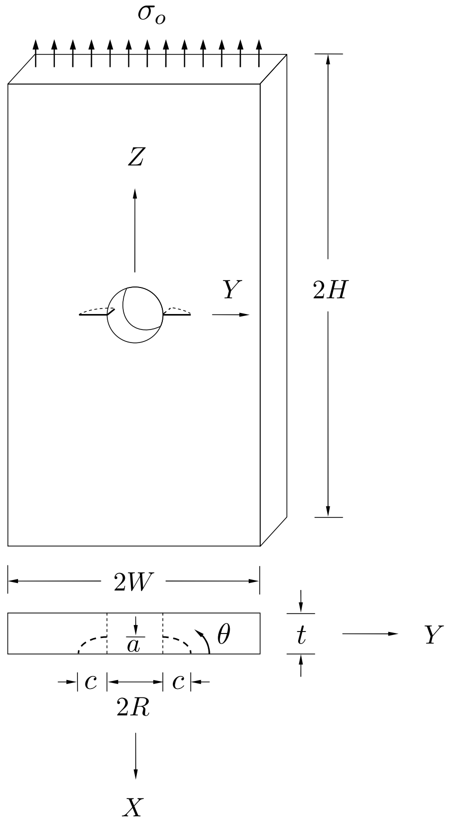

Figure 3.19: Schematic of quarter-elliptic cracks at a circular hole in a rectangular plate with $R/t = 2$, $a/t = 0.2$, $a/c = 0.8$, $R/W = 0.2$ and $H/W = 2$.

elastic symmetry for the last two materials is taken to direct along the Z axis. The plate is loaded by a uniform normal traction σ_o at both ends while other surfaces are traction free. By exploiting the symmetry of the geometry and loading about the plane $Y = 0$ and the material symmetry, only half of the problem ($Y \geq 0$) is used for modeling the plate with appropriate treatment of boundary conditions. This particular loading gives rise to a pure mode-I problem where the stress intensity factor varies along the crack front.

Three meshes associated with the reduced domain adopted by Xiao [45] as shown schematically in Figure 3.20, 3.21 and 3.22 are employed to obtain numerical solutions. The normalized mode-I stress intensity factor obtained for each mesh is plotted as a function of an angular position θ in Figure 3.23 for three materials considered. The excellent agreement between the numerical solutions for each mesh is observed. In addition, the presence of material anisotropy significantly changes

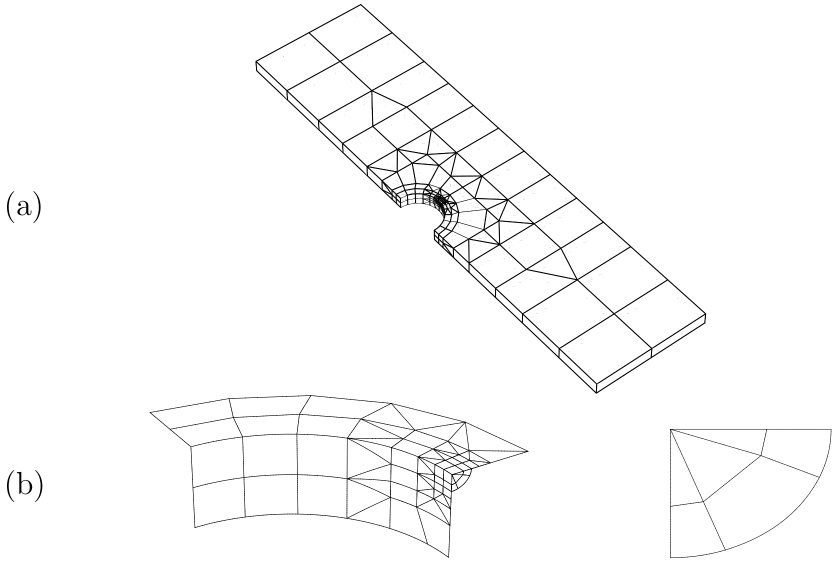

Figure 3.20: (a) Coarse mesh for plate with hole containing quarter-elliptic corner cracks. (b) Details of mesh for region near the crack, and mesh for the crack.

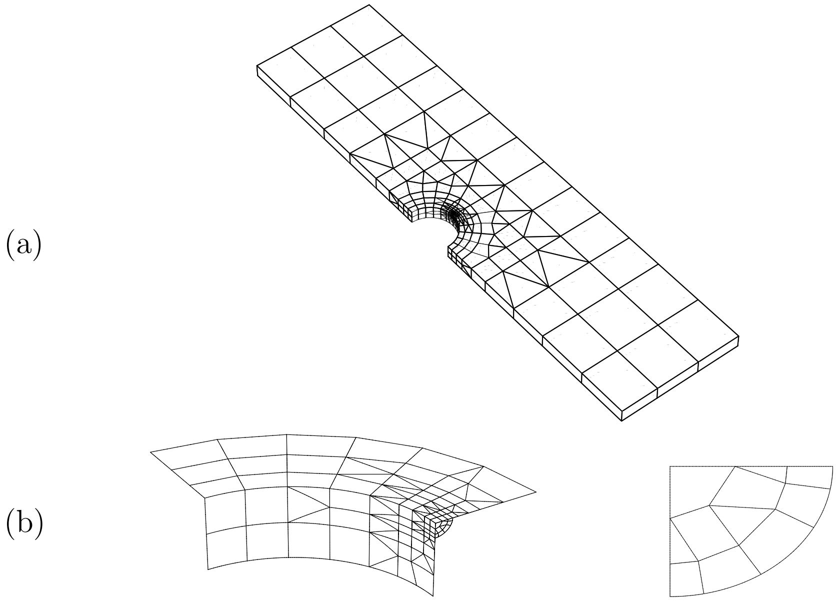

Figure 3.21: (a) Intermediate mesh for plate with hole containing quarter-elliptic corner cracks. (b) Details of mesh for region near the crack, and mesh for the crack.

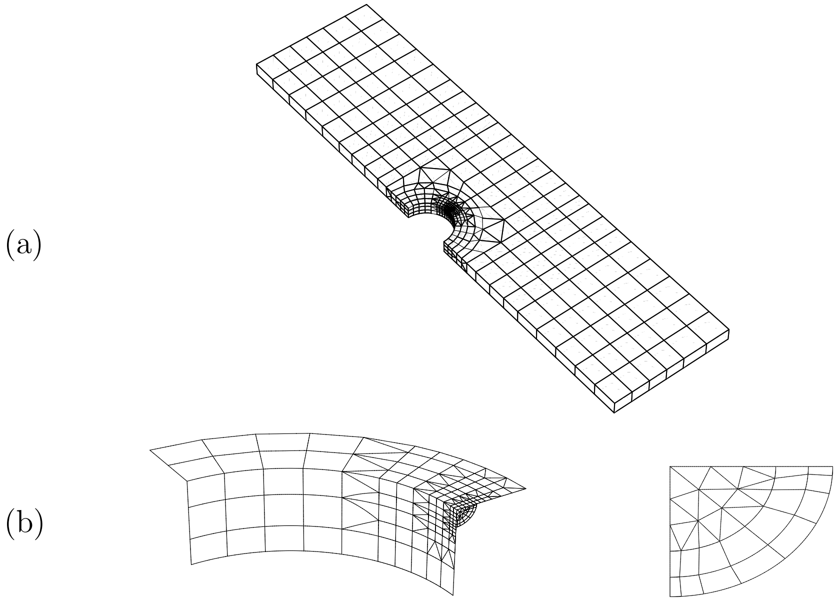

Figure 3.22: (a) Fine mesh for plate with hole containing quarter-elliptic corner cracks. (b) Details of mesh for region near the crack, and mesh for the crack.

the stress intensity factor from that for isotropy especially for the case that the plate is made from a graphite-reinforced composite. For special case of isotropy, the comparison of the results obtained from the SGBEM and other methods was given by Bakuckas [3].

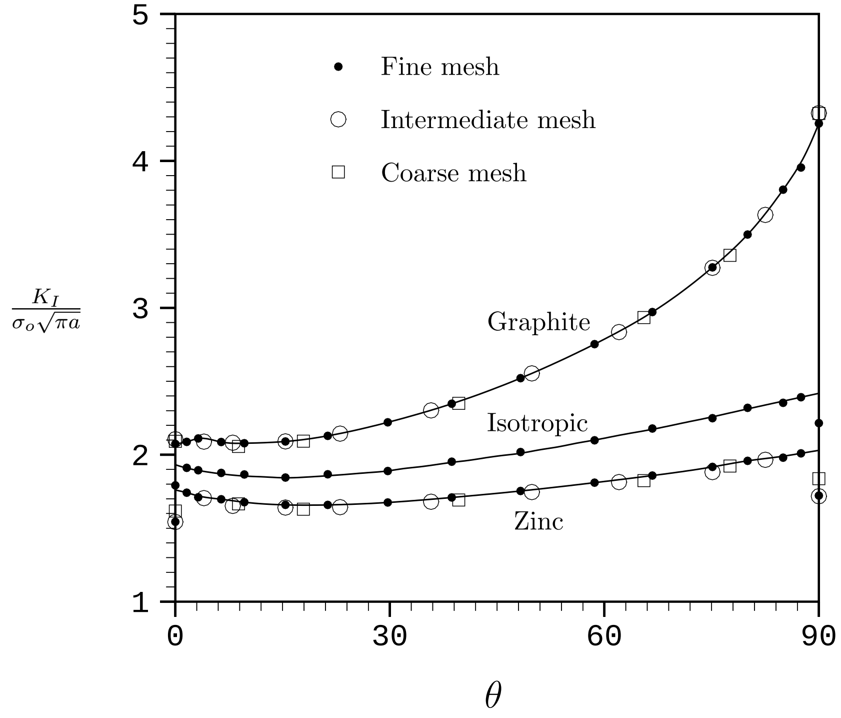

Figure 3.23: Normalized mode-I stress intensity factor for quarter-elliptic cracks at a circular hole in a rectangular plate subjected to uniform normal traction σ_o at the ends. The results are for zinc, a graphite-reinforced composite and isotropic material where the result for isotropic case is shown for Mesh 3.

Edge cracked bar

Consider a rectangular bar which contains a through-the-thickness surface breaking crack as shown schematically in Figure 3.24. The bar is made from a transverse isotropic material with its axis of material symmetry perpendicular to the plane of the crack and for this particular problem, both zinc and a graphite-reinforced composite are considered. The bar is subjected to two types of loading, one of which is for uniform normal traction σ_o applied at top and bottom surfaces of the bar as shown in Figure 3.24(b) while the other is for uniform shear traction τ_o applied on the top surface with the bottom surface rigidly fixed as shown in Figure 3.24(c). The geometry of the bar and the crack is taken to be $w/t = 1.5$, $h/t = 0.875$ and $a/t = 0.5$, and three meshes adopted as shown in Figure 3.24 are employed to obtain numerical results.

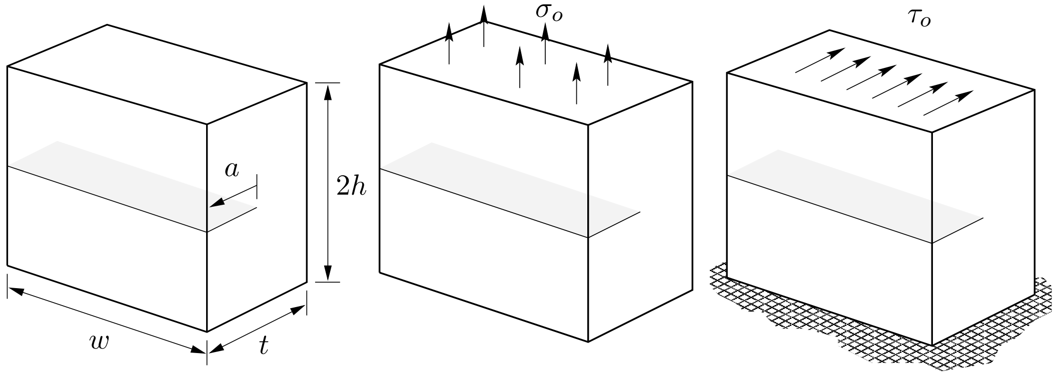

(a) (b) (c)

Figure 3.24: (a) Geometry of an edge cracked rectangular bar. (b) Edge cracked rectangular bar subjected to uniform normal traction σ_o at both ends. (c) Edge cracked bar under uniform shear traction τ_o at the top with the bottom rigidly fixed.

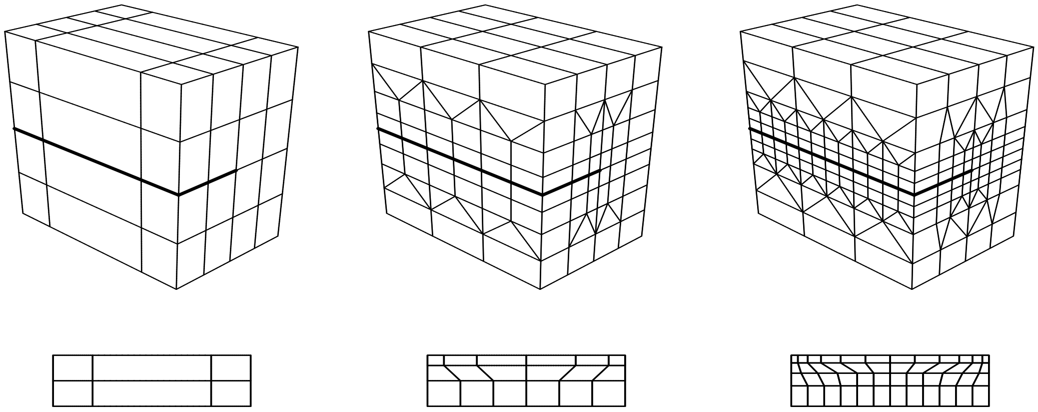

Mesh 1 Mesh 2 Mesh 3

Figure 3.25: Meshes for an edge cracked bar with $h/t = 0.875$, $a/t = 0.5$ and $w/t = 1.5$. Meshes for crack are shown below those for the regular boundary.

The first type of loading gives rise to a pure mode-I problem and the stress intensity factor along the crack front, as a function of an arc length s measured from the center of the bar, is shown in Figure 3.26(a) for zinc and a graphite-reinforced composite. For second type of loading, fully mixed-mode stress intensity factors are introduced and vary along the crack front. Numerical results for this case are shown in Figure 3.26(b) for mode-I and in Figure 3.27 for mode-II and mode-III. The result for isotropic material with $\nu = 1/3$ (obtained from Mesh 3) is also included for comparison. Despite the region near the surface breaking points, the results obtained for each mesh show a good convergence and note that the coarse mesh (Mesh 1) accurately captures the distribution of stress intensity factors for both pure mode-I and mixed-mode problems. Also note that material anisotropy significantly changes the distribution of mode-II and mode-III stress intensity factors and their behavior in the region near the surface breaking points while slight change of the behavior is observed for mode-I. For isotropy, the comparison among the results obtained from the SGBEM and other methods is available in [40].

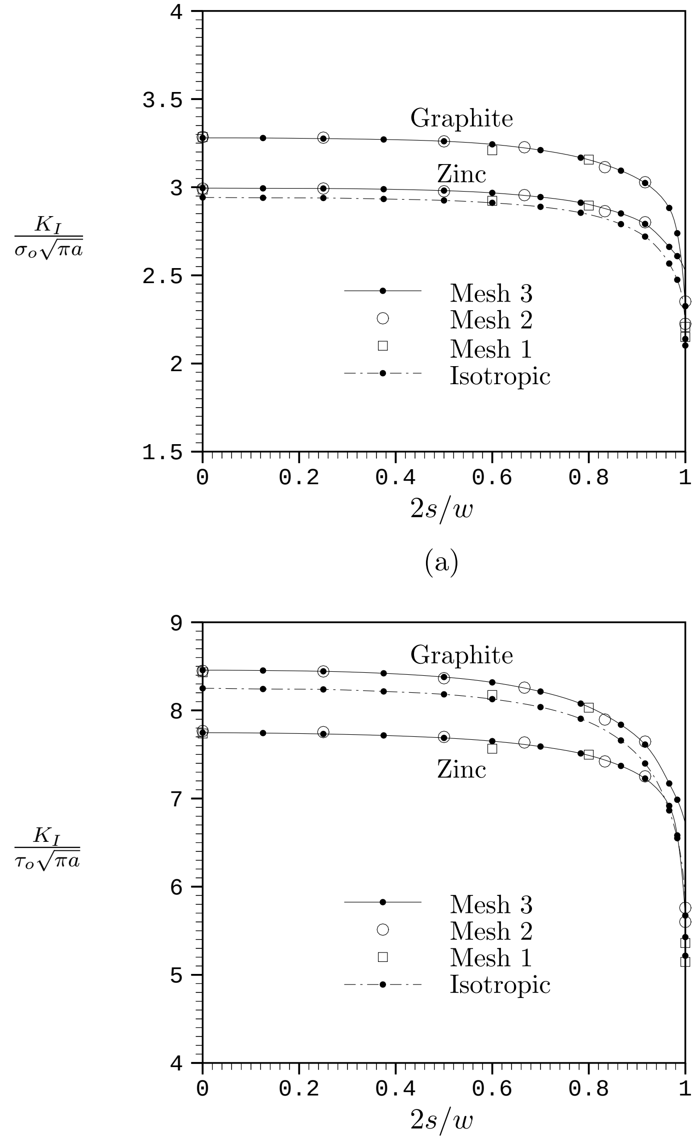

(b)

Figure 3.26: Normalized mode-I stress intensity factor for an edge cracked bar containing a through crack and subjected to (a) uniform normal traction σ_o at the ends and (b) uniform shear traction τ_o at the top with the bottom rigidly fixed. Results are for both zinc, a graphite-reinforced composite and an isotropic material. The result for isotropic case is shown for Mesh 3.

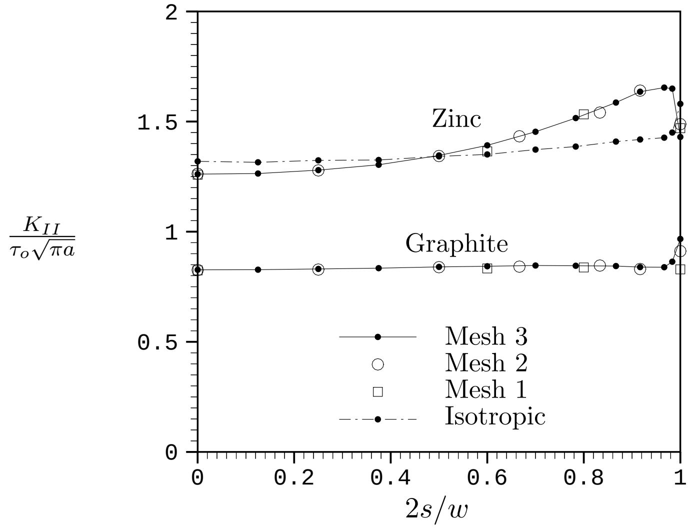

(a)

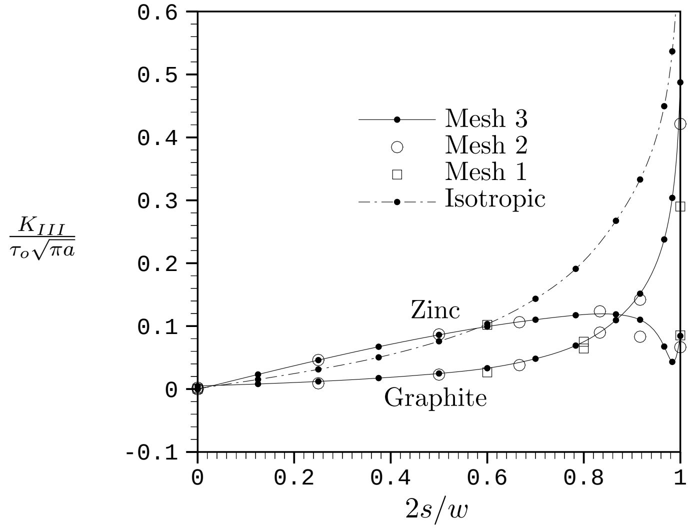

(b)

Figure 3.27: (a) Normalized mode-II and (b) normalized mode-III stress intensity factors for an edge cracked bar containing a through crack and subjected to a uniform shear traction τ_o at the top with the bottom rigidly fixed. Numerical results are for zinc, a graphite-reinforced composite and an isotropic material. The result for isotropic case is shown for Mesh 3.

A square bar with a quarter-circle crack

As a final example, consider a square bar containing a quarter-circle, surface breaking crack as illustrated in Figure 3.28(a). The bar is made from a transversely isotropic material with its axis of elastic symmetry coincide with the axis of the bar, and the dimensions of the bar and the crack used in the analysis are such that $L/W = 4$ and $a/W = 0.5$. Three types of loading are treated as shown in Figure 3.28(b) for uniform normal traction σ_o applied at both ends, in Figure 3.28(c) for linearly varying normal traction associated with moment M_o applied at both ends and in Figure 3.28(d) for uniform shear traction τ_o applied at one end with the other end fixed, and we adopt three meshes as shown in Figure 3.29 for determining the distribution of the stress intensity factors along the crack front.

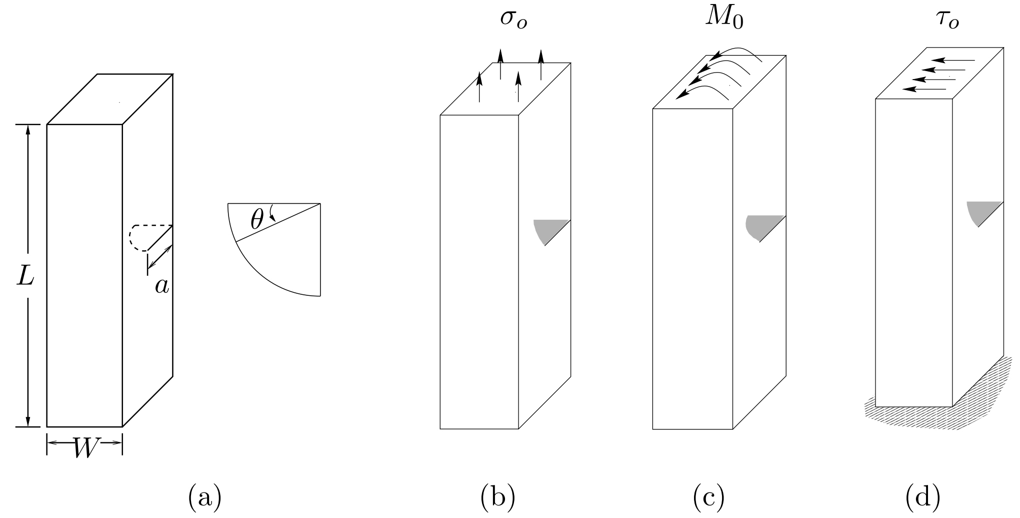

Figure 3.28: (a) Geometry of a square bar containing a quarter-circle crack. (b) Square cracked bar subjected to uniform normal traction at the ends. (c) Square cracked bare subjected to bending moment at the ends. (d) Square cracked bar subjected to uniform shear traction at one end with the other end rigidly fixed.

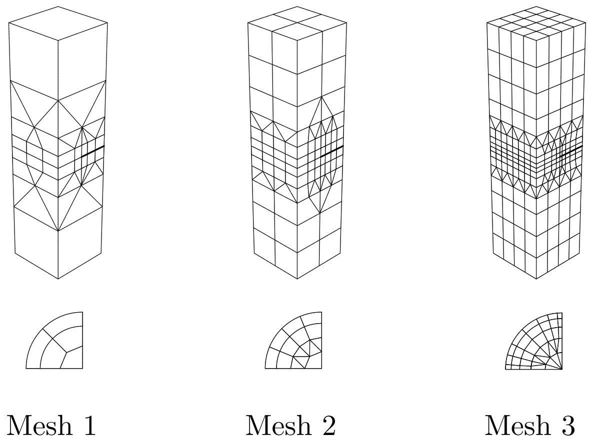

Figure 3.29: Meshes for square bar containing quarter-circle crack ($L/W = 4$, $a/W = 0.5$). Meshes for a crack are shown below those for the regular boundary.

While the first two loadings give rise to a pure mode-I problem, the stress intensity factor varies along the crack front. The numerical results are computed for both zinc and a graphite-reinforced composite and are presented in Figure 3.30(a) for applied uniform normal traction σ_o and in 3.30(b) for applied end moment M_o. For the third loading, the problem is fully mixed-mode and it gives rise to all three stress intensity factors. The distribution of the stress intensity factors are obtained and plotted in Figure 3.31 for mode-I and in Figure 3.32 for mode-II and mode-III. Note that the result for an isotropic material obtained for Mesh 3 ($\nu = 0.3$) is included in each plot for comparison. Based upon obtained results, numerical solutions indicate good convergence for both pure mode-I and fully mixed-mode problems and, in particular, the accurate distribution of the stress intensity factors can be obtained using a relatively coarse mesh except in the region close to surface breaking points. It is also important to remark that material anisotropy significantly affects the distribution and the behavior at surface breaking points of mode-II and -III stress intensity factors as indicated in Figure 3.32.

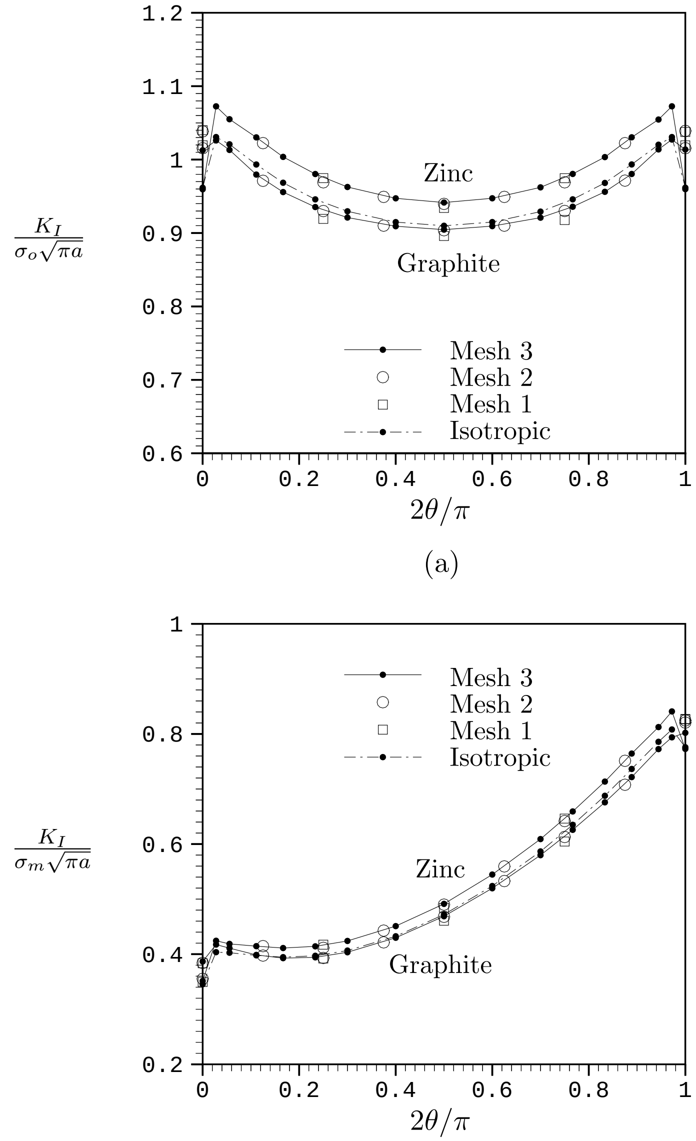

(a)

(b)

Figure 3.30: Normalized mode-I stress intensity factor for a square bar containing a quarter-circle crack and subjected to (a) uniform normal traction σ_o and (b) bending moment M_o at the ends where $\sigma_m = 6M_o/W^3$. Numerical results are for zinc, a graphite-reinforced composite and an isotropic material. The result for isotropic case is shown for Mesh 3.

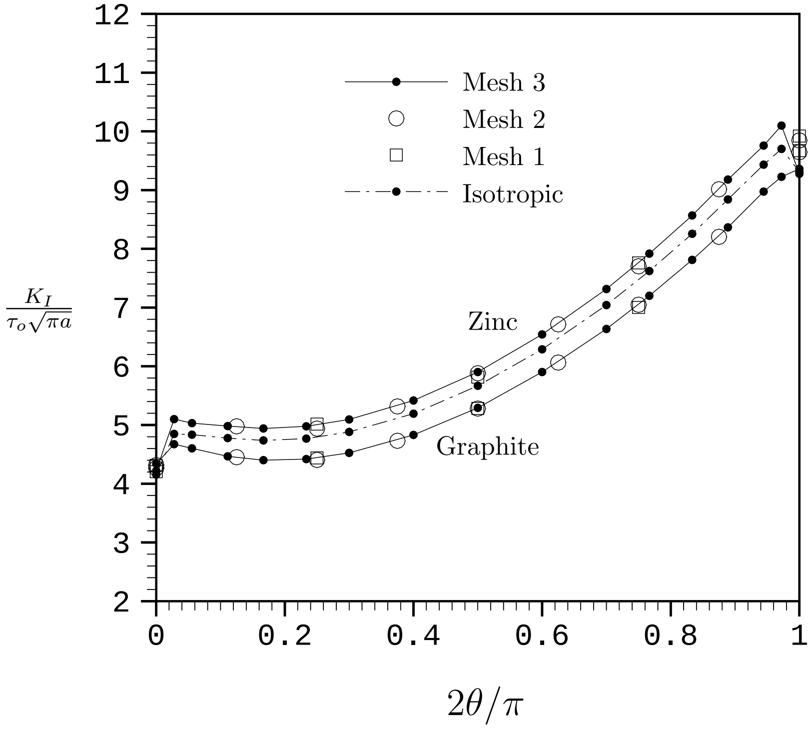

Figure 3.31: Normalized mode-I stress intensity factor for a square bar containing a quarter-crack and subjected to uniform shear traction τ_o at one end with the other end fixed. Numerical results are for zinc, a graphite-reinforced composite and an isotropic material. The result for isotropic case is shown for Mesh 3.

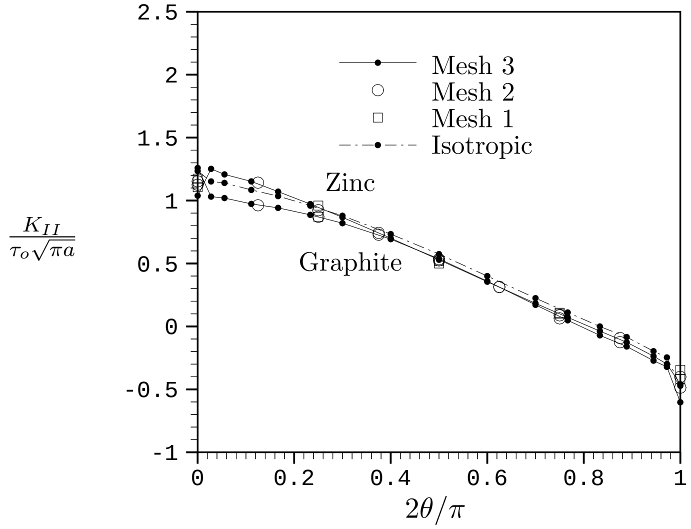

(a)

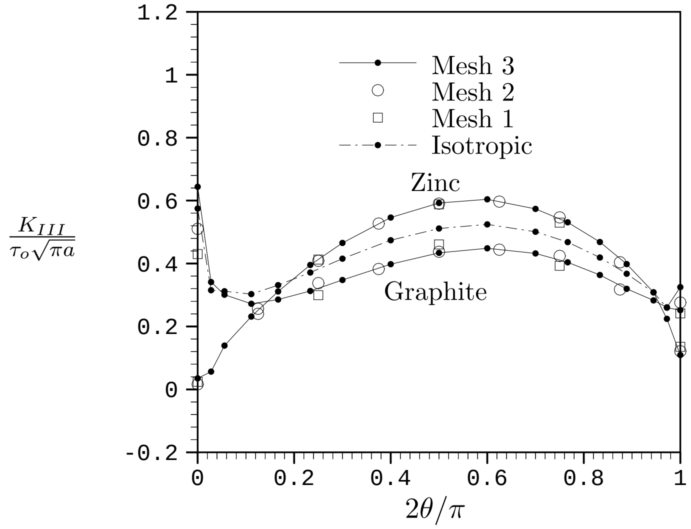

(b)

Figure 3.32: (a) Normalized mode-II and (b) normalized mode-III stress intensity factors for a square bar containing a quarter-circle crack and subjected to a uniform shear traction τ_o at one end with the other end fixed. Numerical results are for zinc, a graphite-reinforced composite and an isotropic material. The result for isotropic case is shown for Mesh 3.

3.4 Summary

A symmetric Galerkin boundary element method (SGBEM), based upon a pair of the weakly-singular weak-form displacement and traction integral equations, has been developed for analysis of fractures in three dimensional anisotropic, linearly elastic solids. The method is applicable for treating cracks in both an unbounded domain and a finite domain where the latter involves both an embedded crack and a surface breaking crack. The resulting symmetric integral equations governing the boundary valued problem contain only weakly-singular kernels (of order $1/r$) which allows the application of standard C^o elements in the numerical implementation. The important feature of the method is that it utilizes a special crack tip element to accurately model the relative crack-face displacement in the region near the crack front. The use of this crack tip element allows the mixed-mode stress intensity factors to be efficiently determined as a function of position along the crack front. In addition, the method employs an efficient algorithm, based upon the interpolation technique and material symmetry, to evaluate values of the kernels, for general anisotropy, appearing in the integrals equation.

Several numerical examples including cracks in an unbounded domain and a finite domain are solved to demonstrate the modeling capability and accuracy of the method. It has been found that numerical solutions exhibit slight mesh dependence and, as a consequence, the highly accurate (mixed-mode) stress intensity factors can be determined with a relatively coarse mesh. The presence of material anisotropy show significant effect on both the magnitude and distribution of the stress intensity factors along the crack front in comparison with those for isotropic cases. In addition, it has been observed that for a simple loading which gives rise to pure mode-I and mode-III problems for isotropic case, the presence of material anisotropy can introduce a fully mixed-mode problem with all the stress intensity factors are of the same order of magnitude. Finally, we remark that while the SGBEM provides an accurate means for linear fracture analysis, the method possesses limitation in modeling complex structures where the large number of degrees of freedom is required to properly model the problems.

Chapter 4

Coupling of SGBEM and FEM for Analysis of Fractures in 3D Anisotropic Media

The strength of the symmetric Galerkin boundary element method developed in the previous chapter is that it provides a means to obtain highly accurate mixed-mode stress intensity factor data for three-dimensional fracture problems. In principle the method can be utilized to model structural components which have arbitrarily complex geometric features (or which otherwise require a large number of degrees of freedom to be modeled properly) but, as with other boundary element methods, the computational time tends to increase rapidly with increasing problem size. The method does possess the desirable feature that the coefficient matrix is symmetric, but nonetheless this matrix is dense and each of its entries must be computed by means of a double surface integration involving a weakly-singular kernel.

To obtain a computational procedure which retains the advantages of the SGBEM for fracture modeling while at the same time allowing complicated structural components to be modeled efficiently, we now pursue a coupling of the boundary element procedure with the standard finite element method (FEM). In this coupling, we seek to utilize the SGBEM only for treatment of the crack and a region immediately surrounding the crack, while employing standard FEM techniques to model the remaining (possibly very complex) structure. Partitioning the domain into a region to be modeled with the SGBEM and a region to be modeling with the FEM gives rise, naturally, to a need to consider continuity of the field variables across the interface separating these regions, and here continuity of the tractions and the displacements across the interface is enforced in a weak sense. This weak enforcement of continuity allows for separate (non-conforming) meshing on the boundary element and finite element regions and includes, as a special case, discretizations for which the meshes on the interface conform.

We begin with a formulation of the boundary value problem with the weakly-singular, weak-form integral equations developed in Chapter 2 applied to the subregion containing the crack and with the usual principle of virtual work applied to the remainder of the domain (i.e. the FEM region). It is shown that, by an appropriate use of the weak-form displacement and traction integral equations, an overall symmetric formulation is obtained. A discretization in terms of standard C^o elements is then introduced and the final system of algebraic equations governing the discretized problem is established. A computer code based on these coupled SGBEM-FEM equations is developed, and the utility of the method is demonstrated for a number of fracture problems. Finally, a coupling of the SGBEM with the commercial finite element package ABAQUS is illustrated.

4.1 SGBEM-FEM formulation

Consider a homogeneous, linearly elastic body Ω containing a crack as shown schematically in Figure 4.1(a). As before, we denote the (geometrically coincident) surfaces of the crack by S_C^+ and S_C^-, and we select $S_C \equiv S_C^+$ as a single surface to be utilized

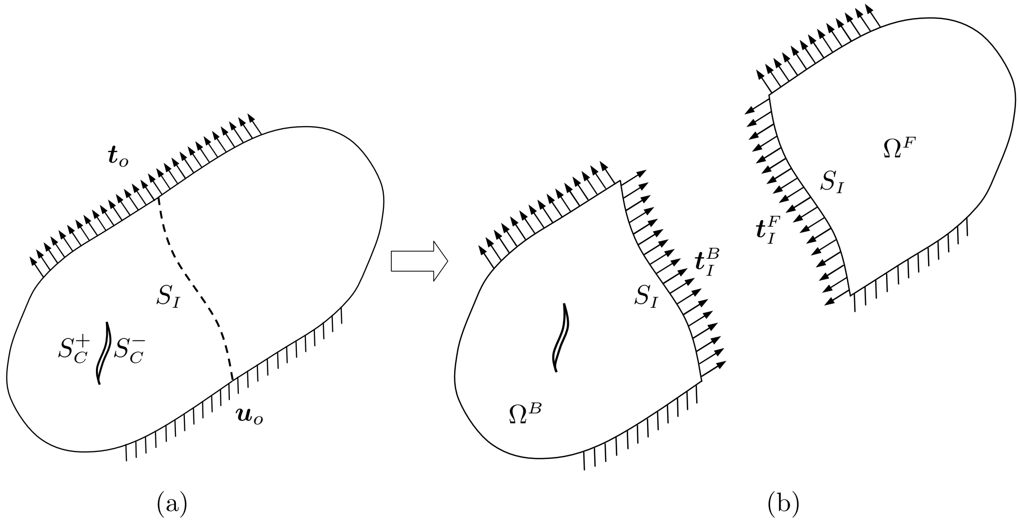

Figure 4.1: Schematic of an elastic body comprised of two subregions.

in representing the crack. The surfaces of the crack are subjected only to prescribed tractions $\boldsymbol{t}_c \equiv \boldsymbol{t}_c^+ = -\boldsymbol{t}_c^-$, while in general the ordinary boundary of the domain is comprised of a portion on which displacements $\boldsymbol{u} = \boldsymbol{u}_o$ are prescribed and a portion on which tractions $\boldsymbol{t} = \boldsymbol{t}_o$ are prescribed.

We now partition the domain along an imaginary surface S_I giving rise to a 'BEM-region' Ω^B and a 'FEM-region' Ω^F. In the development it is assumed that the crack is strictly contained in the subregion Ω^B as indicated in Figure 4.1(b), but the key restriction is actually that the crack front be fully contained in this region. We remark that whereas the discussion is carried out for a single crack, the formulation is readily extended to any number of cracks as long as the cracks are contained within one or more BEM-regions. We also note that there is no restriction that either the BEM-region or the FEM-region be simply connected.

4.1.1 Formulation for Ω^B

Consider first the subregion Ω^B. The ordinary boundary of this region (not including the crack or the interface) consists of a portion S_U on which displacements $\boldsymbol{u}_o$ are prescribed and a portion S_{T_o} on which tractions $\boldsymbol{t}_o$ are prescribed. Tractions $\boldsymbol{t}_c$ are prescribed on the crack surface S_C, and for purposes of presentation we let $S_T = S_{T_o} \cup S_c$ denote the net surface on which tractions are prescribed. On the interface S_I neither the traction nor displacement are known a priori, and to clearly indicate the role of these quantities in the formulation for Ω^B we denote them as $\boldsymbol{t}_I^B$ and $\boldsymbol{u}_I^B$, respectively. Finally, we let $S_o = S_{T_o} \cup S_U \cup S_I$ denote the 'outer boundary' of the domain and we let $S = S_o \cup S_C$ denote the total boundary.

The formulation for Ω^B is based upon the weakly-singular, weak-form displacement and traction integral equations developed in Chapter 2. When specialized to Ω^B, these integral equations take the form

$$\begin{aligned}
\frac{1}{2}\int_{S_o} v_p(\boldsymbol{y})\,\tilde{t}_p(\boldsymbol{y})\,dS(\boldsymbol{y}) \quad = \quad & \int_{S_o} \tilde{t}_p(\boldsymbol{y}) \int_S G^p_{mj}\; D_m v_j(\boldsymbol{\xi})\; dS(\boldsymbol{\xi})\,dS(\boldsymbol{y}) \\
- \quad & \int_{S_o} \tilde{t}_p(\boldsymbol{y}) \int_S n_i(\boldsymbol{\xi})\; H^p_{ij}\; v_j(\boldsymbol{\xi})\; dS(\boldsymbol{\xi})\,dS(\boldsymbol{y}) \\
+ \quad & \int_{S_o} \tilde{t}_p(\boldsymbol{y}) \int_{S_o} U^p_i\; t_i(\boldsymbol{\xi})\; dS(\boldsymbol{\xi})\,dS(\boldsymbol{y}) \qquad (4.1)
\end{aligned}$$

$$\begin{aligned}
-\int_S c(\boldsymbol{y}) t_k(\boldsymbol{y}) \tilde{v}_k(\boldsymbol{y}) dS(\boldsymbol{y}) \quad = \quad & \int_S D_t\tilde{v}_k(\boldsymbol{y}) \int_S C^{tk}_{mj}\; D_m v_j(\boldsymbol{\xi})\; dS(\boldsymbol{\xi}) dS(\boldsymbol{y}) \\
+ \quad & \int_S D_t\tilde{v}_k(\boldsymbol{y}) \int_{S_o} G^j_{tk}\; t_j(\boldsymbol{\xi})\; dS(\boldsymbol{\xi}) dS(\boldsymbol{y}) \\
+ \quad & \int_S \tilde{v}_k(\boldsymbol{y}) \int_{S_o} n_l(\boldsymbol{y})\; H^j_{lk}\; t_j(\boldsymbol{\xi})\; dS(\boldsymbol{\xi}) dS(\boldsymbol{y}) \quad (4.2)
\end{aligned}$$

where

$$v_j(\boldsymbol{\xi}) = \begin{cases} u_j(\boldsymbol{\xi}) & , \quad \boldsymbol{\xi} \in S_o \\ \Delta u_j(\boldsymbol{\xi}) & , \quad \boldsymbol{\xi} \in S_C \end{cases} \quad ; \quad \tilde{v}_k(\boldsymbol{y}) = \begin{cases} \tilde{u}_k(\boldsymbol{y}) & , \quad \boldsymbol{y} \in S_o \\ \Delta\tilde{u}_k(\boldsymbol{y}) & , \quad \boldsymbol{y} \in S_C \end{cases} \qquad (4.3)$$

and where

$$c(\boldsymbol{y}) = \begin{cases} 1/2 \quad , \quad \boldsymbol{y} \in S_o \\ \quad 1 \quad , \quad \boldsymbol{y} \in S_C \end{cases} \tag{4.4}$$

The surface differential operator D_m which appears in these equations is given by (2.10), and the kernels $H^p_{ij}(\boldsymbol{\xi}-\boldsymbol{y})$, $U^p_i(\boldsymbol{\xi}-\boldsymbol{y})$, $G^p_{mj}(\boldsymbol{\xi}-\boldsymbol{y})$ and $C^{tk}_{mj}(\boldsymbol{\xi}-\boldsymbol{y})$ are given by equations (2.5), (2.43), (2.44) and (2.45), respectively.

Toward obtaining a symmetric system of integral equations governing Ω^B, we first employ the weak-form displacement integral equation (4.1) on S_U (with $\tilde{\boldsymbol{t}} = \boldsymbol{0}$ on $S_{T_o} \cup S_I$) and we utilize the weak-form traction integral equation (4.2) on S_T (with $\tilde{\boldsymbol{u}} = \boldsymbol{0}$ on $S_U \cup S_I$). Next, on the interface S_I we employ *both* the weak-form displacement and traction integral equations; for the displacement equation we take $\tilde{\boldsymbol{t}} = \boldsymbol{0}$ on $S_{T_o} \cup S_U$ while for the traction equation we take $\tilde{\boldsymbol{v}} = \boldsymbol{0}$ on $S_U \cup S_T$. The resulting system of integral equations can be expressed as

$$\begin{array}{rcl}
\mathcal{A}_{UU}(\tilde{\boldsymbol{t}},\boldsymbol{t}) + \mathcal{B}_{UT}(\tilde{\boldsymbol{t}},\boldsymbol{v}) + \mathcal{A}_{UI}(\tilde{\boldsymbol{t}},\boldsymbol{t}^B_I) + \mathcal{B}_{UI}(\tilde{\boldsymbol{t}},\boldsymbol{u}^B_I) & = & \mathcal{R}_1(\tilde{\boldsymbol{t}}) \\
\mathcal{B}_{UT}(\boldsymbol{t},\tilde{\boldsymbol{v}}) + \mathcal{C}_{TT}(\tilde{\boldsymbol{v}},\boldsymbol{v}) + \mathcal{B}_{IT}(\boldsymbol{t}^B_I,\tilde{\boldsymbol{v}}) + \mathcal{C}_{TI}(\tilde{\boldsymbol{v}},\boldsymbol{u}^B_I) & = & \mathcal{R}_2(\tilde{\boldsymbol{v}}) \\
\mathcal{A}_{IU}(\tilde{\boldsymbol{t}}^B_I,\boldsymbol{t}) + \mathcal{B}_{IT}(\tilde{\boldsymbol{t}}^B_I,\boldsymbol{v}) + \mathcal{A}_{II}(\tilde{\boldsymbol{t}}^B_I,\boldsymbol{t}^B_I) + \mathcal{D}_{II}(\tilde{\boldsymbol{t}}^B_I,\boldsymbol{u}^B_I) & = & \mathcal{R}_3(\tilde{\boldsymbol{t}}^B_I) \\
\mathcal{B}_{UI}(\boldsymbol{t},\tilde{\boldsymbol{u}}^B_I) + \mathcal{C}_{IT}(\tilde{\boldsymbol{u}}^B_I,\boldsymbol{v}) + \mathcal{D}_{II}(\boldsymbol{t}^B_I,\tilde{\boldsymbol{u}}^B_I) + \mathcal{C}_{II}(\tilde{\boldsymbol{u}}^B_I,\boldsymbol{u}^B_I) & = & \mathcal{R}_4(\tilde{\boldsymbol{u}}^B_I) - 2\mathcal{F}^B_I(\tilde{\boldsymbol{u}}^B_I,\boldsymbol{t}^B_I)
\end{array} \tag{4.5}$$

in which (with subscripts $P, Q \in \{U, T_o, T, C, I\}$ introduced to specify the surface of integration) the bilinear integral operators $\mathcal{A}_{PQ}, \mathcal{B}_{PQ}, \mathcal{C}_{PQ}$ and $\mathcal{D}_{II}$ are given by

$$\mathcal{A}_{PQ}(\boldsymbol{X},\boldsymbol{Y}) = \int_{S_P} X_p(\boldsymbol{z}) \int_{S_Q} U^p_i \; Y_i(\boldsymbol{\xi}) \; dS(\boldsymbol{\xi})\, dS(\boldsymbol{z}) \tag{4.6}$$

$$\mathcal{B}_{PQ}(\boldsymbol{X},\boldsymbol{Y}) = \int_{S_P} X_k(\boldsymbol{z}) \int_{S_Q} G^k_{mj} \; D_m Y_j(\boldsymbol{\xi}) \; dS(\boldsymbol{\xi})\, dS(\boldsymbol{z}) \tag{4.7}$$

$$- \int_{S_P} X_k(\boldsymbol{z}) \int_{S_Q} n_m(\boldsymbol{\xi}) \; H^k_{mj} \; Y_j(\boldsymbol{\xi}) \; dS(\boldsymbol{\xi})\, dS(\boldsymbol{z}) \tag{4.8}$$

$$\mathcal{C}_{PQ}(\boldsymbol{X},\boldsymbol{Y}) = \int_{S_P} D_t X_k(\boldsymbol{z}) \int_{S_Q} C^{tk}_{mj} \; D_m Y_j(\boldsymbol{\xi}) \; dS(\boldsymbol{\xi})\, dS(\boldsymbol{z}) \tag{4.9}$$

$$\mathcal{D}_{II}(\boldsymbol{X},\boldsymbol{Y}) = \mathcal{B}_{II}(\boldsymbol{X},\boldsymbol{Y}) - \mathcal{F}^B_I(\boldsymbol{X},\boldsymbol{Y}) \tag{4.10}$$

with

$$\mathcal{F}^B_P(\boldsymbol{X},\boldsymbol{Y}) \;=\; \frac{1}{2}\int_{S_P} X_i(\boldsymbol{z})\; Y_i(\boldsymbol{z})\, dS(\boldsymbol{z}) \tag{4.11}$$

The linear operators $\mathcal{R}_1, \mathcal{R}_2, \mathcal{R}_3$ and $\mathcal{R}_4$ which appear on the right hand side of (4.5) are given by

$$\begin{aligned}
\mathcal{R}_1(\tilde{\boldsymbol{t}}) &= -\mathcal{A}_{UT_o}(\tilde{\boldsymbol{t}},\boldsymbol{t}_o) - \mathcal{B}_{UU}(\tilde{\boldsymbol{t}},\boldsymbol{u}_o) + \mathcal{F}^B_U(\tilde{\boldsymbol{t}},\boldsymbol{u}_o)\\
\mathcal{R}_2(\tilde{\boldsymbol{v}}) &= -\mathcal{B}_{T_oT}(\boldsymbol{t}_o,\tilde{\boldsymbol{v}}) - \mathcal{C}_{TU}(\tilde{\boldsymbol{v}},\boldsymbol{u}_o)\\
&\quad -\mathcal{F}^B_{T_o}(\tilde{\boldsymbol{u}},\boldsymbol{t}_o) - 2\mathcal{F}^B_C(\Delta\tilde{\boldsymbol{u}},\boldsymbol{t}_c)\\
\mathcal{R}_3(\tilde{\boldsymbol{t}}^B_I) &= -\mathcal{A}_{IT_o}(\tilde{\boldsymbol{t}}^B_I,\boldsymbol{t}_o) - \mathcal{B}_{IU}(\tilde{\boldsymbol{t}}^B_I,\boldsymbol{u}_o)\\
\mathcal{R}_4(\tilde{\boldsymbol{u}}^B_I) &= -\mathcal{C}_{IU}(\tilde{\boldsymbol{u}}^B_I,\boldsymbol{u}_o) - \mathcal{B}_{TI}(\boldsymbol{t}_o,\tilde{\boldsymbol{u}}^B_I)
\end{aligned} \tag{4.12}$$

Clearly the bilinear operators $\mathcal{A}_{PQ}(\boldsymbol{X},\boldsymbol{Y})$ and $\mathcal{C}_{PQ}(\boldsymbol{X},\boldsymbol{Y})$ are symmetric in the sense that

$$\begin{aligned}
\mathcal{A}_{PQ}(\boldsymbol{X},\boldsymbol{Y}) &= \mathcal{A}_{QP}(\boldsymbol{Y},\boldsymbol{X})\\
\mathcal{C}_{PQ}(\boldsymbol{X},\boldsymbol{Y}) &= \mathcal{C}_{QP}(\boldsymbol{Y},\boldsymbol{X})
\end{aligned} \tag{4.13}$$

and, as a consequence, the left hand side of the system of equations (4.5) is in a symmetric form. Of course, the tractions on the interface are not prescribed and as such the quantity $2\mathcal{F}^B_I(\tilde{\boldsymbol{u}}^B_I,\boldsymbol{t}^B_I)$ which appears on the right hand side of (4.5) does not constitute a loading term; this term will be addressed after the formulation for Ω^F is presented.

4.1.2 Formulation for Ω^F

We now turn attention to the subregion Ω^F. The boundary of this region consists of a portion S_U on which displacements $\boldsymbol{u_o}$ are prescribed, a portion S_T on which tractions $\boldsymbol{t_o}$ are prescribed, and the interface S_I on which neither the traction or displacement are known a priori. Here we denote the traction and displacement on S_I by $\boldsymbol{t}^F_I$ and $\boldsymbol{u}^F_I$, respectively, in order to distinguish them from the quantities which appear in the formulation for Ω^B. Of course, continuity of tractions and displacements across the interface dictates that $\boldsymbol{u}_I^F = \boldsymbol{u}_I^B$ and $\boldsymbol{t}_I^F = -\boldsymbol{t}_I^B$, but we retain the distinction to allow for an (approximate) weak enforcement of continuity within the context of the discretized problem to be considered further below.

The formulation adopted for Ω^F follows in the usual way from the principle of virtual work and can be stated in the form

$$\mathcal{K}_{FF}(\tilde{\boldsymbol{u}}, \boldsymbol{u}) \;=\; 2\mathcal{F}_I^F(\tilde{\boldsymbol{u}}_I^F, \boldsymbol{t}_I^F) + 2\mathcal{F}_T^F(\tilde{\boldsymbol{u}}, \boldsymbol{t}_o) \tag{4.14}$$

in which $\tilde{\boldsymbol{u}}$ is a suitably well behaved test function, $\tilde{\boldsymbol{u}}_I^F$ is the restriction of $\tilde{\boldsymbol{u}}$ on S_I, and

$$\mathcal{K}_{FF}(\tilde{\boldsymbol{u}}, \boldsymbol{u}) \;=\; \int_{\Omega^F} E_{ijkl} \left[\frac{\partial \tilde{u}_i}{\partial y_j}(\boldsymbol{y})\right] \left[\frac{\partial u_k}{\partial y_l}(\boldsymbol{y})\right] dV(\boldsymbol{y}) \tag{4.15}$$

$$\mathcal{F}_P^F(\boldsymbol{X}, \boldsymbol{Y}) \;=\; \frac{1}{2}\int_{S_P} X_i(\boldsymbol{y})\; Y_i(\boldsymbol{y})\; dS(\boldsymbol{y}) \tag{4.16}$$

with $P \in \{I, T\}$. We remark that the factor of one-half in (4.16) has been introduced for convenience to cast this term in a form analogous to that for $\mathcal{F}_P^B(\boldsymbol{X}, \boldsymbol{Y})$ given by (4.11), and this then leads to the factor of two appearing on the right hand side of (4.14). Of course, the operator $\mathcal{F}_P^F$ is defined on a portion of the boundary of Ω^F whereas $\mathcal{F}_P^B$ is defined on a portion of the boundary of Ω^B; this distinction will be particularly important in what follows.

4.1.3 Overall symmetric formulation

To obtain a weak statement of the original boundary value (for the entire domain), the variational statement (4.14) is used in conjunction with the set of integral equations (4.5). Specifically, (4.14) is combined with the last equation of (4.5) to obtain the symmetric system

$$\begin{aligned}
&\mathcal{A}_{UU}(\tilde{\boldsymbol{t}}, \boldsymbol{t}) + \mathcal{B}_{UT}(\tilde{\boldsymbol{t}}, \boldsymbol{v}) + \mathcal{A}_{UI}(\tilde{\boldsymbol{t}}, \boldsymbol{t}_I^B) + \mathcal{B}_{UI}(\tilde{\boldsymbol{t}}, \boldsymbol{u}_I^B) = \mathcal{R}_1(\tilde{\boldsymbol{t}})\\
&\mathcal{B}_{UT}(\boldsymbol{t}, \tilde{\boldsymbol{v}}) + \mathcal{C}_{TT}(\tilde{\boldsymbol{v}}, \boldsymbol{v}) + \mathcal{B}_{IT}(\boldsymbol{t}_I^B, \tilde{\boldsymbol{v}}) + \mathcal{C}_{TI}(\tilde{\boldsymbol{v}}, \boldsymbol{u}_I^B) = \mathcal{R}_2(\tilde{\boldsymbol{v}})\\
&\mathcal{A}_{IU}(\tilde{\boldsymbol{t}}_I^B, \boldsymbol{t}) + \mathcal{B}_{IT}(\tilde{\boldsymbol{t}}_I^B, \boldsymbol{v}) + \mathcal{A}_{II}(\tilde{\boldsymbol{t}}_I^B, \boldsymbol{t}_I^B) + \mathcal{D}_{II}(\tilde{\boldsymbol{t}}_I^B, \boldsymbol{u}_I^B) = \mathcal{R}_3(\tilde{\boldsymbol{t}}_I^B)\\
&\mathcal{B}_{UI}(\boldsymbol{t}, \tilde{\boldsymbol{u}}_I^B) + \mathcal{C}_{IT}(\tilde{\boldsymbol{u}}_I^B, \boldsymbol{v}) + \mathcal{D}_{II}(\boldsymbol{t}_I^B, \tilde{\boldsymbol{u}}_I^B) + \left[\mathcal{C}_{II} - \mathcal{K}_{FF}\right] = \mathcal{R}_4(\tilde{\boldsymbol{u}}_I^B) - 2\mathcal{F}_T^F(\tilde{\boldsymbol{u}}, \boldsymbol{t}_o) + \mathcal{E}
\end{aligned} \tag{4.17}$$

in which

$$[\mathcal{C}_{II} - \mathcal{K}_{FF}] = \mathcal{C}_{II}(\tilde{\boldsymbol{u}}_I^B, \boldsymbol{u}_I^B) - \mathcal{K}_{FF}(\tilde{\boldsymbol{u}}, \boldsymbol{u}) \tag{4.18}$$

and where $\mathcal{E}$ is given by

$$\mathcal{E} \quad = \quad -2\Big[\mathcal{F}_I^B(\tilde{\boldsymbol{u}}_I^B, \boldsymbol{t}_I^B) + \mathcal{F}_I^F(\tilde{\boldsymbol{u}}_I^F, \boldsymbol{t}_I^F)\Big] \tag{4.19}$$

Strong continuity of the tractions and displacement test functions across the interface (i.e. $\boldsymbol{t}_I^B = -\boldsymbol{t}_I^F$ and $\tilde{\boldsymbol{u}}_I^B = \tilde{\boldsymbol{u}}_I^F$) implies that $\mathcal{E} = 0$. We retain this term, however, so that it can be discussed in the context of the numerical solution procedure to be introduced next.

4.2 Discretization

A Galerkin strategy is adopted to construct an approximate numerical solution to the system of equations (4.17). For the subregion Ω^B, only the boundary (including the crack surface and the interface) requires discretization, and here standard two dimensional isoparametric C^o elements are employed except along the crack front where the special crack tip element introduced in Chapter 3 is utilized. For the subregion Ω^F, standard three dimensional isoparametric C^o elements are employed throughout. It should be noted that the discretizations of the two subdomains are considered to be independent so that, in particular, the meshes on the interface need not conform.

To distinguish the discretization on the interface associated with Ω^B from that associated with Ω^F, we now let S_I^B denote the (approximate, discretized) interface for the BEM-region and S_I^F that for the FEM-region. Furthermore, we introduce yet another representation for the interface which is denoted by S_I^R and which will be referred to as the reference interface; this surface (while ideally coincident with S_I) can be discretized separately from the other two in terms of standard

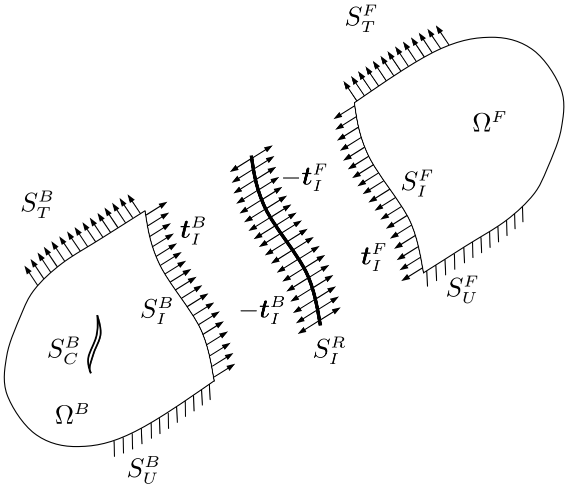

(b)

Figure 4.2: Schematic of approximate geometries of two subregions resulting from discretization.

two dimensional isoparametric C^o elements. The reference interface will be used to connect interfacial quantities associated with Ω^F to those associated with Ω^B, and at times it will be viewed as an 'interlayer' having infinitesimal thickness such that it is appropriate to consider its equilibrium.

The (independent) displacement trial and test functions associated with S_I^B, S_I^F and S_I^R are given by

$$\boldsymbol{u}_I^B = \boldsymbol{\Phi}_B^{\mathrm{T}} \boldsymbol{U}_I^B \quad , \quad \boldsymbol{u}_I^F = \boldsymbol{\Phi}_F^{\mathrm{T}} \boldsymbol{U}_I^F \quad , \quad \boldsymbol{u}_I^R = \boldsymbol{\Phi}_R^{\mathrm{T}} \boldsymbol{U}_I^R \tag{4.20}$$

$$\tilde{\boldsymbol{u}}_I^B = \boldsymbol{\Phi}_B^{\mathrm{T}} \tilde{\boldsymbol{U}}_I^B \quad , \quad \tilde{\boldsymbol{u}}_I^F = \boldsymbol{\Phi}_F^{\mathrm{T}} \tilde{\boldsymbol{U}}_I^F \quad , \quad \tilde{\boldsymbol{u}}_I^R = \boldsymbol{\Phi}_R^{\mathrm{T}} \tilde{\boldsymbol{U}}_I^R \tag{4.21}$$

in which, with $Q \in \{B, F, R\}$, the quantities $\boldsymbol{U}_I^Q$ and $\tilde{\boldsymbol{U}}_I^Q$ are column vectors of nodal values, $\boldsymbol{\Phi}_Q$ is a column vector of nodal shape functions, and $\boldsymbol{\Phi}_Q^{\mathrm{T}}$ is the transpose of $\boldsymbol{\Phi}_Q$. The traction trial and test functions associated with S_I^B and S_I^F are given by

$$\boldsymbol{t}_I^B = \boldsymbol{\Phi}_B^{\mathrm{T}} \boldsymbol{T}_I^B \quad , \quad \boldsymbol{t}_I^F = \boldsymbol{\Phi}_F^{\mathrm{T}} \boldsymbol{T}_I^F \tag{4.22}$$

$$\tilde{\boldsymbol{t}}_I^B = \boldsymbol{\Phi}_B^{\mathrm{T}} \tilde{\boldsymbol{T}}_I^B \quad , \quad \tilde{\boldsymbol{t}}_I^F = \boldsymbol{\Phi}_F^{\mathrm{T}} \tilde{\boldsymbol{T}}_I^F \tag{4.23}$$

in which $\boldsymbol{T}_{I}^{Q}$ and $\tilde{\boldsymbol{T}}_{I}^{Q}$ (with $_{Q} \in \{_{B}, _{F}\}$) are column vectors of nodal quantities. Note that the traction quantities are interpolated in terms of the same nodal shape functions used to interpolate the displacement quantities. Also note that the traction on the interface associated with Ω^{B} appears naturally as a variable in the integral equation representation for this region, while the traction $\boldsymbol{t}_{I}^{F}$ associated with Ω^{F} is considered to be 'prescribed' in the sense that it will eventually be connected to $\boldsymbol{t}_{I}^{B}$ and, in fact, eliminated from the final system of equations.

4.2.1 Continuity conditions and constraint matrices

Owing to the fact that separate discretization are allowed on the BEM and FEM regions, continuity of the approximate trial and test functions across the interface cannot in general be enforced in the strong sense. Furthermore, the approximate surface S_{I}^{B} need not be identically coincident with S_{I}^{F}, and so these surfaces must be distinguished for purposes of integration of quantities over the interface.

Within the context of the discretization for the interface, continuity of the displacement trial and test functions is enforced in the weak sense. Specifically,

$$\int_{S_I^B} \left[\boldsymbol{u}_{I}^{B}(\boldsymbol{y}) - \boldsymbol{u}_{I}^{R}(\boldsymbol{y}_p) \right] \cdot \tilde{\boldsymbol{w}}_{I}^{B}(\boldsymbol{y}) dS(\boldsymbol{y}) \quad = \quad 0 \quad , \quad \forall\, \tilde{\boldsymbol{w}}_{I}^{B} \in H^{h}(S_{I}^{B}) \tag{4.24}$$

$$\int_{S_I^F} \left[\boldsymbol{u}_{I}^{F}(\boldsymbol{y}) - \boldsymbol{u}_{I}^{R}(\boldsymbol{y}_p) \right] \cdot \tilde{\boldsymbol{w}}_{I}^{F}(\boldsymbol{y}) dS(\boldsymbol{y}) \quad = \quad 0 \quad , \quad \forall\, \tilde{\boldsymbol{w}}_{I}^{F} \in H^{h}(S_{I}^{F}) \tag{4.25}$$

and

$$\int_{S_I^B} \left[\tilde{\boldsymbol{u}}_{I}^{B}(\boldsymbol{y}) - \tilde{\boldsymbol{u}}_{I}^{R}(\boldsymbol{y}_p) \right] \cdot \tilde{\boldsymbol{w}}_{I}^{B}(\boldsymbol{y}) dS(\boldsymbol{y}) \quad = \quad 0 \quad , \quad \forall\, \tilde{\boldsymbol{w}}_{I}^{B} \in H^{h}(S_{I}^{B}) \tag{4.26}$$

$$\int_{S_I^F} \left[\tilde{\boldsymbol{u}}_{I}^{F}(\boldsymbol{y}) - \tilde{\boldsymbol{u}}_{I}^{R}(\boldsymbol{y}_p) \right] \cdot \tilde{\boldsymbol{w}}_{I}^{F}(\boldsymbol{y}) dS(\boldsymbol{y}) \quad = \quad 0 \quad , \quad \forall\, \tilde{\boldsymbol{w}}_{I}^{F} \in H^{h}(S_{I}^{F}) \tag{4.27}$$

where $\tilde{\boldsymbol{w}}_{I}^{Q} = \boldsymbol{\Phi}_{Q}^{\mathrm{T}} \tilde{\boldsymbol{W}}_{I}^{Q}$ is a test function, $H^{h}(S_{I}^{Q})$ denotes the finite dimensional subspace of H^{1} defined by the shape functions $\boldsymbol{\Phi}_{Q}$, and $\boldsymbol{y}_p$ denotes the closest point projection of $\boldsymbol{y}$ (e.g. if the integration surface is S_{I}^{B}, $\boldsymbol{y}_p \in S_{I}^{R}$ is the closest point projection of $\boldsymbol{y} \in S_I^B$). There remains to consider the tractions associated with S_I^B and S_I^F, and here continuity of these quantities is enforced (approximately) by means of

$$\int_{S_I^R} \Big[\boldsymbol{t}_I^B(\boldsymbol{y}_p) + \boldsymbol{t}_I^F(\boldsymbol{y}_p) \Big] \cdot \tilde{\boldsymbol{w}}_I^R(\boldsymbol{y}) dS(\boldsymbol{y}) = 0 \quad , \quad \forall\ \tilde{\boldsymbol{w}}_I^R \in H^h(S_I^R) \tag{4.28}$$

Note that the latter relation can be interpreted as a weak statement of equilibrium for the reference interface in terms of the tractions 'exerted on it' by Ω^B and Ω^F.

Displacement constraints

With the use of (4.20) and the fact that $\tilde{\boldsymbol{W}}_I^Q$ is an arbitrary column vector, we obtain an explicit form for the constraints implied by (4.24) and (4.25) as

$$\boldsymbol{U}_I^B = \bar{\boldsymbol{\Lambda}}_{BR} \boldsymbol{U}_I^R \qquad , \qquad \boldsymbol{U}_I^F = \bar{\boldsymbol{\Lambda}}_{FR} \boldsymbol{U}_I^R \tag{4.29}$$

where (with $Q \in \{B, F\}$)

$$\bar{\boldsymbol{\Lambda}}_{QR} = \boldsymbol{\Pi}_Q^{-1} \boldsymbol{\Lambda}_{QR} \tag{4.30}$$

in which

$$\boldsymbol{\Pi}_Q \;=\; \int_{S_I^Q} \boldsymbol{\Phi}_Q(\boldsymbol{y})\ \boldsymbol{\Phi}_Q^{\mathrm{T}}(\boldsymbol{y})\ dS(\boldsymbol{y}) \tag{4.31}$$

$$\boldsymbol{\Lambda}_{QR} \;=\; \int_{S_I^Q} \boldsymbol{\Phi}_Q(\boldsymbol{y})\ \boldsymbol{\Phi}_R^{\mathrm{T}}(\boldsymbol{y}_p)\ dS(\boldsymbol{y}) \tag{4.32}$$

Similarly, using (4.21) we obtain the constraints implied by (4.26) and (4.27)as

$$\tilde{\boldsymbol{U}}_I^B = \bar{\boldsymbol{\Lambda}}_{BR} \tilde{\boldsymbol{U}}_I^R \qquad , \qquad \tilde{\boldsymbol{U}}_I^F = \bar{\boldsymbol{\Lambda}}_{FR} \tilde{\boldsymbol{U}}_I^R \tag{4.33}$$

Traction continuity implied by $\mathcal{E} = 0$

Next, we turn attention to the weak statement of traction continuity (4.28). We note that, within the context of the discretization, $\mathcal{E}$ given by (4.19) can be expressed in the form

$$\mathcal{E} = \mathcal{E}^{trac} + \mathcal{E}_B^{disp} + \mathcal{E}_F^{disp} + \mathcal{E}_B^{geom} + \mathcal{E}_F^{geom} \quad , \ \ \forall\ \tilde{\boldsymbol{u}}_I^R \in H^h(S_I^R) \tag{4.34}$$

where

$$\mathcal{E}^{trac} = -\int_{S_I^R} \left[\boldsymbol{t}_I^B(\boldsymbol{y}_p) + \boldsymbol{t}_I^F(\boldsymbol{y}_p) \right] \cdot \tilde{\boldsymbol{u}}_I^R(\boldsymbol{y}) dS(\boldsymbol{y}) \tag{4.35}$$

and where

$$\mathcal{E}_B^{disp} = \int_{S_I^B} \left[\tilde{\boldsymbol{u}}_I^R(\boldsymbol{y}_p) - \tilde{\boldsymbol{u}}_I^B(\boldsymbol{y}) \right] \cdot \boldsymbol{t}_I^B(\boldsymbol{y}) dS(\boldsymbol{y}) \tag{4.36}$$

$$\mathcal{E}_F^{disp} = \int_{S_I^F} \left[\tilde{\boldsymbol{u}}_I^R(\boldsymbol{y}_p) - \tilde{\boldsymbol{u}}_I^F(\boldsymbol{y}) \right] \cdot \boldsymbol{t}_I^F(\boldsymbol{y}) dS(\boldsymbol{y}) \tag{4.37}$$

$$\mathcal{E}_B^{geom} = \int_{S_I^R} \boldsymbol{t}_I^B(\boldsymbol{y}_p) \cdot \tilde{\boldsymbol{u}}_I^R(\boldsymbol{y}) dS(\boldsymbol{y}) - \int_{S_I^B} \boldsymbol{t}_I^B(\boldsymbol{y}) \cdot \tilde{\boldsymbol{u}}_I^R(\boldsymbol{y}_p) dS(\boldsymbol{y}) \tag{4.38}$$

$$\mathcal{E}_F^{geom} = \int_{S_I^R} \boldsymbol{t}_I^F(\boldsymbol{y}_p) \cdot \tilde{\boldsymbol{u}}_I^R(\boldsymbol{y}) dS(\boldsymbol{y}) - \int_{S_I^F} \boldsymbol{t}_I^F(\boldsymbol{y}) \cdot \tilde{\boldsymbol{u}}_I^R(\boldsymbol{y}_p) dS(\boldsymbol{y}) \tag{4.39}$$

From (4.26) and (4.27) along with the fact that $\boldsymbol{t}_I^Q = \boldsymbol{\Phi}_Q^{\mathrm{T}} \boldsymbol{T}_I^Q \in H^h(S_I^Q)$, it follows that $\mathcal{E}_B^{disp} = 0$ and $\mathcal{E}_F^{disp} = 0$. The terms $\mathcal{E}_B^{geom}$ and $\mathcal{E}_F^{geom}$ are associated with the geometric mismatch between the approximate surfaces S_I^B, S_I^F and the reference interface S_I^R (as well as the procedure utilized to obtain the closest point projection). It is evident that $\mathcal{E}_B^{geom} = \mathcal{E}_F^{geom} = 0$ for the special case of conforming discretizations, but these terms will also vanish for nonconforming discretizations under certain circumstances (e.g. a flat interface with a polygonal edge). When these geometric terms do in fact vanish, setting $\mathcal{E} = 0$ implies that $\mathcal{E}^{trac} = 0$ which is equivalent to the weak statement of traction continuity given by (4.28). Here we set $\mathcal{E} \equiv 0$ for all cases and in this way we obtain a symmetric system of equations for which equilibrium of the reference interface is ensured (to within the small error which may be induced by neglecting $\mathcal{E}_B^{geom}$ and $\mathcal{E}_F^{geom}$).

4.2.2 Final discrete equations

For the FEM-region, the discretization follows a standard finite element procedure, and here the column vector of displacement nodal quantities associated with the discretization is denoted $\boldsymbol{U}_{total}^F$. To clearly indicate the role of the interface in the equations to follow, the vector $\boldsymbol{U}^F_{total}$ is partitioned as $\boldsymbol{U}^F_{total} = [\boldsymbol{U}^F_I \ \boldsymbol{U}^F]^{\mathrm{T}}$ in which the column vector $\boldsymbol{U}^F_I$ contains the displacement nodal quantities for the interface S^F_I and the vector $\boldsymbol{U}^F$ contains the remaining nodal quantities.

For the BEM-region, we now denote the various discretized surfaces by means of a superscript B (i.e. S^B_U, $S^B_{T_o}$, S^B_C and S^B_I). The traction and displacement variables are approximated in terms of nodal quantities and nodal basis functions in a fashion similar to that given by (4.20)-(4.23). This gives rise to column vectors $\boldsymbol{U}^B$, $\boldsymbol{U}^B_I$ and $\Delta\boldsymbol{U}^B$ associated with displacement nodal quantities on $S^B_{T_o}$, S^B_I and S^B_C, respectively, and to column vectors $\boldsymbol{T}^B$ and $\boldsymbol{T}^B_I$ associated with traction nodal quantities on S^B_U and S^B_I, respectively.

The discrete system of equations governing the boundary value problem then follows from (4.17) (with $\mathcal{E} \equiv 0$) through an appropriate use of the constraint equations (4.29) and (4.33). In forming these equations, nodal quantities associated with S^B_I and S^F_I are eliminated in favor of those associated with S^R_I. The final system takes the form

$$\begin{bmatrix} \boldsymbol{A}_{UU} & \boldsymbol{B}_{UT_o} & \boldsymbol{B}_{UC} & \boldsymbol{A}_{UI} & \bar{\boldsymbol{B}}_{UI} & \boldsymbol{O} \\ \boldsymbol{B}^{\mathrm{T}}_{UT_o} & \boldsymbol{C}_{T_oT_o} & \boldsymbol{C}_{T_oC} & \boldsymbol{B}^{\mathrm{T}}_{IT_o} & \bar{\boldsymbol{C}}_{TI} & \boldsymbol{O} \\ \boldsymbol{B}^{\mathrm{T}}_{UC} & \boldsymbol{C}^{\mathrm{T}}_{T_oC} & \boldsymbol{C}_{CC} & \boldsymbol{B}^{\mathrm{T}}_{IC} & \bar{\boldsymbol{C}}_{CI} & \boldsymbol{O} \\ \boldsymbol{A}^{\mathrm{T}}_{UI} & \boldsymbol{B}_{IT_o} & \boldsymbol{B}_{IC} & \boldsymbol{C}_{II} & \bar{\boldsymbol{D}}_{II} & \boldsymbol{O} \\ \bar{\boldsymbol{B}}^{\mathrm{T}}_{UI} & \bar{\boldsymbol{C}}^{\mathrm{T}}_{T_oI} & \bar{\boldsymbol{C}}^{\mathrm{T}}_{CI} & \bar{\boldsymbol{D}}^{\mathrm{T}}_{II} & \bar{\boldsymbol{C}}_{II} - \bar{\boldsymbol{K}}_{II} & -\bar{\boldsymbol{K}}_{IF} \\ \boldsymbol{O} & \boldsymbol{O} & \boldsymbol{O} & \boldsymbol{O} & -\bar{\boldsymbol{K}}^{\mathrm{T}}_{IF} & -\boldsymbol{K}_{FF} \end{bmatrix} \begin{bmatrix} \boldsymbol{T}^B \\ \boldsymbol{U}^B \\ \Delta\boldsymbol{U}^B \\ \boldsymbol{T}^B_I \\ \boldsymbol{U}^R_I \\ \boldsymbol{U}^F \end{bmatrix} = \begin{bmatrix} \boldsymbol{R}_1 \\ \boldsymbol{R}_2 \\ \boldsymbol{R}_3 \\ \boldsymbol{R}_4 \\ \bar{\boldsymbol{R}}_5 \\ \boldsymbol{R}_6 \end{bmatrix} \tag{4.40}$$

in which

$$\begin{aligned} \bar{\boldsymbol{B}}_{UI} &= \boldsymbol{B}_{UI}\bar{\boldsymbol{\Lambda}}_B \ , & \bar{\boldsymbol{C}}_{TI} &= \boldsymbol{C}_{T_oI}\bar{\boldsymbol{\Lambda}}_B \ , & \bar{\boldsymbol{C}}_{CI} &= \boldsymbol{C}_{CI}\bar{\boldsymbol{\Lambda}}_B \\ \bar{\boldsymbol{D}}_{II} &= \boldsymbol{D}_{II}\bar{\boldsymbol{\Lambda}}_B \ , & \bar{\boldsymbol{C}}_{II} &= \bar{\boldsymbol{\Lambda}}^{\mathrm{T}}_B\boldsymbol{C}_{II}\bar{\boldsymbol{\Lambda}}_B \ , & \bar{\boldsymbol{R}}_5 &= \bar{\boldsymbol{\Lambda}}^{\mathrm{T}}_B\boldsymbol{R}_5 \\ \bar{\boldsymbol{K}}_{IF} &= \bar{\boldsymbol{\Lambda}}^{\mathrm{T}}_F\boldsymbol{K}_{IF} \ , & \bar{\boldsymbol{K}}_{II} &= \bar{\boldsymbol{\Lambda}}^{\mathrm{T}}_F\boldsymbol{K}_{II}\bar{\boldsymbol{\Lambda}}_F \end{aligned} \tag{4.41}$$

In these expressions, the sub-matrices $\boldsymbol{K}_{II}$, $\boldsymbol{K}_{IF}$ and $\boldsymbol{K}_{FF}$ are associated with the operator $\mathcal{K}_{FF}$ by means of the partitioning $\boldsymbol{U}^F_{total} = [\boldsymbol{U}^F_I \; \boldsymbol{U}^F]^{\mathrm{T}}$, and the loading term $\boldsymbol{R}_6$ is associated with $\mathcal{F}^F_T$. Toward discussing the terms arising from the SGBEM formulation, we first note that the statement (4.17) involves the entire surface $S_T = S_{T_o} \cup S_C$ on which tractions are prescribed, whereas here the surfaces S_{T_o} and S_C have been distinguished in order to explicitly reveal the degrees of freedom $\Delta\boldsymbol{U}^B$ on the crack. Having distinguished these two surfaces, the integral operators $\mathcal{A}_{PQ}, \mathcal{B}_{PQ}, \mathcal{C}_{PQ}$ and $\mathcal{D}_{II}$ (with $P, Q \in \{U, T, I\}$) give rise to the sub-matrices $\boldsymbol{A}_{PQ}$, $\boldsymbol{B}_{PQ}$, $\boldsymbol{C}_{PQ}$ and $\boldsymbol{D}_{II}$ (with $P, Q \in \{U, T_o, C, I\}$), the operator $\mathcal{R}_1$ gives rise to the load vector $\boldsymbol{R}_1$, the operator $\mathcal{R}_2$ gives rise to the *pair* of load vectors $\boldsymbol{R}_2$ and $\boldsymbol{R}_3$ and, finally, the operator $\mathcal{R}_4$ gives rise to the load vector $\boldsymbol{R}_5$. The numerical evaluation of these SGBEM sub-matrices and load vectors is essentially the same as that described in Chapter 3.

We remark that the coefficient matrices $\boldsymbol{A}_{UU}, \boldsymbol{A}_{II}, \boldsymbol{K}_{II}$ and $\boldsymbol{K}_{FF}$ are symmetric and positive definite, whereas $\boldsymbol{C}_{TT}, \boldsymbol{C}_{CC}$ and $\boldsymbol{C}_{II}$ are symmetric and negative definite. This gives rise to a system of linear equations in terms of a symmetric non-definite coefficient matrix.

4.2.3 Additional discussion of constraint equations

In general, the reference interface S^R_I can be discretized independently of both S^B_I and S^F_I. However, in the numerical implementation followed here, the reference surface S^R_I is chosen to be coincident with either S^B_I or S^F_I (i.e. $S^R_I \in \{S^B_I, S^F_I\}$). When the choice $S^R_I = S^B_I$ is made, the constraint relations reduce to

$$\boldsymbol{U}^F_I = \bar{\boldsymbol{\Lambda}}_{FB} \boldsymbol{U}^B_I \qquad , \qquad \tilde{\boldsymbol{U}}^F_I = \bar{\boldsymbol{\Lambda}}_{FB} \tilde{\boldsymbol{U}}^B_I \tag{4.42}$$

in which $\bar{\boldsymbol{\Lambda}}_{FB} = \boldsymbol{\Pi}_F^{-1} \boldsymbol{\Lambda}_{FB}$ with $\boldsymbol{\Pi}_F$ and $\boldsymbol{\Lambda}_{FB}$ given by (4.31) and (4.32). Similarly, when the choice $S^R_I = S^B_I$ is made we have

$$\boldsymbol{U}^B_I = \bar{\boldsymbol{\Lambda}}_{BF} \boldsymbol{U}^F_I \qquad , \qquad \tilde{\boldsymbol{U}}^B_I = \bar{\boldsymbol{\Lambda}}_{BF} \tilde{\boldsymbol{U}}^F_I \tag{4.43}$$

where $\bar{\boldsymbol{\Lambda}}_{BF} = \boldsymbol{\Pi}_{B}^{-1} \boldsymbol{\Lambda}_{BF}$.

The evaluation of each entry of $\boldsymbol{\Pi}_{B}$ and $\boldsymbol{\Pi}_{F}$ follows a standard numerical integration scheme (specifically Gaussian quadrature) since the integrand is completely defined on a single surface. In contrast, each entry of $\boldsymbol{\Lambda}_{BF}$ and $\boldsymbol{\Lambda}_{FB}$ involves an integral whose integrand is the product of nodal basis functions defined on two different interfaces (S_{I}^{B} and S_{I}^{F}), and the special integration strategy described in Appendix F is adopted to treat these matrices.

Conforming meshes

For the particular case in which the meshes on the interface conform (i.e. $S_{I}^{B} = S_{I}^{F} = S_{I}^{R}$), the matrices $\boldsymbol{\Pi}_{B}$, $\boldsymbol{\Lambda}_{BR}$, $\bar{\boldsymbol{\Lambda}}_{BR}$, $\boldsymbol{\Pi}_{F}$, $\boldsymbol{\Lambda}_{FR}$ and $\bar{\boldsymbol{\Lambda}}_{FR}$ all reduce, naturally, to an identity matrix. In turn, the constraint conditions (4.29) and (4.33) reduce to the (strong) continuity conditions

$$\begin{aligned} \boldsymbol{U}_{I}^{B} &= \boldsymbol{U}_{I}^{F} = \boldsymbol{U}_{I}^{R} && (4.44) \\ \tilde{\boldsymbol{U}}_{I}^{B} &= \tilde{\boldsymbol{U}}_{I}^{F} = \tilde{\boldsymbol{U}}_{I}^{R} && (4.45) \end{aligned}$$

Non-conforming meshes: collocation

By ignoring the requirement that $\tilde{\boldsymbol{w}}_{I}^{Q} \in H^{h}(S_{I}^{Q})$ (with $Q \in \{B, F\}$) and choosing $\tilde{\boldsymbol{w}}_{I}^{Q}$ to be the dirac-Delta function centered at nodal points on S_{I}^{Q} , we obtain collocation-type constraints which are in the same form as (4.29) and (4.33) but with the entries of $\boldsymbol{\Pi}_{Q}$ and $\boldsymbol{\Lambda}_{QR}$ given by

$$[\boldsymbol{\Pi}_{Q}]_{ij} = \delta_{ij} \qquad , \qquad [\boldsymbol{\Lambda}_{QR}]_{ij} = [\boldsymbol{\Phi}_{R}(\boldsymbol{x}_{p_{(i)}}^{Q})]_{j} \tag{4.46}$$

in which $\boldsymbol{x}_{p_{(i)}}^{Q} \in S_{I}^{R}$ is the closest point projection of the i^{th} node onto S_{I}^{Q}. It is important to note that for this type of constraint the terms $\mathcal{E}_{B}^{disp}$ and $\mathcal{E}_{F}^{disp}$ appearing in (4.34) do not in general vanish and, as a consequence, enforcing $\mathcal{E} \equiv 0$ (to obtain a symmetric formulation) violates equilibrium of the reference interface. As shown below, this can lead to significant error in the numerical solution of the boundary value problem (depending upon the choice of the reference interface).

4.3 Numerical Results

To demonstrate the versatility and capability of the technique, several numerical examples including embedded and surface breaking cracks in finite domains are considered. The primary quantities of interest are the stress intensity factors which are obtained as a function of position along the crack front. To assure the accuracy and convergence of numerical solutions, results for each problem are obtained for different levels of refinement and for certain cases, results are compared with available results obtained from SGBEM. The materials used in the analysis are an isotropic material with poisson ratio $\nu = 0.3$ and two transversely isotropic materials, zinc and a graphite-reinforced composite, with elastic moduli given in Table 4.1. The collection of all results are organized such that the results for conforming and non-conforming discretizations are presented first in the context of the developed stand alone code and certain examples illustrating the coupling of SGBEM and ABAQUS are presented subsequently.

Materials	E_{1111}	E_{1122}	E_{1133}	E_{3333}	E_{1313}
Zinc	16.09	3.35	5.01	6.10	3.83
Graphite-reinforced composite	2.130	1.013	0.808	20.996	0.587

Table 4.1: Elastic constants for zinc and a graphite-reinforced composite (x10^6 psi, [26], [25]). The axis of symmetry is taken along the x_3 coordinate direction.

4.3.1 Results for conforming discretization

In this section, we consider results for several crack problems involving embedded and surface breaking cracks and general loading conditions which give rise to mixed-mode stress intensity factors. The discretization of the two subregions, the BEM-region and the FEM-region, is such that meshes along the interface is conforming. To examine the accuracy and convergence of results, numerical solutions are obtained for three levels of refinement and compared with available solutions obtained from the SGBEM. We note that in partitioning a body, the size of the BEM-region containing crack is chosen, in certain extent, arbitrary.

Embedded penny-shaped crack in a cylinder

Consider a solid circular cylinder of radius R and length $2L$ which contains penny-shaped crack of radius a as depicted in Figure 4.3. The cylinder is subjected to two types of loading, one of which is for uniform normal traction σ_o applied at both ends of the cylinder while the other is for linearly varying shear traction applied at both ends. Note that the shear traction is associated with applied torque T_o and $\sigma_o = 2T_o/\pi R^3$ denotes an associated maximum shear traction. The dimensions used in the analysis are taken such that $a/R = 0.5$ and $L/R = 4$ and three types of materials, isotropic material with $\nu = 0.3$, zinc and a graphite-reinforced composite, are considered. For zinc and a graphite-reinforced composite, the axis of elastic symmetry is directed along the axis of the cylinder. In this analysis, three meshes are adopted as shown in Figure 4.4.

The pure mode-I and pure mode-III stress intensity factors are given in Table 4.2 where results are normalized by the stress intensity factor obtained from the SGBEM with the mesh shown in Figure4.4(b). From these results, computed stress intensity factors obtained for three meshes indicate excellent agreement with each other and with the bench mark solution.

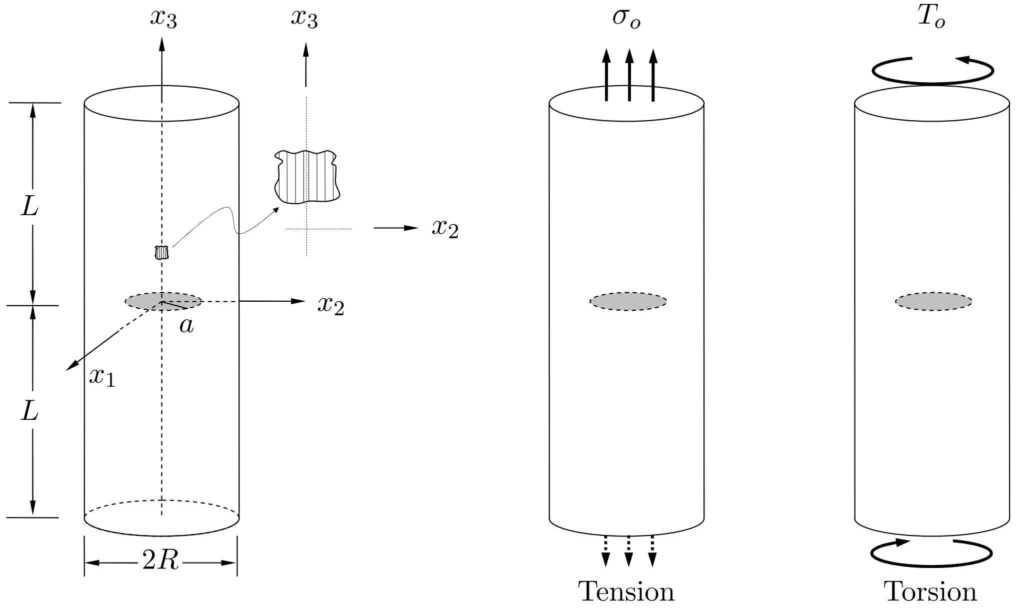

(a) (b) (c)

Figure 4.3: (a) Schematic of a penny-shaped crack in a cylinder, (b) cylinder subjected to uniform normal traction σ_o at the ends and (c) cylinder subjected to torque T_o at the ends.

	(a) K_I/K_I^{ref}			(b) K_{III}/K_{III}^{ref}		
Mesh	Isotropic	Zinc	Graphite	Isotropic	Zinc	Graphite
1	0.9844	0.9660	0.9915	0.9955	0.9954	0.9947
2	0.9975	0.9945	0.9968	1.0018	0.9969	0.9973
3	1.0007	1.0006	0.9992	0.9999	0.9990	0.9991

Table 4.2: Normalized stress intensity factors for a penny shape crack in a cylinder subjected to (a) uniform normal traction and (b) torque at the ends. The reference stress intensity factors are obtained from the SGBEM with Mesh 4 (for isotropic material: $K_I^{ref} = 0.6867\sqrt{\pi a}\ \sigma_o$ and $K_{III}^{ref} = 0.2147\sqrt{\pi a}\ \tau_o$, for zinc: $K_I^{ref} = 0.6978\ \sqrt{\pi a}\ \sigma_o$ and $K_{III}^{ref} = 0.2148\ \sqrt{\pi a}\ \tau_o$ and for a graphite-reinforced composite: $K_I^{ref} = 0.6783\ \sqrt{\pi a}\ \sigma_o$ and $K_{III}^{ref} = 0.2148\ \sqrt{\pi a}\ \tau_o$).

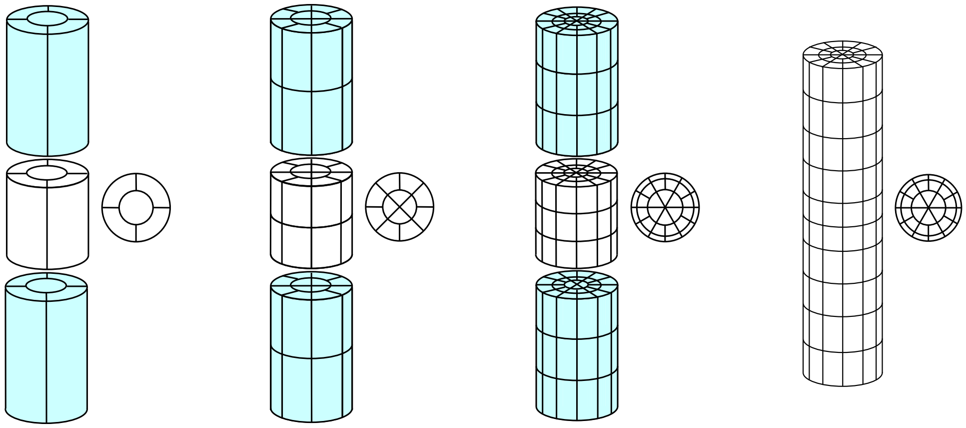

Mesh 1 Mesh 2 Mesh 3 Mesh 4

Figure 4.4: Meshes for a penny-shaped crack in a cylinder ($a/R = 0.5$, $L/R = 4$). Mesh 1, 2 and 3 are adopted for the SGBEM-FEM coupling where colored meshes are associated with the FEM-region and unshaded meshes are associated with the BEM-region including crack. Mesh 4 is adopted for the SGBEM.

To examine the influence of the size of the BEM-region on the numerical solution, we adopt three different meshes as shown schematically in Figure 4.5 where the Mesh b are identical to Mesh 3 in Figure 4.4. The normalized stress intensity factor obtained for all three mesh is shown in Table 4.3 and this result indicates that, for this particular example, there is no significant dependence of the numerical solution on the size of the BEM-region used.

	(a) K_I/K_I^{ref}			(b) K_{III}/K_{III}^{ref}		
Mesh	Isotropic	Zinc	Graphite	Isotropic	Zinc	Graphite
a	0.9995	1.0001	0.9964	1.0009	0.9991	0.9991
b	1.0007	1.0006	0.9992	0.9999	0.9990	0.9991
c	1.0001	0.9996	0.9997	0.9996	0.9990	0.9991

Table 4.3: Normalized stress intensity factors for a penny shape crack in a cylinder subjected to (a) uniform normal traction (b) torque at the ends. The results are obtained for meshes shown in Figure 4.5 and the reference stress intensity factors are the same as those shown in Table 4.2.

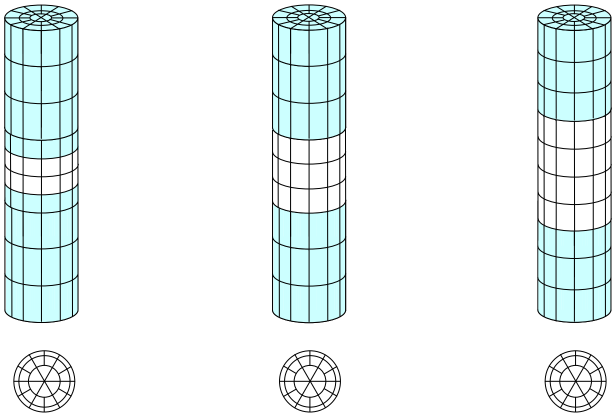

Mesh a Mesh b Mesh c

Figure 4.5: Meshes for a penny-shaped crack in a cylinder used in examining the effect of the size of the BEM-region. Note that Mesh b is identical to Mesh 3 in Figure 4.4 and meshes for crack are shown below those for the entire region.

Circumferential crack in a cylinder

Consider a circumferential crack of depth a which is contained in a solid circular cylinder of radius R and length $2L$ as shown schematically in Figure 4.6. Two types of loading, uniform normal traction σ_o and torque T_o (with $\sigma_o = 2T_o/\pi R^3$) applied at both ends of the cylinder, are examined. Note that the uniform normal traction gives rise to pure mode-I while the torsion loading introduces pure mode-III. Materials and the orientation of the axis of elastic symmetry are taken to be the same as those considered in the previous example. Three meshes used in the analysis are adopted such that $a/R = 0.5$ and $L/R = 2$ and are shown in Figure 4.7.

The computed stress intensity factors are normalized by the stress intensity factor obtained from Mesh 4 (shown in Figure 4.7) with SGBEM and are given in Table 4.4. From these results, the good agreement among numerical solutions from each mesh is observed and this indicates that solutions are only slightly mesh dependent. The relatively coarse mesh can be employed to obtain accurate results.

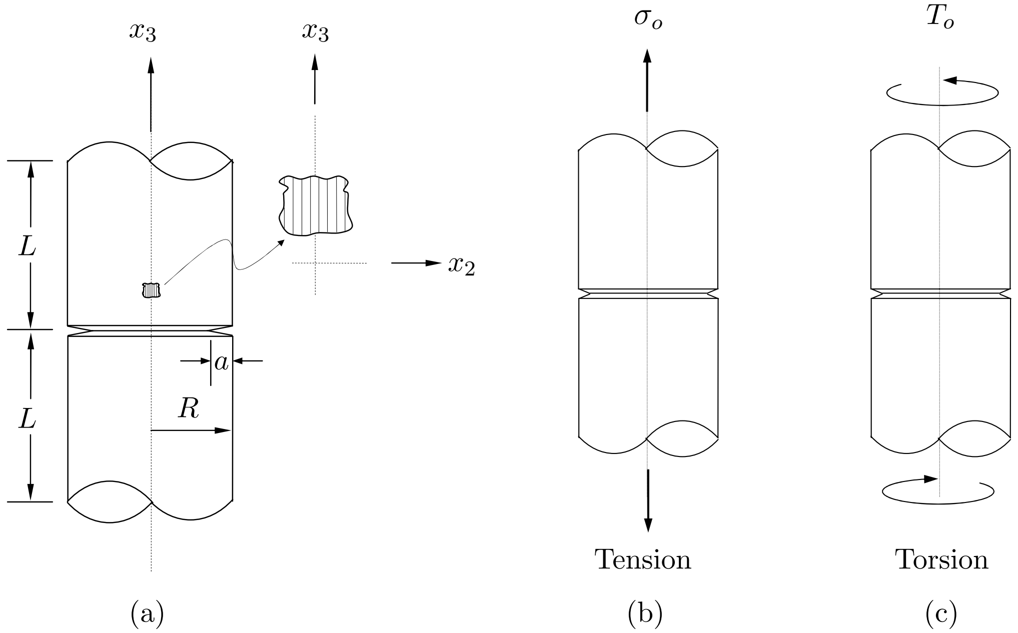

(a) (b) (c)

Figure 4.6: (a) Schematic of a circumferential crack in a cylinder, (b) cylinder subjected to uniform normal traction σ_o at the ends and (c) cylinder subjected to torque T_o at the ends.

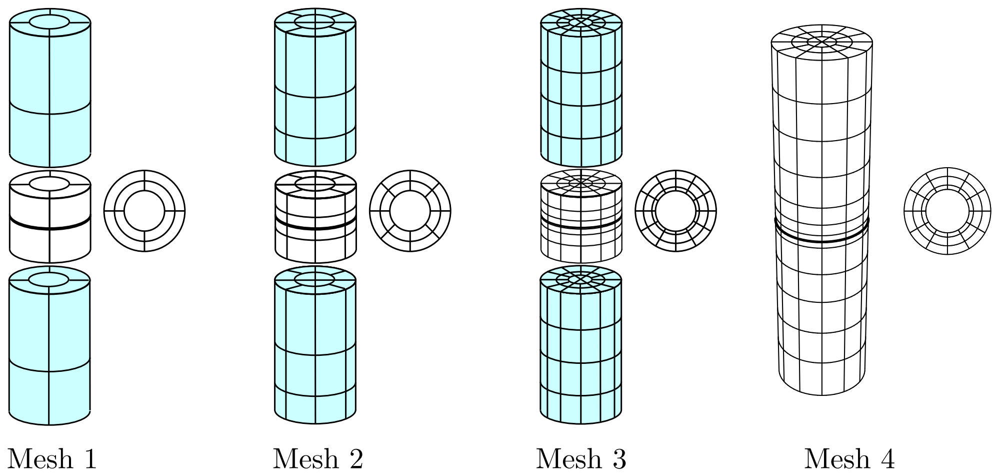

Mesh 1 Mesh 2 Mesh 3 Mesh 4

Figure 4.7: Meshes for a circumferential crack in a cylinder ($a/R = 0.5$, $L/R = 4$). Mesh 1, 2 and 3 are adopted for the SGBEM-FEM coupling where colored meshes are associated with the FEM-region and unshaded meshes are associated with the BEM-region including crack. Mesh 4 is adopted for the SGBEM.

	(a) K_I/K_I^{ref}			(b) K_{III}/K_{III}^{ref}		
Mesh	Isotropic	Zinc	Graphite	Isotropic	Zinc	Graphite
1	0.9880	0.9917	0.9717	0.9706	0.9703	0.9703
2	0.9957	0.9965	0.9979	0.9949	0.9947	0.9942
3	1.0001	0.9999	0.9986	0.9996	0.9999	0.9986

Table 4.4: Normalized stress intensity factors for a circumferential crack in a cylinder subjected to (a) uniform normal traction and (b) torque at the ends. The reference stress intensity factors are obtained from the SGBEM with Mesh 4 (for isotropic material: $K_I^{ref} = 1.9445\sqrt{\pi a}\ \sigma_o$ and $K_{III}^{ref} = 2.9811\sqrt{\pi a}\ \tau_o$, for zinc: $K_I^{ref} = 1.9753\ \sqrt{\pi a}\ \sigma_o$ and $K_{III}^{ref} = 2.9809\ \sqrt{\pi a}\ \tau_o$ and for a graphite-reinforced composite: $K_I^{ref} = 1.9311\ \sqrt{\pi a}\ \sigma_o$ and $K_{III}^{ref} = 2.9818\ \sqrt{\pi a}\ \tau_o$).

Quarter elliptical cracks at circular hole in thin plate

Next, we consider a rectangular thin plate containing circular hole of radius R at the center. The quarter-elliptic surface breaking cracks are present at the hole as shown schematically in Figure 4.8. The dimensions are taken to be $a/t = 0.2$, $a/t = 0.8$, $R/t = 2$, $R/W = 0.2$ and $H/W = 2$ which are the same as those considered in Section 3.3. Isotropic material with $v = 0.3$ and a graphite-reinforced composite are treated for this particular problem where for the latter case the axis of elastic symmetry is directed along Z axis. The plate is loaded by a uniform normal traction σ_o at both ends while other surfaces are traction free. By exploiting the symmetry of geometry and loading about a plane $Y = 0$, only half of the problem ($Y \geq 0$) is used for modeling the problem with appropriate treatment of boundary conditions. Three levels of refinement associated with the reduced domain are shown in Figure 4.9.

The loading considered gives rise to a pure mode-I and the stress intensity factor along the crack front is of interest. The normalized stress intensity factor for is presented as a function of an angular position θ in Figure 4.10 along with the result from SGBEM obtained from mesh shown in Figure 3.22. The excellent

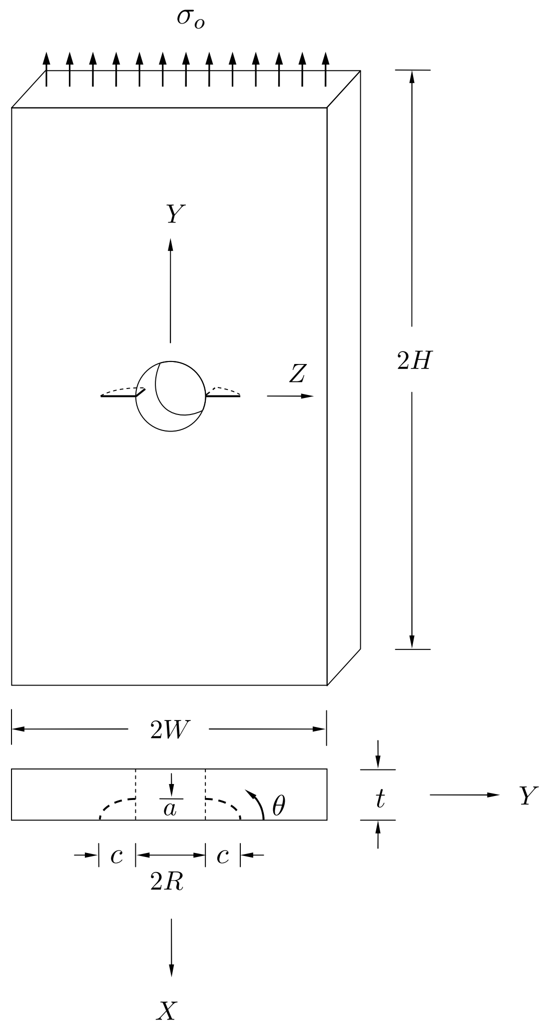

Figure 4.8: Schematic of quarter-elliptic cracks at circular hole in a rectangular plate with $R/t = 2$, $a/t = 0.2$, $a/c = 0.8$, $R/W = 0.2$ and $H/W = 2$.

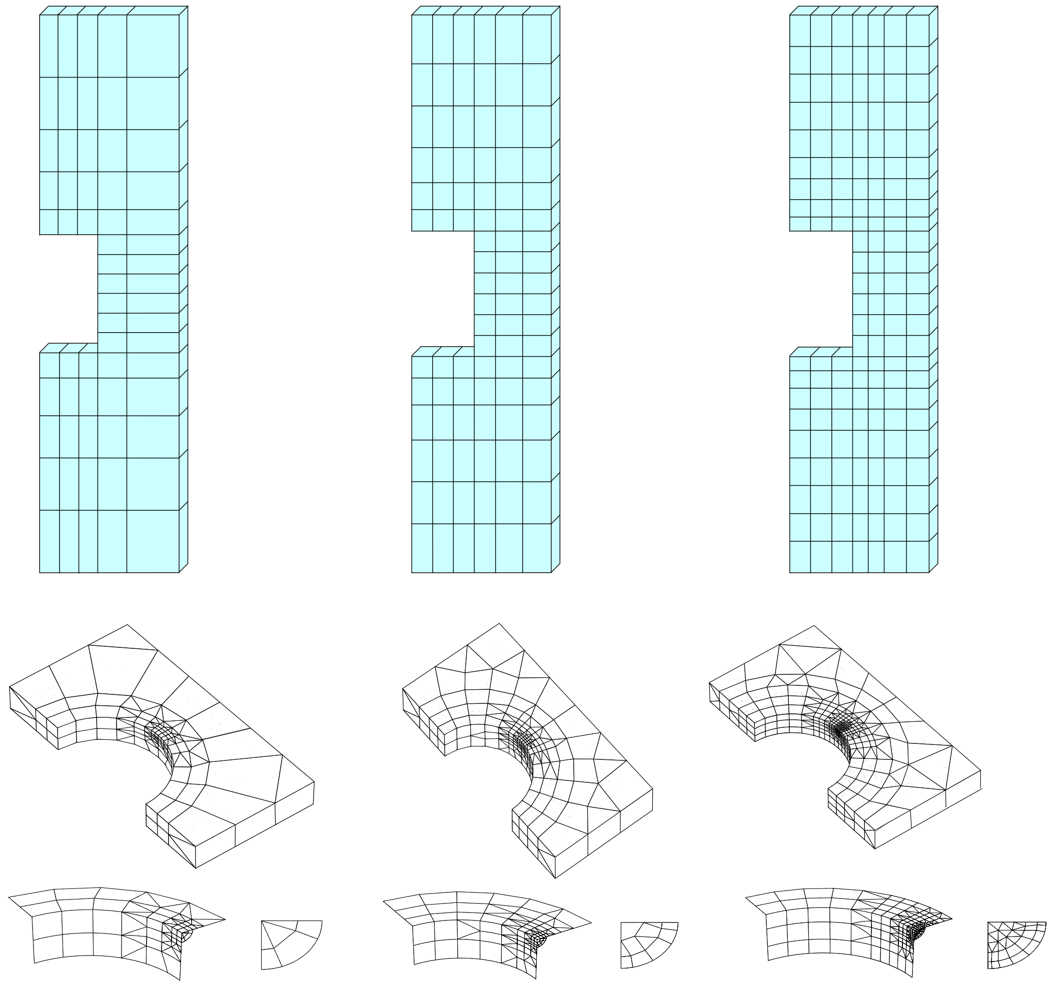

Mesh 1 Mesh 2 Mesh 3

Figure 4.9: Meshes for quarter elliptical cracks at a circular hole in a rectangular plate ($R/t = 2$, $a/t = 0.2$, $a/c = 0.8$, $R/W = 0.2$ and $H/W = 2$). Colored meshes are associated with the FEM-region and unshaded meshes are associated with the BEM-region including crack.

agreement between numerical solutions from each mesh and the result from SGBEM was observed for both material considered.

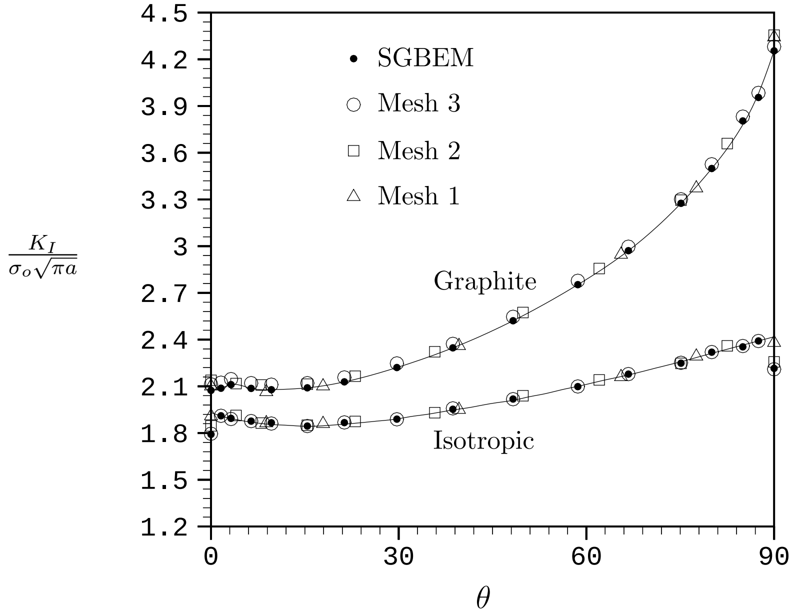

Figure 4.10: Normalized mode-I stress intensity factor for quarter-elliptic crack at a circular hole in a rectangular plate subjected to uniform normal traction σ_o at the ends.

Surface flaw in cantilever beam

Consider a cantilever beam, with rectangular cross section, of length $2L$ as shown in Figure 4.11. The beam contains semi-circular, surface breaking flaw of radius a at the center of the beam and it is subjected to a uniform shear traction corresponding to total load P_o. In the analysis, dimensions of the beam are chosen such that $L/h = 4$, $h/b = 1$ and $b/a = 4$ and three materials, isotropic with $\nu = 0.3$, zinc and a graphite-reinforced composite are considered where the last two materials are treated such that the axis of elastic symmetry is along the axis of the beam.

The considered loading gives rise to mixed-mode stress intensity factors, but, in fact, mode-I is primarily dominated and mode-II and mode-III are present due to the presence of the shear stress.

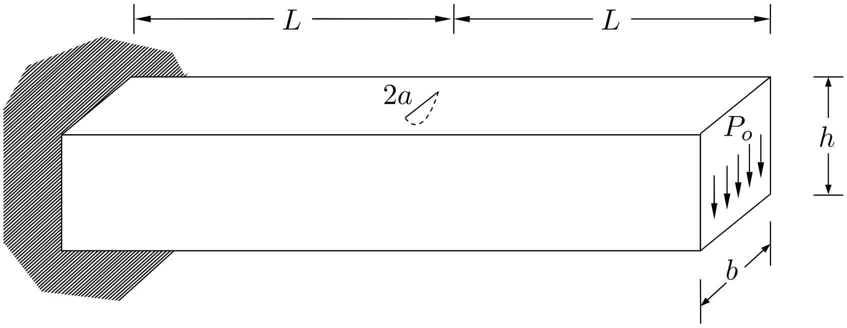

Figure 4.11: Schematic of a cantilever beam containing a surface flaw which is subjected to uniform shear traction at the end. The dimensions are taken such that $L/h = 4$, $b/h = 1$ and $b/a = 4$.

The mixed-mode stress intensity factors are obtained along the crack front from three meshes adopted as indicated in Figure 4.12. The normalized stress intensity factors are plotted as a function of an angular position θ as shown in Figure 4.13 for mode-I, in Figure 4.14 for mode-II and in Figure 4.15 for mode-III. The excellent agreement between the results obtained from three meshes indicate convergence of numerical solutions and slight mesh dependence. We remark that the subdominant stress intensity factors (mode-II and mode-III) which are of second order of magnitude can be accurately obtained with a relatively coarse mesh. In addition, the convergence of numerical solutions depends slightly upon the degree of material anisotropy as indicated by slight difference of results from Mesh 3 for a graphite-reinforced composite which possesses a very high stiffness in the direction of the axis of elastic symmetry.

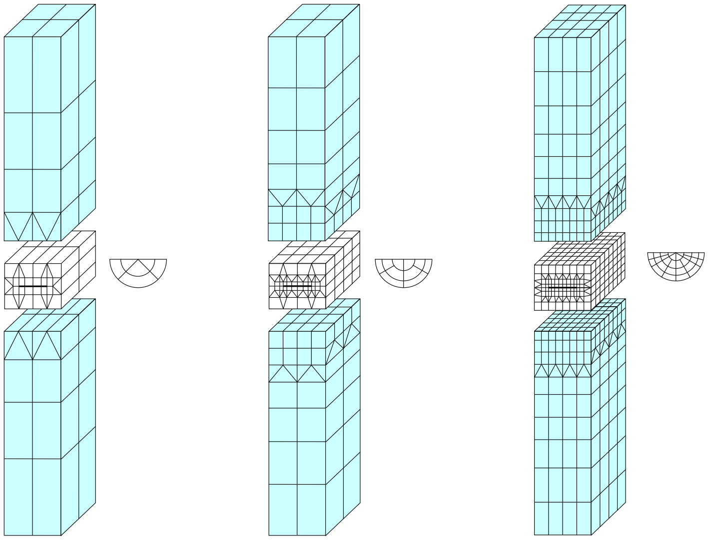

Figure 4.12: Meshes for a cantilever beam containing a semi-circular surface flaw. Colored meshes are associated with the FEM-region and unshaded meshes are associated with the BEM-region including crack.

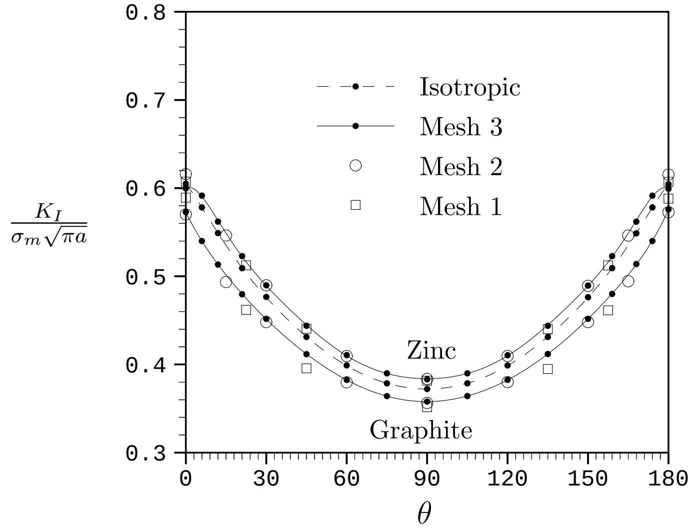

Figure 4.13: Normalized mode-I stress intensity factor for a semi-circular surface flaw in a cantilever beam subjected to uniform shear traction at the end where $\sigma_m = 6P_oL/bh^2$.

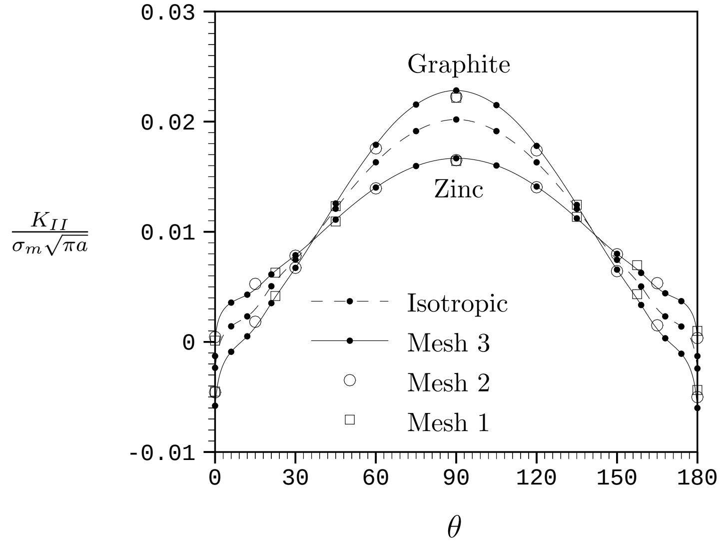

Figure 4.14: Normalized mode-II stress intensity factor for a semi-circular surface flaw in a cantilever beam subjected to uniform shear traction at the end where $\sigma_m = 6P_oL/bh^2$.

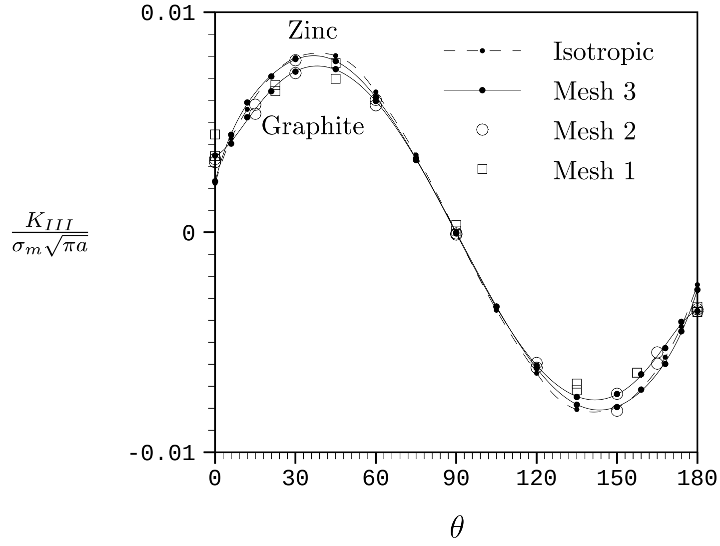

Figure 4.15: Normalized mode-III stress intensity factor for a semi-circular surface flaw in a cantilever beam subjected to uniform shear traction at the end where $\sigma_m = 6P_oL/bh^2$.

Double cantilever beam specimen

As a final example for conforming discretization, consider a double cantilever beam specimen with its geometry shown in Figure 4.16. Two types of loading are treated, one of which is for uniform shear traction associated with total load P_o applied to each leg of the specimen (Figure 4.16(a)) while the other is for linearly varying normal traction corresponding to moment M_o applied to each leg of the specimen (Figure 4.16(b)). The specimen is made from isotropic material with poisson ratio $\nu = 0.3$ and a graphite-reinforced composite with its axis of elastic symmetry directed along the longitudinal direction of the specimen. While the problem is only of pure mode-I type as a result of the geometry, loading and material behavior, the stress intensity factor varies along the crack front. To demonstrate the capability of the method in modeling a relatively thin body, the dimensions of the problem are taken such that $L/t = 24$, $B/t = 16$ and $w/t = 10$. For convergence

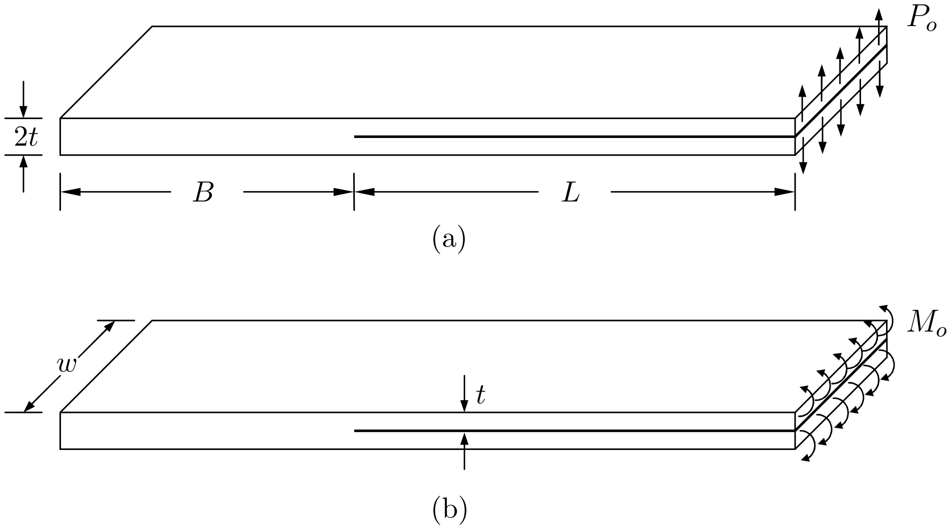

Figure 4.16: Schematic of a double cantilever beam specimen subjected to two types of loading (a) applied end load P_o and (b) applied end moment M_o.

study, three levels of refinement, coarse, intermediate and fine meshes, are adopted as shown in Figure 4.17. Remark that for this particular problem, we have chosen the BEM-region containing the crack front and only the immediate surrounding region while the FEM-region includes the main portion of the crack surface which is treated as two separate subregions.

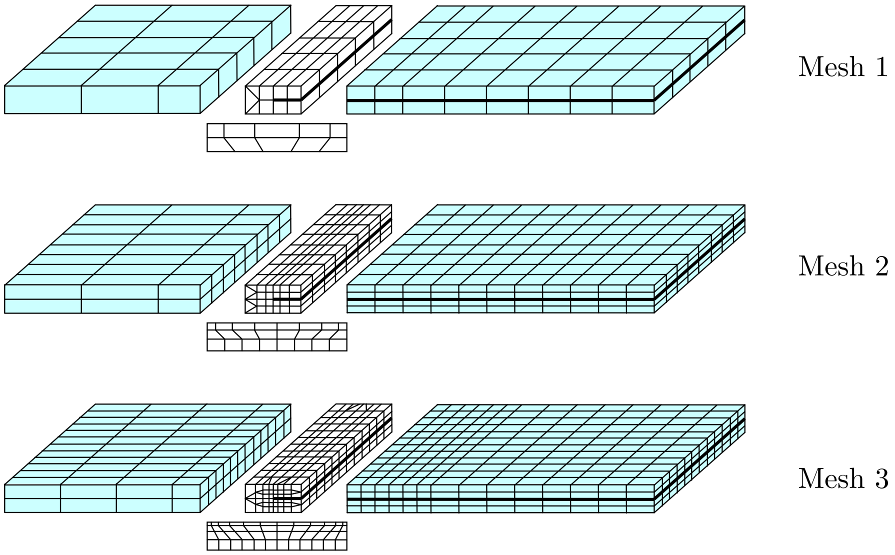

Figure 4.17: Meshes for a double cantilever beam specimen where its dimensions are taken such that $L/t = 24$, $B/t = 16$ and $w/t = 10$. Colored meshes are associated with the FEM-region and unshaded meshes are associated with the BEM-region including crack.

The stress intensity factor are plotted as a function of distance s measured from the center of the crack front in Figure 4.18(a) for applied end load P_o and in Figure 4.18(b) for applied end moment M_o. The agreement between the solutions obtained from three meshes indicates that the results are very accurate and slightly mesh dependent, except possibly in the region in the neighborhood of the surface

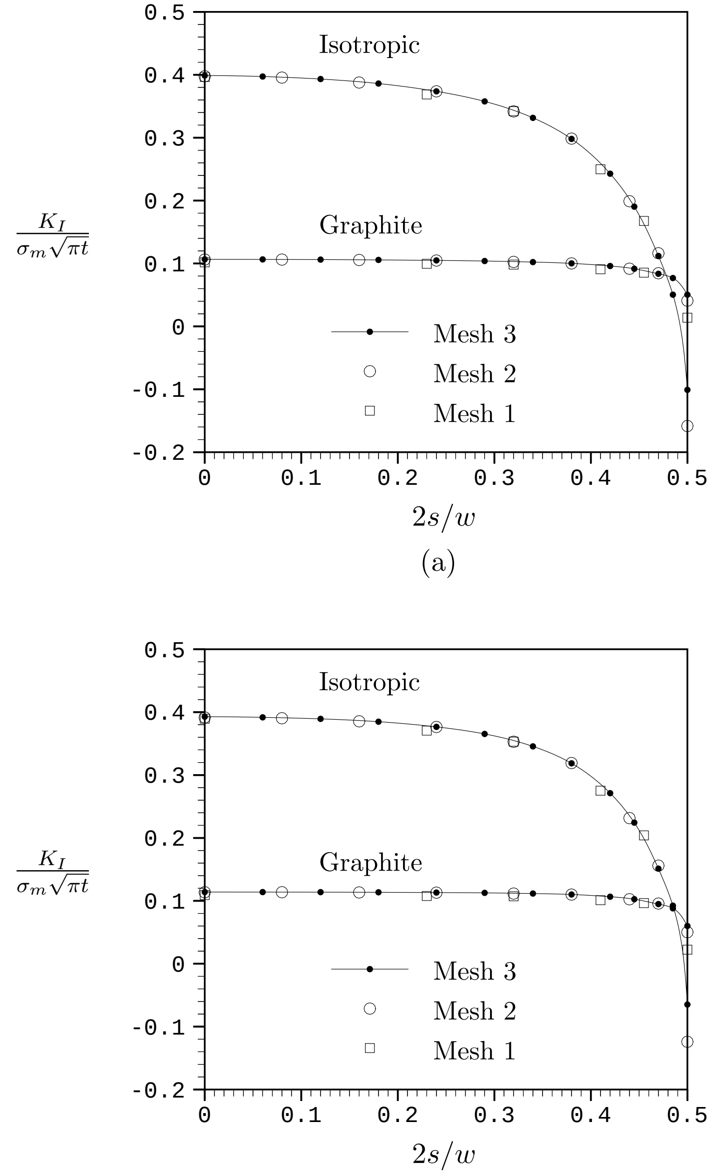

(a)

(b)

Figure 4.18: Normalized mode-I stress intensity factor for a double cantilever beam specimen subjected to (a) end load P_o and (b) end moment M_o. The distance s is measured from the center of the crack front.

breaking points where the stress intensity factor decays rapidly to zero for both materials considered. In addition, with the use of an equivalent maximum bending stress σ_m associated with bending moment in each leg of the specimen at the crack front ($\sigma_m = 6P_oL/wt^2$ for applied end load P_o and $\sigma_m = 6M_o/wt^2$ for applied end moment M_o) to normalize the stress intensity factor, these two types of loading yields no significant difference of results.

4.3.2 Results for nonconforming discretization

In this section, the results for certain examples are presented to illustrate the accuracy and robust of the method in the context of nonconforming discretization. For each problem, meshes for BEM-region and FEM-region are constructed and similar to the conforming case, the size of BEM-region is chosen arbitrary. We illustrate and discuss the quality of numerical solutions obtained by using two types of constraint on the interface. For purpose of further reference, we use the term "weak enforcement constraint" to represent the constraint associated with (4.42)-(4.43) and the term "collocation constraint" to refer to the constraint corresponding to (4.46). In addition, the influence of the choice of the reference interface on numerical solutions is also discussed.

Quarter elliptical cracks at circular hole in thin plate

To illustrate the convergence and accuracy of the method, we consider first the thin plate problem presented in Section 4.3.1 where the numerical solution from SGBEM is available. The geometry of the problem, loading and material behavior are identical to those previously treated. Here, we adopt three meshes with nonconforming meshes on the interface as shown in Figure 4.19 where meshes for BEM-region are identical to those shown in Figure 4.9. Note that the BEM- and FEM-region are taken to be the same as those utilized in the conforming case.

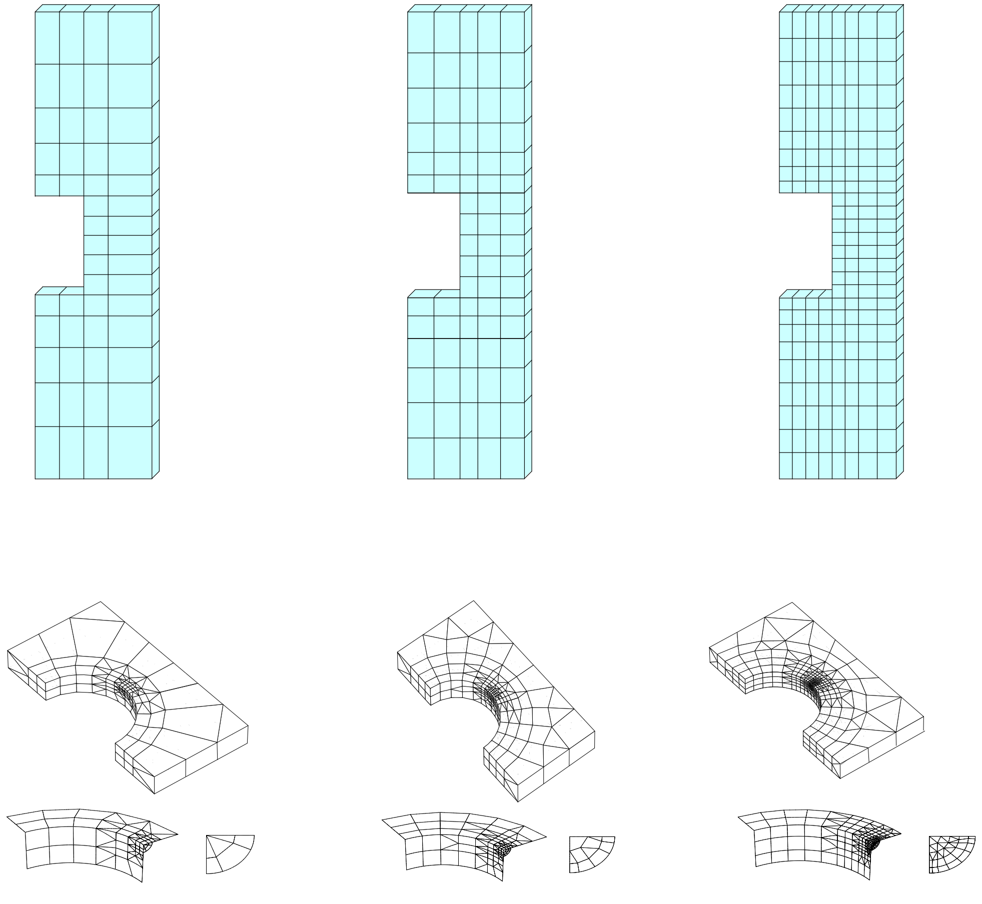

Mesh 1 Mesh 2 Mesh 3

Figure 4.19: Nonconforming meshes for quarter elliptical cracks at a circular hole in a rectangular plate ($R/t = 2$, $a/t = 0.2$, $a/c = 0.8$, $R/W = 0.2$ and $H/W = 2$). Colored meshes are associated with the FEM-region and unshaded meshes are associated with the BEM-region including crack.

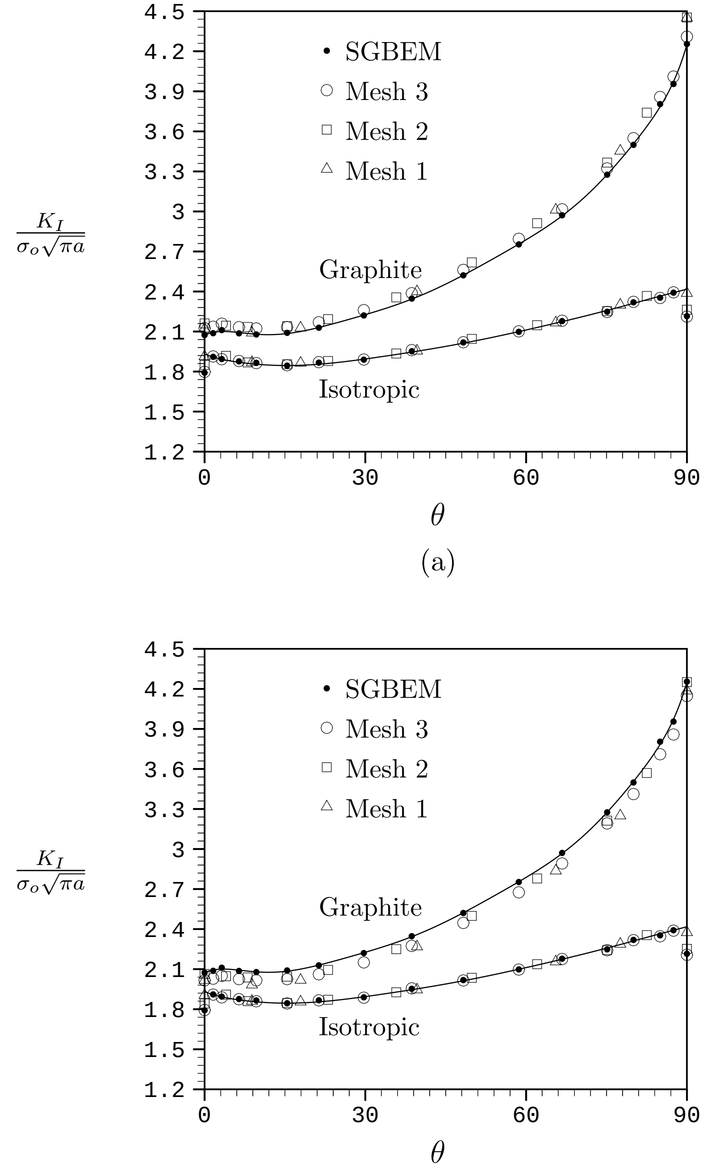

(a)

(b)

Figure 4.20: Normalized mode-I stress intensity factor for quarter-elliptic crack at a circular hole in a rectangular plate subjected to uniform normal traction σ_o at the ends. The collocation constraint is utilized with two choices of the reference interface (a) S_I^B and (b) S_I^F.

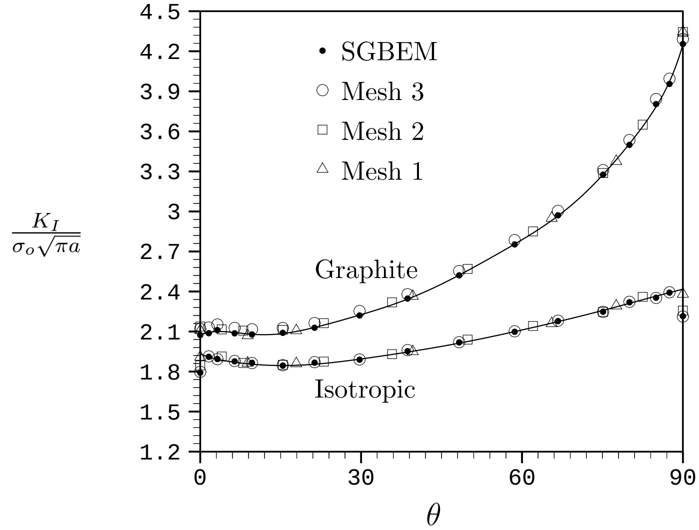

(a)

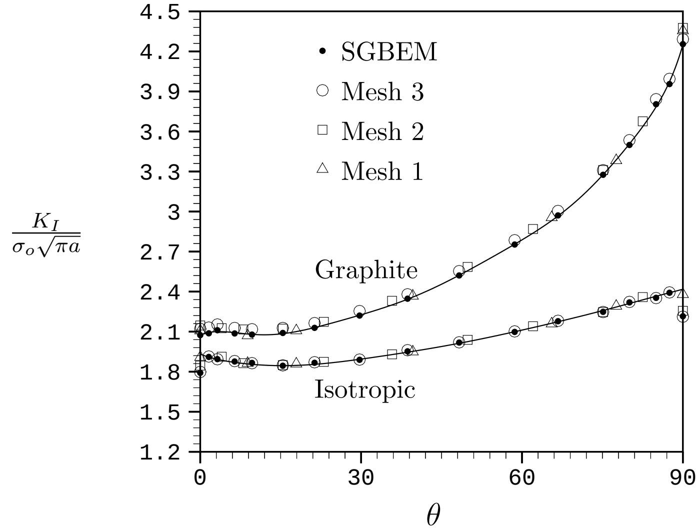

(b)

Figure 4.21: Normalized mode-I stress intensity factor for quarter-elliptic crack at a circular hole in a rectangular plate subjected to uniform normal traction σ_o at the ends. The weak enforcement constraint is utilized with two choices of the reference interface (a) S_I^B and (b) S_I^F.

Numerical solutions for mode-I stress intensity factor obtained is presented in Figure 4.20 for the collocation constraint and in Figure 4.21 for the weak enforcement constraint. For each case, two choices of the reference interface, S_I^B and S_I^F, are considered, and results are plotted and compared with that from the SGBEM (obtained from mesh shown in Figure 3.22). Results for isotropic case indicate the excellent agreement for three meshes and for the one from SGBEM and no dependence on the type of constraint and the choice of the reference interface was observed. In contrast, results for graphite-reinforce composite, which has a very high stiffness in the direction of the axis of elastic symmetry, indicate that more accurate numerical solutions can be obtained via the use of weak enforcement constraint for both choices of the reference interface.

Surface flaw in cantilever beam

Consider again the cantilever beam containing a semi-circular surface flaw as illustrated in the section 4.3.1. For comparison purpose, the dimensions of the problem and loading are taken to be the same as those utilized in the conforming case. As a consequence of the slight influence of material anisotropy on the stress intensity factors indicated previously for this particular problem, only isotropic case with $\upsilon = 0.3$ is treated. Three meshes with nonconforming mesh on the interface are adopted and shown in Figure 4.22. We remark that meshes for BEM-region are identical to those utilized in the conforming case and meshes for FEM-region can be conveniently constructed without the transition region.

The mixed-mode stress intensity factors are then computed and results are plotted as a function of an angular position along the crack front. The results shown in Figure 4.23 and Figure 4.24 are mode-I stress intensity factors associated with the collocation and weak enforcement constraints, respectively; similarly, Figure 4.25 and Figure 4.26 are associated with mode-II stress intensity factor and Figure 4.27

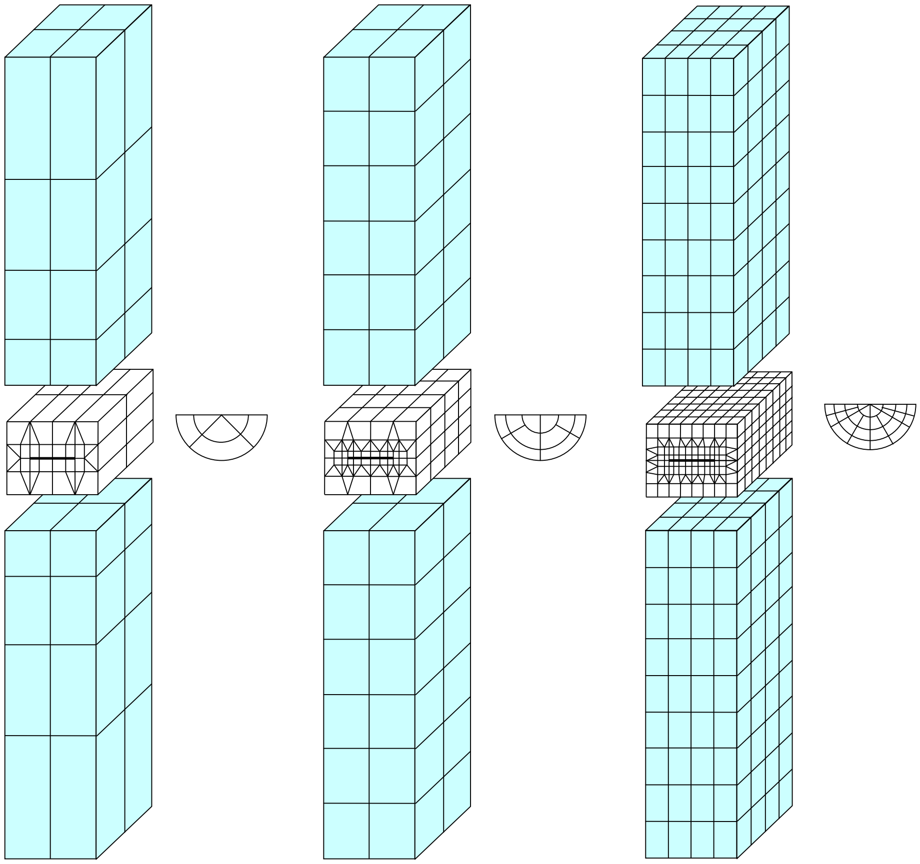

Mesh 1 Mesh 2 Mesh 3

Figure 4.22: Nonconforming meshes for a cantilever beam with a semi-circular surface flaw. Colored meshes are associated with the FEM-region and unshaded meshes are associated with the BEM-region including crack.

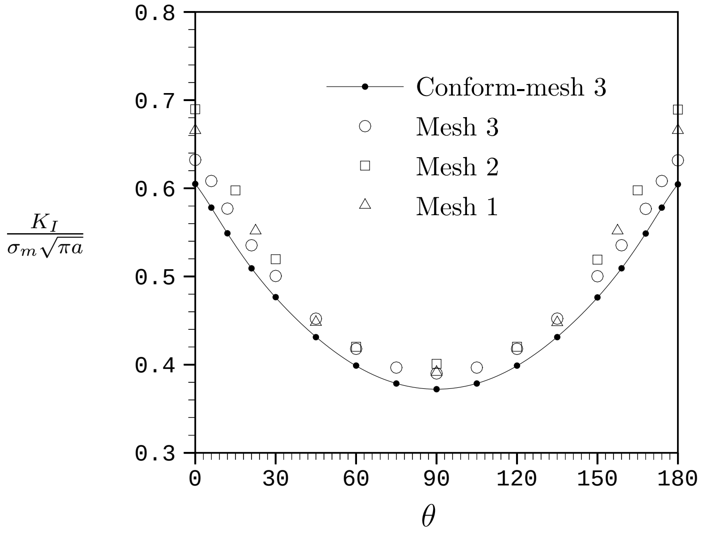

(a)

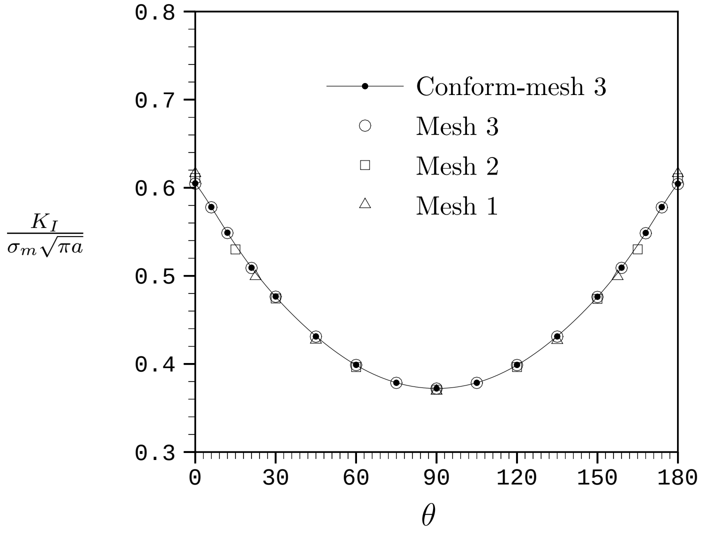

(b)

Figure 4.23: Normalized mode-I stress intensity factor for a cantilever beam containing a semi-circular surface flaw subjected to end load P_o with the use of collocation constraint and two different choices of reference interface (a) S_I^B and (b) S_I^F. Numerical results are for the isotropic material ($\nu = 0.3$) which are plotted along with the result obtained from Mesh 3 in Figure 4.12.

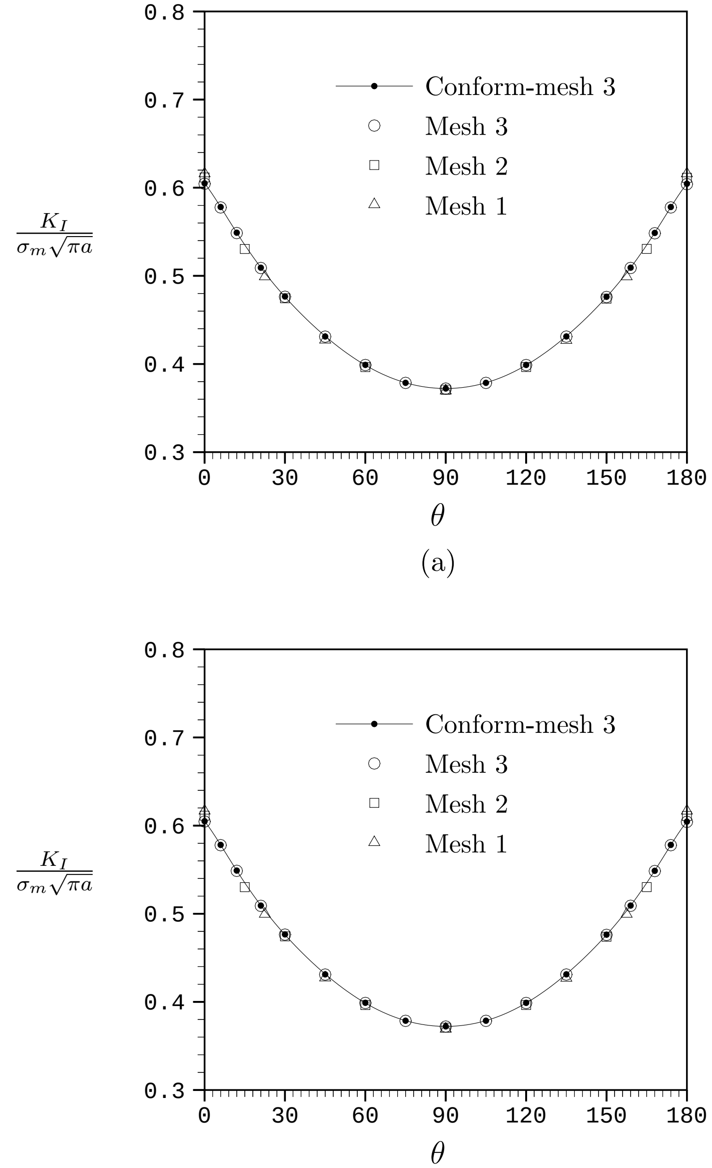

(a)

(b)

Figure 4.24: Normalized mode-I stress intensity factor for a cantilever beam containing a semi-circular surface flaw subjected to end load P_o with the use of weak enforcement constraint and two different choices of reference interface (a) S_I^B and (b) S_I^F. Numerical results are for the isotropic material ($\nu = 0.3$) which are plotted along with the result obtained from Mesh 3 in Figure 4.12.

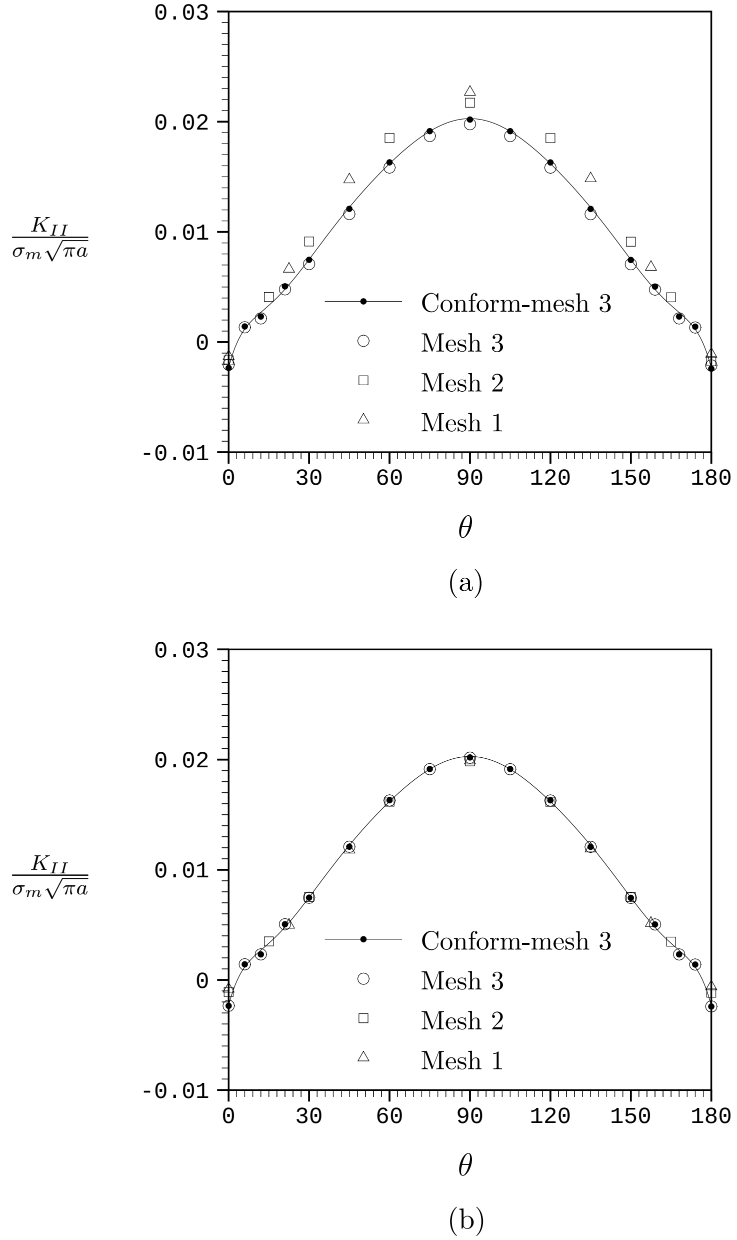

Figure 4.25: Normalized mode-II stress intensity factor for a cantilever beam containing a semi-circular surface flaw subjected to end load P_o with the use of collocation constraint and two different choices of reference interface (a) S_I^B and (b) S_I^F. Numerical results are for the isotropic material ($\nu = 0.3$) which are plotted along with the result obtained from Mesh 3 in Figure 4.12.

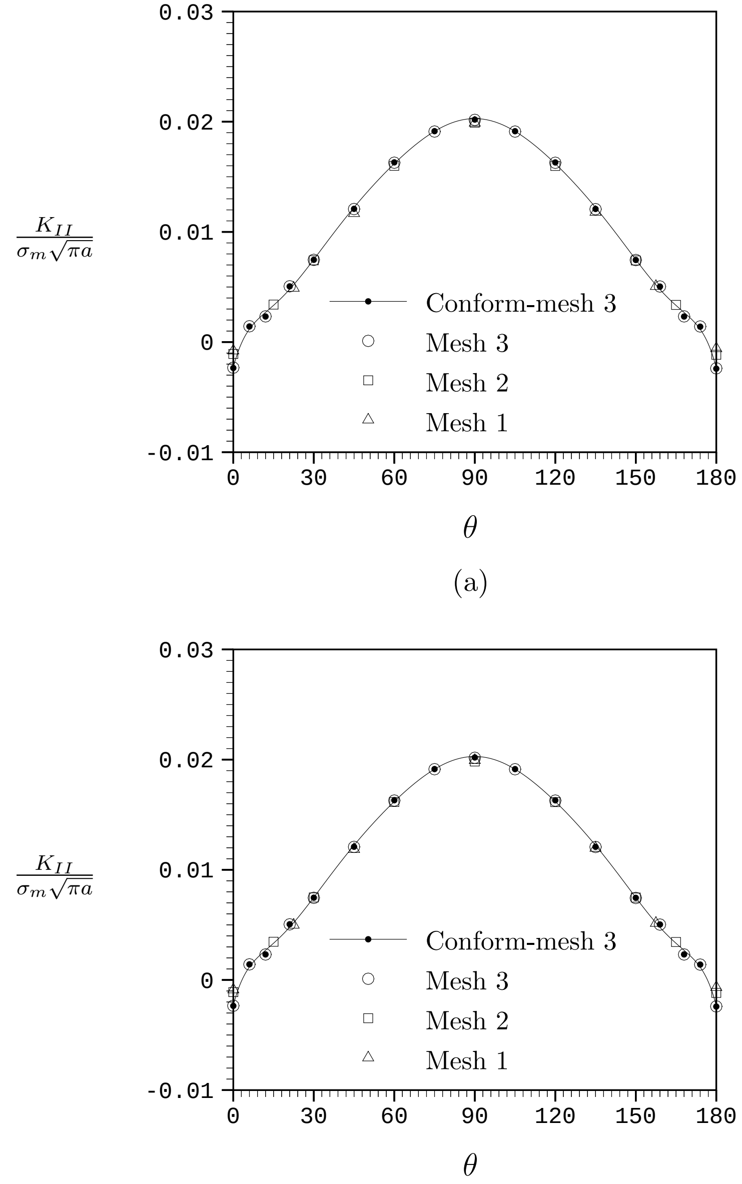

(a)

(b)

Figure 4.26: Normalized mode-II stress intensity factor for a cantilever beam containing a semi-circular surface flaw subjected to end load P_o with the use of weak enforcement constraint and two different choices of reference interface (a) S_I^B and (b) S_I^F. Numerical results are for the isotropic material ($\nu = 0.3$) which are plotted along with the result obtained from Mesh 3 in Figure 4.12.

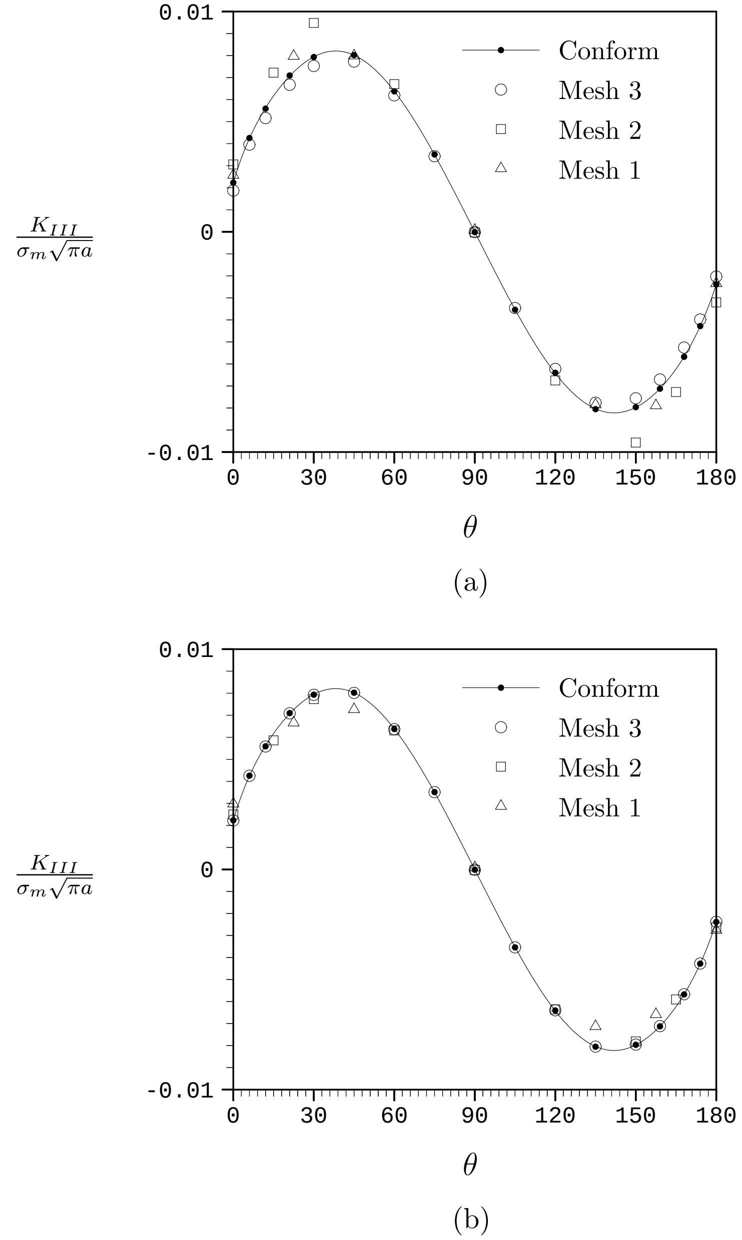

Figure 4.27: Normalized mode-III stress intensity factor for a cantilever beam containing a semi-circular surface flaw subjected to end load P_o with the use of collocation constraint and two different choices of reference interface (a) S_I^B and (b) S_I^F. Numerical results are for the isotropic material ($\nu = 0.3$) which are plotted along with the result obtained from Mesh 3 in Figure 4.12.

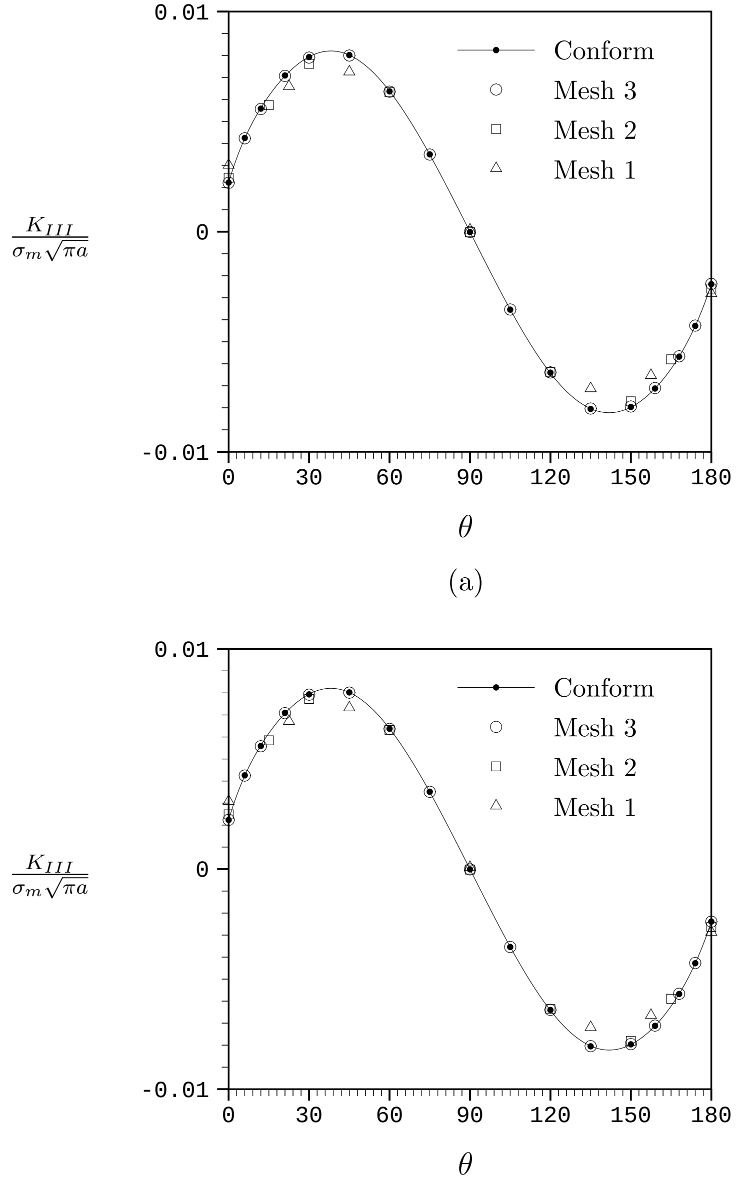

(a)

(b)

Figure 4.28: Normalized mode-III stress intensity factor for a cantilever beam containing a semi-circular surface flaw subjected to end load P_o with the use of weak enforcement constraint and two different choices of reference interface (a) S_I^B and (b) S_I^F. Numerical results are for the isotropic material ($\nu = 0.3$) which are plotted along with the result obtained from Mesh 3 in Figure 4.12.

and Figure 4.28 are associated with mode-III stress intensity factor. The numerical solution for the conforming case which is obtained from the fine mesh is used as a benchmark solution. For this particular problem, it is evident that the result obtained using collocation constraint with $S_I^R = S_I^B$ (note that mesh on S_I^B is finer than that on S_I^F) shows significant difference from the bench mark solution even if the Mesh 3 is utilized; however, if the S_I^F is chosen to be the reference interface, the numerical solution indicates good convergence and slight mesh dependence. The potential source of error is due to the fact that the weak continuity of tractions on the interface is not satisfied (equilibrium is not fulfilled in the weak sense) as discussed in section 4.2. The difference of test functions $\tilde{\boldsymbol{u}}_I^B - \tilde{\boldsymbol{u}}_I^F$ becomes significant when levels of refinement on S_I^B and S_I^B are very different and the finer mesh is chosen to be the reference interface and employed to construct the interpolant for nodal quantities on the coarser interface. Note that the difference of test functions becomes less significant when the coarser interface is chosen to be the reference interface. In contrast to the collocation constraint, the results obtained with the use of weak enforcement constraint show no dependence on the choice of the reference interface and numerical solutions for all three modes indicate excellent convergence.

In addition, the influence of the size of the BEM-region on the numerical solution is examined for this particular example. Three meshes with different BEM-regions are adopted as shown in Figure 4.29. The normalized stress intensity factors obtained from these meshes are plotted in Figure 4.30 for mode-I, in Figure 4.31 for mode-II and in Figure 4.32 for mode-III. Note that all results are compared with those obtained from Mesh 3 shown in Figure 4.12 in the conforming case. It is found that there is no significant difference of numerical results due to the use of different BEM-regions.

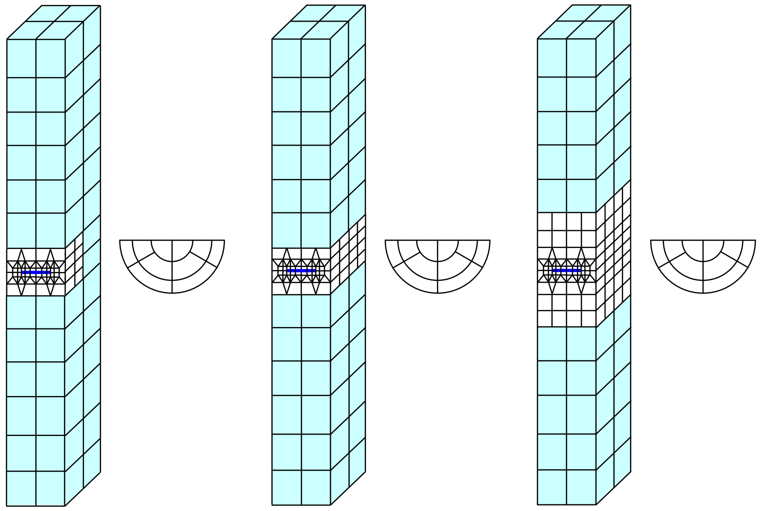

Mesh a Mesh b Mesh c

Figure 4.29: Nonconforming meshes for a cantilever beam containing a semi-circular surface flaw used in examining the effect of the size of BEM-region. Colored meshes are associated with the FEM-region and unshaded meshes are associated with the BEM-region including crack. Mesh b is identical to Mesh 2 in Figure 4.22.

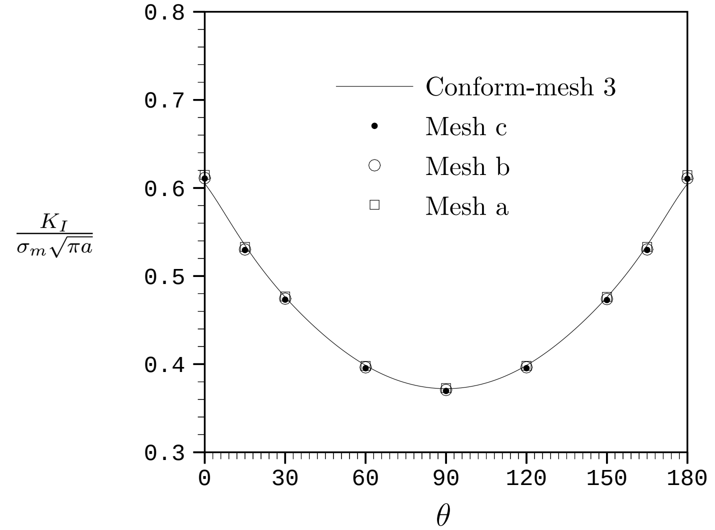

Figure 4.30: Normalized mode-I stress intensity factor for a cantilever beam containing a semi-circular surface flaw subjected to uniform shear traction at the end (with the use of weak enforcement constraint and $S_I^R = S_I^B$). Results are for isotropic material with $\nu = 0.3$.

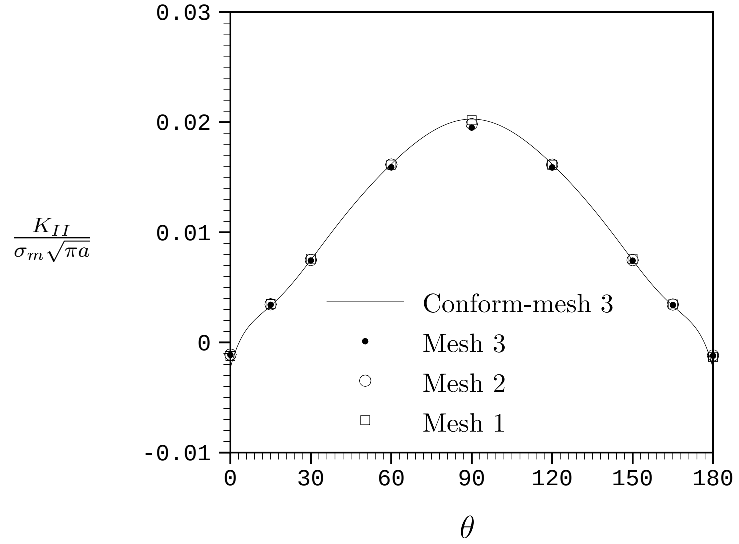

Figure 4.31: Normalized mode-II stress intensity factor for a cantilever beam containing a semi-circular surface flaw subjected to uniform shear traction at the end (with the use of weak enforcement constraint and $S_I^R = S_I^B$). Results are for isotropic material with $\nu = 0.3$.

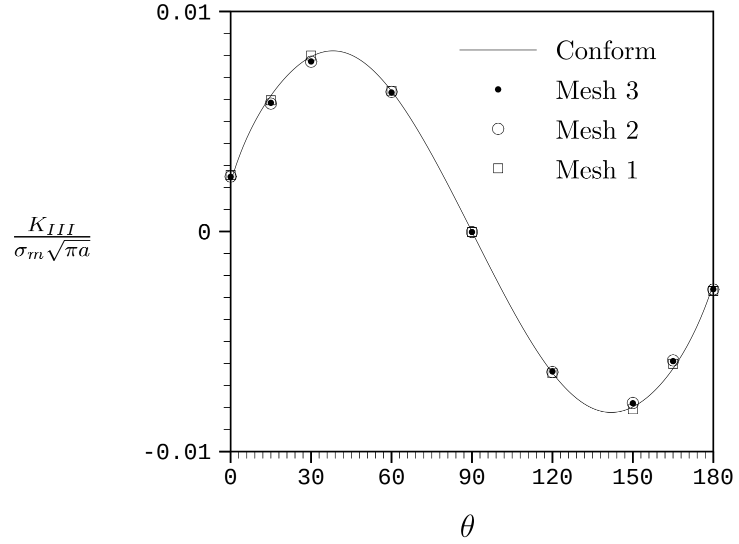

Figure 4.32: Normalized mode-III stress intensity factor for a cantilever beam containing a semi-circular surface flaw subjected to uniform shear traction at the end (with the use of weak enforcement constraint and $S_I^R = S_I^B$). Results are for isotropic material with $\nu = 0.3$.

Surface breaking flaw in pipe

Consider a pipe of length $2L$ with a hollow circular cross section as shown schematically in Figure 4.33(a). The inner radius and the thickness of the pipe are denoted by R and t, respectively. The surface breaking flaw which is a segment of an ellipse with semi-major axis a and semi-minor axis b as shown in Figure 4.33(b). The orientation of the flaw is denoted by an angle ϕ as indicated in Figure 4.33(a). Three types of loading including applied uniform normal traction σ_o at both ends of the pipe, applied linearly varying shear traction at both ends of pipe and applied internal pressure p_o are considered as shown in Figure 4.34. Note that the second type of loading corresponds to an equivalent pure torsion loading with the maximum shear traction τ_o and that the top and bottom surfaces of the pipe is constrained

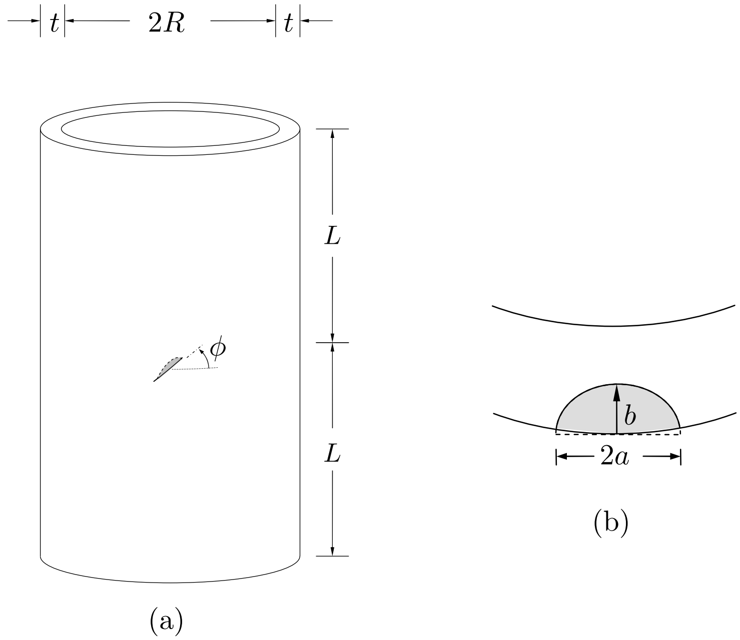

(a)

(b)

Figure 4.33: (a) Schematic of a pipe containing a surface breaking flaw. (b) Geometry of the surface breaking flaw.

in the longitudinal direction. In the analysis, isotropic material with $\nu = 0.3$, zinc and a graphite-reinforced composite are considered and dimensions of the problem are such that $L/(R+t) = 2$, $(R+t)/a = 10$, $a/t = 0.5$, $b/a = 0.8$ and $\phi = 45^o$. Three levels of refinement are adopted for both BEM- and FEM-region as depicted in Figure 4.35.

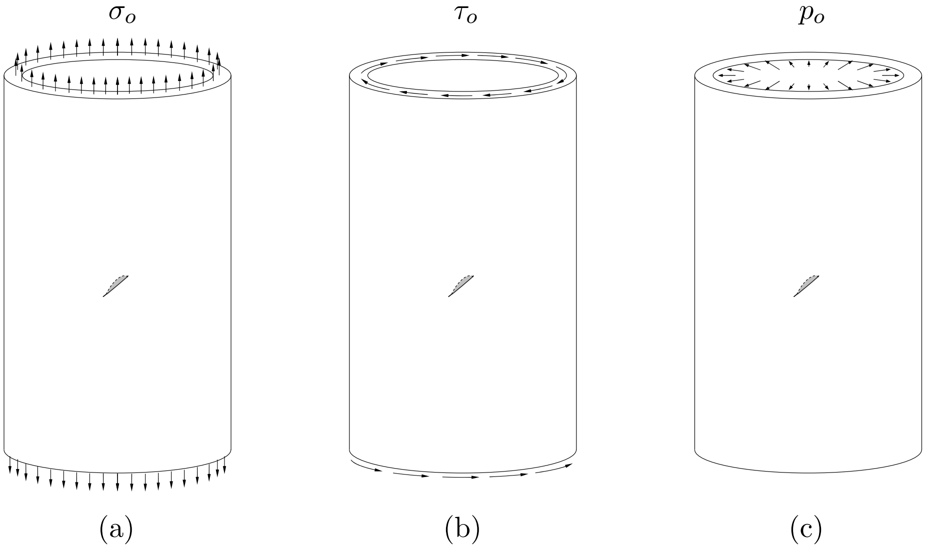

Figure 4.34: Schematic of a pipe subjected to three types of loading (a) uniform normal traction σ_o applied at the ends, (b) linearly varying shear traction corresponding to pure torsion loading applied at the ends and (c) uniform internal pressure p_o with constraint in the longitudinal direction at top and bottom surface.

Three types of loading treated give rise to a fully mixed-mode problem as a consequence of the orientation of the flaw. As suggested by two previous examples, using weak enforcement constraint on the interface is preferable and it provides accurate results with no dependence on the choice of the reference interface. Therefore, the computed stress intensity factors along the crack front are presented only for the case that the weak enforcement constraint is employed and the interface on

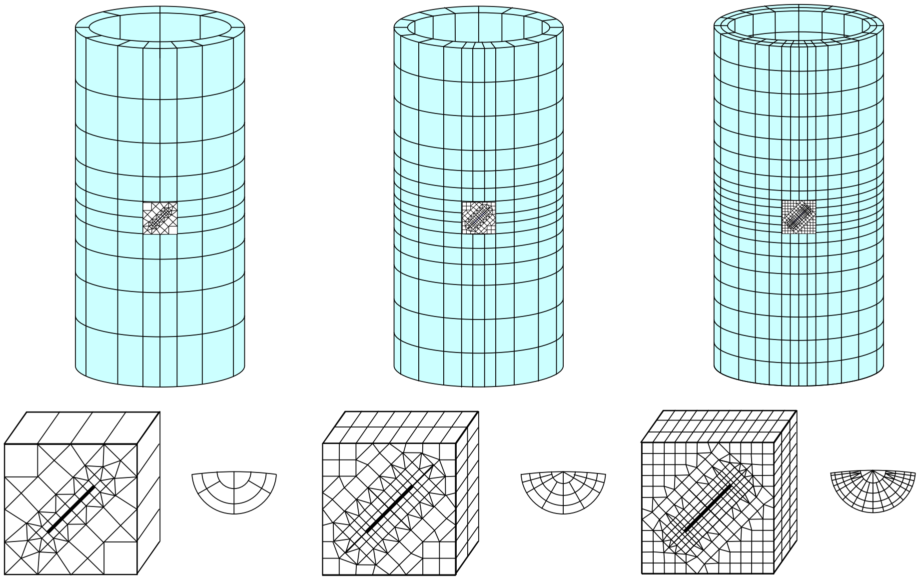

Mesh 1 Mesh 2 Mesh 3

Figure 4.35: Nonconforming meshes for a pipe containing a surface breaking flaw. Colored meshes are associated with the FEM-region and unshaded meshes are associated with the BEM-region including crack.

the FEM-region is treated as the reference interface. The stress intensity factors for each loading condition are obtained for three meshes and results are presented for three materials. Mode-I, mode-II and mode-III stress intensity factors are plotted in Figure (4.36), (4.37), (4.38) for uniform normal traction loading, in Figure (4.39), (4.39), (4.39) for linearly varying shear traction loading and in Figure (4.42), (4.42), (4.42) for internal pressure loading. The excellent agreement of numerical solutions obtained from three meshes has been observed for all cases. Additionally, accurate results for mixed-mode stress intensity factor can be achieved with a relatively coarse mesh for both isotropic and transversely isotropic materials.

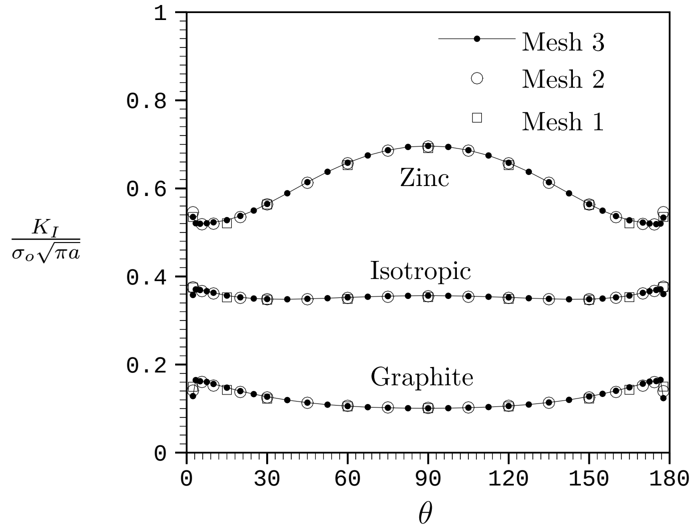

Figure 4.36: Normalized mode-I stress intensity factor for a surface breaking flaw in a pipe subjected to uniform normal traction σ_o at the ends.

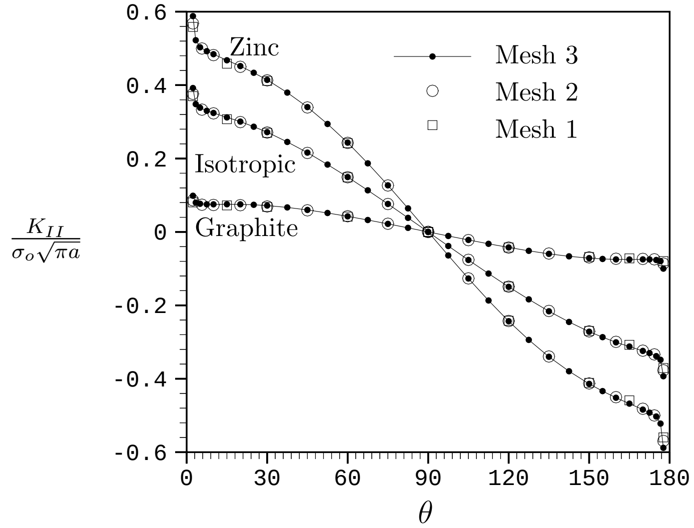

Figure 4.37: Normalized mode-II stress intensity factor for a surface breaking flaw in a pipe subjected to uniform normal traction σ_o at the ends.

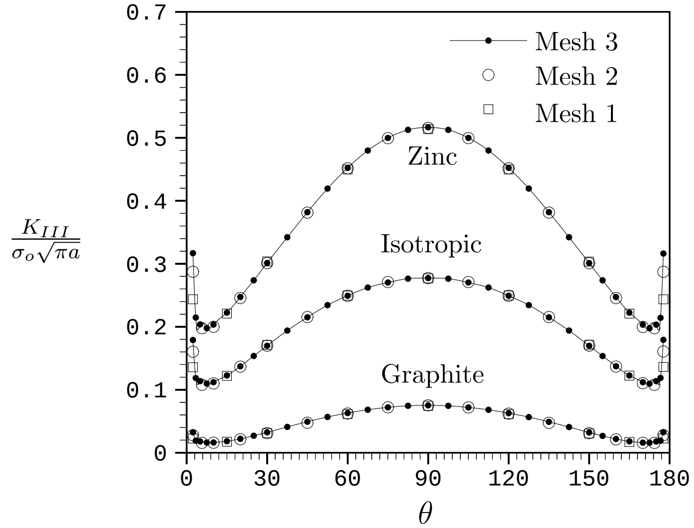

Figure 4.38: Normalized mode-III stress intensity factor for a surface breaking flaw in a pipe subjected to uniform normal traction σ_o at the ends.

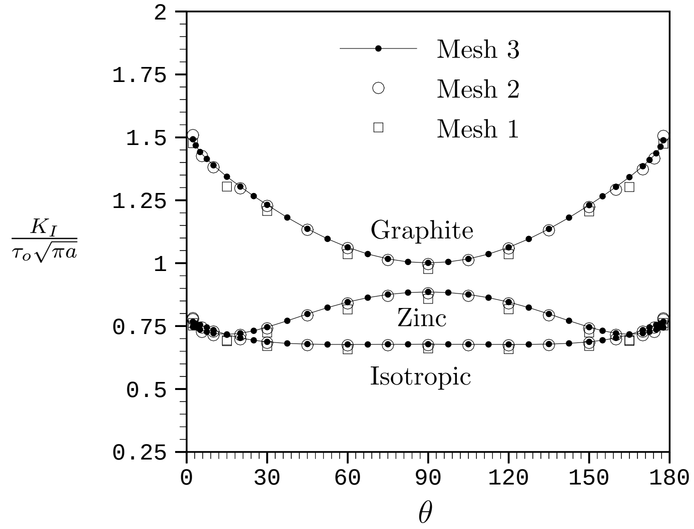

Figure 4.39: Normalized mode-I stress intensity factor for a surface breaking flaw in a pipe subjected to linearly varying shear traction where τ_o denote the maximum shear traction.

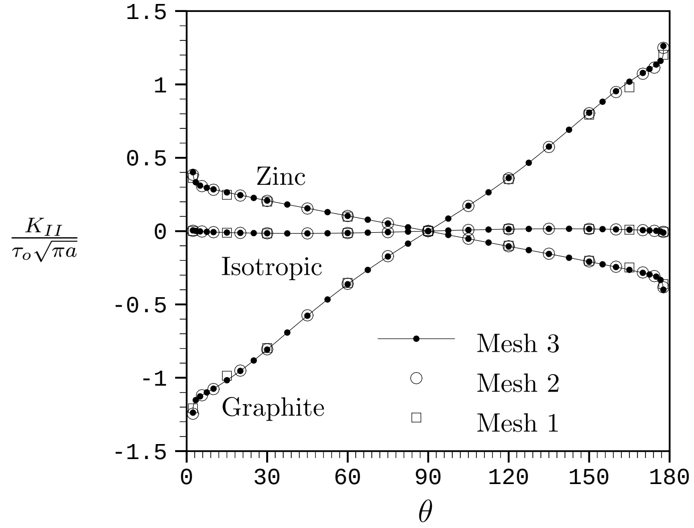

Figure 4.40: Normalized mode-II stress intensity factor for a surface breaking flaw in a pipe subjected to linearly varying shear traction where τ_o denote the maximum shear traction.

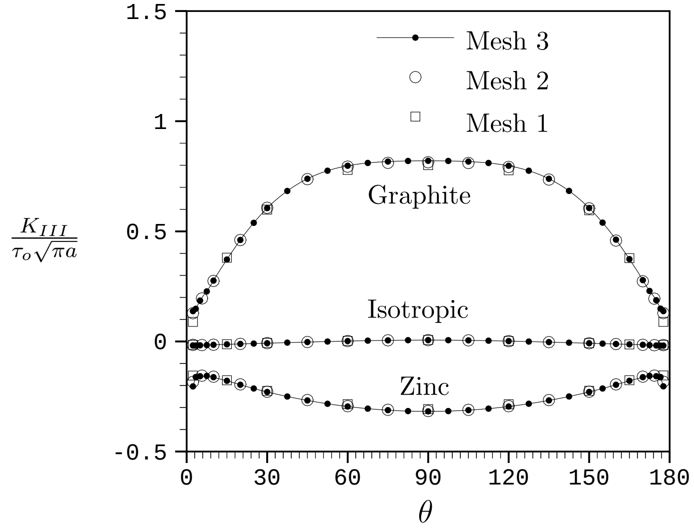

Figure 4.41: Normalized mode-III stress intensity factor for a surface breaking flaw in a pipe subjected to linearly varying shear traction where τ_o denote the maximum shear traction.

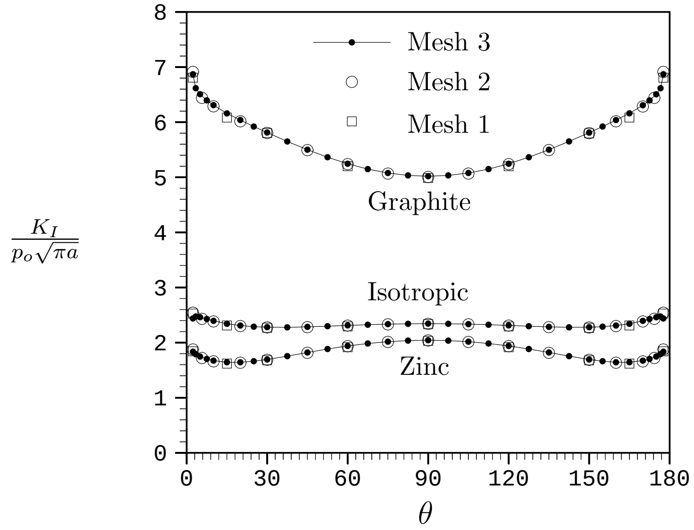

Figure 4.42: Normalized mode-I stress intensity factor for a surface breaking flaw in a pipe subjected to internal pressure p_o.

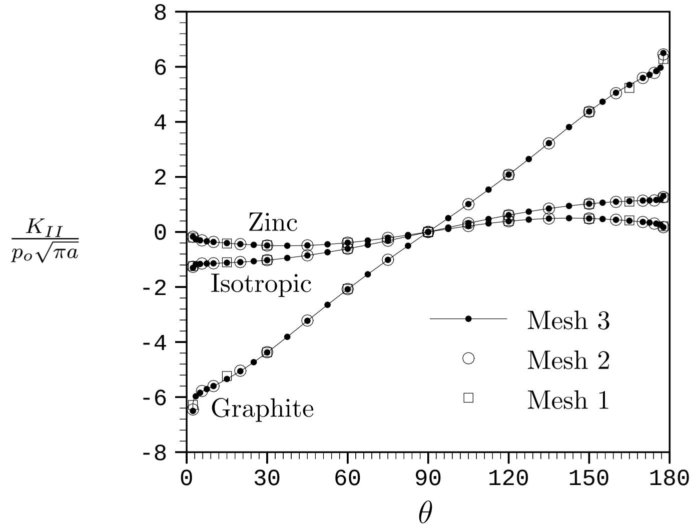

Figure 4.43: Normalized mode-II stress intensity factor for a surface breaking flaw in a pipe subjected to internal pressure p_o.

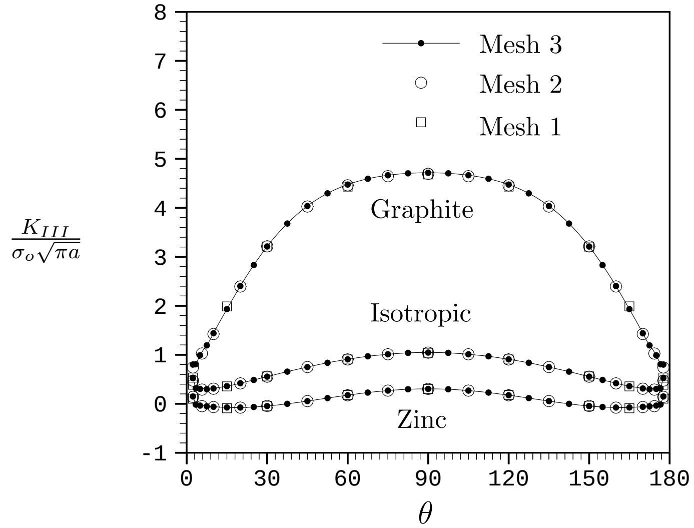

Figure 4.44: Normalized mode-III stress intensity factor for a surface breaking flaw in a pipe subjected to internal pressure p_o.

Rectangular plate with through crack

As a final example, consider a rectangular plate containing a through crack of length $2a$ at the center of the plate. The orientation of the crack is denoted by an angle ϕ and other dimensions are shown in Figure 4.45. The plate is made from an isotropic material with poisson's ration $\nu = 0.3$ and is subjected to a uniform normal traction σ_o at both ends. For this particular problem, it is of interest to examine the effect of the crack orientation on the mixed-mode stress intensity factors and the advantage of the nonconforming discretization in constructing series of meshes for various angle ϕ serves this purpose. Specifically, the BEM-region is chosen to be a circular disk with a center at the center of the crack and two particular meshes

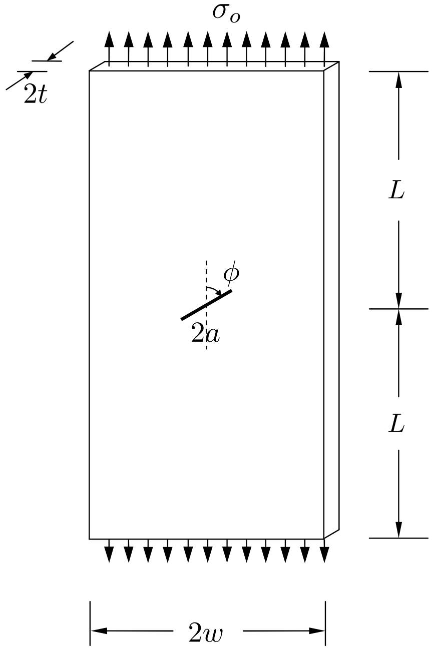

Figure 4.45: Schematic of a rectangular plate containing a through crack subjected to uniform normal traction at the ends.

(coarse and fine meshes) are constructed for $\phi = 90$ as shown in Figure 4.46. Meshes for other angles can be readily obtained via the rotation of those for $\phi = 90$.

The normalized stress intensity factors are plotted as a function of normalized distance $s/2t$ where s is measured from center of the crack front. Four crack orientations associated with $\phi = 30^o, 45^o, 60^o$ and 90^o are treated and results are

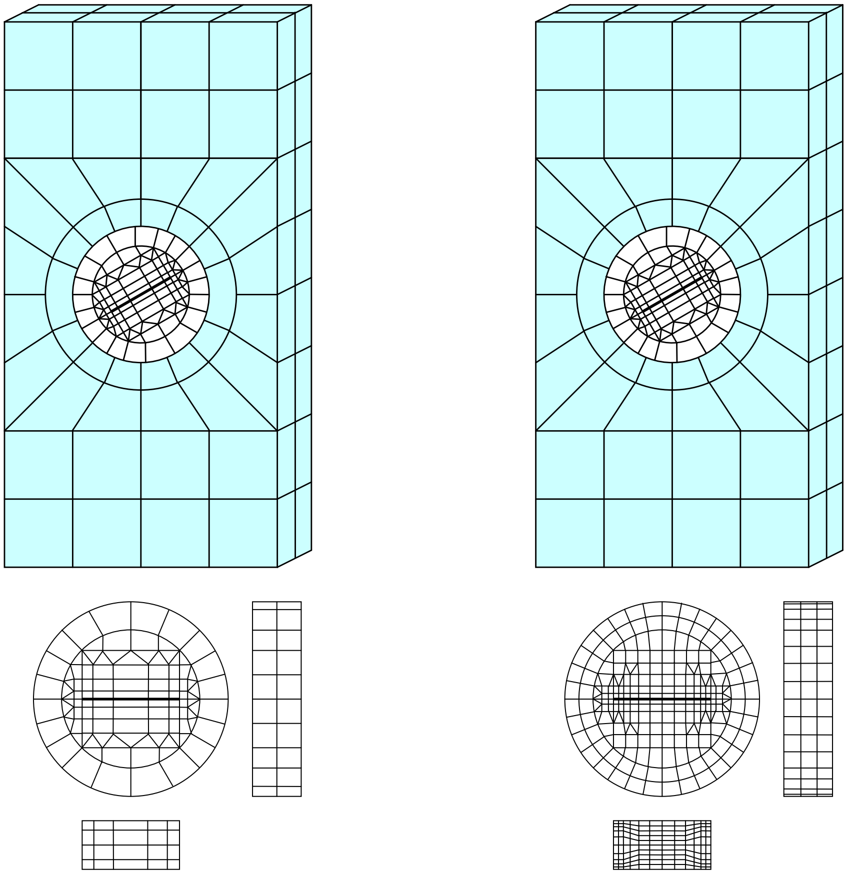

Mesh 1

Mesh 2

Figure 4.46: Nonconforming meshes for a rectangular plate containing a through crack with dimensions taken to be such that $L/w = 2$, $w/t = 8$ and $w/a = 4$. Colored meshes are associated with the FEM-region and unshaded meshes are associated with the BEM-region including crack.

presented in Figure 4.47 for mode-I, in Figure 4.48 for mode-II and in Figure 4.49 for mode-III. A good agreement between the numerical solutions obtained for two meshes is observed everywhere along the crack front except a very thin layer in the vicinity of surface breaking points. Remark for this particular problem that at vertices where the crack front meet the boundary, the order of singularity is less than square-root for mode-I while it is higher than square-root for mode II and III. Based on obtained results, it is found that mode-I stress intensity factor increases as the angle ϕ increases and it reaches maximum at $\phi = 90^o$. In addition, mode-II stress intensity factor at $\phi = 45^o$ is larger than those at $\phi = 30^o$ and $\phi = 60^o$ which are comparable, while no significant difference of the stress intensity factor was observed at $\phi = 30^o$, 45^o and 60^o.

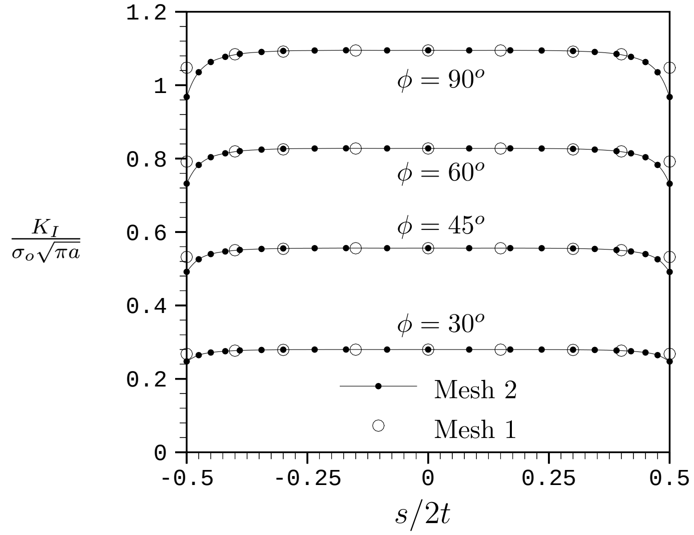

Figure 4.47: Normalized mode-I stress intensity factor for a through crack in a rectangular plate subjected to uniform normal traction σ_o at the ends. The distance s is measured from the center of the crack front.

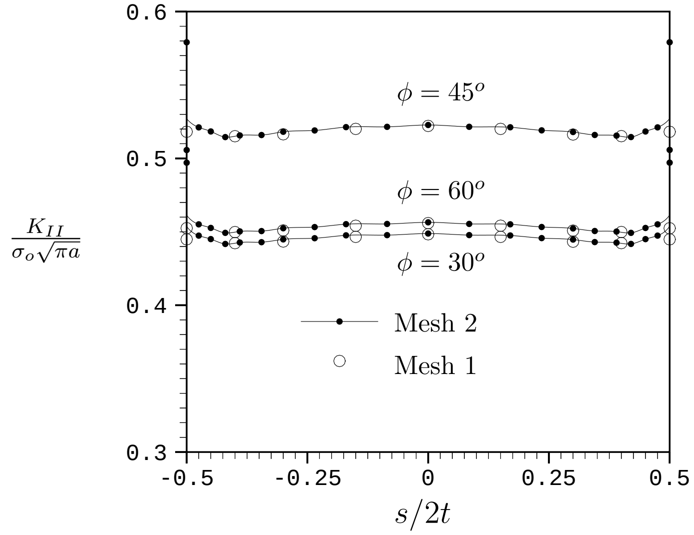

Figure 4.48: Normalized mode-II stress intensity factor for a through crack in a rectangular plate subjected to uniform normal traction σ_o at the ends. The distance s is measured from the center of the crack front.

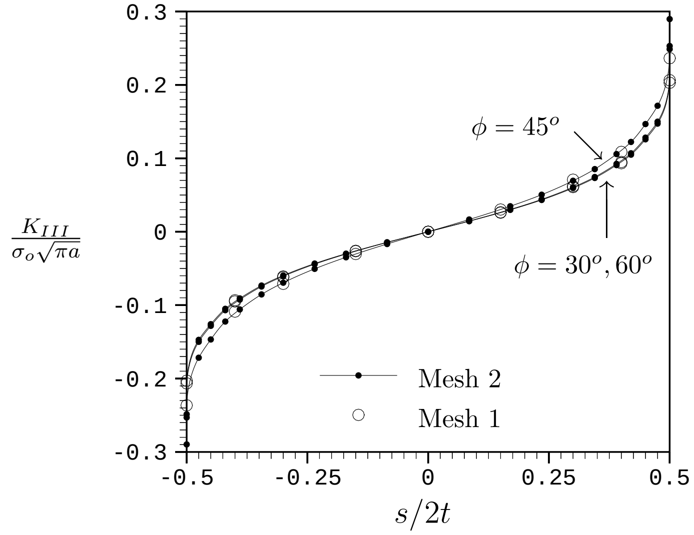

Figure 4.49: Normalized mode-III stress intensity factor for a through crack in a rectangular plate subjected to uniform normal traction σ_o at the ends. The distance s is measured from the center of the crack front.

4.4 Coupling of SGBEM with ABAQUS

The coupling of the SGBEM and the FEM for analysis of three dimensional crack problems has been successfully implemented. However, the stand-alone FEM code developed here to demonstrate the coupling has limited capabilities in comparison with available commercial FEM codes. For this reason, we now pursue a coupling of the SGBEM with the commercial finite element code ABAQUS.

What is sought is the ability to exploit the vast features and modeling capability of ABAQUS to treat complex structures while retaining the SGBEM to model a local region surrounding the crack. The similarities of the SGBEM and the FEM (i.e. both are symmetric formulations utilizing a Galerkin approximation scheme, standard C^o elements can be employed, etc.) renders the coupling of the two methods quite natural. The treatment for both conforming and nonconforming discretizations can be performed by employing certain features available in ABAQUS, namely a user-defined element capability and a linear constraint command. Here, we briefly summarize the essential ingredients of the implementation.

4.4.1 Treatment of Ω^B and Ω^F

The body is first partitioned into two subregions, the BEM-region Ω^B which contains the crack and the FEM-region Ω^F. The modeling of the FEM-region (which is envisioned to be the main portion of the structure) by a standard finite element procedure can be readily treated by exploiting the vast features in ABAQUS (e.g. mesh generation, element and material specification and treatment of general loading).

The treatment of the subregion Ω^B by the SGBEM requires special attention. The boundary of the subregion, including the crack surface, is discretized. The coefficient matrix (containing $\boldsymbol{A}_{PQ}$,$\boldsymbol{B}_{PQ}$,$\boldsymbol{C}_{PQ}$ and $\boldsymbol{D}_{II}$ with ${\scriptstyle PQ} \in \{{\scriptstyle U}, {\scriptstyle T_o}, {\scriptstyle C}, {\scriptstyle I}\}$) and the known column vector (containing $\boldsymbol{R}_1$, $\boldsymbol{R}_2$, $\boldsymbol{R}_3$, $\boldsymbol{R}_4$ and $\boldsymbol{R}_5$) associated with this discretization are then computed by means of the SGBEM stand-alone code. The coefficient matrix can be viewed as a stiffness matrix for a 'super element' containing all the degrees of freedom from the BEM-region, and the known column vectors correspond to the element load vector. These coefficient matrix and load vector can then be assembled with element stiffness matrices contributed from the FEM-region in the same manner as that utilized in a standard finite element method. To import this essential element information into ABAQUS, we utilize a user-defined element subroutine (UEL) which allows specification of each entries of an element coefficient matrix and an element load vector and parameters facilitating the assembling procedure. While this feature allow the importation of necessary information to be achieved, it possesses a limitation that the number of degrees of freedom in each user-defined element must not exceed 999. To overcome this difficulty, the BEM-region is treated as a collection of fictitious elements where their number of degrees of freedom is between 1 and 999. As a consequence, the coefficient matrix and known vector must be partitioned into symmetric sub-matrices and sub-vectors corresponding to these fictitious element. The element coefficient matrix and the element known vector for each fictitious element are then imported into ABAQUS via the user-defined element subroutine. We remark that each nodal point on the interface of BEM-region contains six degrees of freedom, three degrees of freedom for displacement and three degrees of freedom for traction. These nodes need to be treated specially as double-nodes where they consist of two geometrically identical nodes with two different numberings, one for displacement degrees of freedom and one for traction degrees of freedom.

4.4.2 Treatment of interface constraints

To combine the coefficient matrix and the known vector contributed from the BEM-region and FEM-region in the assembling procedure, the information on the interface of the two regions is essential. Specifically, a relationship between degrees of freedom on the interface, known as interface constraints, must be enforced properly to obtain a unique numerical solution to the boundary value problem. In the implementation, two types of constraints associated with (4.29) and (4.46) are treated in the context of conforming and nonconforming discretization. Note, in particular, that for conforming discretization these two constraints are identical.

First, we treat the interface constraints in the context of conforming discretization. In this case, the coefficient matrix and the load vector associated with each fictitious element on the BEM-region can be readily assembled with those corresponding to elements on the FEM-region by employing proper nodal numbering. Specifically, the numbering of nodal points on the interface of the BEM-region is chosen to be identical to that of nodal points (associated with the same degrees of freedom) on the interface of FEM-region. The remaining nodes on the BEM-region must be numbered different from that of nodes on the FEM-region, especially for the numbering used for traction degrees of freedom of double-nodes. In this sense, the assembling procedure follows naturally that for a standard finite elements.

In the context of nonconforming discretization, the interface constraints are treated by employing certain features in ABAQUS which allows the specification of linear constraints. In particular, the reference interface S_I^R is chosen such that $S_I^R \in \{S_I^B, S_I^F\}$; and, as a consequence, constraints follow (4.42) and (4.43) for weak enforcement of continuity and (4.46) for collocation. To utilize the weak enforcement of continuity to perform the coupling, one of the constraint matrices ($\bar{\mathbf{\Lambda}}_{FB}$ or $\bar{\mathbf{\Lambda}}_{BF}$) depending on the choice of the reference interface is first computed and then imported into ABAQUS via the linear constraint command called $EQUATION$. This command allows the specification of nodal points and degrees of freedom involved in the constraint and entries of the coefficient matrix. We remark that the numbering of nodal points on the BEM-region must be different from that of nodal points on the FEM-region. If the collocation constraints is utilized, the importation of constraint data into ABAQUS can be achieved in two different ways. The first approach, the $EQUATION$ command can be readily applied as discussed above; however, the constraints matrix $\bar{\mathbf{\Lambda}}_{BF}$ or $\bar{\mathbf{\Lambda}}_{FB}$ is required to be determined in a priori by the user similar to the case of weak enforcement of continuity. The second option is to utilize the multi-point constraint command (MPC) which requires no specification of the constraint matrix and suits ideally this type of constraint. In detail, this command allows the specification of an element (defined by a collection of nodal points) on the reference interface S_I^R ($\in \{S_I^B, S_I^F\}$) which is used to define the interpolant and a nodal point on the other interface where its projection point lies on this specified element. A procedure to carry out the corresponding constraint matrix is achieved automatically via the use of MPC command.

4.4.3 Determination of stress intensity factors

The primary quantities of interest are the stress intensity factors along the crack front. This quantities can be obtained directly in terms of nodal data associated with degrees of freedom along the crack front (see Chapter 3). After the analysis is complete, this set of data can be readily extracted from the ABAQUS output file by employing available output features in ABAQUS. The post processing of this data to obtain the stress intensity factors requires the information of crack tip elements along the crack front and material properties, and this can be readily achieved by means of the developed stand alone code.

4.4.4 SGBEM-ABAQUS results

In this section, we present two examples, a circumferential crack and an embedded crack contained in a cylinder and a cantilever beam with a surface flaw, to illustrate the capability of SGBEM-ABAQUS coupling. The conforming discretization is considered in the first problem and the nonconforming discretization with two types of constraint, the collocation and the weak enforcement constraints, is treated in the second problem. The results are obtained and then compared with those obtained from the developed stand-alone code. We remark that the coarser interface is chosen to be the reference interface.

Embedded and circumferential cracks in a cylinder

Consider again embedded and circumferential cracks in a cylinder as presented in section 4.3.1. The uniform normal traction σ_o is applied at both ends of the cylinder and the geometry is taken to be the same as previously treated. Mesh used in the analysis for each problem is shown in Figure 4.50. The normalized mode-I stress intensity factors obtained from the SGBEM-ABAQUS coupling and from the developed stand alone code are listed in table 4.5. The obtained results indicate the good agreement between the developed code and SGBEM-ABAQUS coupling; in fact, the results are almost identical.

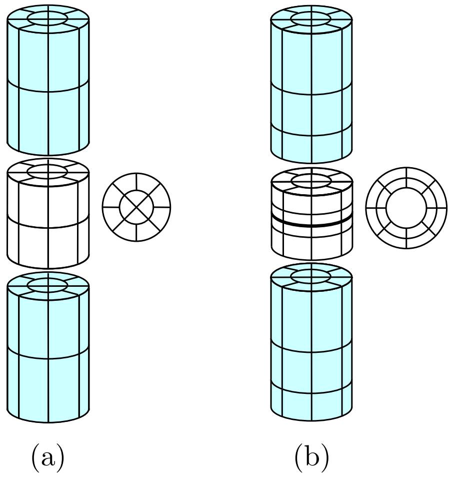

Figure 4.50: (a) Conforming mesh for an embedded crack and (b) Conforming mesh for a circumferential crack in a cylinder adopted for the SGBEM-ABAQUS coupling.

	(a) K_I/K_1^{ref}		(b) K_I/K_2^{ref}	
	Developed code	ABAQUS	Developed code	ABAQUS
isotropic	0.9975	0.9973	0.9957	0.9957
zinc	0.9945	0.9946	0.9965	0.9966

Table 4.5: Normalized stress intensity factors for (a) an embedded crack and (b) a circumferential crack in a cylinder subjected to uniform normal traction σ_o at the ends. The results are for isotropic material with $\nu = 0.3$ and zinc. The reference stress intensity factors are obtained from SGBEM with Mesh 4 shown in Figure 4.4 and in Figure 4.7 ($K_1^{ref} = 0.6867\sqrt{\pi a}\ \sigma_o$ and $K_2^{ref} = 1.9445\sqrt{\pi a}\ \sigma_o$ for isotropic material, and $K_1^{ref} = 0.6978\sqrt{\pi a}\ \sigma_o$ and $K_2^{ref} = 1.9753\sqrt{\pi a}\ \sigma_o$ for zinc).

Surface flaw in cantilever beam

As a final example, we revisit the cantilever beam containing a surface flaw and subjected to end load P_o. Here, we illustrate the coupling of ABAQUS with the SGBEM in the context of nonconforming discretization. Both types of constraint, the collocation and the weak enforcement, are treated and the interface with a coarser mesh is chosen to be the reference interface. In this study, the mesh 1 indicated in Figure 4.51 (identical to Mesh 1 shown in 4.22) is utilized to obtain the stress in tensity factors along the crack. The stress intensity factors are plotted in Figure 4.52, Figure 4.53 and Figure 4.54 for both types of constraint along with those obtained from the developed stand alone code. It can be concluded from obtained results that there is no significant difference between the solutions from ABAQUS-SGBEM coupling and the developed code for both cases which demonstrates the capability of performing coupling of SGBEM and ABAQUS with accurate results.

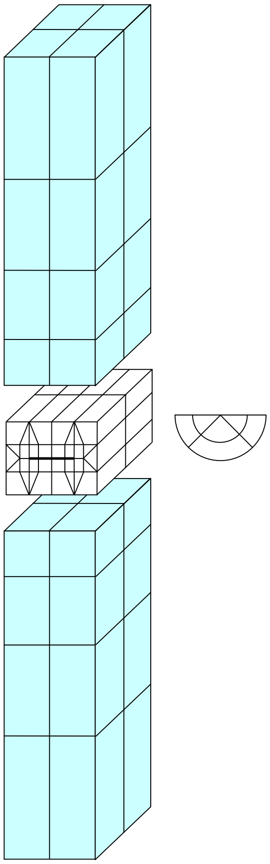

Figure 4.51: The conforming mesh for a cantilever beam containing a semi-circular surface flaw adopted for SGBEM-ABAQUS coupling. Note that this mesh is identical to Mesh 1 shown in Figure 4.22.

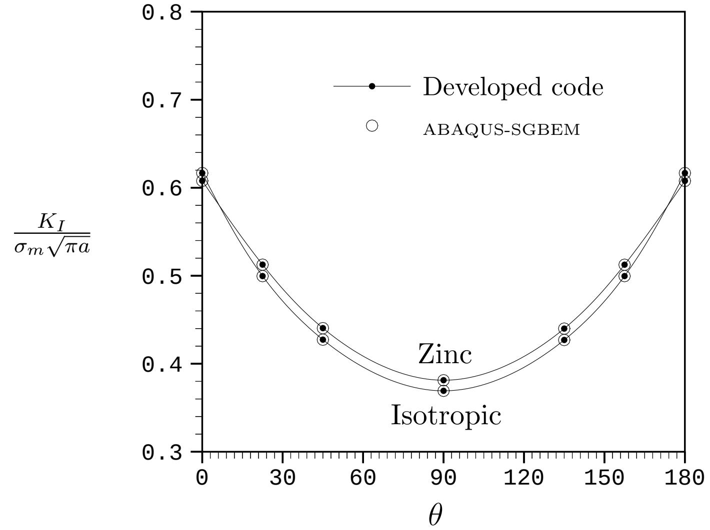

(a)

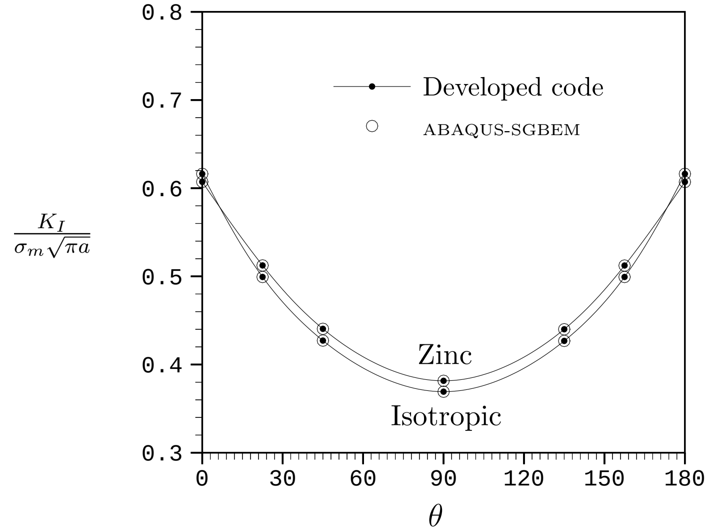

(b)

Figure 4.52: Normalized mode-I stress intensity factor for a cantilever beam containing a surface flaw subjected to uniform shear traction at the ends: (a) use collocation constraint and (b) use weak enforcement constraint. Note that $S_I^R = S_I^F$ and $\sigma_m = 6P_oL/bh^2$.

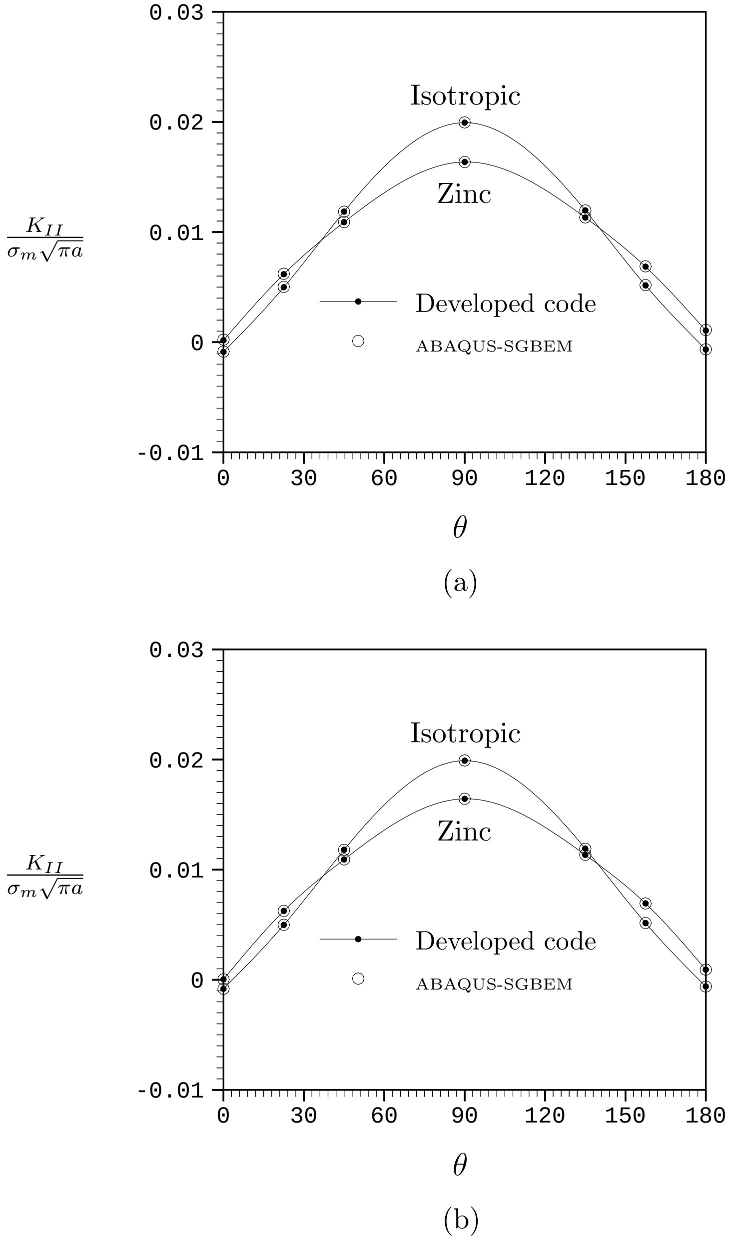

Figure 4.53: Normalized mode-II stress intensity factor for a cantilever beam containing a surface flaw subjected to uniform shear traction at the ends: (a) use collocation constraint and (b) use weak enforcement constraint. Note that $S_I^R = S_I^F$ and $\sigma_m = 6P_oL/bh^2$.

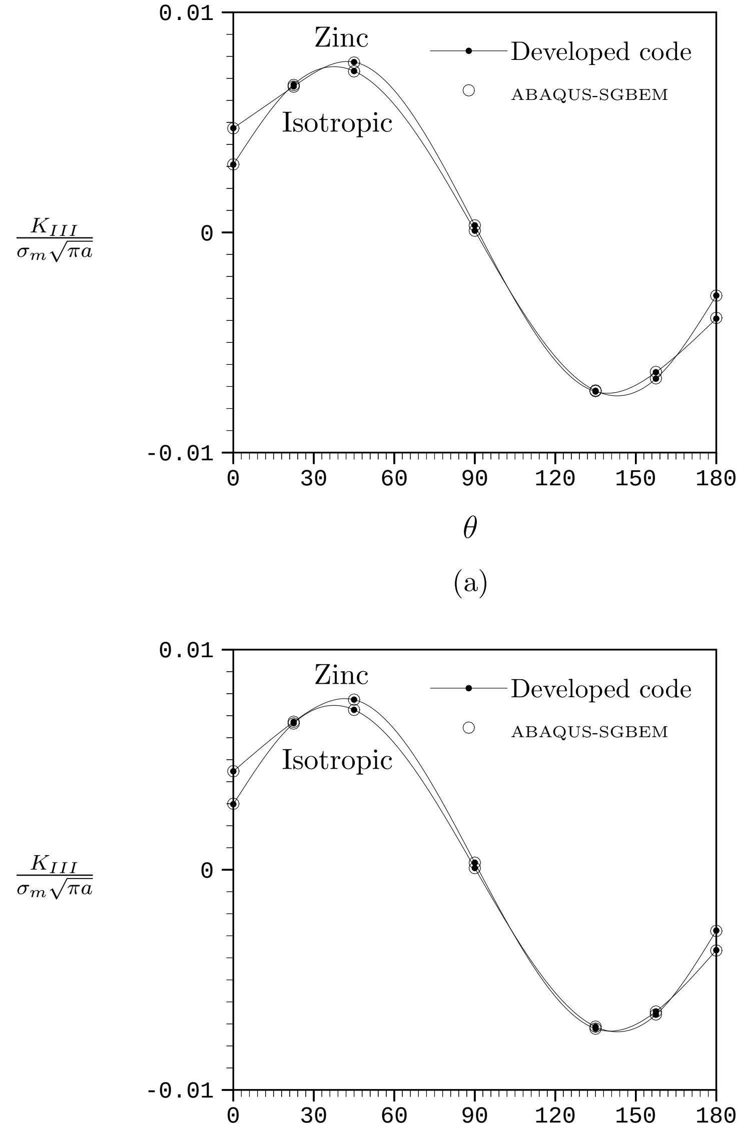

(a)

(b)

Figure 4.54: Normalized mode-III stress intensity factor for a cantilever beam containing a surface flaw subjected to uniform shear traction at the ends: (a) use collocation constraint and (b) use weak enforcement constraint. Note that $S_I^R = S_I^F$ and $\sigma_m = 6P_oL/bh^2$.

4.5 Summary

The coupling strategy between the SGBEM based upon weakly-singular integral equations and the standard FEM has been established to treat cracks in three dimensional anisotropic, linearly elastic media. The formulation is symmetric and combines advantages of both methods, e.g. the capability of SGBEM to accurately modeling cracks and their immediate surroundings and the vast features of FEM to treat the (possibly very complex) remaining region. The discretized governing equation is achieved both in the context of conforming and nonconforming discretization at the interface where the latter allows the flexibility of meshing with possible use of different levels of refinement for each subregion. Note that the final coefficient matrix is symmetric and diagonally-sparse provided that the SGBEM is only utilized locally. Remark that for nonconforming discretization, the weak continuity of traction at the interface is fully satisfied if the weak enforcement constraints associated with (4.42) and (4.43) is utilized while it is not if the collocation constraints given by (4.46) is employed.

Various numerical examples are examined to illustrate the accuracy and the robust character of the technique in obtaining the stress intensity factors, especially in the context of mix-mode problems and material anisotropy. The numerical solutions indicate excellent convergence with slight mesh dependence for both conforming and nonconforming cases. It is also observed, by comparing with available bench mark solutions from the SGBEM, that a relatively coarse mesh can be utilized to obtain accurate numerical results. Finally, we remark that the weak enforcement constraint is preferable to the collocation constraint since the former yields more accurate numerical results with no dependence on the choice of the reference interface.

Chapter 5

Conclusions

A symmetric Galerkin boundary element method (SGBEM) has been developed for analysis of fractures in three dimensional anisotropic, linearly elastic media. The method rests upon a pair of weak-form integral equations (one for displacement and one for traction) which have been established as part of this work. The kernels involved in these governing integral equations are weakly-singular (of order $1/r$) and are given in an explicit and concise form for general anisotropy. An important feature of the method is that standard C^o elements can be employed, and in the numerical treatment followed here standard isoparametric elements have been adopted exclusively apart from the use of a special crack-tip element. The crack-tip element has the novel feature that, associated with nodes along the crack front, there exist degrees of freedom which are directly related to the mixed-mode stress intensity factors.

The utility of the method for treating cracks in anisotropic media has been demonstrated by considering various example problems, including ones for cracks in an unbounded domain and ones for embedded and surface breaking cracks in a finite domain. It has been found that highly accurate stress intensity factor data can be obtained with relatively coarse meshes even for cases involving a high degree of material anisotropy.

While the SGBEM developed here provides a means to obtain very accurate stress intensity factors, it tends to become computationally inefficient as the number of degrees of freedom becomes large. To remedy this shortcoming, the SGBEM has been coupled with the standard finite element method (FEM) in such a way as to retain a symmetric coefficient matrix. In the development and implementation of this coupling, the ability to have nonconforming discretizations (on the interface separating the SGBEM and FEM regions) has been treated by means of a weak enforcement of the continuity conditions. The freedom afforded by such nonconforming discretizations can significantly reduce the modeling effort since it allows the SGBEM and FEM sub-regions to be meshed independently. It has been demonstrated that the SGBEM-FEM strategy is effective for obtaining highly accurate fracture data, and it is believed that it is an efficient computational tool for three-dimensional fracture analysis. Indeed, the coupling of the SGBEM with the commercial code ABAQUS (which has also been carried out as part of this work) may prove to be a particularly valuable computational tool.

One aspect of fracture analysis which has not been addressed in this work is crack evolution. The SGBEM is an attractive strategy for treating crack growth since only the crack surface needs to be remeshed as the crack advances (rather than the domain around the crack as in the FEM), and certainly re-meshing strategies could be adopted for this purpose. However, to properly treat crack growth requires knowledge of a growth criterion, and such a criterion has not yet been fully established for general mixed-mode conditions. Indeed, such growth laws are lacking even for isotropic materials (although simple, assumed laws are often adopted based upon well developed criteria for two-dimensional crack growth). Accurate computational strategies such as the one developed here could, perhaps, be beneficial in developing such growth laws through their use in supporting careful experimental studies.

Appendix A

Discussion of U_i^p, S_{ij}^p and Σ_{ij}^{kl}

We denote the displacement and stress associated with the unit Kelvin state as $\{U_i^p, S_{kl}^p\}$ such that, for a concentrated load F_p acting at a point $\boldsymbol{x}$, the displacement and stress at a point $\boldsymbol{\xi}$ are given by $u_i(\boldsymbol{\xi} - \boldsymbol{x}) = U_i^p(\boldsymbol{\xi} - \boldsymbol{x})F_p$ and $\sigma_{kl}(\boldsymbol{\xi} - \boldsymbol{x}) = S_{kl}^p(\boldsymbol{\xi} - \boldsymbol{x})F_p$, respectively. With partial differentiation with respect to ξ_i denoted by a comma (i.e. $(\cdot)_{,i} \equiv \partial(\cdot)/\partial\xi_i$), the Kelvin state satisfies

$$S_{kl,k}^p = E_{klij}U_{i,kl}^p = \delta_{lp}\,\delta(\boldsymbol{\xi} - \boldsymbol{x}) \tag{A.1}$$

where $\delta(\boldsymbol{\xi} - \boldsymbol{x})$ is the Dirac-delta function centered at $\boldsymbol{x}$. For purposes of presentation, we refer to U_i^p as the 'displacement fundamental solution' and to S_{ij}^p as the 'stress fundamental solution'.

Equation (2.12) is readily established by using (A.1) and noting the symmetries of the elastic moduli. Equation (2.13) follows from

$$\begin{aligned}
\Sigma_{ij,l}^{lk}(\boldsymbol{\xi} - \boldsymbol{x}) &= E_{lkpq}S_{ij,ql}^p = E_{lkpq}E_{ijmn}U_{m,nql}^p \\
&= E_{ijmn}E_{lkpq}U_{p,qnl}^m = E_{ijmn}S_{lk,ln}^m \\
&= -[E_{ijkl}\delta(\boldsymbol{\xi} - \boldsymbol{x})]_{,l}
\end{aligned} \tag{A.2}$$

where the reciprocity-relation $U_i^j = U_j^i$ has been employed in addition to (A.1). We note that the observations $\Sigma^{lk}_{ij,i} = 0$ for $\boldsymbol{\xi} \neq \boldsymbol{x}$ and $\Sigma^{lk}_{ij,l} = 0$ for $\boldsymbol{\xi} \neq \boldsymbol{x}$ have been utilized in various earlier investigations (e.g. Becache *et al.*[4] and Bonnet [8]).

Appendix B

Radon transform

Here we provide only a brief summary of certain properties of the Radon transform which are pertinent to our development. See Bacon *et al.*[2] for a more in depth summary, and see [13, 19, 23] for an extensive development of this integral transform.

The Radon transform involves two independent transform parameters: a unit vector $\boldsymbol{z}$ and a scalar α with $-\infty < \alpha < \infty$. For a given $\boldsymbol{z}$ and α, the relation $\boldsymbol{z} \cdot \boldsymbol{\xi} = \alpha$ defines a plane in Euclidian space $\mathbb{R}^3$, and the Radon transform of a (scalar, vector or tensor valued) function $f = f(\boldsymbol{\xi})$ is defined in terms of an integral over such planes as

$$\hat{f}(\boldsymbol{z}, \alpha) = \mathcal{R}\{f\} = \int_{\boldsymbol{z}\cdot\boldsymbol{\xi}=\alpha} f(\boldsymbol{\xi})\, dS(\boldsymbol{\xi}) = \int_{\mathbb{R}^3} f(\boldsymbol{\xi})\, \delta(\alpha - \boldsymbol{z} \cdot \boldsymbol{\xi})\, dV(\boldsymbol{\xi}) \tag{B.1}$$

The function $f(\boldsymbol{\xi})$ is then given in terms of its Radon transform $\hat{f}(\boldsymbol{z}, \alpha)$ by the inversion formula

$$f(\boldsymbol{\xi}) = -\frac{1}{8\pi^2} \int_{||\boldsymbol{z}||=1} \frac{\partial^2 \hat{f}(\boldsymbol{z}, \alpha)}{\partial \alpha^2} dS(\boldsymbol{z}) \tag{B.2}$$

in which the integral is to be carried out over the surface of the unit sphere $||\boldsymbol{z}|| = 1$. Certain useful properties and results concerning the Radon transform are summarized below.

(1) The Radon transform of a derivative of a function satisfies

$$\mathcal{R}\left\{\frac{\partial f(\boldsymbol{\xi})}{\partial \xi_k}\right\} = z_k \frac{\partial \hat{f}(\boldsymbol{z},\alpha)}{\partial \alpha} \tag{B.3}$$

(2) The Radon transform of the Dirac-delta function $\delta(\boldsymbol{\xi}-\boldsymbol{x})$ is given by

$$\mathcal{R}\{\delta(\boldsymbol{\xi}-\boldsymbol{x})\} \;=\; \int_{R^3} \delta(\boldsymbol{\xi}-\boldsymbol{x})\delta(\alpha-\boldsymbol{z}\cdot\boldsymbol{\xi})dV(\boldsymbol{\xi}) \;=\; \delta(\alpha-\boldsymbol{z}\cdot\boldsymbol{x}) \tag{B.4}$$

(3) Recall that

$$\Delta\left(\frac{-1}{4\pi r}\right) = \delta(\boldsymbol{\xi}-\boldsymbol{x}) \tag{B.5}$$

Taking the Radon transform of (B.5) we have

$$z_i z_i \frac{\partial^2}{\partial \alpha^2}\widehat{\left(\frac{1}{r}\right)} = -4\pi\mathcal{R}\{\delta(\boldsymbol{\xi}-\boldsymbol{x})\} \tag{B.6}$$

which, upon noting that $z_i z_i = 1$ and employing (B.4), leads to

$$\frac{\partial^2}{\partial \alpha^2}\widehat{\left(\frac{1}{r}\right)} = -4\pi\delta(\alpha-\boldsymbol{z}\cdot\boldsymbol{x}) \tag{B.7}$$

(4) Let $f = f(\boldsymbol{\xi}-\boldsymbol{x})$ be a function for which

$$\frac{\partial^2 \hat{f}(\boldsymbol{z},\alpha-\boldsymbol{z}\cdot\boldsymbol{x})}{\partial \alpha^2} = g(\boldsymbol{z},\alpha-\boldsymbol{z}\cdot\boldsymbol{x})\,\delta(\alpha-\boldsymbol{z}\cdot\boldsymbol{x}) \tag{B.8}$$

Employing the Radon transform inversion formula we obtain

$$f(\boldsymbol{\xi}-\boldsymbol{x}) = -\frac{1}{8\pi^2}\int_{||\boldsymbol{z}||=1} g[\boldsymbol{z},\boldsymbol{z}\cdot(\boldsymbol{\xi}-\boldsymbol{x})]\,\delta[\boldsymbol{z}\cdot(\boldsymbol{\xi}-\boldsymbol{x})]\,dS(\boldsymbol{z}) \tag{B.9}$$

and, since $\delta(ax) = \delta(x)/|a|$, it follows that

$$f(\boldsymbol{\xi}-\boldsymbol{x}) = -\frac{1}{8\pi^2 r}\int_{||\boldsymbol{z}||=1} g[\boldsymbol{z},\boldsymbol{z}\cdot(\boldsymbol{\xi}-\boldsymbol{x})]\,\delta(\boldsymbol{z}\cdot\boldsymbol{e})\,dS(\boldsymbol{z}) \tag{B.10}$$

where $\boldsymbol{r} = (\boldsymbol{\xi}-\boldsymbol{x})$, $r = ||\boldsymbol{r}||$ and $\boldsymbol{e} = \boldsymbol{r}/r$. From the sifting property of the Dirac-delta function, equation (B.10) reduces to (e.g. [18])

$$f(\boldsymbol{\xi}-\boldsymbol{x}) \;=\; -\frac{1}{8\pi^2 r}\oint_{\boldsymbol{z}\cdot\boldsymbol{r}=0} g[\boldsymbol{z},\boldsymbol{z}\cdot(\boldsymbol{\xi}-\boldsymbol{x})]\,ds(\boldsymbol{z}) \tag{B.11}$$

in which the integral is to be evaluated over the unit circle $||\boldsymbol{z}|| = 1$ in a plane for which $\boldsymbol{z}\cdot\boldsymbol{r} = 0$.

Appendix C

Existence and nonuniqueness of G^p_{mj} and C^{tk}_{mj}

C.1 Kernel G^p_{mj}

To establish the existence (and nonuniqueness) of the kernel G^p_{mj}, it suffices to show that the system of linear equations (2.28) admits an infinite number of solutions. Now, it can be readily shown that the adjoint of the linear operator $\mathcal{L} = \epsilon_{ikm} z_k$ is $\mathcal{L}^* = \epsilon_{imk} z_k$ and, further, that the null space $\mathcal{N}$ of $\mathcal{L}$ and the null space $\mathcal{N}^*$ of $\mathcal{L}^*$ coincide and satisfy

$$\mathcal{N}^*(\epsilon_{imk} z_k) = \{c_m = \rho z_m : \forall \rho \in \mathbb{R}\} \tag{C.1}$$

That the vector on the right hand side of (2.28) is orthogonal to all elements of $\mathcal{N}^*$ (i.e. that the equations are consistent) follows from

$$\begin{aligned} c_i \Omega_{ijp} \delta(\alpha - \boldsymbol{z} \cdot \boldsymbol{x}) &= \Big[\delta_{pj} z_i z_i - z_i E_{ijdc} z_c (\boldsymbol{z}, \boldsymbol{z})^{-1}_{pd} \Big] \rho \delta(\alpha - \boldsymbol{z} \cdot \boldsymbol{x}) \\ &= \Big[\delta_{pj} - (\boldsymbol{z}, \boldsymbol{z})_{jd} (\boldsymbol{z}, \boldsymbol{z})^{-1}_{pd} \Big] \rho \delta(\alpha - \boldsymbol{z} \cdot \boldsymbol{x}) \\ &= \Big[\delta_{pj} - \delta_{jp} \Big] \rho \delta(\alpha - \boldsymbol{z} \cdot \boldsymbol{x}) \end{aligned}$$

$$\equiv \quad 0 \tag{C.2}$$

and this ensures the existence of $\partial^2 \hat{G}^p_{mj}/\partial\alpha^2$. Since the dimension of the null space of $\mathcal{L}$ is not zero, the solution for $\partial^2 G^p_{mj}/\partial\alpha^2$ is not unique and, in fact, there is an infinite number of solutions. From (C.1) it is evident that, for any particular solution $\partial^2 \hat{G}^p_{mj}/\partial\alpha^2$, the quantity $\partial^2 \hat{G}^p_{mj}/\partial\alpha^2 + z_m \partial^2 \hat{L}^p_j/\partial\alpha^2$ is also a solution. Applying the Radon transform inversion it then follows that if G^p_{mj} is a particular kernel, then the quantity $G^p_{mj} + \partial L^p_j/\partial\xi_m$ is also a valid kernel for every (suitably well behaved) function L^p_j. If attention is restricted to kernels which are functions of $(\boldsymbol{\xi} - \boldsymbol{x})$ and which are homogeneous of degree $\lambda = -1$, it is then consistent to restrict attention to functions $L^p_j(\boldsymbol{\xi} - \boldsymbol{x})$ which are homogeneous of degree $\lambda = 0$.

C.2 Kernel C^{tk}_{mj}

The existence and nonuniqueness of the kernel C^{tk}_{mj} is established by showing that (2.34) admits an infinite number of solutions. Toward demonstrating this, we first represent the components of the linear operator $\epsilon_{ism}\epsilon_{lrt}z_s z_r$ in matrix form as

$$[\epsilon_{ism}\epsilon_{lrt}z_s z_r] = \begin{bmatrix} \mathbf{0} & -z_3\boldsymbol{Z} & z_2\boldsymbol{Z} \\ z_3\boldsymbol{Z} & \mathbf{0} & -z_1\boldsymbol{Z} \\ -z_2\boldsymbol{Z} & z_1\boldsymbol{Z} & \mathbf{0} \end{bmatrix} \tag{C.3}$$

in which the p^{th}-row and q^{th}-column of the matrix correspond to the indicies $\{i, m, l, t\}$ appearing in the linear operator according to $p = [3(i-1)+l]$ and $q = [3(m-1)+t]$, the matrix $\boldsymbol{Z}$ is defined by

$$\boldsymbol{Z} = \begin{bmatrix} 0 & -z_3 & z_2 \\ z_3 & 0 & -z_1 \\ -z_2 & z_1 & 0 \end{bmatrix} \tag{C.4}$$

and $\mathbf{0}$ denotes the 3×3 matrix for which all entries are zero.

Now, since $\boldsymbol{Z}$ is skew-symmetric it follows that the operator $\epsilon_{ism}\epsilon_{lrt}z_s z_r$ is symmetric and self-adjoint. Further, since the matrix in (C.3) is singular with rank equal to four, the dimension of the null space of the operator is five. To construct a basis for the null space, we observe that a solution to

$$\epsilon_{ism}\epsilon_{lrt}z_s z_r c_{mt} = 0 \tag{C.5}$$

is given by $c_{mt} = \eta_m z_t + \kappa_t z_m$ in which η_m and κ_t are arbitrary. It is then easily verified that, by making appropriate choices for η_m and κ_t, a set of five linearly independent elements $c_{mt}^{(i)}$ (with $i = \{1,2,3,4,5\}$) can be generated to form a basis for the null space. Indeed, the particular choices $c_{mt}^{(i)} = \delta_{im}z_t$ for $i = \{1,2,3\}$ and $c_{mt}^{(3+i)} = \delta_{it}z_m$ for $i = \{1,2\}$ serve this purpose. (Note that the element $c_{mt}^{(6)} = \delta_{3t}z_m$ can be expressed as a linear combination of the previous five elements; this is readily shown by expressing the elements $c_{mt}^{(i)}$ in the form of a 9-vector.) Hence, the null space of $\epsilon_{ims}\epsilon_{ltr}z_s z_r$ is given by

$$\mathcal{N}(\epsilon_{ims}\epsilon_{ltr}z_s z_r) = \{c_{mt} = \eta_m z_t + \kappa_t z_m : \forall\, \eta_m, \kappa_t \in \mathbb{R}\} \tag{C.6}$$

A necessary and sufficient condition for $\partial^2 \hat{C}_{mj}^{tk}/\partial\alpha^2$ to exist is that the term on the right hand side of (2.34) be orthogonal to all elements in the null space of the (self-adjoint) linear operator $\epsilon_{ims}\epsilon_{ltr}z_s z_r$, and that this holds can be demonstrated as follows:

$$\begin{aligned}
c_{il}\Lambda_{ijkl}\delta(\alpha - \boldsymbol{z}\cdot\boldsymbol{x}) &= \eta_i\left[z_l E_{ijkl} - (z_l E_{lkpq} z_q) E_{ijab} z_b (\boldsymbol{z},\boldsymbol{z})^{-1}_{ap}\right]\delta(\alpha - \boldsymbol{z}\cdot\boldsymbol{x}) \\
&+ \kappa_l\left[z_i E_{ijkl} - (z_i E_{ijab} z_b) E_{lkpq} z_q (\boldsymbol{z},\boldsymbol{z})^{-1}_{ap}\right]\delta(\alpha - \boldsymbol{z}\cdot\boldsymbol{x}) \\
&= \eta_i\left[z_l E_{ijkl} - (\boldsymbol{z},\boldsymbol{z})_{kp} E_{ijab} z_b (\boldsymbol{z},\boldsymbol{z})^{-1}_{ap}\right]\delta(\alpha - \boldsymbol{z}\cdot\boldsymbol{x}) \\
&+ \kappa_l\left[z_i E_{ijkl} - (\boldsymbol{z},\boldsymbol{z})_{ja} E_{lkpq} z_q (\boldsymbol{z},\boldsymbol{z})^{-1}_{ap}\right]\delta(\alpha - \boldsymbol{z}\cdot\boldsymbol{x}) \\
&= \eta_i\left[z_l E_{ijkl} - z_b E_{ijkb}\right]\delta(\alpha - \boldsymbol{z}\cdot\boldsymbol{x})
\end{aligned}$$

$$
\begin{aligned}
&+ \quad \kappa_l \left[z_i E_{ijkl} - z_q E_{lkjq} \right] \delta(\alpha - \boldsymbol{z} \cdot \boldsymbol{x}) \\
&\equiv \quad 0
\end{aligned}
\tag{C.7}
$$

That $\partial^2 \hat{C}^{tk}_{mj} / \partial\alpha^2$ is non-unique is evident from the fact that the dimension of the null space of $\epsilon_{ims}\epsilon_{ltr} z_s z_r$ is not zero. From (C.6) it is clear that, for any particular solution $\partial^2 \hat{C}^{tk}_{mj}/\partial\alpha^2$, the quantity $\partial^2 \hat{C}^{tk}_{mj}/\partial\alpha^2 + z_m \partial^2 \hat{M}^{tk}_j/\partial\alpha^2 + z_t \partial^2 \hat{N}^k_{mj}/\partial\alpha^2$ is also a valid solution. This implies that given any particular kernel C^{tk}_{mj}, the quantity $C^{tk}_{mj} + \partial M^{tk}_j/\partial\xi_m + \partial N^k_{mj}/\partial\xi_t$ is also a valid kernel. Here it suffices to restrict attention to functions $M^{tk}_j(\boldsymbol{\xi} - \boldsymbol{x})$ and $N^k_{mj}(\boldsymbol{\xi} - \boldsymbol{x})$ which are homogeneous of degree $\lambda = 0$.

Appendix D

Discussion of the solid angle $\Phi(\boldsymbol{x})$

The quantity H_{ip}^{p} admits a representation in the form

$$H_{ip}^{p}(\boldsymbol{\xi}-\boldsymbol{x}) = 3\epsilon_{ikm}\frac{\partial\omega_m(\boldsymbol{\xi},\boldsymbol{x})}{\partial\xi_k} \tag{D.1}$$

where

$$\omega_m(\boldsymbol{\xi},\boldsymbol{x}) = \frac{1}{3}\int_{\Gamma(\boldsymbol{x})}\epsilon_{mrt}\,H_{rp}^{p}(\boldsymbol{\xi}-\boldsymbol{z})\,dz_t \tag{D.2}$$

in which $\Gamma(\boldsymbol{x})$ is any path originating at $\boldsymbol{x}$ and extending to infinity (without passing through the field point $\boldsymbol{\xi}$). To establish this result, we first note that $H_{ip}^{p} \to 0$ as $r \to \infty$, that $\partial H_{ip}^{p}/\partial\xi_k = -\partial H_{ip}^{p}/\partial x_k$ and that $\partial H_{ip}^{p}/\partial\xi_i = -3\delta(\boldsymbol{\xi}-\boldsymbol{x})$. Then from (D.2) along with the delta-epsilon identity we find

$$\begin{aligned} 3\epsilon_{ikm}\frac{\partial\omega_m(\boldsymbol{\xi},\boldsymbol{x})}{\partial\boldsymbol{\xi}_k} &= \int_{\Gamma(\boldsymbol{x})}\frac{\partial H_{ip}^{p}(\boldsymbol{\xi}-\boldsymbol{z})}{\partial\xi_t}\,dz_t - \int_{\Gamma(\boldsymbol{x})}\frac{\partial H_{kp}^{p}(\boldsymbol{\xi}-\boldsymbol{z})}{\partial\xi_k}\,dz_i \\ &= -\int_{\Gamma(\boldsymbol{x})}\frac{\partial H_{ip}^{p}(\boldsymbol{\xi}-\boldsymbol{z})}{\partial z_t}\,dz_t \\ &= H_{ip}^{p}(\boldsymbol{x}-\boldsymbol{\xi}) \end{aligned} \tag{D.3}$$

Substituting (D.1) into (2.51) yields

$$\Omega(\boldsymbol{x}) = 4\pi \int_S n_i(\boldsymbol{\xi})\epsilon_{ikm} \frac{\partial \omega_m(\boldsymbol{\xi}, \boldsymbol{x})}{\partial \boldsymbol{\xi}_k} \, dS(\boldsymbol{\xi}) \tag{D.4}$$

which, upon an application of Stokes' theorem (with $x \notin S$ and with the path $\Gamma(\boldsymbol{x})$ being such that it does not intersect S), gives rise to

$$\Omega(\boldsymbol{x}) = 4\pi \int_{\partial S} \omega_m(\boldsymbol{\xi}, \boldsymbol{x}) \, d\xi_m \tag{D.5}$$

We remark that a related development (in terms of somewhat different notation) is given by Li and Mear [28].

Appendix E

Equivalence of kernels and reduction for isotropy

The kernel G^p_{mj} given by (2.33) and the kernel C^{tk}_{mj} given by (2.40) are valid for general anisotropy. To specialize them to isotropic material behavior we note that for such materials (e.g. [2])

$$E_{klpq} = \mu\left(\delta_{kp}\delta_{lq} + \delta_{kq}\delta_{lp} + \frac{2\nu}{1-2\nu}\delta_{kl}\delta_{pq}\right) \tag{E.1}$$

$$(\boldsymbol{z},\boldsymbol{z})_{ij} = \mu\left(\delta_{ij} + \frac{1}{1-2\nu}z_i z_j\right) \tag{E.2}$$

$$(\boldsymbol{z},\boldsymbol{z})^{-1}_{ij} = \frac{1}{\mu}\left(\delta_{ij} - \frac{1}{2(1-\nu)}z_i z_j\right) \tag{E.3}$$

Utilizing these relations we readily reduce (2.33) to

$$G^p_{mj}(\boldsymbol{\zeta}) = \{G^p_{mj}(\boldsymbol{\zeta})\}_{(2.61)} + \bar{G}^p_{mj}(\boldsymbol{\zeta}) \tag{E.4}$$

$$\tag{E.5}$$

and (2.40) to

$$C^{tk}_{mj}(\boldsymbol{\zeta}) = \{C^{tk}_{mj}(\boldsymbol{\zeta})\}_{(2.62)} + \bar{C}^{tk}_{mj}(\boldsymbol{\zeta}) \tag{E.6}$$

in which $\{G^p_{mj}\}_{(2.61)}$ and $\{C^{tk}_{mj}\}_{(2.62)}$ denote the kernels given by (2.61) and (2.62), respectively, and where

$$\begin{aligned}
\bar{G}^p_{mj}(\boldsymbol{\zeta}) &= \frac{\epsilon_{jpk}}{8\pi}\left(\frac{\zeta_k}{r}\right)_{,m} && \text{(E.7)}\\
\bar{C}^{tk}_{mj}(\boldsymbol{\zeta}) &= -\frac{\mu}{8\pi}\Big[\delta_{tk}\, r_{,jm} + \delta_{mj}\, r_{,kt}\Big] - \frac{\nu\mu}{4\pi(1-\nu)}\Big[\delta_{tj}\, r_{,km} + \delta_{mk}\, r_{,jt}\Big] \\
&\quad + \frac{\mu}{16\pi(1-\nu)}\left[\left(\frac{\zeta_j\zeta_k}{r}\right)_{,mt} - (1-2\nu)\delta_{jk}\, r_{,mt}\right] && \text{(E.8)}
\end{aligned}$$

In these relations, $\boldsymbol{\zeta} = (\boldsymbol{\xi}-\boldsymbol{x})$, $r = ||\boldsymbol{\zeta}||$ and a comma indicates partial differentiation (i.e. $(\cdot)_{,m} \equiv \partial(\cdot)/\partial\xi_m$). Clearly, within the context of the non-uniqueness expressed by (2.60), the terms $\bar{G}^p_{mj}$ and $\bar{C}^{tk}_{mj}$ can be discarded without loss. We remark that the kernels $\{G^p_{mj}\}_{(2.61)}$ and $\{C^{tk}_{mj}\}_{(2.62)}$ appear to be in their 'most reduced form' in the sense that they do not contain any additional terms in the form of a gradient of a function which can be discarded by (2.60).

Next we consider Blin's [6] kernel for isotropic media given by

$$C^{tk}_{mj}(\boldsymbol{\zeta}) = \frac{\mu}{4\pi(1-\nu)r}\left[(1-\upsilon)\delta_{tk}\delta_{mj} - (1-2\nu)\delta_{mk}\delta_{jt} - \delta_{jk}\delta_{mt} + \epsilon_{ikt}\epsilon_{pjm}\frac{\zeta_i\zeta_p}{r^2}\right] \tag{E.9}$$

Upon employing the identity

$$\begin{aligned}
\epsilon_{umv}\epsilon_{wts} &= \delta_{uw}(\delta_{mt}\delta_{vs} - \delta_{ms}\delta_{vt}) + \delta_{ut}(\delta_{ms}\delta_{vw} - \delta_{mw}\delta_{vs}) \\
&+ \delta_{us}(\delta_{mw}\delta_{vt} - \delta_{mt}\delta_{vw}) && \text{(E.10)}
\end{aligned}$$

it can be shown that this kernel can be re-expressed in the form (E.6) with the additional term $\bar{C}^{tk}_{mj}$ given by

$$\bar{C}^{tk}_{mj}(\boldsymbol{\zeta}) = \frac{\mu}{4\pi(1-\nu)}\left[\left(\frac{\delta_{jk}\zeta_t}{2r} - \frac{\delta_{jt}\zeta_k}{r}\right)_{,m} + \left(\frac{\delta_{jk}\zeta_m}{2r} - \frac{\delta_{mk}\zeta_j}{r}\right)_{,t}\right] \tag{E.11}$$

Clearly the additional term $\bar{C}^{tk}_{mj}$ can be discarded without loss.

Finally, we consider Lothe's kernel for general anisotropy. By employing (E.10), Lothe's kernel (2.63) can be re-expresses as

$$C_{mj}^{tk}(\boldsymbol{\zeta}) = \{C_{mj}^{tk}(\boldsymbol{\zeta})\}_{(2.40)} + \bar{C}_{mj}^{tk}(\boldsymbol{\zeta}) + \bar{\bar{C}}_{mj}^{tk}(\boldsymbol{\zeta}) \tag{E.12}$$

where $\{C_{mj}^{tk}(\boldsymbol{\zeta})\}_{(2.40)}$ denotes the kernel given by (2.40) and where the additional terms $\bar{C}_{mj}^{tk}$ and $\bar{\bar{C}}_{mj}^{tk}$ are given by

$$\bar{C}_{mj}^{tk}(\boldsymbol{\zeta}) = \frac{E_{ujku}}{8\pi}\left(\frac{\zeta_t}{r}\right)_{,m} = \frac{E_{ujku}}{8\pi}\left(\frac{\zeta_m}{r}\right)_{,t} \tag{E.13}$$

and

$$\bar{\bar{C}}_{mj}^{tk}(\boldsymbol{\xi}-\boldsymbol{x}) = -\frac{1}{8\pi^2 r}\oint_{||\boldsymbol{z}||=1} z_m z_t z_c z_d (\boldsymbol{z},\boldsymbol{z})_{en}^{-1} E_{ajec} E_{dnka} ds \tag{E.14}$$

Clearly the term $\bar{C}_{mj}^{tk}$ can be discarded without loss (since it is in terms of a gradient with respect to ξ_m or ξ_t). While the term $\bar{\bar{C}}_{mj}^{tk}$ must itself be expressible as a gradient with respect to ξ_m or ξ_t, we have not attempted to directly show this. Rather, we simply verify (by use of the Radon transform) that

$$\epsilon_{ism}\frac{\partial}{\partial \xi_s}\epsilon_{lrt}\frac{\partial \bar{\bar{C}}_{mj}^{tk}(\boldsymbol{\xi}-\boldsymbol{x})}{\partial \xi_r} = 0 \tag{E.15}$$

hence the term $\bar{\bar{C}}_{mj}^{tk}$ can also be discarded without loss.

Appendix F

Numerical treatment of $\boldsymbol{\Lambda}_{BR}$ and $\boldsymbol{\Lambda}_{FR}$

The entries of $\boldsymbol{\Lambda}_{BR}$ are obtained through a summation of the contributions from each of the M_B elements comprising the discretized surface S_I^B as

$$[\boldsymbol{\Lambda}_{BR}]_{ij} = \sum_{e=1}^{M_B} [\boldsymbol{\Lambda}_{BR}^e]_{ij} \tag{F.1}$$

in which

$$[\boldsymbol{\Lambda}_{BR}^e]_{ij} = \int_{S_e^B} [\boldsymbol{\Phi}_B(\boldsymbol{y})]_i \; [\boldsymbol{\Phi}_R(\boldsymbol{y}_p)]_j \; dS(\boldsymbol{y}) \tag{F.2}$$

is the contribution from the element which occupies the portion S_e^B of S_I^B. In this relation, $\boldsymbol{y}_p \in S_I^R$ is the closest point projection of $\boldsymbol{y} \in S_e^B$.

The integrand appearing in (F.2) does not, in general, have a continuous gradient over the entire element S_e^B and, as a consequence, standard gaussian quadrature is not an effective means for evaluating $[\boldsymbol{\Lambda}_{BR}^e]_{ij}$. For this reason, a numerical integration scheme based upon the trapezoidal rule is utilized instead.

To discuss the integration technique, consider a pair of master elements $\hat{S}_e^B$ and $\hat{S}_e^R$ which are associated with a physical element S_e^B on S_I^B and a physical

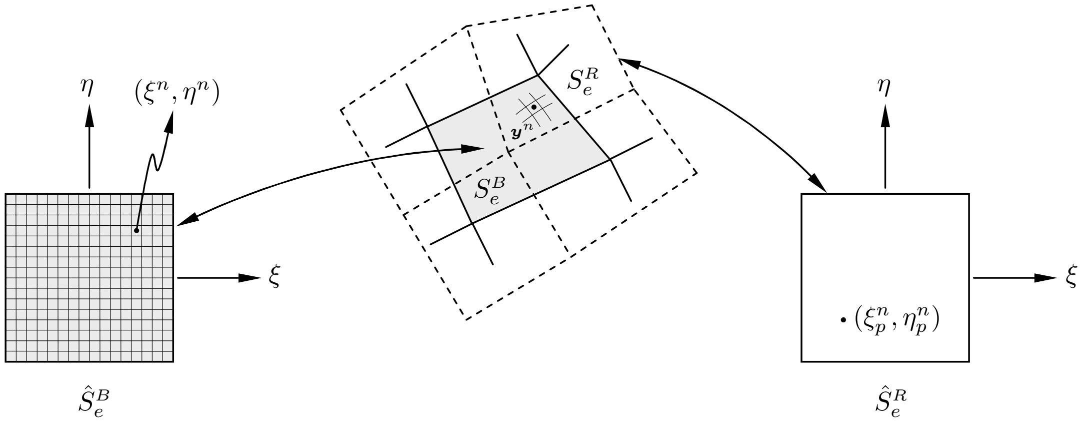

Figure F.1: Schematic indicating numerical numerical treatment of $[\mathbf{\Lambda}^e_{BR}]_{ij}$. In the center figure, elements associated with S_I^B are indicated in solid line whereas those associated with S_I^R are indicated in dashed line.

element S_e^R on S_I^R, respectively, as shown schematically in Figure F.1. The master element $\hat{S}_e^B$ is partitioned into N equal-size squares. Let the centroid of the n^{th} square be given by (ξ^n, η^n), and note that it corresponds to a point $\boldsymbol{y}^n \in S_e^B$ in physical space. The closest point projection of $\boldsymbol{y}^n$ onto S_e^R is denoted by $\boldsymbol{y}_p^n \in S_e^B$ and its coordinates on the master element $\hat{S}_e^R$ are given by (ξ_p^n, η_p^n). The approximation of (F.2), in terms of the trapezoidal integration rule, takes the form

$$[\mathbf{\Lambda}^e_B]_{ij} \;\approx\; \sum_{n=1}^{N} [\hat{\mathbf{\Phi}}_B(\xi^n, \eta^n)]_i \; [\hat{\mathbf{\Phi}}_R(\xi_p^n, \eta_p^n)]_j \; J(\xi^n, \eta^n) \; A_n \tag{F.3}$$

where $\hat{\mathbf{\Phi}}_B$ and $\hat{\mathbf{\Phi}}_R$ are nodal basis functions defined on $\hat{S}_e^B$ and $\hat{S}_e^R$, respectively, $J(\xi^n, \eta^n)$ is the jacobian of the transformation evaluated at (ξ^n, η^n) and A_n is the area of the n^{th} square. Note that the procedure to obtain $\mathbf{\Lambda}_{FR}$ is identical to that for $\mathbf{\Lambda}_{BR}$. Finally, we remark that the specific procedure utilized to obtain the closest point projection is analogous to that introduced by Xiao [45] in his treatment of nearly-singular integrals.

Bibliography

[1] D. M. Barnett and R. J. Asaro, The fracture mechanics of slit-like cracks in anisotropic elastic media, *J. Mech. Phys. Solids*, **20** (1972) 353-366.

[2] D. J. Bacon, D. M. Barnett and R. O. Scattergood, Anisotropic continuum theory of lattice defects, *Prog. Mat. Science*, **23** (1979) 51-262.

[3] J. G. Bakukas, Comparison of boundary correction factor solutions for two symmetric cracks in a straight-shank hole, *Engrg. Fracture Mech.*, **68** (2001) 1095-1106.

[4] E. Becache, J. C. Nedelec and N. Nishimura, Regularization in 3D for anisotropic elastodynamic crack and obstacle problems, *J. Elasticity*, **31** (1993) 25-46.

[5] G. E. Blandford, A. R. Ingraffea and J. A. Ligget, Two-dimensional stress intensity factor computation using boundary element method, *Internat. J. Numer. Methods Engrg.*, **17** (1981) 387-440.

[6] J. Blin, *Act. Met.*, **3** (1955) 199.

[7] M. Bonnet and H. D. Bui, Regularization of the displacement and traction BIE for 3D elastodynamics using indirect methods, in: J. H. Kane, G. Maier, N. Tosaka and S. N. Atluri, ed., *Advances in Boundary Element Techniques*, (Springer, Berlin, 1993).

[8] Bonnet M. Bonnet, Regularized direct and indirect symmetric variational BIE formulations for three-dimensional elasticity, *Engineering Analysis with Boundary Elements,* **15** (1995) 93-102.

[9] H. D. Bui, An integral equation method for solving the problem of a plane crack of arbitrary shape, *J. Mech. Phys. Solids*, **25** (1977) 29-39.

[10] J. M. Burgers, *Proc. Kon. Ned. Akad. Wetenschap.*, **42** (1939) 293-398.

[11] T. A. Cruse, *Boundary Element Analysis in Computational Fracture Mechanics*, (Kluwer Academic Publishers, 1988).

[12] T. A. Cruse and J. D. Richardson, Non-singular Somigliana stress identities in elasticity, *Internat. J. Numer. Methods Engrg.*, **39** (1996) 3273-3304.

[13] S. R. Deans, *The Radon transform and some of its applications*, (John Wiley & Sons, 1983).

[14] W. M. Elleithy, H. J. Al-Gahtani and M. El-Gebeily, Iterative coupling of BE and FE methods in elastostatics, *Engrg. Anal. Bound. Elem.*, **25** (2001) 685-695.

[15] W. M. Elleithy and M. Tanaka, Interface relaxation algorithms for BEM-FEM coupling and FEM-BEM coupling, *Comput. Methods Appl. Mech. Engrg.*, **192** (2003) 2977-2992.

[16] A. Frangi and G. Novati, BEM-FEM coupling for 3D fracture mechanics applications, *Comp. Mech.*, **77** (1996) 243-262.

[17] S. Ganguly, J. B. Layton and C. Balakrishna, Symmetric coupling of multi-zone curved Galerkin boundary elements with finite elements in elasticity, *Internat. J. Numer. Methods Engrg.*, **48** (2000) 633-654.

[18] I. M. Gel'fand and G. E. Shilov, *Generalized functions*, Vol. 1 (Academic Press, 1964).

[19] I. M. Gel'fand , M. I. Graev and N. Ya. Vilenkin, *Generalized functions: Integral geometry and representation theory*, Vol. 5 (Academic Press, 1966).

[20] L. J. Gray, L. F. Martha and A. R. Ingraffea, Hypersingular integrals in boundary element analysis, *Internat. J. Numer. Methods Engrg.*, **39** (1990) 387-404.

[21] H. D. Gu and C. H. Yew, Finite element solution of a boundary equation for mode-I embedded three-dimensional fracture, *Internat. J. Numer. Methods Engrg.*, **26** (1988) 1525-1540.

[22] M. Haas and G. Kuhn, Mixed-dimensional, symmetric coupling of FEM and BEM, *Engrg. Anal. Bound. Elem.*, **27** (2003) 575-582.

[23] S. Helgason, *The Radon Transform*, 2^{nd} edition (Progress in Mathematics vol. 5, 1999).

[24] P. J. Hirth and J. Lothe, *Theory of Dislocations*, 2^{nd} Edition (A Wiley-Interscience Publication, New York, 1982).

[25] M. W. Hyer, *Stress Analysis of Fiber-Reinforced Composite Materials*, (McGraw-Hill, New York, 1998).

[26] M. K. Kassir and G. C. Sih, *Mechanics of fracture, Three-dimensional crack problems*, Volume 2 (Noordhoff International Publishing Leyden, 1975).

[27] G. Leibfried, Versetzungen in anisotropem Material, *Zeitschrift für Physik*, **135** (1953) 23-43.

[28] S. Li and M. E. Mear, Singularity-reduced integral equations for discontinuities in three-dimensional linear elastic media, *Internat. J. Fracture*, **93** (1998) 87-114.

[29] S. Li, M. E. Mear and L. Xiao, Symmetric weak-form integral equation method for three dimensional fracture analysis, *Comput. Methods Appl. Mech. Engrg.*, **151** (1998) 435-539.

[30] Y. Liu and T. J. Rudophi, Some identities for fundamental solutions and their applications to weakly-singular boundary element formulations, *Engrg. Anal. Bound. Elem.*, **8** (1991) 301-311.

[31] J. Lothe, Dislocations in anisotropic media: The interaction energy, *Phil. Mag. A*, **46** (1982) 177-180.

[32] P. A. Martin and F. J. Rizzo, Hypersingular integrals: how smooth must the density be?, *Internat. J. Numer. Methods Engrg.*, **39** (1996) 687-704.

[33] J. C. Nedelec, Integral equations with nonintegrable kernels, *Integral Equations and Operator Theory*, **5** (1982) 563-572.

[34] Y. C. Pan and T. W. Chou, Point force solution for an infinite transversely isotropic solid, *J. Appl. Mech., Transactions ASME*, **43** (1976) 608-612.

[35] A. Sáez, M. P. Ariza, and J. Dominguez, Three-dimensional fracture analysis in transversely isotropic solids, *Engrg. Anal. Bound. Elem.*, **20** (1997) 287-298.

[36] E. Schnack and K. Türke, Domain decomposition with BEM and FEM, *Internat. J. Numer. Methods Engrg.*, **40** (1997) 2593-2610.

[37] V. Sládek and J. Sládek, Three dimensional crack analysis for an anisotropic body, *Appl. Math. Modeling*, **6** (1982) 374-380.

[38] V. Sládek and M. Tanaka, Regularization of hypersingular and nearly singular integrals in the potential theory and elasticity, *Internat. J. Numer. Methods Engrg.*, **36** (1993) 1609-1628.

[39] V. Sládek, J. Sládek and A. Le Van, Completely regularized integral representations and integral equations for anisotropic bodies with initial strains, *Math. Mech.*, **78** (1998) 771-780.

[40] N. Sukumar, N. Moës, B. Moran and T. Belytschko, Extended finite element method for three-dimensional crack modeling, *Internat. J. Numer. Methods Engrg.*, **48** (2000) 1549-1570.

[41] T. C. T. Ting, *Anisotropy elasticity: theory and applications*, (Oxford University Press, 1996).

[42] C. T. Ting and Vengen Lee, The three-dimensional elastostatic green's function for general anisotropic linear elastic solids, *Quart. J. Mech. appl. Math.*, **50** (1997) 407-426.

[43] J. Weaver, Three-dimensional crack analysis, *Internat. J. Solids and Structures*, **13** (1977) 321-330.

[44] C.-Y. Wang, Elastic fields produce by a point source in solids of general anisotropy, *J. Engrg. Math.*, **32** (1997) 41-52.

[45] L. Xiao, Symmetric weak-form integral equation method for three dimensional fracture analysis, *Ph.D. Dissertation*, The University of Texas at Austin, (1998).

[46] G. Xu and M. Ortiz, A variational boundary integral method for the analysis for 3-D cracks of arbitrary geometry modeled as continuous distributions of dislocation loops, *Internat. J. Numer. Methods Engrg.*, **36** (1993) 3675-3701.

[47] G. Xu, A variational boundary integral method for the analysis of three-dimensional cracks of arbitrary geometry in anisotropic elastic solids, *J. Appl. Mech.*, **67** (2000) 403-408.

[48] G. Y. Yu, A symmetric boundary element method/finite element method coupling procedure for two-dimensional elastodynamic problems, *J. Appl. Mech.*, **70** (2003) 451-454.

Vita

Jaroon Rungamornrat was born in Suphanburi, Thailand on July 27, 1974, the son of Yookloong Rungamornrat and Boonma Rungamornrat. After his work at Matthayomthanbin High School, he entered Chulalongkorn University in 1993, where he received the degree of Bachelor of Science in 1997. He was admitted to the Graduate School of The University of Texas at Austin in May 1998 and received the Master degree of science in 2000. In 2001, he was admitted and enrolled in the Aerospace Engineering and Engineering Mechanics Department.

Permanent Address: 1/5 Donmanaw, Songpinong
Suphanburi, Thailand, 72110

This dissertation was typeset with LaTeX 2_ε[1] by the author.

---

[1] LaTeX 2_ε is an extension of LaTeX. LaTeX is a collection of macros for TeX. TeX is a trademark of the American Mathematical Society. The macros used in formatting this dissertation were written by Dinesh Das, Department of Computer Sciences, The University of Texas at Austin, and extended by Bert Kay and James A. Bednar.